ISBN 978-82-326-3522-1 (printed version)
ISBN 978-82-326-3523-8 (electronic version)
ISSN 1503-8181

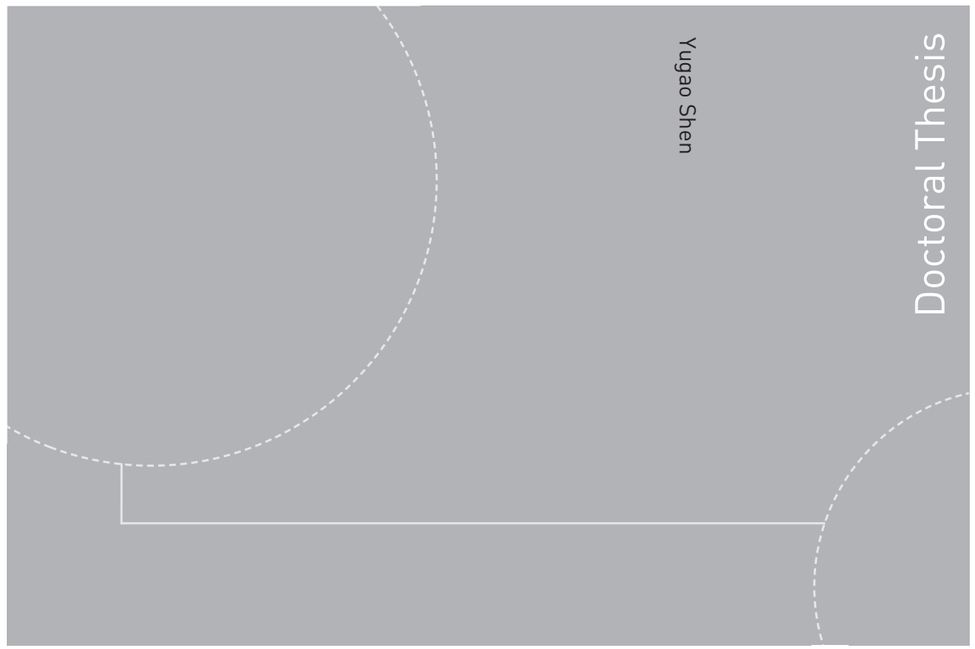

Doctoral theses at NTNU, 2018:367

Yugao Shen

Operational limits for floating-collar fish farms in waves and current, without and with well-boat presence

NTNU
Norwegian University of
Science and Technology

Doctoral theses at NTNU, 2018:367

NTNU

NTNU
Norwegian University of
Science and Technology
Faculty of Engineering Science and Technology
Department of Marine Technology

NTNU
Norwegian University of
Science and Technology

Yugao Shen

Operational limits for floating-collar fish farms in waves and current, without and with well-boat presence

Thesis for the degree of Philosophiae Doctor

Trondheim, November 2018

Norwegian University of Science and Technology
Faculty of Engineering Science and Technology
Department of Marine Technology

NTNU
Norwegian University of
Science and Technology

NTNU
Norwegian University of Science and Technology

Thesis for the degree of Philosophiae Doctor

Faculty of Engineering Science and Technology
Department of Marine Technology

ISBN 978-82-326-3522-1 (printed version)
ISBN 978-82-326-3523-8 (electronic version)
ISSN 1503-8181

Doctoral theses at NTNU, 2018:367

Printed by Skipnes Kommunikasjon as

Abstract

Dynamic response of a floating circular collar-type fish farm, without and with well-boat presence, in current, regular and irregular waves is analyzed. A modern design well boat and a realistic fish farm (with single cage) are considered. The latter comprises a floating collar, an elastic sinker tube, a flexible-closed net cage and a complex mooring system. The main purpose is to determine the operational conditions for the isolated fish farm and for the well boat-fish farm system. This study involves theoretical development, numerical investigations and analysis of experiments on a realistic fish-farm model (not carried out in this research).

A time-domain numerical solver for the fish farm is developed with the different components modeled with the state-of-the-art theoretical and numerical formulations. For instance, the motions of the floating collar and the sinker tube are described by a curved beam equation with consideration of axial stiffness and curvature effects. In terms of the net cage, the net twines are modeled as linear elastic trusses. The hydrodynamic loads on the net cage are estimated by the screen-load model, which accounts for hydrodynamic net-shadow and Reynolds number effects. Proper strategies are suggested to deal with the coupling between the different components and a solution algorithm, with a criterion to prevent unphysical negative net tensions, is proposed. The modeling of the different components is validated by comparing against documented experiments, involving simplifications of the various components.

The validated numerical tool is used to analyze a realistic aquaculture fish-farm system (with single cage). The mooring loads obtained from the numerical simulations are compared against available experimental data. Satisfactory agreement is demonstrated both in regular and irregular waves. A sensitivity analysis is also performed to identify important parameters influencing the mooring loads, showing which net cage related parameters are crucial. The operational limits of the fish farm are determined through systematic simulations in regular waves and current, indicating that the net volume reduction is the main constraint preventing the studied fish farm operating in more exposed regions.

Theoretical models of a well boat operating at a fish farm in current and in long-crested irregular waves and current are also introduced. The transverse viscous loads on the boat are estimated based on the cross-flow principle and the corresponding drag coefficients are evaluated based on an empirical approach accounting for Reynolds number, rigid free-surface condition, three-dimensional flow at ship ends, Keulegan-Carpenter number and the ratio between current velocity

and a characteristic wave velocity. The proposed estimation strategy is validated by available experimental results. The coupling between the well boat and fish farm is carefully modeled. The numerical modeling of the slow-drift motions of the well boat, in particular the slow-drift sway motion, is outlined and verified by comparing the mean value and standard deviation of the motion from time-domain and frequency-domain solutions. The importance of different slow-drift damping terms is also discussed.

A physical investigation of the coupled system in long-crested irregular waves and current is then performed. The most critical scenario with the well boat placed at the weather side of the fish farm is analyzed in detail. From the simulations, the well-boat presence will significantly increase the maximum anchor loads and the maximum floating-collar stress, which are two important variables for the structural integrity of the fish farm. In particular, an increment of more than 300% is observed for both variables in moderate exposure sea states. A sensitivity study is also performed to figure out important parameters influencing the two variables and the possibility to increase the computational efficiency by simplifying the modeling. The results highlight that the netting has a small influence on the maximum floating-collar stress when current is present. Systematic simulations are also performed to determine the operational conditions of the coupled system. Numerical results show that the maximum stress in the floating collar can be close to the yield stress when the system operates in moderate exposure sea states, thus it should be of major concern.

The applicability of using equivalent regular waves to represent irregular waves is also discussed in terms of the mooring loads. For the isolated fish farm, the mooring loads in equivalent regular waves are of similar magnitude, but generally more conservative than those in irregular waves.

Preface

This thesis is submitted to the Norwegian University of Science and Technology (NTNU) for partial fulfilment of the requirements for the degree of philosophiae doctor (PhD).

This doctor work has been carried out at the Center for Autonomous Marine Operations and Systems (AMOS), Department of Marine Technology, NTNU, Trondheim, with Professor Marilena Greco as the main supervisor and with Professor Odd M. Faltinsen at Department of Marine Technology, NTNU and Dr. Arne Freidheim from SINTEF Ocean AS as co-supervisors.

This work was financially supported by the Research Council of Norway through the Centers of Excellence funding scheme AMOS, project number 223254. This support is greatly appreciated.

Acknowledgements

First and foremost, I would like to express my sincere gratitude to my supervisor Prof. Marilena Greco for her guidance and supervision during my PhD study. She was always available when I needed help and could always provide valuable and enlightening suggestions. I am also deeply impressed by her passion and enthusiasm on scientific research. I also would like to extend my gratitude to my co-supervisor Prof. Odd M. Faltinsen for his great contribution to this thesis. His immense knowledge and practical ways to solve problems benefited me a lot. His encouragement and patience during our many discussions motivated me to complete this work.

In addition, I want to thank my co-supervisor Dr. Arne Fredheim and Mr. Ivar Nygaard from SINTEF Ocean AS for providing the valuable experimental data for a realistic fish farm. This has been essential for the more in-depth analysis in the thesis. I am grateful to Dr. Egil Jullumstrø and Rolls-Royce Marine for providing the geometry information of the well boat.

I want to thank Dr. Peng Li for his help with the use of the software WAMIT and Bureau Veritas for the free access of HydroStar. The help from Dr. Guillaume de-Hauteclocque for the practical use of HydroStar is also acknowledged. I appreciate the valuable discussions with Prof. Trygve Kristiansen, Dr. Mohsen Bardestani, Dr. Zhaolong Yu, Isar Ghamari, Finn-Christian W. Hanssen, Shaojun Ma and Mohd Atif Siddiqui. I am thankful to my friends and colleagues at NTNU, Dr. Xiaopeng Wu, Dr. Lin Li, Dr. Zhengshun Cheng, Dr. Wei Chai, Zhao He, to name a few who have always been helpful. The kind help from the administrative staffs is also greatly appreciated.

My deepest gratitude goes to my family in China for their love and understanding, and to my girlfriend Jingxing for her support and encouragement.

Nomenclature

General Rules

- Only the most used symbols are listed in the following sections
- Meaning of symbols are given when introduced in the thesis
- Sometimes the same symbol is used to indicate different quantities
- Vectors are represented by bold symbols

Abbreviations

2D	Two-dimensional
3D	Three-dimensional
CFD	Computational Fluid Dynamics
COG	Center of gravity
FEM	Finite Element Method
HBEM	High-order Boundary Element Method
HDPE	High-density polyethylene
JONSWAP	Joint North Sea Wave Project
WAMIT	Linear frequency-domain potential-flow solver

Bold Symbols

$\mathbf{a}$	Acceleration vector
$\mathbf{F}$	Force vector
$\mathbf{n}$	Normal vector
$\mathbf{u}$, $\mathbf{U}$	Velocity vector
$\mathbf{x}$	Position vector

Greek and Mathematical Symbols

α_c	Current angle
α_w	Incident wave angle
β	Radial angle along the floating collar
Δt	Time step
γ	Flow reduction coefficient; spectrum peakedness

λ	Wave length
ν	Kinematic viscosity of water
ω	Circular wave frequency
ω_e	Frequency of encounter
Φ	Error function
ρ	Mass density of water
σ	Standard deviation; stress
$\sum$	Summation
θ	Angle between the normal of the net panel and local inflow
ε	Phase angle defined in degrees
φ_0	Incident wave potential
ζ	Instantaneous incident-wave elevation
ζ_a	Wave amplitude of incident waves
η_k	Displacement ($k = 1, 2, ...6$ represents surge, sway, heave, roll, pitch and yaw, respectively

Roman Letters

(x_f, y_f, z_f)	Motions of the floating collar
$\bar{B}_{22}^{SD}$	Mean wave-drift damping in sway
$\bar{F}_2$	Mean wave load in sway
a_n	Generalized coordinate of vertical $\cos(n\beta)$ mode
$a_{11}^{(n)}$	Sectional horizontal added mass coefficient of mode n
$a_{33}^{(n)}$	Sectional vertical added mass coefficient of mode n
B_D	Eddy-making damping
b_n	Generalized coordinate of vertical $\sin(n\beta)$ mode
$b_{11}^{(n)}$	Sectional horizontal damping coefficient of mode n
B_{22}^{e}	Equivalent linear damping coefficient
B_{22}^{SD}	Slow-drift damping in sway
B_{22}^{WD}	Wave-drift damping in sway
$b_{33}^{(n)}$	Sectional vertical damping coefficient of mode n
C_D	Drag force coefficient
C_F	Frictional coefficient
c_f	Radius of the cross section of the tube
C_M	Mass coefficients
c_n	Generalized coordinate of radial $\cos(n\beta)$ mode
C_{22}	Restoring coefficient in sway

C_X	Quadratic damping coefficient in surge
D	Diameter of the net cage; draft of the well boat
d_f	Diameter of the cross section of the tube
d_n	Generalized coordinate of radial $\sin(n\beta)$ mode
d_w	Net-twine diameter
EI_H	Structural bending stiffness in horizontal direction of the floating collar
EI_V	Structural bending stiffness in vertical direction of the floating collar
F_2^{SV}	Slow-drift excitation force in sway
F_D	Drag force
f_p	Frequency of spectral peak in [HZ]
g	Acceleration of gravity
H	Wave height of incident regular wave
H_s	Significant wave height of incident irregular wave
k	Wave number
k_c	Contact stiffness
$k_{11}^{(n)}$	Sectional horizontal retardation function of mode n
$k_{33}^{(n)}$	Sectional vertical retardation function of mode n
l, L	length
N_H	Number of trusses in horizontal direction
N_h	Number of horizontal structural modes
N_V	Number of trusses in vertical direction
N_v	Number of vertical structural modes
$O_B x_B y_B z_B$	An Earth-fixed Cartesian coordinate system with origin in position O_B
$O_E x_E y_E z_E$	An Earth-fixed Cartesian coordinate system with origin in position O_E
$O_F x_F y_F z_F$	An Earth-fixed Cartesian coordinate system with origin in position O_F
p	Center-to-center distance between the two tubes of the floating collar
$S(f)$	Wave spectrum
T	Wave period of incident regular waves
t	Time
T_p	Peak wave period of incident irregular waves; pre-tension
T_n	Natural period
U_M	Velocity amplitude of incident oscillatory flow

V	Net-cage volume
v_f	Local horizontal (radial) elastic deformation of the floating collar
w_f	Local vertical elastic deformation of the floating collar
w_s	Mass per meter of the sinker tube
KC	Keulegan-Carpenter number
Rn	Reynolds number
Sn	Solidity ratio

Super-scripts

n	Mode n; time instant n
(1)	First-order motion
(2)	Slow-drift motion

Sub-scripts

r	horizontal modes of the floating collar
z	Vertical modes of the floating collar
0	Nominal value

Contents

Chapter 1

Introduction

1.1 Background and motivation

According to the Food and Agriculture Organization of the United Nations (FAO), the world's population is expected to increase with 2 billion, reaching up to 9.73 billion by 2050 (FAO, 2017). This raises a challenge of how we can meet the growing demand of food while still guarantee sustainable development of natural resources. The total bio production measured in calories is equally divided between land and water (Field et al., 1998). However, only about 2% of the food production used for human consumption comes from water, while at the same time, the land and water resources available to grow more food on land is becoming scarce (FAO, 2006). So increasing food production from the sea may be a better alternative to further land development. Owing to the excess fishing pressure, about 31 percent of marine fish stocks were estimated to be either overexploited (28 percent) or depleted (3 percent) (FAO, 2010). So current over-exploitation in wild fisheries means that fisheries cannot provide a sustainable solution. According to FAO (2016), output from aquaculture has become the major source of fish for human consumption and is expected to overtake total output from captured fisheries by 2021. Land-based aquaculture and marine-based aquaculture are the two basic concepts of aquaculture and the fish farming is the most common form of aquaculture. Expansion of land-based aquaculture and coastal aquaculture faces constraints because of an increasing lack of suitable land and water sites and possible conflicts with other users. For these reasons, it is believed that the expansion of aquaculture into deeper and less sheltered marine waters is a high priority and should be facilitated through research, development and appropriate regulatory management (Lovatelli et al., 2013). Offshore aquaculture takes place in the exposed areas where fish-farm structures are subjected to strong wind, waves and current. The equipment and servicing vessels also need to operate and survive in severe sea conditions. In order to guarantee the reliability and integrity of the fish farm structures and safe servicing vessel operations at the fish farm, more research needs to be performed. This is the main motivation for the present work.

1.1.1 Norwegian aquaculture nowadays

The development of commercial aquaculture in Norway began around 1970, since that time aquaculture has developed into a major industry in coastal areas (FAO, 2005). In 2016, the produced salmon from the industry reached a value of more than 60 billion NOK, see Figure 1.1. The industry has a goal that within 2050 the production volume of the industry shall reach a value of 5 million tons, which represents a 5-fold increase in production volumes than nowadays (Trude et al., 2012). A prerequisite is that the industry is able to manage the environmental challenges and able to procure sufficient food for the fish.

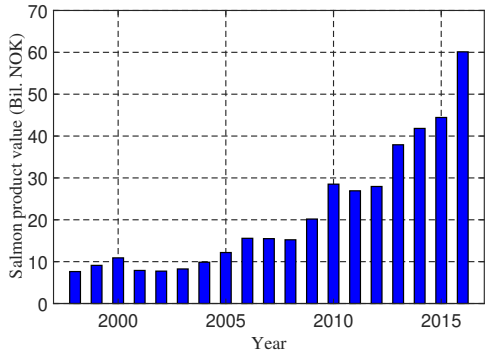

Figure 1.1: Product value (in Billion NOK) of salmon in Norway from 1996 to 2016 (Norwegian Directorate of Fisheries, 2017).

There exit also multiple challenges for the Norwegian fish-farm industry nowadays. One of the big problems has been the rise of sea lice. It has become increasingly serious as the sea lice have become more resistant to chemicals used to treat them. Escaped fish is another concern. Damages and collapses of floating fish farms have led to escape of fish and thereby major economic losses, as well as pollution, with risk for the surrounding ecosystem and wild fish. Damages can be caused by operational failures, breaking of mooring lines, anchor pull out, contacts between chains or ropes with the net or collisions with ships. In addition, due to limited nearshore area and increasing impact to the local eco-system, the Norwegian aquaculture industry is trying to move the fish farms from nearshore to more exposed sea regions where waves and current are stronger. This will greatly increase the probability of structural failure, consequently fish escape. All these challenges call for more investigations and novel designs.

1.1.2 Fish-farm concepts

There exists a variety of fish-farm concepts and these concepts can be classified in different ways. For example, Loverich and Gace (1997) classified sea cages into four types based on the structural means used to hold the shape of the cage, i.e. gravity cages, anchor-tension cages, semi-rigid cages and rigid cages. Ryan (2004) proposed one more type, named tension-leg cages, and mentioned other cage designs that

are difficult to categorize. Detailed examples of different fish-farm types are also provided. Table 1.1 illustrates cage types likely to be used in different sites shown in Figure 1.2.

Table 1.1: Cage types likely to be found in sites of Classes 1-4 (Ryan, 2004).

Class	Site Description	Cage Type Used
1	Sheltered Inshore Site	Surface Gravity
2	Semi-Exposed Inshore Site	Surface Gravity
3	Exposed Offshore Site	Surface Gravity, Anchor Tension
4	Open Ocean Offshore Site	Surface Gravity, Surface Rigid, Anchor Tension, Submerged Gravity, Submerged Rigid

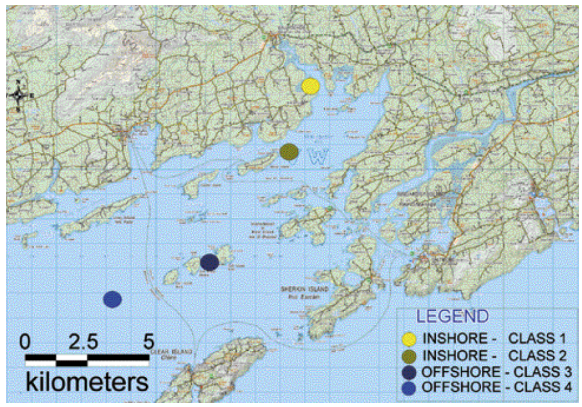

Figure 1.2: The site classification scheme (Ryan, 2004).

The gravity cages are by far the most widely used concepts in the fish farming industry both in Norway and abroad, thus are explained in detail here. They rely on the force of gravity to maintain net volume, by providing a surface buoyancy system and an underwater weighting system for the net. An intrinsic characteristic of the gravity cage in conventional configuration is its susceptibility to net deformity and volume loss in currents and wave action, which is a result of a lack of support structure for the net (Ryan, 2004). There exits different materials and geometries of the buoyancy system. The most commonly used in Norway are the circular plastic floaters and the interconnected hinged steel floaters, as shown in Figure 1.3. The cage with circular plastic floaters will be the research focus of the present thesis, thus a detailed description of the cage is given below.

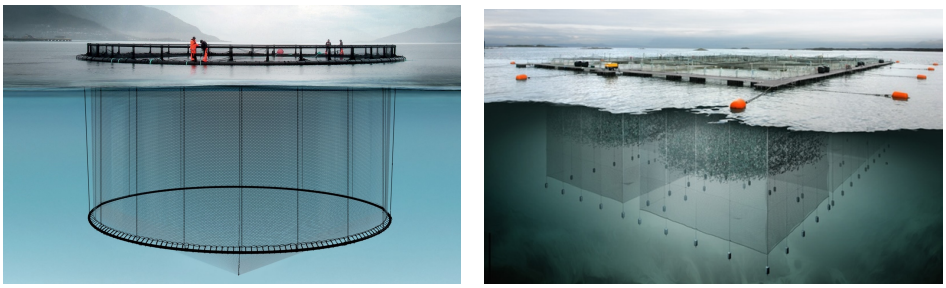

Figure 1.3: Left: circular plastic cage (www.akvagroup.com). Right: hinged square steel cages (www.egersundnet.no).

Cage with circular plastic floater

Figure 1.4 shows the sketch of a typical fish cage with circular plastic floater used in Norway, including all the main components, i.e. a floating collar, a net cage, a sinker tube and a mooring system.

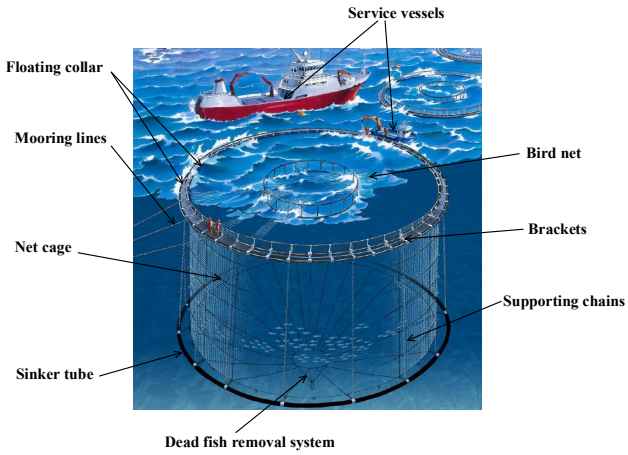

Figure 1.4: Sketch of a typical fish cage with circular plastic floater (www.aqualine.no).

The floating collar provides buoyancy for the whole system and is common with two nearly semi-submerged concentric circular tubes. The two tubes are held together by steel brackets and the high-density polyethylene (HDPE) is widely used as their main material. The usage of the net is to protect the fish from predators and provide a suitable habitat. The most common materials for nets and ropes are nylon or polyamide (PA), polyester (PES), polypropylene (PP) and high-performance polyethylene (Dyneema or Spectra). The net is highly flexible, so it will experience deformation when subjected to external loads from waves and

current. A bottom weight ring (sinker tube) is often attached to the cage bottom to ensure sufficient volume of the net cage. In reality, there exist multiple cages at real sites with cages arranged in mooring grid in single or double rows, see the upper plot in Figure 1.5. The mooring system normally used by the HDPE circular cages is a square-shaped grid system held on the seabed with an array of mooring lines. The mooring system is divided in two main groups of components, the mooring lines and the grid system; see the lower plot in Figure 1.5. The mooring lines include the anchors, ground chains, ropes and related shackles, and buoys. The grid system includes the frame ropes, mooring buoys, connector rings or plates, bridles, and related shackles (FAO, 2015). Similar material as that for the nets is used for the ropes in the mooring system.

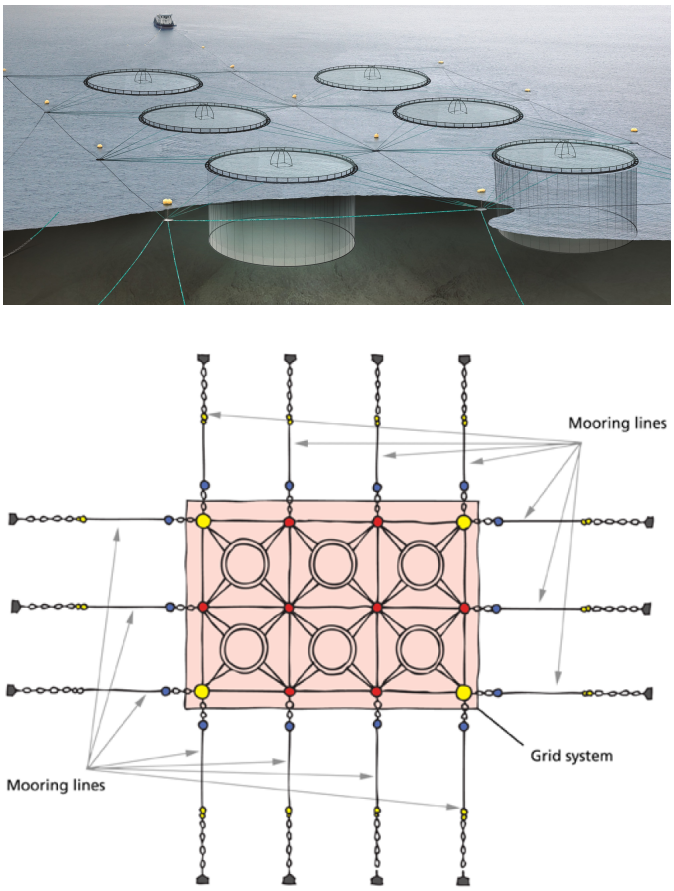

Figure 1.5: Upper: cage and mooring arrangement at real fish-farm sites (www.akvagroup.com). Lower: sketch of grid system and mooring lines in a framing module of six cages (FAO, 2015).

Novel fish-farm concepts

To meet the challenges faced by the Norwegian fish-farm industry (see Section 1.1.1), new fish-farm designs are emerging. Closed fish-cage concepts are proposed to have a better control over the water quality, and especially to avoid the problem of salmon lice. The closed cages can be divided into flexible cages, semi-flexible cages and rigid cages. New open cage fish-farm concepts are also under development to operate in more exposed sea regions or even in open sea, by combining the best of existing technology and solutions from the Norwegian fish farming industry and the offshore oil and gas sector. Two examples are given here, i.e. the rigid semi-submersible fish farm developed by the Ocean Farming AS and the vessel-shaped fish farm proposed by the Nordlaks Company, see Figure 1.6.

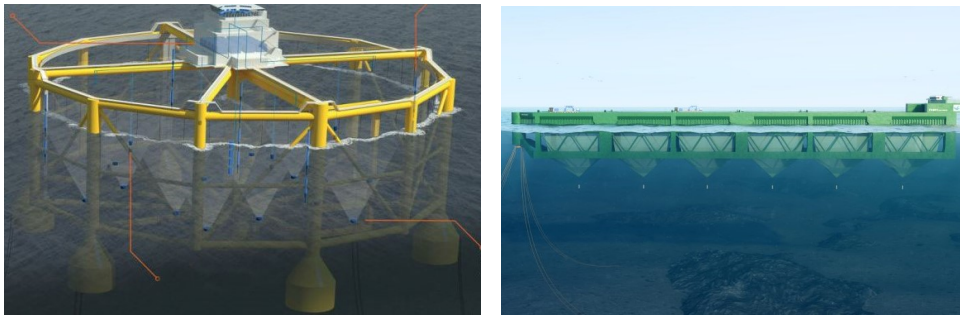

Figure 1.6: Left: rigid semi-submersible fish farm (www.km.kongsberg.com). Right: vessel-shaped fish farm (www.nskshipdesign.com).

1.1.3 Challenges for operating fish farms in more exposed regions

The expansion of near shore aquaculture is getting more difficult due to the shrinking of available sheltered near-shore place and increasingly environmental impacts. In addition, the size of the fish farms is expected to increase and sufficient water exchange inside the net is essential to guarantee the welfare of the fish. Therefore, more fish farms will operate at more exposed sea regions where waves and current are more energetic. An idea about wave and current conditions at different exposure sites can be found in Table 1.2. Operating fish farms in strong waves and current enlarges the risk of structural failure and consequently fish escape, which is a major issue for fish farms. A detailed discussion about the challenges faced by the floating-collar fish farms with circular fish cages is given below.

Waves and current loads affect the various components of a floating-collar fish farm in different ways. The floating collar will tend to follow long waves and will deform considerably or even collapse in very severe sea states. Since the floating collar provides buoyancy for the whole system, its failure will endanger the integrity of the complete fish-farm system. The net cage will deform significantly in strong current and thereby lead to a strong reduction of the net cage volume. The latter

Table 1.2: Environmental classification given in terms of significant wave height H_s, peak period T_p and current velocity U_∞ according to Norwegian Standard NS9415 (2009). It is assumed irregular waves for each wave class. If regular wave is considered, the standard says that the corresponding wave height H can be assumed to be 1.9 times the significant wave height.

Wave	H_s(m)	T_p(s)	**Exposure**	**Current**	U_∞(m/s)	**Exposure**
A	0.0 - 0.5	0.0 - 2.0	Small	a	0.0 - 0.3	Small
B	0.5 - 1.0	1.6 - 3.2	Moderate	b	0.3 - 0.5	Moderate
C	1.0 - 2.0	2.5 - 5.1	Heavy	c	0.5 - 1.0	Heavy
D	2.0 - 3.0	4.0 - 6.7	High	d	1.0 - 1.5	High
E	>3.0	5.3 - 18.0	Extreme	e	>1.5	Extreme

is important to guarantee the fish welfare. The netting may consequently get in contact with the weight rope or with the chains supporting a bottom weight ring with the possibility of damaging the netting. A not properly designed bottom weight ring may considerably deform in severe weather conditions and damage the net. Large snap loads due to the relative motion between the floating collar and the net/mooring lines can occur. Mooring lines may break due to high waves and current loads on the fish farm. In order to guarantee the robustness of the fish farms, it is necessary to check the survival conditions of them and the possibilities to use them in exposed regions. To achieve this goal, a reliable prediction of the hydrodynamic forces and motions of each part of the fish-farm system under waves and current is necessary.

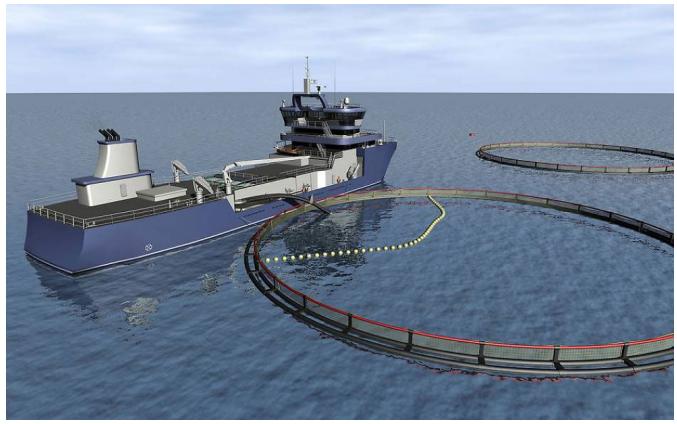

Figure 1.7: Sketch of a well boat operating at a fish farm (www.tu.no).

Apart from the challenges from the fish farm perspective, operating fish farms in exposed areas will also increase the probability of service-vessel, in particular well-boat, routine operations in severe weather conditions. A well boat is a fishing vessel with a well or tank for the storage and transport of live fish, and is essential to ensure the fish welfare. A typical well-boat operation can be categorized into three

phases: approaching, loading/offloading and leaving. During the loading/offloading phase, the well boat is moored directly to the fish farm, see Figure 1.7. Large relative motion between the well boat and the floating collar makes it difficult to perform loading/offloading operations in severe sea states. Also, the well boat has comparable size of the fish farm, connecting the well boat directly to the net cage can significantly increase the mooring loads and the floating collar deformations and thus endanger the structural integrity of the fish farm. Therefore, there is also a need to have a detailed investigation of the influence of the well boat on the fish farm and identify the operational conditions for performing such loading/offloading operation.

1.2 Previous studies

In the present work, the focus is on the floating-collar fish farm with circular open cages. Many documented investigations have been done to examine the responses of this system from structural and hydrodynamic perspective by model tests and numerical simulations. A detailed review of most recent studies on the topic can be found in Shen et al. (2018) and Faltinsen and Shen (2018) and is outlined below.

1.2.1 The floating collar

Kristiansen and Faltinsen (2009) presented model test results in two-dimensional (2D) flow conditions of a semi-submerged floater without netting in regular waves and validated a CIP-based finite difference method that solved Navier-Stokes equations for laminar flow with a one-fluid representation of air and water. The Computational Fluid Dynamics (CFD) calculations illustrated that overtopping of waves and flow separation can matter.

Li et al. (2016, 2018) studied experimentally and theoretically vertical accelerations of a moored floating elastic torus without netting in regular waves of different steepnesses and periods in deep water. Wavelengths of practical interest are of the order of the torus diameter but long relative to the cross-sectional diameter. An Euler beam model with additional curvature and axial tension effects was applied for vertical torus deformations. Three-dimensional (3D) flow, hydroelasticity and strong hydrodynamic frequency dependency matter. Strip theory is normally adopted to model the hydrodynamic loads on the floating collar, for example in Huang et al. (2006), Dong et al. (2010), but this may lead to a poor approximation of generalized added mass, damping and wave excitation loads, in particular for vertical loads. The experimental vertical accelerations showed increasing importance of nonlinearities and higher harmonics with increasing wave steepness. Wave overtopping occurred in the steepest waves. A linear frequency-domain potential-flow method gave satisfactory predictions of the first harmonic component of vertical accelerations. This was true both using state-of-the art boundary element methods as well as the low-frequency linear slender-body theory by Li and Faltinsen (2012). The second-harmonic acceleration component can partly be explained by a second-order theory for low wave steepnesses, i.e. higher-order effects affect the

second-harmonic acceleration component even at low wave steepness. The experiments showed that the third and fourth harmonic acceleration components matter and cannot be explained by a perturbation method with the wave steepness as a small parameter. Ideally, we need a fully nonlinear 3D CFD method that accounts for hydroelasticity to capture the features highlighted by the experiments.

1.2.2 The net cage

The fact that the netting may have 10 million meshes limits the use of CFD and complete structural modeling. Kristiansen and Faltinsen (2012) proposed an experimentally based screen type of force model for the viscous hydrodynamic load on nets in ambient current. The model divides the net into a number of flat net panels, or screens. The knots are neglected, and circular twine cross-sections are assumed. The force components on a panel are functions of the solidity ratio, the inflow angle and the Reynolds number. The solidity ratio is for a plane netting the ratio of the area of the shadow projected by wire (twine) meshes on a plane parallel to the screen to the total area contained within the frame of the screen. The relevant Reynolds number is that based on the physical twine diameter. Shielding effects by the twines are implicitly accounted for. A uniform turbulent wake is assumed inside the cage based on the theoretical formula proposed by Løland (1991) for cross-flow past a plane net. The fact that some of the incident flow goes around the net cage is neglected. The latter effect gets increased importance with increasing solidity ratio. Kristiansen and Faltinsen (2012) used the dynamic truss model by Marichal (2003) to describe the net structure. Number of trusses and their arrangement follow from convergence studies. It is unnecessary to represent the net cage with a fine numerical mesh. The net shape is solved in a time stepping procedure that involves solving a linear system of equations for the unknown tensions at each time step. It means that the problem in current only is solved as an initial value problem instead of iterating to find the steady net configuration. Satisfactory agreement between experimental and numerical prediction of drag and lift on circular bottomless net cages in steady current as function of the solidity ratio of the net and of the current velocity is documented. The latter is not true for large current velocities when Morison's equation is applied, which is normally used to estimate the net cage hydrodynamic load (e.g. Xu et al. 2013, Shainee et al. 2014). The reason is associated with large net deformation and shielding effects of twines.

Kristiansen and Faltinsen (2015) investigated the mooring loads on an aquaculture net cage in current and waves by model tests and numerical simulations. Their net model was generalized to combined waves and current and by applying the wake model inside the cage only to the steady flow. The net cage is bottomless, flexible and circular. It is attached to a circular, elastic floater at the top and has 16 sinker weights at the bottom. The system is nearly linearly moored with four crowfeet mooring lines. The mean loads in general dominate over the dynamic part of the loads in combined current and waves, and they significantly increase in long and steep waves, relative to current only. Numerical calculations showed that a rigid floater significantly alters the loads in the mooring lines compared to a

realistic, elastic floater. The theoretical model for the wave matters. The mooring loads are rather insensitive to frequency dependent added mass/damping and to nonlinear Froude-Kriloff and hydrostatic restoring loads on the floater.

The fluid-structure interaction for the net cage is gaining increasingly more attention. Zhao et al. (2013), Bi et al. (2014) and recently Yao et al. (2016) studied the flow inside and around a fish cage in current by solving the Navier-Stokes equation. The net was taken as a porous medium. Both rigid and flexible cages were investigated. Their studies showed that numerical results would overestimate the hydrodynamic loads on the cage when compared with the experimental data if the effect of fluid-structure interaction is not considered. Although it maybe questionable to consider the net cage as porous medium (most common practice), their work is valuable to show us the effect of considering the fluid-structure interaction.

In addition, Bardestani and Faltinsen (2013) studied experimentally and theoretically snap loads in the netting in two-dimensional conditions in waves; the reason was independent relative vertical motions of the floater and sinker tube. Reasonable agreement between theory and experiments was documented. They pointed out that the net experienced cyclic snap loads in higher wave amplitudes and periods which could also happen for full-scale offshore fish farms and should be of concern for the net design.

1.2.3 Influence of fish on the mooring loads

He et al. (2018) studied experimentally the influence of fish in a net cage on mooring loads. Model tests in scale 1:25 were performed with more than 800 salmon of length 16cm inside a net cage in waves and current. The salmon occupied approximately 2.5% of the net cage volume at rest, which is representative for a full-scale condition. If the fish touched the netting in current, there was more than 10% increase in the mooring loads. Numerical calculations were made by changing the solidity ratio in the contact area between the fish and the net in such way that the numerical net configuration agreed with the experimental one. Good agreement between numerical and experimental values were obtained consequently. If the fish did not touch the netting, the loading influence was the order of 3%. An important question is if the fish behavior is representative for a full-scale scenario. If the fish do not touch the netting, an estimate of the net loading can be made as follows. The fact that the fish displaces the water causes a flow and can be analyzed for a single fish by slender-body potential-flow theory; a first-order approximation of the far-field behavior can be obtained by summing up the individual contribution from each fish in terms of source distributions without considering the hydrodynamic interaction between the fishes. The latter procedure combined with the effect of local ambient flow and realistic fish speeds, enables to assess the importance of corresponding net loading by using the screen-force model by Kristiansen and Faltinsen (2012). However, there are in addition a viscous wake due to the fishes and a flow caused by fish propulsion, which need to be quantified. The waves could cause the fish to go to the bottom of the net cage resulting in a non-negligible experimentally documented increase in mooring loads.

1.2.4 Well-boat influence on a fish farm

Little research has been done for the scenario when a well boat operates at the fish farm. In particular, to the author' knowledge no experimental study has been carried out so far. Jia et al. (2012) investigated numerically the hydrodynamic coupling between a well boat and a rigid torus using a linear potential-flow solver in the frequency domain. The well boat was placed at the weather side of the torus and beam-sea regular waves were considered. They showed that the wave excitation forces of the torus were more affected by the well boat in shorter waves (wave period $T \leq 6$s). The detailed influence of the well boat on the fish farm was not considered. The effect of the well boat is seldom considered in the design of fish farms.

1.3 Outline of the present thesis

This thesis focuses on the operational limits of floating-collar fish farms in waves and current, and examines well-boat presence. The performed research is documented in seven chapters, organized as follows.

Chapter 1: presents the background and motivation of the present thesis, gives an overview on previous studies of the floating-collar fish farm, outlines the thesis structure and summarizes the main research contributions and physical findings.

Chapter 2: introduces the theoretical model for each individual component of a realistic floating-collar fish farm (with single cage). The structural model and hydrodynamic-load model for the different components are provided. The coupling of the equations of motion for the different components and the time-evolution strategy for the complete system are explained.

Chapter 3: presents the assessment of the numerical modeling adopted for the different fish-farm components by comparing against experimental data available in literature. A sensitivity analysis is also performed to examine the influence of using alternative numerical models.

Chapter 4: presents a numerical and experimental investigation on mooring loads of a realistic floating-collar fish farm (with single cage) in waves and current. Both regular and long-crested irregular waves are examined. Numerical sensitivity analysis is also performed to identify important parameters influencing the mooring loads. Survival conditions of the fish farm are also determined.

Chapter 5: introduces numerical modeling of a well boat operating at a fish farm in current only and in combined long-crested irregular waves and current. The transverse viscous loads on the boat are obtained by using the cross-flow principle and the cross-sectional drag coefficients are estimated empirically and validated against available experiments. The strategy used for the well boat-fish farm coupling is also explained. Theory for predicting the slow-drift motions of the well

boat in irregular waves is outlined.

Chapter 6: presents the numerical results of a well boat operating at a fish farm in current only and in long-crested irregular waves and current. The modeling of the slow-drift motions of the well boat is verified and the influence of the well boat on the fish farm is quantified. The operational conditions of the well boat when operating at the fish farm are also determined.

Chapter 7: presents general conclusions of this study and suggestions for further work.

1.4 Main contributions

The main scientific contribution of the present work is summarized in the following.

An efficient and reliable time-domain numerical solver is developed to predict the response of a realistic floater-collar fish farm (with single cage), with and without well-boat presence, in current, regular and irregular waves. The operational conditions for the isolated fish farm and for the well boat-fish farm system are determined through systematic simulations. The developed numerical solver makes the statistical analysis of the fish farm (e.g. mooring loads and floating-collar stress), without and with well-boat presence, possible. Contributions that are more detailed are outlined below separately for the fish farm only and for the coupled well boat-fish farm system from the theoretical and physical perspectives.

1.4.1 Fish-farm system

Theoretical contribution

- The theoretical model proposed by Li et al. (2016) for predicting the vertical response of an isolated-elastic floating torus with symmetric loading is generalized to solve the motions (in horizontal and vertical directions) of a floating collar with two concentric tubes in generic environmental conditions.
- The structural and hydrodynamic-load model for a simplified bottomless net cage in regular waves and current from Kristiansen and Faltinsen (2012, 2015) is generalized to study more realistic closed fish cage in both regular and irregular sea states. A simplified method is proposed (and validated) to model the flow around the net cage in current by using Lagally's theorem.
- The complete set-up of the mooring system, which comprises ropes, chains and cylindrical buoys, is properly modeled.
- A new coupling strategy, based on an explicit solution algorithm, is proposed to increase computational efficiency and to make the developed solver easily applicable for other open cage fish-farm concepts. A convergence criterion is suggested to avoid unrealistic truss tensions in the simulations.

Physical findings

- For the anchor loads: the flow reduction in the rear part of the net cage is the most important phenomenon; modeling the flow around the net cage will improve the numerical prediction; modeling the floating collar as a rigid body, neglecting the axial stiffness and using zero frequency instead of the frequency-dependent added mass will lead to small error. Using the sinker tube or equivalent discrete sinker weights will yield similar mooring loads, but with larger net-cage volume reduction for the latter case.
- The dominant limit of operating the fish farm in more exposed areas is the net volume reduction. The maximum floating-collar stress and mooring loads are moderate, even in extreme sea states.
- Mooring loads in equivalent regular waves are of similar magnitude, but generally more conservative than those in irregular waves.

1.4.2 Coupled well boat-fish farm system

Theoretical contribution

- The transverse viscous loads on the boat in current only and in oscillatory flow and current are evaluated by the cross-flow principle and a systematic procedure, combining the use of available empirical formulas, was proposed to estimate the corresponding cross-sectional drag coefficients. The Reynolds number, rigid free-surface condition, three-dimensional flow at ship ends, Keulegan-Carpenter number and the ratio between current velocity and a characteristic wave velocity were accounted for. The approach was successfully validated by experiments available in literature.
- A direct method and an indirect method are proposed to deal with the contact between the well boat and the fish farm. When both are applicable, they provide consistent predictions. As the indirect method is more versatile and easy to implement, it is used in the investigations documented in the thesis.
- The well-boat shading effect on the net inflow is approximated by assuming that the mean velocity distribution behind the boat follows a plane mixing layer flow with curved shear layer.

Physical findings

- The well-boat presence significantly increases the floating collar horizontal deformations and anchor loads.
- The maximum floating-collar stress due to the horizontal deformations occurs at the region where contact happens.
- The maximum anchor load will not exceed the anchor-line breaking limit even in high exposure sea conditions. The maximum floating-collar stress could be close to its yield stress when the system operates in moderate exposure sea states.
- The technique to use equivalent regular waves is not applicable for well boat-fish farm system. In particular, unrealistic (too high) mean-drift loads occur in regular waves.

1.5 List of publications

The following papers submitted and published are considered part of this thesis.

Journal papers

- Shen, Y.-G., Greco, M. and Faltinsen, O. M. (2018a), Numerical study of a well boat operating at a fish farm in current, *Journal of Fluids and Structures*, accepted.
- Shen, Y.-G., Greco, M. and Faltinsen, O. M. (2018b), Numerical study of a well boat operating at a fish farm in long-crested irregular waves and current, *Journal of Fluids and Structures*, accepted.
- Shen, Y.-G., Greco, M., Faltinsen, O. M., Nygaard, I., 2018. Numerical and experimental investigations on mooring loads of a marine fish farm in waves and current. *Journal of Fluids and Structures* 79, 115-136.
- Faltinsen, O. M., Shen, Y.-G., 2018. Wave and current effects on floating fish farms. *Journal of Marine Science and Application, accepted.*

Conference paper

- Shen, Y.-G., Greco, M., Faltinsen, O. M., 2016. Numerical study of a coupled well boat-fish farm system in waves and current during loading operations. In: *The 12th International Conference on Hydrodynamics (ICHD 2016), Egmond aan Zee, The Netherlands.* Online proceedings, document No.98.

The following co-authored paper is considered background for the thesis.

Journal paper

- Yu, Z.-L., Shen, Y.-G., Amdahl, J., Greco, M., 2016. Implementation of linear potential- flow theory in the 6dof coupled simulation of ship collision and grounding accidents. *Journal of Ship Research* 60 (3), 119-144.

Chapter 2

Numerical modeling of a marine fish farm

In this chapter, theoretical models for different components of a realistic floating-collar fish farm are introduced. The fish farm typically comprises a floating collar with two concentric circular floating tubes, a cylindrical flexible net cage with a conical bottom, an elastic sinker tube and a complex mooring system. The structural model and hydrodynamic-load model for the different components are provided. For the floating collar, the motions are solved based on a generalized curved Euler-Bernoulli beam equation that accounts for axial tension and curvature effects. The hydrodynamic loads for both the rigid and elastic modes are modeled within linear potential-flow theory. Curved beam equations are also applied to the sinker tube and the hydrodynamic loads are calculated by a modified Morison's equation, based on the cross-flow principle and by neglecting the longitudinal forces. In terms of the net cage, the net twines are modeled as linear elastic trusses and the hydrodynamic, viscous loads acting on the net cage are estimated by the screen load model. The mooring lines are treated in a similar way as the net and are modeled as elastic trusses. The hydrodynamic forces on the mooring lines are also estimated by the modified Morison's equation, similarly as done for the sinker tube. Finally, the coupling strategy for the different components and how the complete system is evolved in time domain are explained.

2.1 General configuration and definitions of coordinate systems

The main arrangement of a typical floating collar fish-farm system is shown in Figure 2.1, including two concentric floating tubes in a torus configuration, an elastic sinker tube, a cylindrical net cage with a conical bottom and a mooring system comprising bridle lines, mooring frame lines, mooring buoys, coupling plates, chains connecting the coupling plates to the buoys and the anchor lines attaching the system to the seabed. Two different inertial and Earth-fixed coordinate systems are

also defined in the figure. One is the Cartesian right-handed coordinate system $O_E x_E y_E z_E$ with the vertical z_E-axis positive upwards through the center of the floating collar in calm water. The other is the Cartesian right-handed coordinate system $O_F x_F y_F z_F$ with origin O_F in the plane of undisturbed free surface $z_E = 0$ and the vertical z_F-axis positive upwards through the center of the floating collar while the horizontal x_F-axis points towards the wave direction. The incident wave angle α_w and current angle α_c are defined in the figure and α_w=0° means that the waves propagate in the positive x_E direction. The coordinate systems $O_F x_F y_F z_F$ and $O_E x_E y_E z_E$ coincide with each other when α_w=0°.

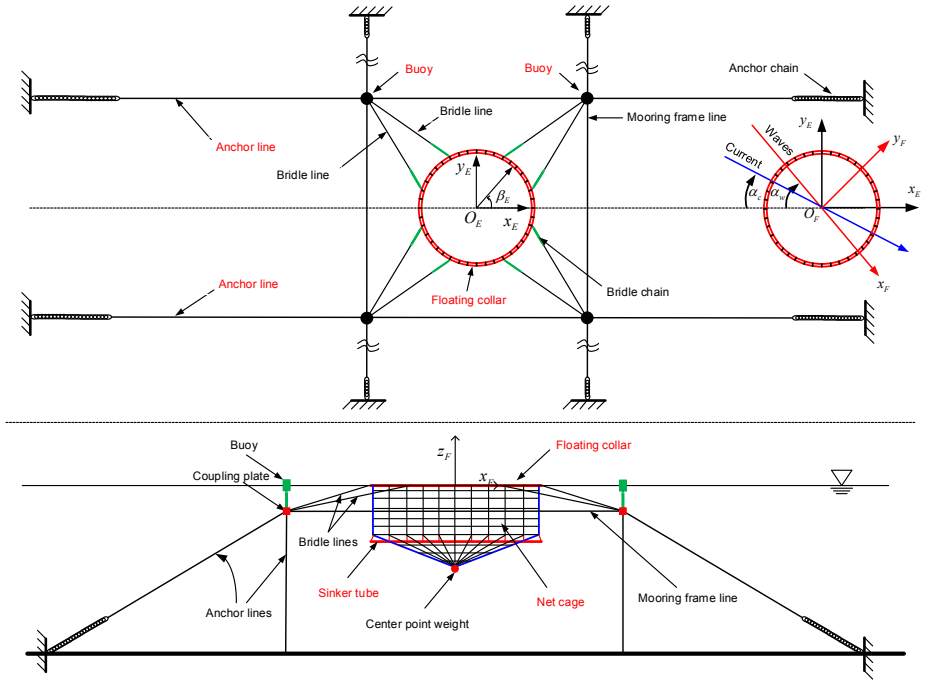

Figure 2.1: Configurations of the fish-farm system with definitions of two coordinate systems. Upper: top view. The floating collar is duplicated in the right part of the sketch to define current direction α_c and wave direction α_w. β_E is the radial angle along the floating collar, defined in the reference frame $O_E x_E y_E z_E$. Lower: side view.

2.2 The floating collar

In this section, the numerical modeling of the floating collar, including the structural model and hydrodynamic-load model, will be introduced. The floating collar of a gravity-type fish-cage system typically comprises two floating tubes, which are

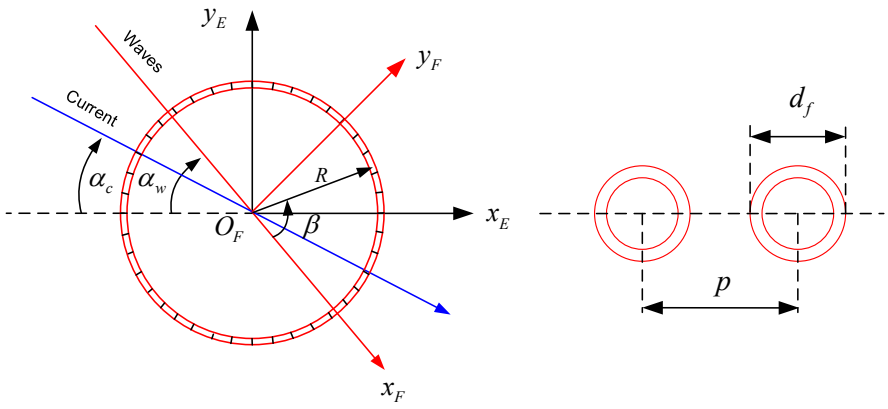

Figure 2.2: Left: zoomed top view of the floating collar and the coordinate systems shown in Figure 2.1. β is the radial angle defined with respect to the reference frame $O_F x_F y_F z_F$ and R is the mean value of the center line radius of the two tubes. Right: cross-section cut of the floating collar. p is the center-to-center distance between the two tubes and $d_f = 2c_f$ is the tube cross-sectional diameter.

placed with a center-to-center distance p, as shown in Figure 2.2. The motions of the floating collar with two concentric tubes are solved by generalizing the method proposed by Li et al. (2016) for predicting the motion of an isolated-elastic floating torus, based on a generalized Euler-Bernoulli beam equation that accounts for axial tension and curvature effects. In their study, linear hydrodynamic potential flow of incompressible water was assumed and waves were considered to be along the positive x_E-axis and consequently only modes symmetric about the x_E-axis could be excited.

In the present study, we will consider more general environmental conditions and both symmetric and asymmetric modes can be excited. To simplify the calculation of the wave excitation forces for different modes of the floating collar, the motions of the floating collar are defined and solved in the coordinate system $O_F x_F y_F z_F$, with positive x_F-axis pointing towards the wave direction. In this way, the incident wave angle with respect to x_F-axis is always zero, so the wave excitation forces for modes that are asymmetric about the x_F-axis is zero. For modes that are symmetric about the x_F-axis, the wave excitation forces can always be expressed by the values with zero incident wave angle, regardless of the actual incident wave direction in the coordinate system $O_E x_E y_E z_E$. This is valid only when the floating collar is circular, as in our case.

It is assumed that the floating collar is circular and half-submerged when at rest and its motions, (x_f, y_f, z_f), are assumed to be a combination of rigid-body motions as well as elastic perturbations around the original circular shape in lateral (radial) and vertical directions. They are expressed by the following Fourier series

$$\begin{aligned} x_f(\beta,t) &= c_1(t) + v_f(\beta,t)\cos\beta, \\ y_f(\beta,t) &= d_1(t) + v_f(\beta,t)\sin\beta, \\ z_f(\beta,t) &= a_0(t) + w_f(\beta,t) \end{aligned} \tag{2.1}$$

at time t and location identified by the radial angle β along the tube, with $\beta = 0^{\circ}$ corresponding to the x_F-axis, as defined in Figure 2.2. Here, the coefficients c_1, d_1 and a_0 represent surge, sway and heave rigid motions, while

$$\begin{aligned} w_f(\beta,t) &= \sum_{n=1}^{\infty}[a_n(t)\cos(n\beta) + b_n(t)\sin(n\beta)] \\ v_f(\beta,t) &= \sum_{n=2}^{\infty}[c_n(t)\cos(n\beta) + d_n(t)\sin(n\beta)] \end{aligned} \tag{2.2}$$

are the local vertical (not including heave) and the lateral (radial) elastic deformations, respectively. The terms $a_n\cos(n\beta)$ and $b_n\sin(n\beta)$ denote the vertical modes that are symmetric and anti-symmetric about the x_F-axis, respectively. Detailed mode shapes are shown in Appendix A. $a_1\cos\beta$ and $b_1\sin\beta$ are the vertical motion due to pitch and roll, respectively. $a_n\cos n\beta$ and $b_n\sin n\beta$, with $n \geq 2$, are purely vertical elastic modes. The coefficients c_n and d_n $(n \geq 2)$ are connected with the horizontal elastic radial mode n. A further transformation is needed if we want to have the motions in the coordinate system $O_E x_E y_E z_E$.

2.2.1 Curved beam equation

The vertical (w_f) and radial (v_f) structural response is assumed to obey the following beam equations

$$\begin{aligned} m_{2D}\frac{\partial^2 w_f}{\partial t^2} + EI_V\left(\frac{\partial^4 w_f}{\partial s^4} + \frac{1}{R^2}\frac{\partial^4 w_f}{\partial s^2}\right) - \frac{\partial}{\partial s}\left(T_{ax}\frac{\partial w_f}{\partial s}\right) &= f_z(s,t) \\ m_{2D}\frac{\partial^2 v_f}{\partial t^2} + EI_H\left(\frac{\partial^4 v_f}{\partial s^4} + \frac{1}{R^2}\frac{\partial^4 v_f}{\partial s^2}\right) - \frac{\partial}{\partial s}\left(T_{ax}\frac{\partial v_f}{\partial s}\right) &= f_r(s,t) \end{aligned} \tag{2.3}$$

where $m_{2D} = 2m_f$ [kg/m] is the mass per unit length for the two-tube system with m_f the mass per unit length for one tube, R is the mean value of the center line radius of the two-tube system, t the time variable, s the curvilinear coordinate along the floating collar, $\partial/\partial s = R^{-1}\partial/\partial\beta$ the differentiation along the curvilinear coordinate of the floating collar. EI_V and EI_H are the structural bending stiffness in vertical and radial direction, respectively. $EI_V = 2EI_f$ with EI_f the bending stiffness for one tube. EI_H for the floating collar with two tubes is expected to be much larger than EI_V and is calculated as $EI_H = 2E(I_f + A_f p^2/4)$ with E the Young's modulus of the tubes' material (high-density polyethylene), I_f the area moment of the cross section for one tube in the horizontal plane, A_f the cross-sectional area of one tube and p the center-to-center distance between the two tubes (see Figure 2.2). T_{ax} is the axial tension along the floating collar and is

estimated by a two-dimensional Finite Element Method (FEM) code, as explained later in the text. f_z and f_r are the vertical and radial forces per unit length of the floater, given by the sum of the contributions from wave excitation forces (f^{excit}), added mass and damping forces ($f^{\text{added mass+damping}}$), restoring forces ($f^{\text{restoring}}$), forces from net cage (f^{netcage}), mooring lines (f^{moorings}) and drag force (f^{drag}) on the tubes, i.e.

$$\begin{aligned} f_z &= f_z^{\text{excit}} + f_z^{\text{added mass+damping}} + f_z^{\text{restoring}} + f_z^{\text{moorings}} + f_z^{\text{netcage}} + f_z^{\text{drag}} \\ f_r &= f_r^{\text{excit}} + f_r^{\text{added mass+damping}} + f_r^{\text{restoring}} + f_r^{\text{moorings}} + f_r^{\text{netcage}} + f_r^{\text{drag}} \end{aligned} \tag{2.4}$$

Note that the restoring forces for the horizontal modes ($f_r^{\text{restoring}}$) and the drag forces for the vertical modes (f_z^{drag}) are zero. The wave excitation forces (including Froude-Kriloff forces and diffraction forces) and the added mass and damping forces on the floating collar are evaluated by the linear frequency-domain potential-flow solver WAMIT (Lee and Newman, 2013), using a High-order Boundary Element Method (HBEM). The possible forces from mooring lines and net cage will be introduced in Section 2.4 and Section 2.5. The evaluation of the drag forces for the horizontal modes is shown in Section 2.2.3.

The equations of motion for surge (c_1), sway (d_1) and heave (a_0) are treated separately, as rigid body modes. For example, assuming steady-state oscillations with the excitation frequency ω, for the heave motion we solve

$$(M + A_{33})\,\ddot{a}_0 + B_{33}\dot{a}_0 = F_3\,(t) \tag{2.5}$$

where $M = 2\pi R m_{2D}$ is the total structural mass of the floating collar, A_{33} and B_{33} are the frequency dependent added mass and damping coefficients in heave and F_3 is the corresponding hydrodynamic force, including wave excitation force, restoring force and net cage and mooring forces integrated along the floater.

In order to decouple the different $\cos(n\beta)$ and $\sin(n\beta)$ modes for both vertical and horizontal modes, Equations (2.2) are inserted into Equations (2.3), and the latter are multiplied successively by $\cos(m\beta), m = 1, \ldots$ and $\sin(m\beta), m = 2, \ldots$ and integrated from $\beta = 0$ to 2π, respectively. The equations of motion for each mode coefficient $a_n(t)$, $b_n(t)$, $c_n(t)$ and $d_n(t)$ are then obtained. Next we will show in detail how to estimate the different modes in vertical direction (see Section 2.2.2) and in radial direction (see Section 2.2.3).

2.2.2 Equations of vertical motions

In this section, we will show the procedure to obtain the motion equations for the modes in vertical direction. The focus is on the $\cos(n\beta)$ modes. First w_f given by Eq. (2.2) is substituted in the corresponding Eq. (2.3) and the latter is multiplied successively by $\cos(m\beta), m = 1, 2$, etc. Then, integrating along the center line of

the torus, Eq. (2.3) for the vertical structural response becomes

$$\int_0^{2\pi} \left\{ \begin{array}{c} \sum_{n=1}^{\infty} \left[m_{2D}\ddot{a}_n + \rho g b_w a_n + \frac{EI_V}{R^4}\left(n^4 - n^2\right) a_n \right] \cos\left(n\beta\right) \\ + \\ \sum_{n=1}^{\infty} \left[m_{2D}\ddot{b}_n + \rho g b_w b_n + \frac{EI_V}{R^4}\left(n^4 - n^2\right) b_n \right] \sin\left(n\beta\right) \end{array} \right\} \cos\left(m\beta\right) R \, \mathrm{d}\beta$$
$$= \int_0^{2\pi} \left(f_z^{\text{added mass}+\text{damping}} + f_z^{\text{excit}} + f_z^{\text{other}} \right) \cos\left(m\beta\right) R \, \mathrm{d}\beta \tag{2.6}$$

In Eq. (2.6), the restoring force for vertical response is caused by the change of buoyancy due to the motion w_f and expressed as $\rho g b_w w_f$, within linear theory. Here ρ is the mass density of water, g is the gravitational acceleration. For a half submerged floating collar with two tubes, $b_w = 4c_f$ with $c_f = d_f/2$ the cross-sectional radius of the tube. f_z^{other} consists of forces from net cage and mooring lines and also the axial stiffness due to the term $\frac{\partial}{\partial s}\left(T_{ax}\frac{\partial w_f}{\partial s}\right)$ in the left-hand side of Eq. (2.3). The equations for the different modes can then be decoupled, using the property of orthogonal functions shown in Eq. (2.7)

$$\int_0^{2\pi} \cos\left(n\beta\right)\cos\left(m\beta\right) \, \mathrm{d}\beta \left\{ \begin{array}{ll} = 0, & m \neq n \\ = \pi, & m = n = 1, 2, \ldots \end{array} \right.$$
$$\int_0^{2\pi} \sin\left(n\beta\right)\cos\left(m\beta\right) \mathrm{d}\beta = 0 \tag{2.7}$$

The equations of motion for the vertical $\cos(m\beta)$ modes read

$$\left(m_{2D} + a_{33}^{(m)}\right)\ddot{a}_m + b_{33}^{(m)}\dot{a}_m + \left[\rho g b_w + \frac{EI_V}{R^4}\left(m^4 - m^2\right)\right] a_m$$
$$= f_{z,m}^{\text{excit}} + f_{z,m}^{\text{other}}, \quad m = 1, 2, \ldots \tag{2.8}$$

where $a_{33}^{(m)}$ and $b_{33}^{(m)}$ are the 2D vertical added mass and damping coefficients for mode m, and $f_{z,m}^{\text{excit}}$ is the corresponding 2D generalized wave excitation force. One should note that subscript "33" in the hydrodynamic coefficients denotes vertical direction, while the involved mode is given by the superscript "(m)". $a_{33}^{(m)}$, $b_{33}^{(m)}$ and $f_{z,m}^{\text{excit}}$ are calculated by the linear potential-flow solver WAMIT. $f_{z,m}^{\text{other}}$ is the generalized f_z^{other} force for mode m and given by

$$f_{z,m}^{\text{other}} = \frac{1}{\pi}\int_0^{2\pi} f_z^{\text{other}} \cos\left(m\beta\right) \, \mathrm{d}\beta \tag{2.9}$$

Detailed explanation of the different terms in $f_{z,m}^{\text{other}}$ will be given later.

If transient effect needs to be captured, for instance in irregular waves, then the hydrodynamic radiation loads for different modes should be expressed in terms of convolution integrals with retardation functions. The motion equations Eq. (2.8)

for the vertical $\cos(m\beta)$ modes then need to be rewritten as

$$\begin{aligned}&\left[m_{2D}+a_{33}^{(m)}(\infty)\right]\ddot{a}_m+\int_0^t k_{33}^{(m)}(\tau)\,\dot{a}_m(t-\tau)\,d\tau\\&+\left[\rho g b_w+\frac{EI_V}{R^4}\left(m^4-m^2\right)\right]a_n=f_{z,m}^{\text{excit}}+f_{z,m}^{\text{other}},\quad m=1,2,...\end{aligned}\tag{2.10}$$

where $a_{33}^{(m)}(\infty)$ and $k_{33}^{(m)}$ are the 2D vertical added mass coefficient at infinity frequency and retardation function for mode m, respectively. $k_{33}^{(m)}$ can be estimated as

$$k_{33}^{(m)}(t)=\frac{2}{\pi}\int_0^\infty b_{33}^{(m)}(\omega)\cos(\omega t)\,\mathrm{d}\omega\tag{2.11}$$

Forces from mooring lines and net cage

For the loads from the mooring lines and the net cage, the generalized force reads

$$\frac{1}{\pi R}\int_0^{2\pi}\sum_{i=1}^{N_\beta}T_{i,3}\delta(\beta-\beta_i)\cos(n\beta)\,\mathrm{d}\beta=\frac{1}{\pi R}\sum_{i=1}^{N_\beta}T_{i,3}\cos(n\beta_i)\tag{2.12}$$

Here $T_{i,3}$ is the vertical component of force from the mooring lines and the net cage. δ is the Dirac delta function. β_i describes angular positions where the mooring lines and the net cage are attached to the floating collar and N_β is the number of the connection positions.

Axial stiffness

The axial tension T_{ax} acting on the two-tube system is estimated by a two dimensional Finite Element Method (FEM) code. This allows us to deal with general mooring line and net cage set-up and to account for time-varying axial tension. This means that the two-tube system is split in N_E elements and T_{ax} is assumed to be constant within each element. The chosen N_E depends on the mooring-line arrangement and on the mesh resolution for the net cage. The axial-stiffness terms in the beam equation Eq. (2.3) do not decouple as the other terms do due to orthogonality shown in Eq. (2.7). For the vertical $\cos(n\beta)$ modes, the term representing the axial stiffness in Eq. (2.9) is given as

$$\frac{1}{\pi}\int_0^{2\pi}\frac{\partial}{\partial s}\left(T_{ax}\frac{\partial w_f}{\partial s}\right)\cos(n\beta)\,\mathrm{d}\beta=\sum_{n=1}^{\infty}\left(p_{mn}a_n+q_{mn}b_n\right)\tag{2.13}$$

where

$$p_{mn} = \frac{n^2}{\pi R^2} \sum_{i=1}^{N_E} T_{ax,i} \int_{\beta_{i-1}}^{\beta_i} \cos(n\beta) \cos(m\beta)\ \mathrm{d}\beta$$
$$q_{mn} = \frac{n^2}{\pi R^2} \sum_{i=1}^{N_E} T_{ax,i} \int_{\beta_{i-1}}^{\beta_i} \sin(n\beta) \cos(m\beta)\ \mathrm{d}\beta \tag{2.14}$$

T_{ax}^i is the axial tension for element i of the FEM analysis and is assumed to be constant, so that the axial tension is piecewise constant along the floating collar. The integration terms in Eq. (2.14) are given analytically, see Appendix B. The term associated with the axial tension T_{ax} will provide coupling effect between different modes.

We have introduced the modeling of the $\cos(m\beta)$ modes in vertical direction, similar procedure can be followed to find solutions for the $\sin(m\beta)$ modes and therefore will not be provided here. One should note that the wave excitation forces for all $\sin(m\beta)$ modes are zero, as we solve the motion equations in the $O_F x_F y_F z_F$ coordinate system (see Figure 2.2). Once the vertical motions of different modes are obtained, then the total vertical motion z_f for a given point on the floating collar can be readily obtained by superposing the vertical motion of each mode according to Eq. (2.1).

2.2.3 Equations of radial motions

The motion equations for the radial modes can be obtained in a similar way as that for the vertical modes, except that there are no restoring terms while there are additional drag-force related terms in the motion equations. So detailed derivations will not be provided. In the following we will mainly address the modeling of the drag force on the floating collar.

Drag on the floating collar

Viscous load on the floating collar is moderate compared with the total force on the system, so it is not necessary to estimate the load by accurate yet time consuming method, as done by Kristiansen (2010) for a horizontal cylinder in waves using an advanced Computational Fluid Dynamics (CFD) method. Here we apply the drag term in the Morison's equation to model the drag force per unit length on a tube in the horizontal plane, given by

$$f_r^{\mathrm{drag}}(\beta, t) = 0.5 \rho C_D^f d_r u_r |u_r| \tag{2.15}$$

where C_D^f is the drag coefficient and $d_r(\beta, t) = \min(\zeta - z_f + c_f, 2c_f)$ is the relative submergence, with ζ the instantaneous incident-wave elevation at the center of the tube's cross section, while the radiation and diffraction waves are neglected. $u_r(\beta, t) = \mathbf{U}_{\mathrm{rel}} \cdot \mathbf{n}_f$ is the local, relative cross-flow velocity at the center line of the tube with $\mathbf{U}_{\mathrm{rel}}$ the instantaneous, relative velocity vector between the undisturbed

inflow and the floating collar and $\mathbf{n}_f = (\cos\beta, \sin\beta, 0)$ the two-dimensional (in the horizontal plane) unit normal vector of the tube when undeformed (circular shape).

The next step is to find the drag coefficients C_D^f for different cross-sections, which is not straightforward. The cross-sections of the floating collar will experience different inflow because the waves and current are not in general aligned with the cross-section. For the floating collar with two tubes, a given cross-section with cross-flow is made by two circular cylinders in tandem arrangement. The flow interaction is important as the downstream cylinder is located in the wake of the upstream cylinder. According to the results from Zdravkovich (1985) for two fully submerged circular cylinders in current, drag coefficients for the upstream and downstream cylinders are strongly dependent on the Reynolds number $\mathrm{Rn} = U_\infty d_f/\nu$ (with U_∞ = current velocity and ν the kinematic viscosity of the water) and on the distance between the two cylinders. Drag coefficient can even be negative for the downstream cylinder when the two cylinders are placed close enough (center-to-center distance $p < 4d_f$, with d_f the cross-sectional diameter of each tube). In the presence of incident waves, over-topping of the floating collar may occur when it is exposed to steep waves and this will affect the actual drag coefficient of the cross-section. Moreover, C_D^f depends on the Keulegan-Carpenter number $\mathrm{KC}=U_M T/d_f$ (with U_M = velocity amplitude of incident oscillatory flow and T = oscillatory period) and on the relative current number, i.e. the ratio between the wave particle amplitude and current velocity in the case of combined waves and current. It it is not practical to account for all these variations of C_D^f and therefore constant drag coefficients for the two cylinders in steady flow will be used in the analysis and a sensitivity analysis will be performed to have an estimate of the error associated with this simplification.

2.3 The sinker tube

The motions of the sinker tube are solved in a similar way as those for the floating collar, i.e. curved beam equations are also applied to the sinker tube. The corresponding hydrodynamic loads are calculated by a modified Morison's equation and detailed explanation is given below.

2.3.1 Forces on the sinker tube

The radial f_r and vertical f_z forces per unit length on the sinker tube are calculated by a modified Morison's equation for a submerged cylinder. By modified Morison's equation is meant that the local body velocities and accelerations are accounted for. In particular, in this case it reads

$$\begin{aligned} f_r &= 0.5\rho C_D^s d_s u_r \sqrt{u_r^2 + u_z^2} + C_M^s \rho\pi \frac{d_s^2}{4}\ddot{r}_w - (C_M^s - 1)\rho\pi\frac{d_s^2}{4}\ddot{v}_s \\ f_z &= 0.5\rho C_D^s d_s u_z \sqrt{u_r^2 + u_z^2} + C_M^s \rho\pi \frac{d_s^2}{4}\ddot{z}_w - (C_M^s - 1)\rho\pi\frac{d_s^2}{4}\ddot{z}_s \end{aligned} \tag{2.16}$$

Here d_s is the cross-sectional diameter of the sinker tube; u_r and u_z are, respectively, the local, radial and vertical relative cross-flow velocity between the sinker tube and the ambient flow, evaluated at the center axis of the sinker tube; $\ddot{v}_s$ and $\ddot{z}_s$ are, respectively, the radial and vertical accelerations of the sinker tube; $\ddot{r}_w$ and $\ddot{z}_w$ are, respectively, the radial and vertical undisturbed wave particle accelerations at the center axis of the sinker tube; C_D^s and C_M^s are, respectively, the cross-sectional drag and mass coefficients. When the effect of the netting is neglected, the main parameters affecting C_D^s and C_M^s for a smooth cylinder in infinite fluid are the Keulegan-Karpenter number KC=$U_M T/d_s$ (with U_M = velocity amplitude of the oscillatory flow at the center of the sinker tube's cross section), Reynolds number $\mathrm{Rn} = U_M d_s/\nu$ and the relative current number. Typically the sinker tube operates at small KC number due to the fact that it is placed far below the free surface, so the corresponding U_M is small. Here we approximately set $C_M^s = 2$, which is consistent with low values of KC number. A constant $C_D^s = 1$ is assumed, neglecting the influence of oscillatory ambient flow and Reynolds number. A sensitivity analysis will be performed to examine the influence of this simplification. The possible occurrence of vortex induced motions (VIM) of the sinker tube is not considered.

2.4 The net cage

In this section we describe the structure model for the net cage and the hydrodynamic model for the viscous load on the net cage. The net structure is highly flexible and can easily deform when subjected to waves and current, so a time-stepping procedure is needed to find its instantaneous configuration. The fact that the netting may have 10 million meshes limits the use of Computational Fluid Dynamics (CFD) and complete structural modeling. Therefore simplified modelings for the net structure and its hydrodynamic loads are needed and introduced in Section 2.4.1 and in Section 2.4.2, respectively.

2.4.1 Truss model

The structural model of the net cage from Kristiansen and Faltinsen (2012, 2015), originally presented by Marichal (2003), is adopted in the present work. The main particular of this truss model is that a linear system of equations for the truss tensions is solved at each time step. The advantage of solving the problem in this way is that better convergence behavior is expected compared with formulations solving the truss tension explicitly. The latter is based on known elongation of the truss at each time step. More detailed explanation of the truss model adopted in the present study is provided below.

A Raschel type knotless netting with square meshes and negligible bending stiffness is considered. This type of netting material is used widely in the aquaculture industry. Negligible bending stiffness means that we can model the net twines as elastic trusses which contain only axial tensions. Due to the large number of meshes in a physical net structure, it is not practical to model each individual twine, so instead equivalent trusses are used by keeping the same solidity ratio as the original

netting, see Figure 2.3. Here the solidity ratio Sn is defined as the ratio between the area of the solid part of a net screen and the total area of the screen. This means that the equivalent trusses have different size compared with the original net twines. Next, we will show how to obtain the system of equations for these truss tensions.

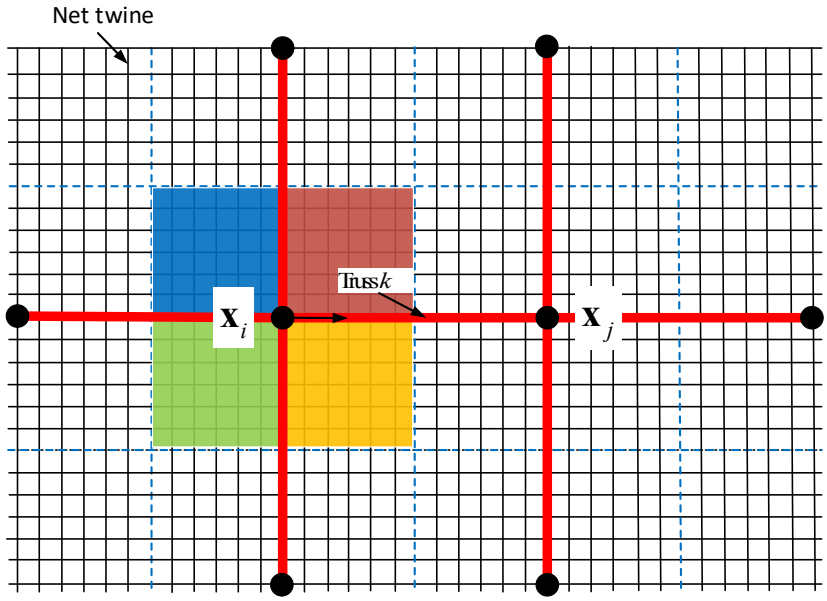

Figure 2.3: Division of a planar net into an equivalent truss model. The solid black circles denote the numerical nodes of the net. The shaded colored areas represent four net panels surrounding a given node and are used to estimate the hydrodynamic forces acting on the node. The red lines represent the equivalent trusses with two end nodes.

Equation of motion for a node

According to Newton's second law, the equation of motion for a node i (see Figure 2.3) can be written as

$$m_i \mathbf{a}_i = \sum \mathbf{F}_i \tag{2.17}$$

where m_i is the local mass of the net represented by the node, the vector $\mathbf{a}_i$ represents the acceleration vector of the node and $\sum \mathbf{F}_i$ is the sum of all forces acting on the part of the net represented by the node. We write

$$\sum \mathbf{F}_i = \sum_{m=1}^{N_T} T_m \mathbf{s}_m + \sum_{m=1}^{N_p} (\mathbf{F}_{Hm} + \mathbf{F}_{am}) \tag{2.18}$$

Here N_T and N_p are the number of trusses connected with the node and the number of panels surrounding the node, respectively. T_m is the tension in one of the trusses connected to the node i and $\mathbf{s}_m$ is the corresponding unit vector tangentially to the truss. For instance, for the truss k in Figure 2.3, $\mathbf{s}_k = (\mathbf{x}_j - \mathbf{x}_i)/l_k$ and points from the node i to the node j. Here l_k is the length of the truss k. $\mathbf{F}_{Hm}$ is the hydrodynamic force, including drag force and lift force, on one of the panels around the node i, while $\mathbf{F}_{am}$ is the corresponding added mass force of the net twines represented by the panel. As a first approximation, $\sum_{m=1}^{N_p} \mathbf{F}_{am} \approx -m_i \mathbf{a}_i$, assuming that: (1) the flow around a submerged net twine resembles that around a circular cylinder; (2) the net weight of the net twine is zero, i.e. the mass of the net twine is equal to the weight of the water displaced. Similar motion equation can be obtained for node j, as well as for any other node of the modeled net.

Kinematic constraint of the twine

For the truss k in Figure 2.3 with end nodes i and j, the kinematic constraint for the truss length l_k^{n+1} at time instant $n+1$ is written as

$$\left(l_k^{n+1}\right)^2 = \left|\mathbf{x}_j^{n+1} - \mathbf{x}_i^{n+1}\right|^2,\ n \geq 0 \tag{2.19}$$

where $\mathbf{x}_j^{n+1}$ and $\mathbf{x}_i^{n+1}$ are the coordinates, respectively, for end nodes i and j. $|\mathbf{x}| = \sqrt{x^2+y^2+z^2}$ with $\mathbf{x} = (x, y, z)$ as Earth-fixed, Cartesian coordinates. Initially, the length of the truss is l_k^0 . If the net is assumed inelastic, then $l_k^n = l_k^0$ for all time steps. Here, the elasticity of the net is considered by incorporating the change of the truss length.

Linear system of equations for truss tensions

At any time instant, the kinematic constraint in Eq. (2.19) is required to be fulfilled. The node position $\mathbf{x}$ and velocity $\mathbf{u}$ are stepped forward in time by using a first order time-marching scheme:

$$\begin{aligned} \mathbf{x}^{n+1} &= \mathbf{x}^n + \Delta t \mathbf{u}^{n+1} \\ \mathbf{u}^{n+1} &= \mathbf{u}^n + \Delta t \mathbf{a}^n \end{aligned} \tag{2.20}$$

Δt is the time step size. Inserting Eq. (2.20) into Eq. (2.19), we obtain the following equation

$$\left(l_k^{n+1}\right)^2 = \left|\boldsymbol{\alpha} + \boldsymbol{\beta}\Delta t + \boldsymbol{\gamma}\Delta t^2\right|^2 \tag{2.21}$$

where the vectors $\boldsymbol{\alpha}$, $\boldsymbol{\beta}$ and $\boldsymbol{\gamma}$ are defined as

$$\begin{aligned} \boldsymbol{\alpha} &= \mathbf{x}_j^n - \mathbf{x}_i^n \\ \boldsymbol{\beta} &= \mathbf{u}_j^n - \mathbf{u}_i^n \\ \boldsymbol{\gamma} &= \mathbf{a}_j^n - \mathbf{a}_i^n \end{aligned} \tag{2.22}$$

Eq. (2.21) is nonlinear in terms of Δt. Upon neglecting high order terms of $\mathcal{O}(\Delta t)^3$ and using the relationship $(l_k^n)^2 = |\boldsymbol{\alpha}|^2$, we have

$$\left(l_k^{n+1}\right)^2 - \left(l_k^n\right)^2 = \Delta t^2 |\boldsymbol{\beta}|^2 + 2\Delta t \boldsymbol{\alpha} \cdot (\boldsymbol{\beta} + \Delta t \boldsymbol{\gamma}) \tag{2.23}$$

Assuming small change of the truss length between the two neighboring time instants, i.e., $l_k^{n+1} \approx l_k^n$, the terms on the left-hand side of Eq. (2.23) can be further approximated as

$$\left(l_k^{n+1} - l_k^n\right)\left(l_k^{n+1} + l_k^n\right) \approx 2l_k^n\left(l_k^{n+1} - l_k^n\right) = 2l_k^n l_k^0\left(\varepsilon_k^n - \varepsilon_k^{n-1}\right) \tag{2.24}$$

Here the strain $\varepsilon_k^n = \left(l_k^{n+1} - l_k^0\right)/l_k^0$ is defined as the elongation of the truss relative to its initial length. Using the tension-strain relationship for the truss k and assuming a linear behavior of the material, we have

$$\varepsilon_k^n - \varepsilon_k^{n-1} = \kappa\left(T_k^n - T_k^{n-1}\right) = \kappa \Delta T_k^n \tag{2.25}$$

Here κ is the elasticity coefficient and ΔT_k^n is the increment of the truss tension within the time step Δt. By substituting Eq. (2.25) and Eq. (2.24) into Eq. (2.23), we can rewrite Eq. (2.23) as

$$\frac{\boldsymbol{\alpha}}{l_k^n} \cdot \boldsymbol{\gamma} = -\frac{|\boldsymbol{\beta}|^2}{2l_k^n} - \frac{\boldsymbol{\alpha}}{l_k^n} \cdot \frac{\boldsymbol{\beta}}{\Delta t} + \frac{\kappa l_k^0 \Delta T_k^n}{\Delta t^2} \tag{2.26}$$

Inserting Eq. (2.22) into Eq. (2.26) and using the fact that $\mathbf{s}_k^n = \boldsymbol{\alpha}/l_k^n$ is the tangential unit vector, we obtain

$$\begin{aligned} &\mathbf{s}_k^n \cdot \left(\mathbf{a}_j^n - \mathbf{a}_i^n\right) - \frac{\kappa l_k^0}{(\Delta t)^2} T_k^n \\ &= -\frac{1}{2l_k^n}\left|\mathbf{u}_j^n - \mathbf{u}_i^n\right|^2 - \frac{1}{\Delta t}\mathbf{s}_k^n \cdot \left(\mathbf{u}_j^n - \mathbf{u}_i^n\right) - \frac{\kappa l_k^0}{(\Delta t)^2} T_k^{n-1} \end{aligned} \tag{2.27}$$

The accelerations on the left-hand side are substituted by forces according to Eq. (2.17) and Eq. (2.18). The hydrodynamic loads on the nodes are pre-calculated and known, then the truss tensions are the only unknown variables. Each truss provides an equation, then we can obtain a linear equations system for unknown tensions when applying Eq. (2.27) for all trusses. Once the unknown truss tensions are solved, then the accelerations can be readily obtained from Eq. (2.17) and the net cage can be evolved in time according to Eq. (2.20).

For nodes of the net cage that are located at the floating collar and at the sinker tube, the above introduced procedure is not applicable and are treated separately. Detailed explanation is given in Section 2.6.

2.4.2 Hydrodynamic model

The experimentally based screen type of force model proposed by Kristiansen and Faltinsen (2012, 2015) is used to estimate the hydrodynamic, viscous loads acting

on the net cage for both cases in current only and in combined waves and current. The screen force model was originally developed for steady flow. However, due to the high KC numbers based on the twine diameter, the flow in waves can be seen as quasi-steady, thus the force model is believed to be also applicable in waves. Kristiansen and Faltinsen (2012) demonstrated that the screen-type force model gave clear improvements in predicting the drag and lift forces on the net cages in current with respect to the estimates by a Morison type of force model, especially when the net cage is subjected to large deformations. A brief outline of the basic parts of the theory is given here for clarity purpose.

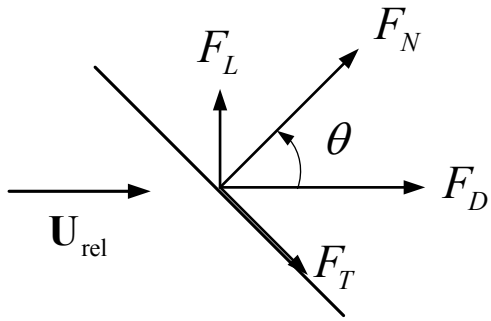

Figure 2.4: Drag (F_D) and lift (F_L) forces on a net panel. F_N and F_T denote the corresponding normal and tangential components. The angle θ is the angle between the normal of the panel and direction of local inflow with velocity U_{rel}.

The model divides the net into a number of flat net panels, or screens, see Figure 2.3. The knots are neglected, and circular twine cross-sections are assumed. Each net panel is assumed to experience a viscous normal force F_N due to a pressure drop proportional to the square of the local, relative flow velocity (defined below), and a tangential force F_T due to the flow deflection by the net twines when going through the net. Here "deflected" means that the flow deviates from its original path. The net-panel force can be, alternatively, decomposed into a drag force F_D and a lift force F_L, as shown in Figure 2.4. The non-dimensional force coefficients corresponding to the different force terms shown in Figure 2.3 are defined as

$$\begin{aligned} C_N &= \frac{F_N}{0.5\rho A|\mathbf{U}_{\text{rel}}|^2}, \; C_T = \frac{F_T}{0.5\rho A|\mathbf{U}_{\text{rel}}|^2} \\ C_D &= \frac{F_D}{0.5\rho A|\mathbf{U}_{\text{rel}}|^2}, \; C_L = \frac{F_L}{0.5\rho A|\mathbf{U}_{\text{rel}}|^2} \end{aligned} \tag{2.28}$$

where A is the net-panel area and $\mathbf{U}_{\text{rel}}$ is the instantaneous, relative flow velocity and taken as

$$\mathbf{U}_{\text{rel}} = \gamma \mathbf{U}_\infty + \mathbf{u}_w - \mathbf{u}_i \tag{2.29}$$

with $\mathbf{U}_\infty$ the ambient current velocity, $\mathbf{u}_w$ the incident-wave particle velocity at the position of the node and $\mathbf{u}_i$ the velocity of the node. γ is a flow reduction

coefficient. In particular, $\gamma = 1$ for the front part of the net, while $\gamma = r < 1$ for the rear half so to account for the shading effect of the net front part. The shading effect for the oscillatory flow is difficult to be incorporated, so as a first approximation, it is assumed that only the steady part of the flow, i.e. the current, is reduced by r.

The force coefficients in Eq. (2.28) are not independent and it follows that

$$\begin{aligned} C_D &= C_N \cos\theta + C_T \sin\theta \\ C_L &= C_N \sin\theta - C_T \cos\theta \end{aligned} \tag{2.30}$$

The examined force coefficients are assumed to be functions of Sn, Rn and θ, where Sn is the solidity ratio of the net panel, Rn is the Reynolds number and θ is the angle between the panel normal vector and the relative, local flow velocity, as shown in Figure 2.4. Detailed dependency of the force coefficients to these three parameters is explained below. The definition of the Reynolds number involved here will be discussed later.

Assuming that the cross-flow principle can be applied (see e.g. Faltinsen, 1990), the normal force coefficient C_N is assumed to obey the following formulation when $0 \le \theta \le \pi/4$

$$C_N(\theta) = C_D^{\text{circ.cyl}} \frac{\text{Sn}\,(1-\text{Sn})}{2(1-\text{Sn})^2} \cos^2\theta \;\; (0 \le \theta \le \pi/4) \tag{2.31}$$

The dependency on Sn is consistent with the experimental data from Blevins (2003) and assumed to be valid for Sn<0.5. The realistic range of Sn for clean nets is between 0.2-0.3, so Eq. (2.31) is applicable. $C_D^{\text{circ.cyl}}$ is the Reynolds number dependent drag coefficient of a circular cylinder and, using the experimental data from Goldstein (1965), can be written as

$$\begin{aligned} C_D^{\text{cir.cyl}} = &-78.46675 + 254.73873\left(\log_{10}^{\text{Rn}}\right) - 327.8864\left(\log_{10}^{\text{Rn}}\right)^2 \\ &+ 223.64577\left(\log_{10}^{\text{Rn}}\right)^3 - 87.92234\left(\log_{10}^{\text{Rn}}\right)^4 + 20.00769\left(\log_{10}^{\text{Rn}}\right)^5 \\ &- 2.44894\left(\log_{10}^{\text{Rn}}\right)^6 + 0.12479\left(\log_{10}^{\text{Rn}}\right)^7 \end{aligned} \tag{2.32}$$

This formula is applicable for $10^{3/2} \le \text{Rn} \le 10^4$. A plot based on Eq. (2.32) is provided in Figure 2.5.

For Rn< $10^{3/2}$, the drag coefficient for a circular cylinder from White (2006) is used, i.e.

$$C_D^{\text{cir.cyl}} = 1 + \frac{10}{\text{Rn}^{2/3}} \tag{2.33}$$

The Rn formulas (2.32) and (2.33) are relevant for the present application as the expected range of Rn in practice is Rn < 2000 - 3000. In terms of the tangential force coefficient, the following formula proposed by Schubauer et al. (1950) is used and given as

$$\frac{C_T(\theta)}{\theta} = \frac{4C_N(\theta)}{8 + C_N(\theta)} \;\; (0 \le \theta \le \pi/4) \tag{2.34}$$

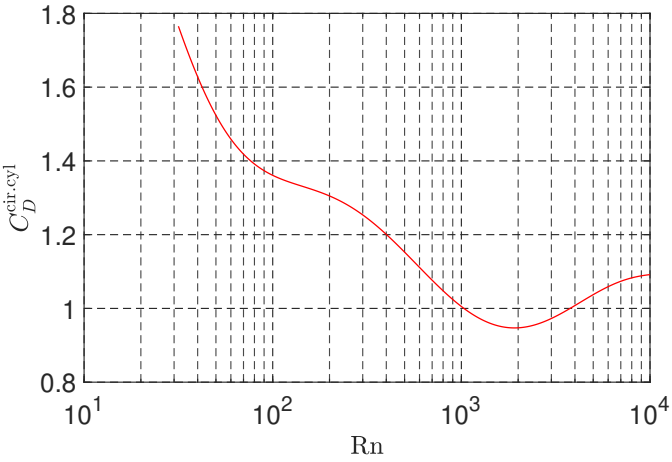

Figure 2.5: The drag coefficient for a smooth circular cylinder as function of Reynolds number.

Once $C_N(\theta)$ and $C_T(\theta)$ are known from Eq. (2.31) and Eq. (2.34), respectively, the drag $C_D(\theta)$ and lift $C_L(\theta)$ coefficients on the panel for $0 \leq \theta \leq \pi/4$ can be obtained from Eq. (2.30). Next we will show briefly how to generalize the model to include scenarios with $\pi/4 \leq \theta \leq \pi/2$, more detailed explanation can be found Kristiansen and Faltinsen (2012). It is assumed that C_D and C_L may formally be represented by the following Fourier series,

$$\begin{aligned} C_D(\theta) &= c_d \sum_{n=1}^{\infty} a_{2n-1} \cos(2n-1)\,\theta \\ C_L(\theta) &= c_l \sum_{n=1}^{\infty} b_{2n} \sin(2n\theta) \end{aligned} \tag{2.35}$$

where $c_d = C_D(0)$ and $c_l = C_L(\pi/4)$. $C_D(0)$ and $C_L(\pi/4)$ can be calculated by Eq. (2.30) combined with Eq. (2.31) and Eq. (2.34). As a first approximation, only the first term in each series is considered, namely

$$\begin{aligned} C_D(\theta) &= c_d \cos\theta \\ C_L(\theta) &= c_l \sin 2\theta \end{aligned} \tag{2.36}$$

with $a_1 = b_2 = 1$. The dependency on θ in Eq. (2.36) is consistent with that derived by Løland (1991) based on the experimental data from Rudi et al. (1988). The approximation is reasonable for net with low solidity ratio, e.g., Sn<0.25-0.3. For net with high solidity ratio, higher harmonic components may need to be included, but the corresponding Fourier coefficients are not straightforward to be determined. For a typical aquaculture fish cage, the solidity ratio is within the applicable region of Eq. (2.36), so the formula will be adopted in the present work.

Reynolds number definition

The relevant Rn should be defined with respect to the physical twine diameter d_w. Kristiansen and Faltinsen (2015) proposed the expression

$$\mathrm{Rn} = (\gamma U_\infty + u_{wa}) d_w / (1 - \mathrm{Sn})\nu \tag{2.37}$$

where u_{wa} is the velocity amplitude of an incident-wave particle at the initial position of the net node, i.e. node position in calm water. The coefficient $1/(1-\mathrm{Sn})$ accounts for the fact that the flow is accelerated at the net twines, due to mass conservation. As mentioned in Eq. (2.29), γ is a flow reduction coefficient and for the rear part of the net the steady flow is reduced by r, with r evaluated by the following formula suggested by Løland (1991)

$$r = 1 - 0.46 c_d \tag{2.38}$$

The Reynolds number in Eq. (2.37) is defined by the characteristic free stream velocity, including the velocity amplitude from incident waves. However, the definition may be difficult to implement in irregular sea scenario. So in the present work the Reynolds number is defined as

$$\mathrm{Rn} = |\mathbf{U}_{\mathrm{rel}}|\, d_w / (1 - \mathrm{Sn})\nu \tag{2.39}$$

using the instantaneous relative velocity instead, as defined in Eq. (2.29).

2.5 The mooring system

The complete set-up of the mooring system is shown in Figure 2.1, which typically comprises ropes and chains, with buoys to support all mooring lines. The buoys are floating circular cylinders. Ropes and chains are treated in a similar way as the net and are modeled as elastic trusses with correct diameter, weight and stiffness. The hydrodynamic forces on the mooring lines are estimated by a modified Morison's equation based on the cross-flow principle and by neglecting the longitudinal forces. In this case, the modified Morison's equation accounts for the local transverse body velocities and accelerations. The motion of each buoy is solved in an inertial coordinate system $O_B x_B y_B z_B$, see Figure 2.6, with the origin of the coordinate system O_B in the plane of undisturbed free surface $z_E = 0$ and the vertical z_B-axis pointing upwards through the center of the buoy in calm water while the horizontal x_B-axis points towards the wave direction (also positive x_F-axis). Because the considered wavelengths are long relative to the buoy diameter, long wave approximation is adopted. It is assumed that there are no coupling terms between the translational and rotational motions as pressure loads are dominant. As an example, the equation for surge motion is

$$M_B \ddot{\eta}_{1,B} = F_{1,B}^{\mathrm{excit}} + F_{1,B}^{\mathrm{added\ mass}} + F_{1,B}^{\mathrm{drag}} + F_{1,B}^{\mathrm{moorings}} \tag{2.40}$$

where M_B is the buoy mass, while $F_{1,B}^{\mathrm{excit}}$, $F_{1,B}^{\mathrm{added\ mass}}$, $F_{1,B}^{\mathrm{drag}}$ and $F_{1,B}^{\mathrm{moorings}}$ are, respectively, wave potential-flow excitation force including Froude-Kriloff force and

diffraction force, the added mass force, the viscous force and the external force from the chain under the buoy, exerted in the surge direction. The excitation force, added mass force and viscous force are estimated by the modified Morison's equation and the corresponding drag coefficient C_D^B and mass coefficient C_M^B are assumed to be constant for simplicity and equal to $C_D^B = 1$ and $C_M^B = 2.0$, even though the coefficients are also influenced by flow parameters such as the Keulegan-Carpenter number, Reynolds number and the ratio between the current velocity and the amplitude of the relative unsteady longitudinal velocity. To assess the importance of accurate values for these two coefficients, a sensitivity analysis will be performed by varying C_D^B and C_M^B. Similar equations can be derived for other degrees of freedom and are omitted here.

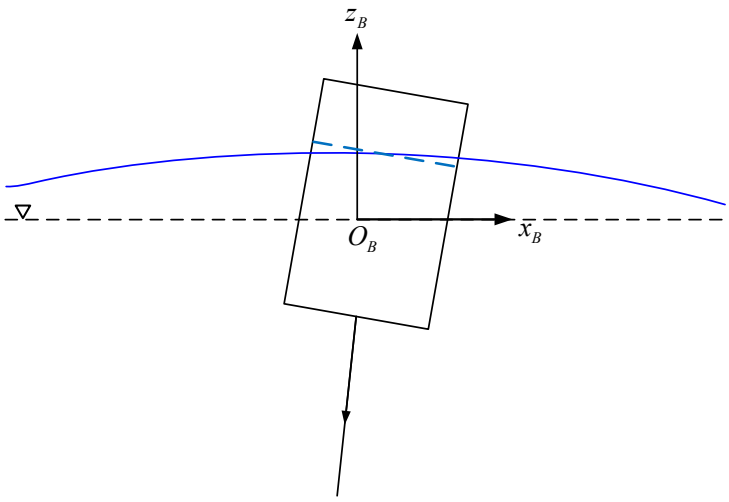

Figure 2.6: Sketch of the buoy system. An Earth-fixed coordinate system $O_B x_B y_B z_B$ is also defined.

2.6 The coupling strategy

In this section, the coupling between the different components of the fish farm, including the floating collar, the sinker tube, the net cage and the mooring lines, is addressed. The essence of the problem is to deal with the acceleration terms in the left-hand side of Eq. (2.27) for nodes located at the floating collar and the sinker tube (named boundary nodes). Here two coupling strategies are adopted, named explicit coupling and implicit coupling, respectively. The implicit coupling strategy is an extension to a realistic fish-farm system of the formulation originally proposed by Kristiansen and Faltinsen (2015) to deal with the coupling between the floater and the net cage for a simplified fish-farm. The explicit coupling strategy is proposed in the present work to reduce the complexity of numerical implementation

and also to make the developed solver easily applicable for other fish-farm concepts. Detailed explanations of the two strategies are given below.

2.6.1 Implicit coupling

In the implicit coupling, when solving the motions of the floating collar and the sinker tube, the loads from the net cage and the mooring lines are unknown, so for the boundary nodes, the acceleration term in the left-hand side of Eq. (2.27) is also connected with unknown truss tensions. This means that the complete system needs to be solved simultaneously. To better explain this coupling strategy, it is assumed that the inflow is in the positive x_E-axis (see Figure 2.2), which implies that only modes symmetric about the x_E-axis, i.e., $\cos(n\beta)$, are excited. For a node located at the floating collar with position β_i, the part of the vertical acceleration due to the unknown tensions from the net cage and mooring lines is given by

$$\begin{aligned}\Delta\ddot{z}_{\beta_i,T} &= \sum_{n=1}^{\infty}\left[\frac{1}{\pi R}\sum_{j}^{N_\beta} T_{j,3}\cos\left(n\beta_j\right)\right]\frac{\cos\left(n\beta_i\right)}{m+a_{33}^{(n)}} + \frac{1}{M+A_{33}}\sum_{j}^{N_\beta} T_{j,3} \\ &= \sum_{j}^{N_\beta} T_{j,3}\left[\frac{1}{\pi R}\sum_{n=1}^{\infty}\frac{\cos\left(n\beta_j\right)\cos\left(n\beta_i\right)}{m+a_{33}^{(n)}} + \frac{1}{M+A_{33}}\right]\end{aligned} \tag{2.41}$$

From the equation, we can see that the unknown part of the vertical acceleration $\Delta\ddot{z}_{\beta_i,T}$ can be expressed in terms of the truss tensions in the connect-lines from the mooring lines and the net cage. Combining this with the known part of the vertical acceleration, we can have the total vertical acceleration $\ddot{z}_{\beta_i}$ for the boundary node. Similar expressions can be obtained for the accelerations in the horizontal plane. By substituting the obtained acceleration vector into the corresponding acceleration term in the left-hand side of Eq. (2.27), we can include the floating-collar motion and the sinker tube motion in the linear equations system for the truss tensions. In this way, the complete fish-farm system is solved simultaneously and relatively better convergence behavior of the developed numerical solver is expected with respect to using the explicit coupling strategy.

2.6.2 Explicit coupling

In the explicit coupling, when solving the motion equations of the floating collar and the sinker tube, the truss tensions in the mooring lines and the net cage are known with values from previous time step. This implies that the accelerations for nodes located at the floating collar and the sinker tube are pre-calculated and used to substitute the corresponding acceleration term in the left-hand side of Eq. (2.27). Thereafter loads in the mooring lines and in the net twines can be obtained by solving a linear system of equations for the unknown truss tensions and the complete fish-farm system can be evolved in a time-stepping procedure accordingly.

The advantage of using this explicit coupling strategy is that we do not need to solve the complete fish-farm system simultaneously. The net cage and the mooring

lines can be solved separately from the rest components, as long as correct boundary conditions (accelerations) are provided. While for the floating collar and the sinker tube, they can be modeled independently, as long as correct external truss tensions are given. Using this strategy, the developed code for the net cage can be easily transferred to other fish-farm concepts, i.e. not limited to the floating-collar fish-farm system. The disadvantage of using such coupling strategy is that numerical simulation may more easily break down due to the occurrence of unphysical negative twine tensions when exposed to very severe sea states. One possible solution is to check the obtained truss tensions at each time step and if negative truss tensions occur, then one should set the truss tensions to zero for those trusses with negative tensions. Then the simulation goes back in time of one step and rerun the calculation for the rest trusses. This is left for further development.

2.7 Flow chart of the numerical solver

The flow chart of the developed time-domain program for a fish-farm system is shown in Figure 2.7. This algorithm is applicable both for implicit and explicit coupling. The first step is to input the designated environment conditions and parameters for the different components of the fish-farm system, as well as the desired spatial discretization, the initial time step Δt_0 and the ending time of the simulation. In the present simulations, Δt_0 is set $T/200$, with T the incident wave period in regular waves or the peak wave period in irregular waves. Both current, regular and irregular waves can be incorporated and just parts of the fish-farm system, i.e. not necessarily including all components, can be examined. Then an automesh subprogram is called to create net nodes, trusses, screen elements together with their connectivity relationship. At this stage the time simulation starts. At a generic time instant (a) the external loads on different components are calculated and distributed to the corresponding nodes, forming a linear equations system for truss tensions, which (b) is solved by a direct sparse solver. Next, (c) the physical soundness of the solution is checked by comparing the drag force on the net with a realistic upper-limit value for the examined conditions. Such value is set as ten times the maximum drag force acting on a solid cylinder with the same dimensions as the net cage under the same environment condition. The drag force on the net is evaluated by the sum of the horizontal components of the tensions in the top-layer trusses, i.e. those connected with the floating collar. In this way, we can check whether unrealistic truss tensions have occurred. If this is the case, they are avoided in the following way.

Two methods are proposed. In the first strategy, if the net drag is larger than the prescribed upper-limit value, the solution goes back in time of one step and the value of the time step is reduced as $\Delta t/5$, with Δt the previous time step. Then the calculations in steps (a)-(c) are performed with the new time-step value. In the second strategy, if the soundness criterion is not satisfied at a certain time instant, the simulation is restarted from the beginning with a time step $\Delta t_0/2^N$ with N the number of times that the simulation has been restarted. The aim is to achieve a solution where the soundness criterion is always satisfied. Normally the

first method is more computational time efficient, however sometimes it may break down in very severe sea states due to accumulated errors, so it still requires more investigation. To be on a safe side, the second method is adopted in the present study, as shown in Figure 2.7.

If the check in step (c) returns a drag force less than the upper-limit value, (d) the configuration of the fish-farm system is updated using the first-order method in Eq. (2.20). Steps (a)-(d) are repeated until the ending time of the simulation is reached.

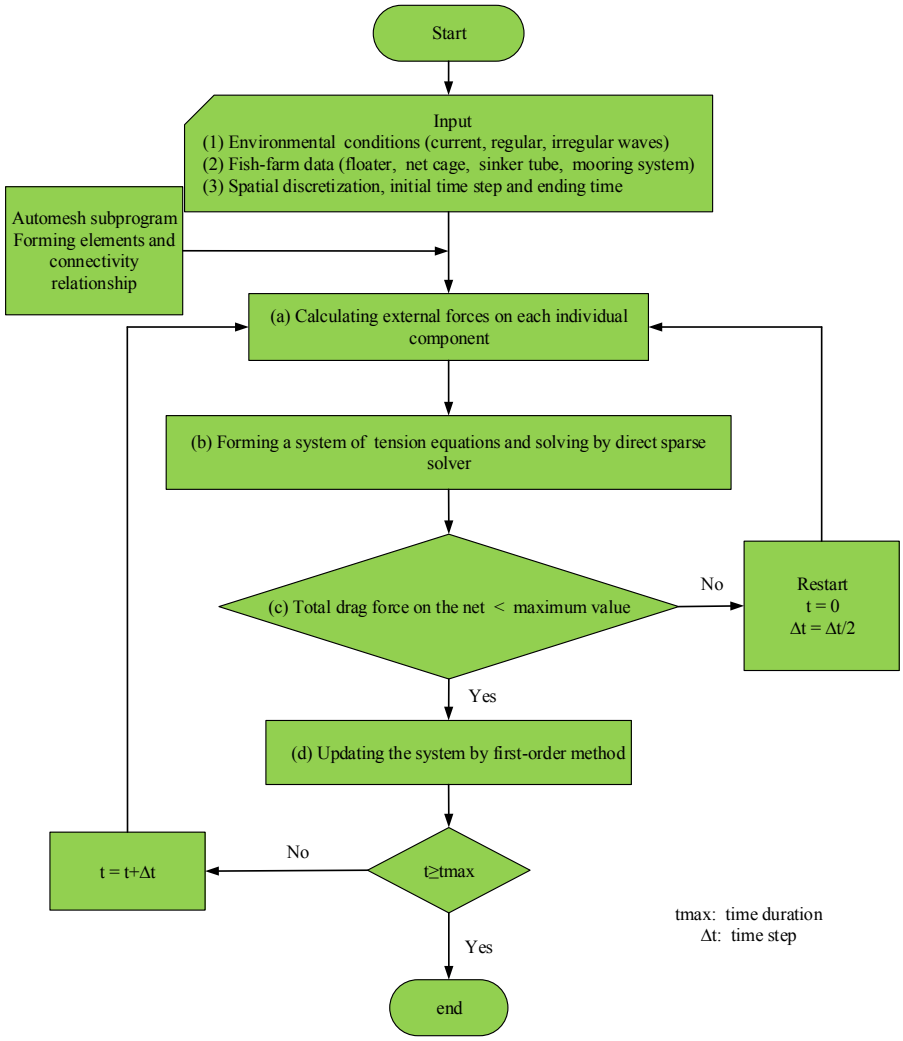

Figure 2.7: Flow chart for numerical simulation.

2.8 Conclusions and following work

The numerical modeling for the different components of a realistic marine fish farm has been introduced. The system comprises a floating collar with two concentric tubes, a flexible net cage and a sinker tube attached directly to the net, moored by a complex mooring system with anchor lines, bridle lines and frame lines. The curved beam equations with consideration of axial stiffness and curvature effects were adopted for solving the motions of the floating collar and the sinker tube. The net cage was modeled by a truss model and the hydrodynamic forces on the cage were predicted by a screen model which accounts for hydrodynamic shadow and Reynolds number effect. For the mooring lines, ropes and chains were treated in a similar way as the net twines and were modeled as elastic trusses with correct diameter, weight and stiffness. The hydrodynamic forces on the mooring lines were estimated by a modified Morison's equation based on the cross-flow principle and by neglecting the longitudinal forces. In the end, two strategies were proposed to deal with the coupling between the different components and the flow chart of the developed numerical solver was provided.

Before using the proposed model to analyze a realistic fish farm, we need to validate the developed numerical tool. This will be done in the following chapter where the numerical modelings of the different fish-farm components and of a simplified fish-farm system are validated with experimental data available in literature.

Chapter 3

Assessment studies of the fish-farm modeling

In this chapter, the modeling adopted for the different fish-farm components is assessed. This is done by comparing against established experiments available in literature. These studies will involve simplifications of the various components, so to reproduce the reference results and also to assess, through a sensitivity analysis, their reliability as alternative models. First, the vertical accelerations induced by regular waves on an isolated floater are considered. The collar is simplified as a single circular floating torus, behaving as flexible or as nearly rigid. Then, the viscous hydrodynamic loads caused by a steady current on a net cage are studied. The net cage is simplified as a rigid-circular cage, a flexible-bottomless circular cage and a deformable, closed net cage. In the first scenario the cage is isolated, while in the others it is attached to a rigid floater and the sinker tube is represented by discrete sinker weights. Finally, the mooring loads for a simplified fish farm in current only and in combined waves and current are examined. The system consists of a single, elastic floater, a flexible-circular-bottomless net cage and sink weights, moored nearly horizontally with mooring lines. Eventually, a detailed sensitivity analysis of the mooring loads to the different modeling parameters is presented.

3.1 The floating collar

In this section, the modeling of the floating collar is validated with available experimental data. It is common to investigate a floating collar with single torus rather than two concentric tubes in model tests, so here we will study the response of a single torus. The modeling of a single torus is similar with that shown in Section 2.2 for a floating collar with two tubes, except that relevant parameters used in the numerical model are for one tube. The experimental data from Li et al. (2014) and Li et al. (2016) are considered, where model tests for a semi-submerged elastic circular torus and for a semi-submerged rigid circular torus in regular deep-water waves were performed. In these studies, the torus was in isolated conditions,

i.e. without a net cage, and the focus was on the induced vertical accelerations, as well as on the importance of hydroelasticity in the wave-body interaction. A list of relevant parameters and dimensions used in the model tests and corresponding full-scale values are given in Table 3.1. The water depth used in the model tests was 1.5 m, ensuring deep water conditions for the examined waves. Detailed discussions for the elastic floater and for the almost rigid floater are shown in Section 3.1.1 and Section 3.1.2, respectively.

Table 3.1: Main dimensions used in the experiments by Li et al. (2014) and Li et al. (2016). Model scale 1 : 25 was adopted. Both model-scale and full-scale values are given. E: Elastic; R: Almost rigid.

Description	Parameter	Model scale	Full scale
Torus diameter	$D = 2R$	1.5 m	37.5 m
Cross-sectional diameter of torus (E)	$d_f = 2c_f$	38 mm	0.95 m
Cross-sectional diameter of torus (R)	$d_f = 2c_f$	36 mm	0.90 m
Torus mass per unit length (E)	m_f	0.602 kg/m	376.0 kg/m
Torus mass per unit length (R)	m_f	0.607 kg/m	379.6 kg/m
Torus bending stiffness (E)	EI_f	0.464 Nm^2	4.53×10^6 Nm^2
Torus bending stiffness (R)	EI_f	23.74 Nm^2	2.32×10^8 Nm^2
Spring stiffness	k_s	17 N/m	10.63 kN/m

3.1.1 A floating elastic torus in regular waves

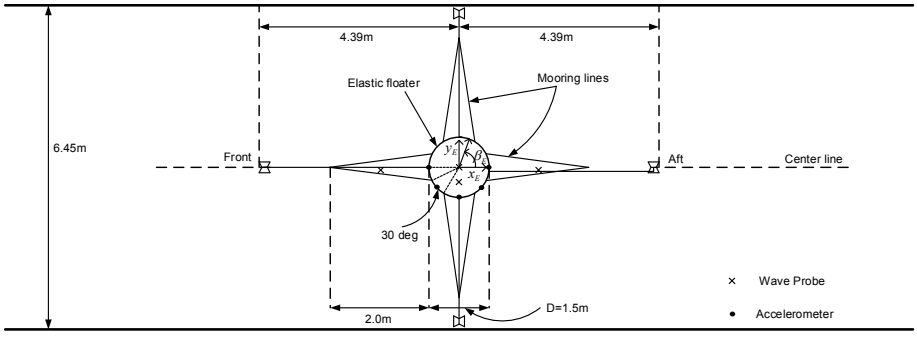

Figure 3.1: Experimental set-up (top view) of the elastic torus model used by Li et al. (2014). Incident regular waves propagate in the positive x_E-axis.

The experimental set-up of the elastic torus model used by Li et al. (2014) is illustrated in Figure 3.1. The elastic torus model was attached to the stationary

carriage in the middle of the tank by means of four identical nearly horizontal mooring lines, at the front, aft, left and right. Each of them was connected to the torus at three locations, resulting in 12 attachment points uniformly distributed along the floater with an interval of 30 degrees. Springs with stiffness $k_s = 17$ N/m were used to connect the torus to the carriage. The pre-tension was $T_p = 5$ N.

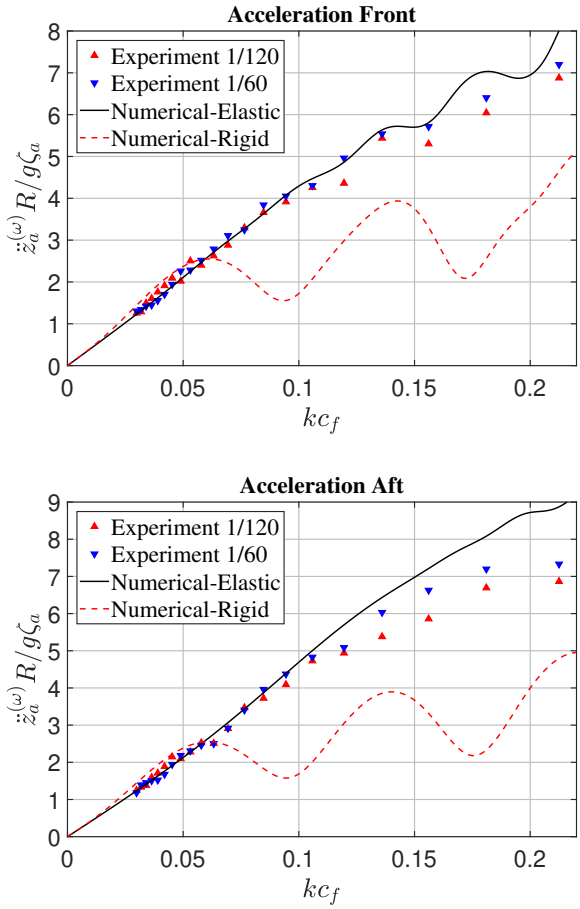

Figure 3.2: Steady-state amplitudes of non-dimensional first-harmonic acceleration $\ddot{z}_a^{(\omega)} R/g\zeta_a$ for an elastic torus versus non-dimensional wave number kc_f. Filled symbols: experimental results from Li et al. (2014) in regular waves with two wave steepness $H/\lambda = 1/120$ and $1/60$. Solid line: numerical results for an elastic torus. Dashed line: numerical results considering a rigid torus.

A comparison of non-dimensional linear vertical acceleration amplitude in front ($\beta_E = \pi$) and aft ($\beta_E = 0$) positions of the elastic floating torus from numerical simulations with the corresponding experimental data is shown in Figure 3.2 as a function of non-dimensional wave number kc_f. Regular waves with frequency ω, amplitude ζ_a and two wave steepness H/λ= 1/120 and 1/60 are examined in the

experiments. Here, $H = 2\zeta_a$ is the wave height and $\lambda = 2\pi/k$ is the wave length. The numerical solutions are obtained in frequency domain according to Eq. (2.8), neglecting the influence of mooring lines. As the incident waves propagate in the positive x_E-axis, only modes that are symmetric about the x_E-axis, i.e. $\cos(n\beta)$ modes, can be excited. In total, twelve modes are used and negligible effect is observed with increasing number of modes. The hydrodynamic coefficients and wave excitation forces for different modes are calculated by the linear potential-flow frequency-domain solver WAMIT, using High-order Boundary Element Method (HBEM). The axial tensions along the floating collar, connected with the axial stiffness, are estimated by a two-dimensional Finite Element Method (2D FEM) and the resulting distribution is shown in Figure 3.3. Axial tension distribution according to a simplified method proposed by Kristiansen and Faltinsen (2015) is also given for comparison. Nice agreement between the two methods is achieved. In terms of the applicability of the two approaches, the FEM approach can be used to deal with general mooring-line arrangement and sea conditions while the simplified method is limited to cases with symmetric loading and specific mooring-line arrangement, for instance the set-up examined here.

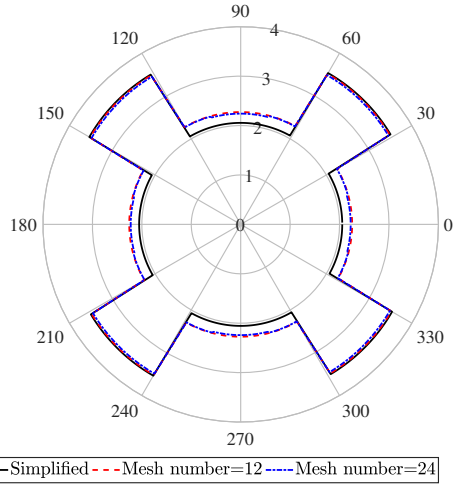

Figure 3.3: Axial tensions along the torus shown in Figure 3.1. Black line: by a simplified method from Kristiansen and Faltinsen (2015), assuming that the axial tension is piecewise constant in each segment meshed by mooring line connection points. Dashed line: by 2D FEM with 12 elements. Dash-dotted line: by 2D FEM with 24 elements.

From Figure 3.2, we can see that the numerical results in general agree reasonably well with the experimental data. Larger difference is observed in higher wave frequency, especially for the aft position. One possible reason is that the structural damping of the floating collar is not included in the numerical model, as the damping level is not straightforward to be determined. Including the structural damping will reduce the vertical acceleration in high frequency and improved nu-

merical results are expected. Also, it is difficult to have an accurate measurement of the bending stiffness of the floating collar in the model tests, especially for the present case with low bending stiffness. Increasing the bending stiffness will also improve the numerical results in higher wave frequencies. Numerical simulations in time-domain including retardation functions (see Equation 2.10) with mooring lines were also performed (not shown here) and small difference is observed compared with the corresponding frequency-domain results. Numerical results considering a rigid floater are also provided in Figure 3.2, showing that the elastic modes matter especially in short waves.

The obtained numerical results are consistent with those from Li et al. (2014), based on the same structural model, but with the hydrodynamic loads given by a low-frequency slender-body theory and the axial tensions estimated by the simplified method. This denotes that the numerical model for the floating collar is correctly implemented in the present study.

3.1.2 A floating nearly rigid torus in regular waves

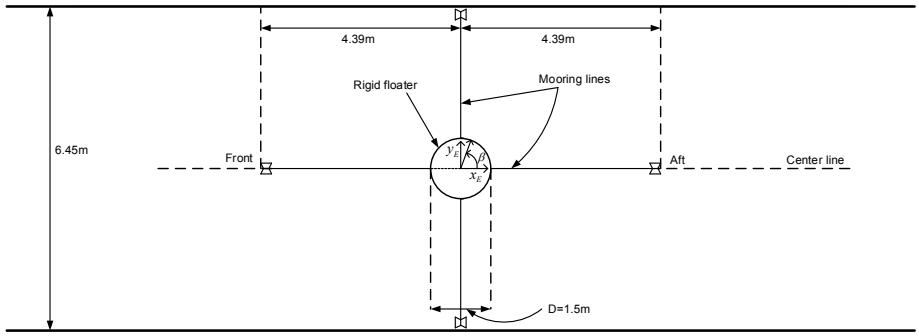

Figure 3.4: Experimental set-up of the almost rigid torus model used by Li et al. (2016).

To examine the influence of the torus flexibility on the structure behavior in waves, Li et al. (2016) studied experimentally also an almost rigid torus in waves. The set-up is the same as that of the elastic model, except the way of connecting the mooring lines to the torus, see Figure 3.4. The rigid torus model was also attached to the stationary carriage in the middle of the tank by means of four identical nearly horizontal mooring lines, at front, aft, left and right and they were connected to the torus through 4 attachment points with an equal interval of 90 degrees.

Similar as in Figure 3.4, Figure 3.5 presents a comparison of the vertical accelerations in the front and aft positions of the almost rigid torus between the numerical results and the experimental data. Numerically, two simulation scenarios were examined, one with a rigid torus and one with a nearly rigid torus, i.e.

including flexible modes in the solution strategy. Only the first-harmonic acceleration term from the model tests is included. From the figure, the numerical results including flexible modes differ from those for a rigid torus, and agree nicely with the experimental data. The obtained numerical results are consistent with those from Li et al. (2016) using a similar numerical model. Although the torus is almost rigid, modeling it as a rigid body will lead to erroneous results.

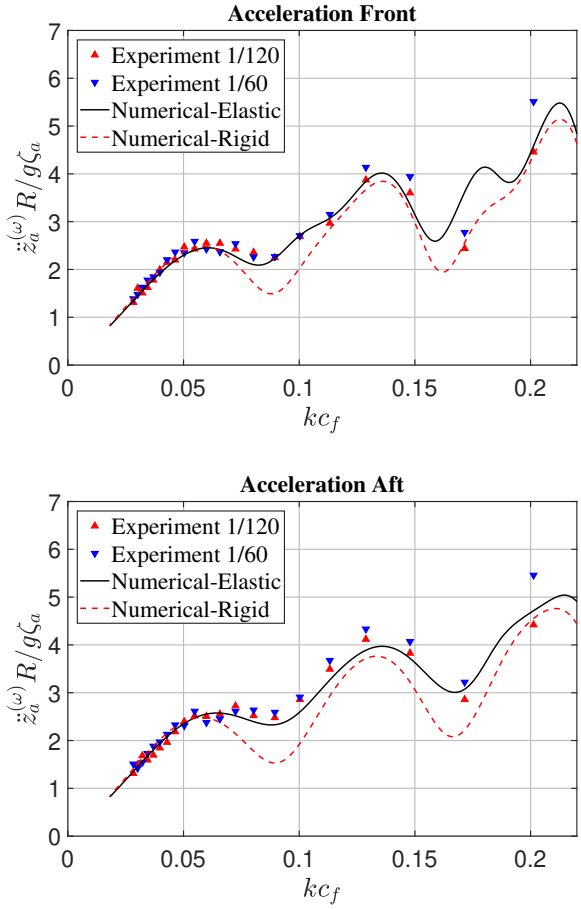

Figure 3.5: Steady-state amplitudes of non-dimensional first-harmonic acceleration $\ddot{z}_a^{(\omega)} R/g\zeta_a$ for a nearly rigid torus versus non-dimensional wave number kc_f. Filled symbols: experimental results from Li et al. (2016) in regular waves with two wave steepness $H/\lambda = 1/120$ and $1/60$. Solid line: numerical results for a nearly rigid torus. Dashed line: numerical results considering a rigid torus.

From Figure 3.2 and Figure 3.5, the floater will experience larger vertical accelerations for the real flexible torus than the almost rigid torus. This indicates that the elasticity of the floater should be carefully modeled, as the vertical acceleration on the floater is important when it comes to the coupling/connection with the net

cage and mooring lines.

3.2 The net cage

In this section, we want to validate the modeling of the net cage by available experimental data. Detailed comparison of the drag force between numerical and experimental results on a rigid-circular net cage, on a flexible-bottomless net cage and on a flexible-closed net cage are shown in Section 3.2.1, Section 3.2.2 and Section 3.2.3, respectively.

3.2.1 Rigid-cylindrical net cage

Drag force on a rigid, cylindrical net cage in current only is investigated at first. By studying a rigid net cage, we can easily check the accuracy and reliability of the hydrodynamic model for the net cage. The experimental data from Zhan et al. (2006) are considered. The corresponding experimental set up is shown in Figure 3.6. The diameter and height of the net cage are 0.414 m and 0.7 m, respectively. Two different solidity ratios Sn=0.128 and 0.223 are examined. The corresponding twine diameters are 0.8 mm and 1.45 mm, respectively. Water depth in the experiments was chosen to guarantee uniform incoming flow for the net cage.

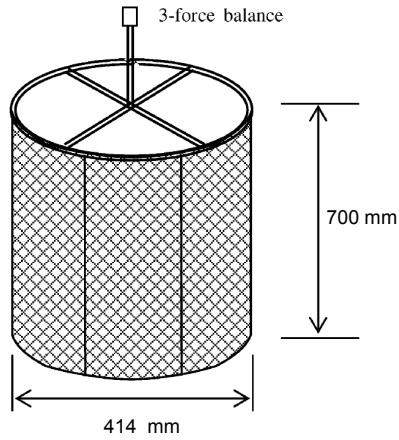

Figure 3.6: Experimental set-up of a rigid net cage model used by Zhan et al. (2006).

A comparison of viscous loads on the cage from the present numerical simulations with the experimental data from Zhan et al. (2006) is shown in Figure 3.7. The figure shows that the screen-type hydrodynamic-load model (solid lines) tends to slightly over-predict the viscous loads on the cage for both solidity ratios. One possible reason leading to the overestimation is that the inflow modification in the

front side of the net cage due to the presence of the cage is not considered in the simulations. This involves a partial flow around the cage and a reduction of the flux through the net. A simplified approach is introduced in the following to account for this effect. The method was originally proposed by Kristiansen and Faltinsen (2012) for a rigid net cage, but their results suggest that the approach could be not correctly implemented. Here, we will follow a similar procedure to the one mentioned by them, but to be used for both rigid and flexible net cages. Detailed explanation of the method is given below.

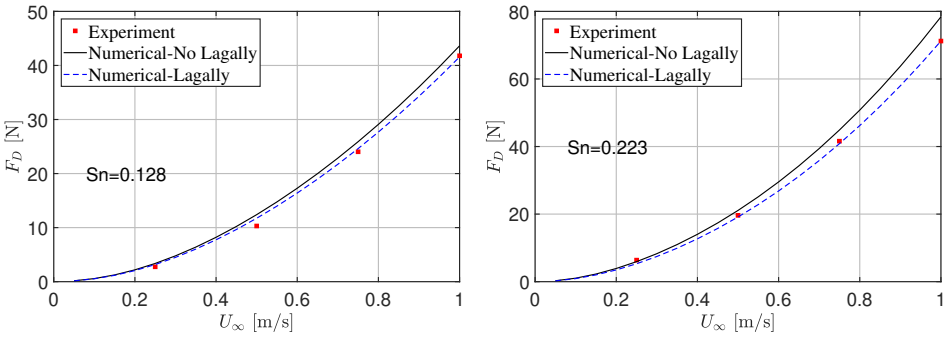

Figure 3.7: Drag forces on a rigid net cage in current from experiments (filled symbols) by Zhan et al. (2006) and from numerical results using the standard formulation (solid lines) and including corrections from Lagally's theorem (dashed lines). Left: solidity ratio Sn=0.128. Right: solidity ratio Sn=0.223.

Flow around the net cage

The method to model the flow around the net cage is introduced here. Several researchers have investigated the flow around and inside a net panel or a three-dimensional cage by Computational Fluid Dynamics (CFD) method. The cage is treated as a porous medium and the disturbance of the net cage to the inflow is represented by a source term in the Navier-Stokes equation, e.g. by Bi et al. (2014) and Yao et al. (2016). However, it is not practical to implement the CFD method if we consider a realistic fish-farm system. Here, we will briefly introduce how we can apply the Lagally's theorem to have a rough estimation of this effect.

It is assumed that the flow is uniform in the vertical direction of the net cage, so the cage can be represented by a two-dimensional source uniformly distributed in vertical direction along the central axis of the cage, see the left plot in Figure 3.8. The source strength is determined by assuming that the source will generate the same drag force as that experienced by the cage. According to the Lagally's theorem, the drag force on a two-dimensional source with source strength q in infinite fluid is $F_{2D} = \rho q U_\infty$ with U_∞ the inflow velocity. F_{2D} is determined as $F_{2D} = F_D/L$, with F_D the total, three-dimensional drag force experienced by the cage and L the draft of the cage. The source strength q is obtained by first calculating the drag F_D without source presence, then setting $q = F_D/\rho U_\infty L$. The

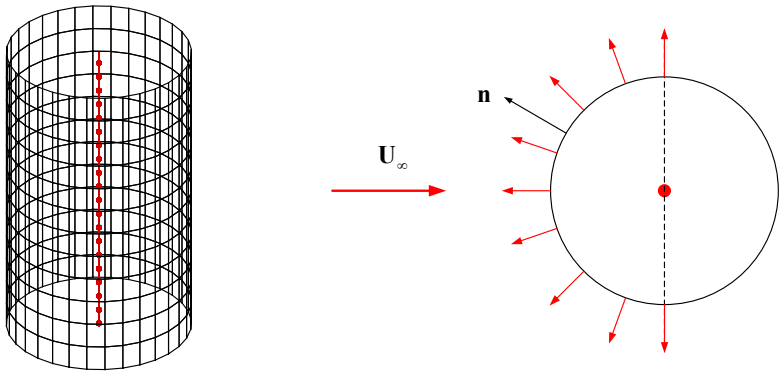

Figure 3.8: Illustration of the solution strategy applying the Lagally's theorem. Left: three-dimensional net cage. Right: cross-sectional cut of the net cage with a source placed at the center. $\mathbf{n}$ is the cage normal vector pointing outwards and $\mathbf{U}_\infty$ is the inflow velocity.

velocity induced by the source is

$$\mathbf{u} = \frac{q}{2\pi R}\mathbf{n} \tag{3.1}$$

with R the radius of the cage, $\mathbf{n}$ the normal vector of the cage, as shown in the right plot of Figure 3.8. Only the flow in the front of the net cage is modified and the modified inflow is $\mathbf{U} = \mathbf{U}_\infty + \mathbf{u}$. Then the new drag force F_D and new source strength q are obtained, and iterations are performed until convergence. It is difficult to determine the position of the source if the net cage is deformed by the interaction with current, so for simplicity the induced velocity is predicted based on the initial geometry but with instantaneous drag force, which is reasonable when the net experiences moderate deformation.

Numerical results of the drag force on the stiff cage considering the flow around the cage are also shown Figure 3.7. The figure documents that better agreement is achieved if Lagally's theorem is applied to model the flow around the net cage. There may also exist other error sources leading to the overestimation of the drag force, but the effect considered seems to provide a promising explanation.

3.2.2 Flexible-bottomless net cage

Here we investigate the drag forces on a flexible-cylindrical-bottomless net cage in current using the experimental data from Kristiansen (2013) as reference. The net cage is attached to a rigid floater and is moored horizontally by two mooring lines in the front and aft positions. The set-up is similar to the one shown in Figure 3.4, but in the present case only front-aft connections to the mooring lines are used. The diameter and height of the net cage are $D = 1.5$ m and $L = 1.3$ m, respectively. The solidity ratio of the net is $\mathrm{Sn} = 0.32$. The twine diameter is approximately d_w

= 6 mm. The net cage is bottomless, with 16 bottom weights attached to it. The submerged weight of each sinker is 68g (in air 75g).

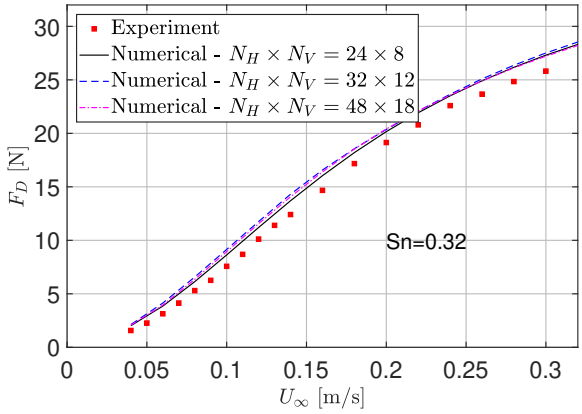

Figure 3.9: Comparison of drag force on a flexible-bottomless net cage in current. Filled symbols: experimental data from Kristiansen (2013). Lines: numerical simulations with $N_H \times N_V = 24 \times 8$ (solid line), with $N_H \times N_V = 32 \times 12$ (dashed line) and with $N_H \times N_V = 48 \times 18$ (dash-dotted line).

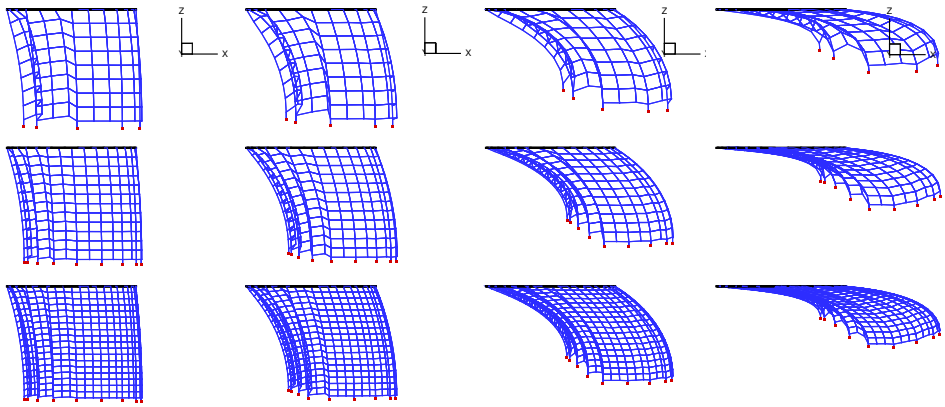

Figure 3.10: Steady-state shapes of a flexible bottomless net cage with different mesh resolutions (side view). From top to bottom: $N_H \times N_V = 24 \times 8$, 32×12 and 48×18. From left to right: $U_\infty = 0.04$, 0.08, 0.16 and 0.32 m/s.

A convergence study was performed and three different meshes were tested. The considered current is in the positive x_E-axis. The drag forces on the net cage from the convergence study are presented in Figure 3.9, together with the experimental data from Kristiansen (2013). Steady shapes of the net cage with different mesh resolutions in four current velocities are presented in Figure 3.10. From Figure 3.9, we can see that a relatively coarse mesh resolution with $N_H \times N_V = 24 \times 8$ is enough

to reach convergence. Here N_H and N_V represent the number of trusses used in the simulation in horizontal and vertical direction, respectively. Note that for this mesh, 8 sinker weights instead of 16 sinker weights are used, but the total weight is kept the same. The motivation to use 8 sinker weights is to ensure that the sinker weights are evenly distributed. Numerical results tend to slightly overestimate the drag force on the cage, but can well follow the trend of the experimental results. This is similar with the comparison for the rigid net cage in Section 3.2.1. Model tests with floater only (without net cage) were also performed by Kristiansen (2013) and showed that the contribution of the floater to the total drag is negligible.

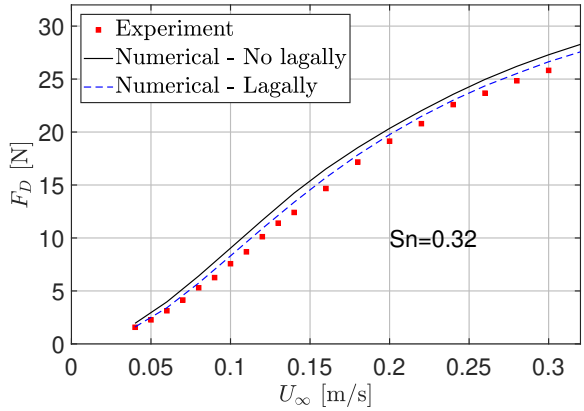

Figure 3.11: The effect of applying Lagally's theorem to model the flow around the net cage. Mesh resolution: $N_H \times N_V = 24 \times 8$.

The inflow modification due to the presence of the cage matter instead. In fact, applying the Lagally's theorem to model the flow around the net cage will improve the numerical results, see Figure 3.11. The chosen mesh resolution is $N_H \times N_V = 24 \times 8$. In higher current velocities (U_∞ >0.2 m/s), the net cage will experience larger deformations, then the assumption used when applying the Lagally's theorem, i.e. that the net cage remains circular and the current is uniform in the vertical direction, is no longer valid. So it becomes questionable using the Lagally's method for high current velocities even if it gives better results according to the examined case. On the other hand, relevant full-scale current velocity at real fish-farm sites will be smaller than 1.0 m/s, corresponding to 0.2 m/s in model scale, so the proposed simplified model of the flow around the net cage still has a practical value.

3.2.3 Flexible-closed net cage

In this part, we investigate the drag forces on a more realistic flexible-closed net cage in current only using the experimental data from He et al. (2015) as reference. The experimental set-up is the same as that used in Section 3.2.2, i.e. the net cage is attached to a rigid floater and is moored horizontally by two mooring lines, except that the net cage is closed with a cylindrical part and a conical part, and

an additional sinker weight is attached to the bottom of the cage. The sketch of the closed net cage is shown in Figure 3.12.

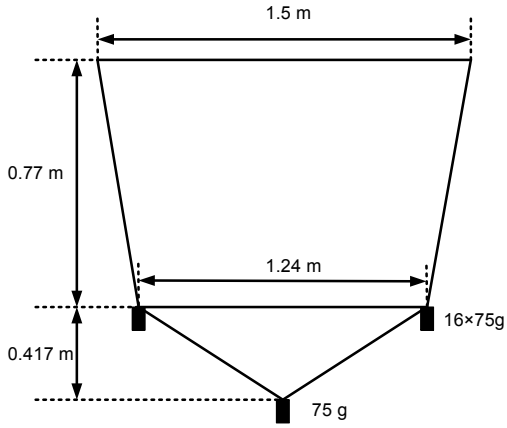

Figure 3.12: Sketch of the closed net cage used by He et al. (2015). The floater and mooring lines are not shown.

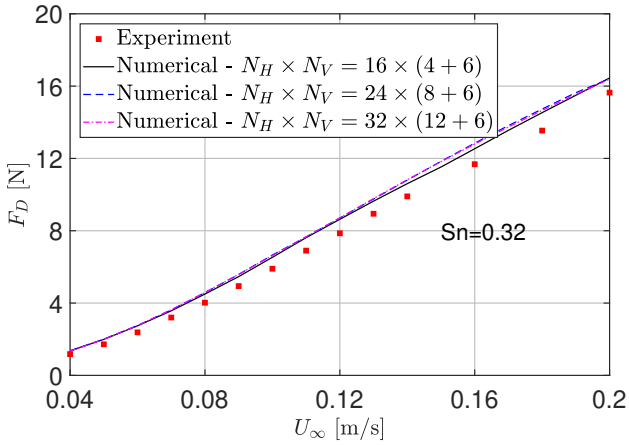

Figure 3.13: Drag forces on a circular, deformable, closed net cage. Filled square symbols: experimental results. Lines: numerical simulations with $N_H \times N_V = 16 \times (4+6)$ (solid line), with $N_H \times N_V = 24 \times (8+6)$ (dashed line) and with $N_H \times N_V = 32 \times (12+6)$ (dash-dotted line).

A comparison of the drag forces on the cage in current only of the present numerical simulations with the experimental data from He et al. (2015) is shown in Figure 3.13. The current is in the positive x_E-axis. Numerical results with three different mesh resolutions are given. The figure shows that a relatively coarse

mesh is enough to reach convergence and numerical results tend to slightly over-predict the drag forces. The steady-state shapes of the net cage from the numerical simulations with $N_H \times N_V = 24 \times (8+6)$ in four current velocities are presented in Figure 3.14. N_V comprises two parts, respectively, meshes for cylindrical and for conical part.

The effect of flow around the cage is also investigated by using the Lagally's theorem and improved numerical results are obtained, see Figure 3.15. One should note that only the cylindrical part of the cage is considered when applying the Lagally's theorem. The main reason is that the shape of the conical part is not consistent with the definition of problem for use of the Lagally's theorem. Also, its contribution to the total viscous load on the net cage is moderate, i.e. about 15%-20%, so the related error due to the flow modification is expected to be small.

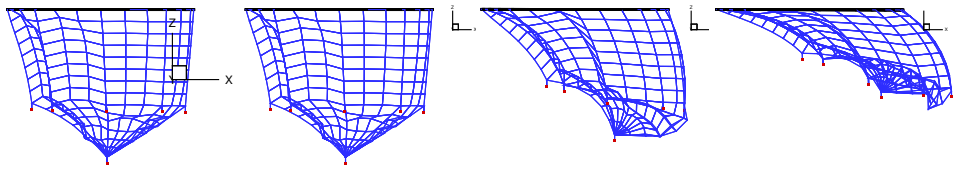

Figure 3.14: Steady-state shapes of a closed net cage (side view) with mesh resolution $N_H \times N_V = 24 \times (8+6)$. From left to right: $U_\infty = 0$, 0.04, 0.12, 0.20 m/s.

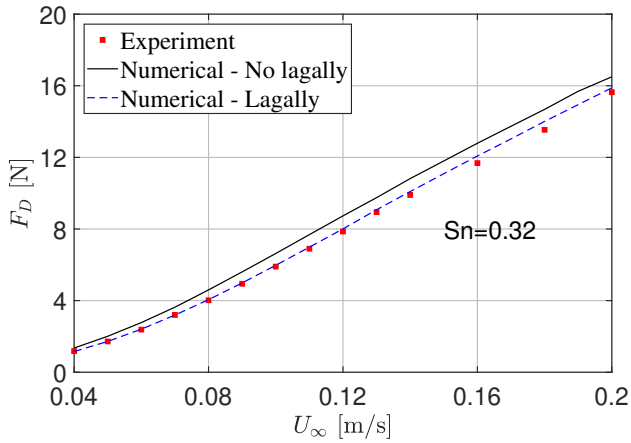

Figure 3.15: Drag forces on a circular, deformable, closed net cage. The effect of applying Lagally's theorem to model the flow around the closed net cage. Mesh $N_H \times N_V = 24 \times (8+6)$ is used in the analysis.

3.2.4 Comments regarding net-cage modeling

In conclusion, the adopted screen-type force model for the net cage can provide a reliable estimation of the viscous current loads on the cage. Numerical results generally slightly over-estimate the viscous loads on the cage. One of the possible reasons is that the flow around the net cage is not considered, i.e. the incoming flow is assumed to be not affected by the presence of the cage. Applying Lagally's theorem to model the flow around the cage will improve numerical results, however we can not rule out other possible reasons of the over-estimations.

3.3 A simplified fish-farm system

In this section, a more complex fish-farm system presented by Kristiansen and Faltinsen (2015) is investigated. The system is simplified compared with a realistic aquaculture fish farm, yet contains all the main components, including a single elastic floater, a flexible-circular-bottomless net cage and sinker weights, moored horizontally with four crow feet mooring lines. The front and aft mooring lines were connected to linear springs (not the two side mooring lines). The arrangement of the mooring lines is the same as that shown in Figure 3.1.

Table 3.2: Main parameters and dimensions used in the model tests by Kristiansen and Faltinsen (2015). Model scale 1 : 25 was adopted. Both model-scale and full-scale values are given.

Description	Parameter	Model scale	Full scale
Floater diameter	$D = 2R$	1.5 m	37.5 m
Cross-sectional diameter of floater	d_f	30 mm	0.75 m
Floater mass per unit length	m_f	0.127 kg/m	79.4 kg/m
Floater bending stiffness	EI_f	0.136 Nm^2	1.33×10^6 Nm^2
Net cage diameter	$D = 2R$	1.5 m	37.5 m
Net depth	L	1.3 m	32.5 m
Net solidity ratio	Sn	0.26	0.26
Diameter of net twines	d_w	0.6 mm	-
Length of net twines	l_w	6 mm	-
Mass of bottom weights in air	M_{bw}	16×75 g	16×1172 kg
Spring stiffness (front and aft)	k_s	44 N/m	27.5 kN/m
Pre-tension	T_p	14 N	218.7 kN/m

A list of relevant parameters and dimensions are given in Table 3.2. Both model-scale and full-scale values are provided. The examined inflow (waves and/or current) is in the positive x_E-axis and the water depth in the model tests ensured deep water conditions. Numerical results for the system in current only and in combined waves and current are presented in Section 3.3.1 and Section 3.3.2,

respectively. The experimentally obtained mooring loads from Kristiansen and Faltinsen (2015) are used to validate the developed numerical code. A sensitivity analysis is also performed in Section 3.3.3 to examine the importance of different parameters for the mooring loads.

3.3.1 Current only

Figure 3.16 presents the net-cage drag force F_D^T estimated as difference between front and aft mooring-line tensions from the present numerical simulations and from the experimental data by Kristiansen and Faltinsen (2015) for the fish-farm system in current only. Two scenarios are examined: with and without spring in the front mooring line. From the figure, numerical predictions agree well with the experimental data for both cases, in particular, the trends are well captured.

The obtained numerical results are similar with those from Kristiansen and Faltinsen (2015) in small to medium current velocities ($U_\infty < 0.2$ m/s), but slightly larger in higher current velocity. A possible reason is that in Kristiansen and Faltinsen (2015) the vertical positions of the sinker weights in calm water are not fixed and depend on the mesh resolution of the net cage, i.e. depend on the size of the bottom layer trusses in the simulations. This may cause error in larger current velocities.

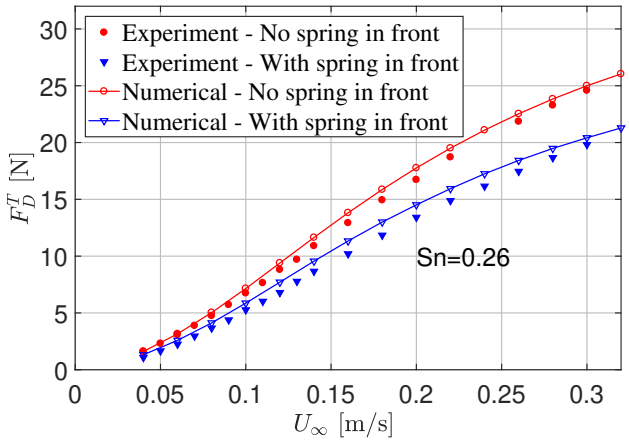

Figure 3.16: The drag force deduced from the front and aft mooring lines in current only. Filled symbols: experimental data from Kristiansen and Faltinsen (2015). Triangular and circular symbols denote experiments with and without a spring in the front mooring line, respectively. Open symbols: the corresponding numerical results. Mesh resolution: $N_H \times N_V = 24 \times 8$.

Examples of time series of mooring-line tensions in the front and aft mooring lines are also provided in Figure 3.17 for current velocity $U_\infty = 0.1$ m/s. Without spring in the front mooring line, the drag force on the net cage F_D is almost equal to F_D^T, i.e. practically balanced by the front and aft mooring lines. With spring, F_D is almost unchanged while F_D^T becomes smaller (see Figure 3.16), so the net

cage drifts in the current direction and the side mooring lines will contribute to the final equilibrium position. Snapshots of the steady shapes of the system (with spring in the front mooring) in four different current velocities are presented in Figure 3.18. The floater, net cage, moorings and sinker weights are shown in the figure.

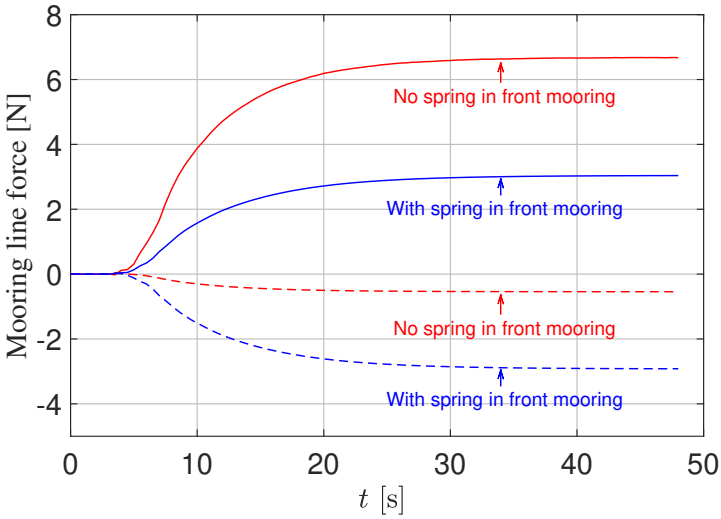

Figure 3.17: Examples of time series of the front and aft mooring line tension from the present numerical simulations. Current velocity $U_\infty = 0.1$ m/s. The pre-tension is subtracted. Solid line: tension in the front mooring line. Dashed line: tension in the aft mooring line.

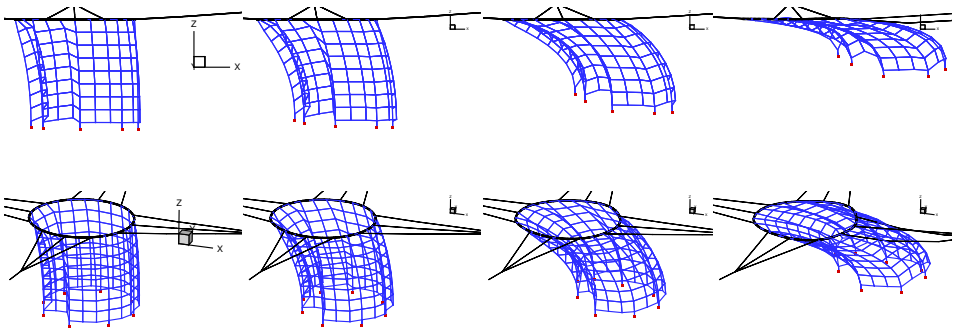

Figure 3.18: Snapshots from the present numerical simulations for cases with springs in the front and aft mooring lines. Mesh: $N_H \times N_V = 24 \times 8$. Upper row: without perspective (side view). Lower row: with perspective. From left to right: $U_\infty = 0.04$, 0.08, 0.16 and 0.32 m/s.

3.3.2 Combined waves and current

In this section, we present results for the fish-farm system in waves only and in combined waves and current. The set-up with linear springs in the front and aft mooring lines is adopted. The focus is on the tension in the front mooring line.

Examples of time series of tension in the front mooring line from numerical simulations are shown in Figure 3.19 for cases in waves only and in combined waves and current. Wave period $T = 1.6$ s, wave steepness $H/\lambda = 1/15$ and two current velocities $U_\infty = 0$ m/s (waves only) and 0.1 m/s (combined wave and current) are examined. For the case with current, the fish farm is investigated first in current only, then, after about 50 s, the waves effect is included. This leads to a fictitious transient phase with increase of the mean mooring force until a steady-state condition is reached, see Figure 3.19. From the figure, the total mooring load in combined waves and current is much larger than that in waves only.

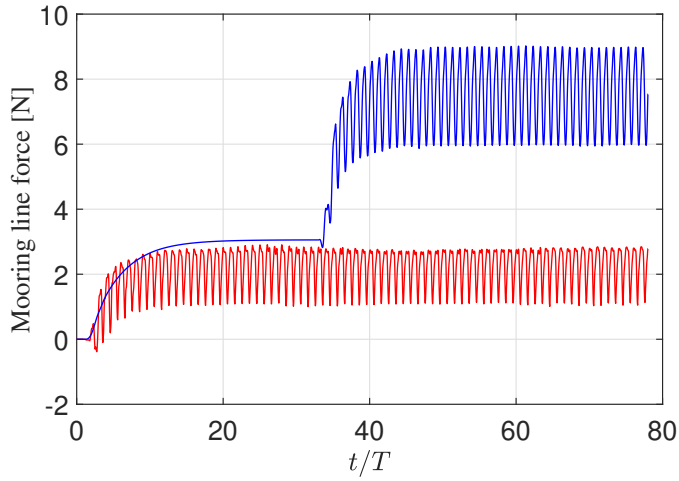

Figure 3.19: Examples of time series of the front mooring-line tension from the present numerical simulations. The pre-tension is subtracted. Upper blue line: $T = 1.6$ s, $H/\lambda = 1/15$ and $U_\infty = 0.1$ m/s. Lower red line: $T = 1.6$ s, $H/\lambda = 1/15$ and $U_\infty = 0$ m/s.

Snapshots from the numerical simulations are shown in Figure 3.20 and Figure 3.21 for cases without and with current, respectively. The linear wave profile is included in the top row. The mesh of the cage is exponentially refined in vertical direction to better resolve the wave kinematics. The floater basically follows the wave due to relatively long wavelength of the incident wave (the wavelength-to-floating collar diameter ratio is $\lambda/D \approx 2.7$), as shown in the figures. Moreover, as expected, the net cage is substantially more deformed when current is present.

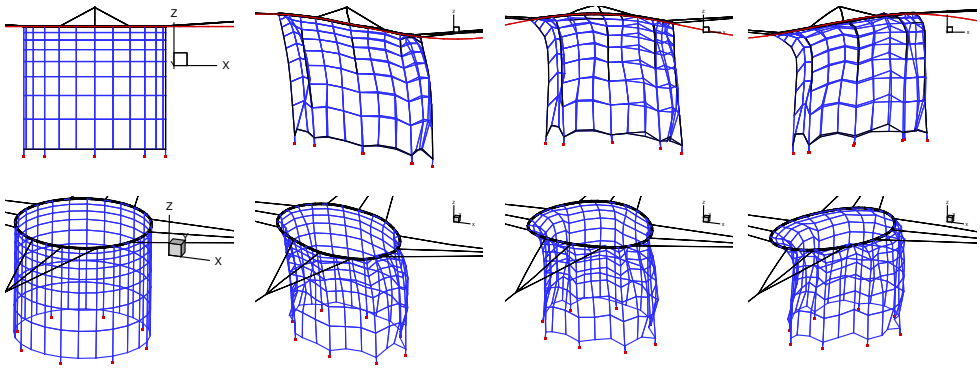

Figure 3.20: Snapshots for different time instants from the present numerical simulation with $N_H \times N_V = 24 \times 8$. Current velocity $U_\infty = 0$ m/s, wave period $T = 1.6$ s and wave steepness $H/\lambda = 1/15$. Upper row: without perspective (side view). Lower row: with perspective. The left snapshot shows the initial shape in calm water.

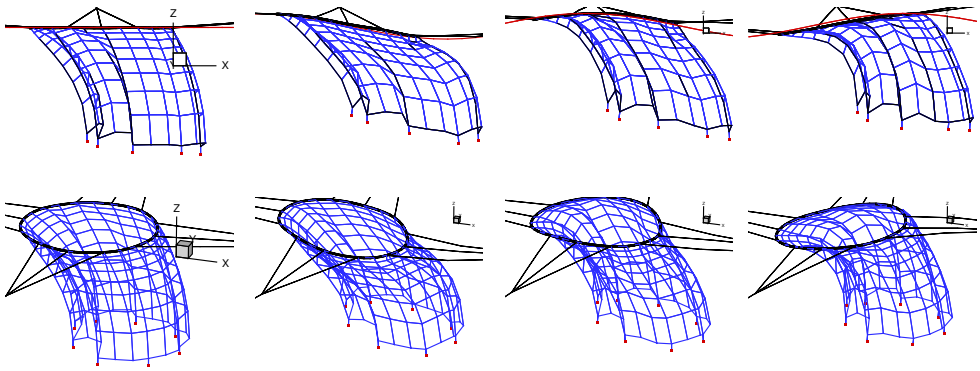

Figure 3.21: Snapshots for different time instants from the present numerical simulation with $N_H \times N_V = 24 \times 8$. $U_\infty = 0.1$ m/s, $T = 1.6$ s and $H/\lambda = 1/15$. Upper row: without perspective (side view). Lower row: with perspective. The left snapshot shows the steady shape in current only.

Systematic comparison of loads (both mean and total values) in the front mooring line from numerical simulations with the experimental data from Kristiansen and Faltinsen (2015) is shown in Figure 3.22, with fair agreement of the results. This serves as a validation of the numerical model. Here the mean force is taken as the mean value of the mooring load from the last 10 wave periods in the simulations and the total force is given as the sum of the mean force and the force amplitude, with the force amplitude equals $\sqrt{2}$ times the standard deviation of the force time-series within the considered time interval. This is consistent with the data analysis of the experiments.

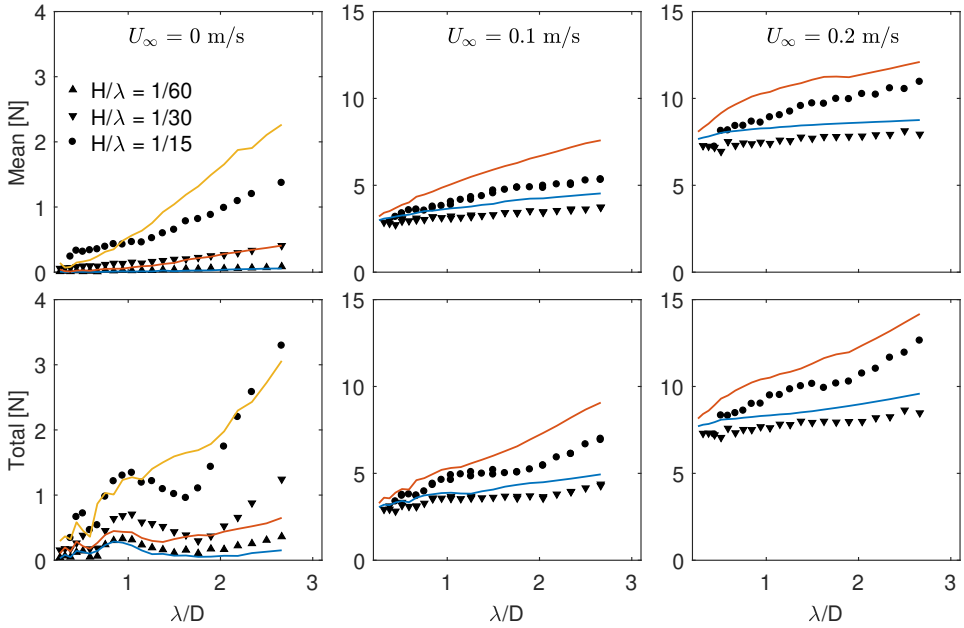

Figure 3.22: Comparison of mean and total forces in the front mooring line. The pre-tension is subtracted. Solid symbols: experimental data from Kristiansen and Faltinsen (2015). Solid lines: numerical results.

Table 3.3: Environmental matrix used in the simulations, showing current velocity, wave steepness and wave period ranges. For each examined wave range, an interval $\Delta T = 0.05$ s is used.

Current U_∞ [m/s]	**Wave steepness** H/λ		
	1/60	1/30	1/15
0.0	0.5-1.6 s	0.5-1.6 s	0.5-1.6 s
0.1	-	0.5-1.6 s	0.5-1.6 s
0.2	-	0.5-1.6 s	0.5-1.6 s

The examined environmental matrix is shown in Table 3.3. The simulations tend to overestimate the mooring loads for cases in combined waves and current. In terms of the total mooring loads, discrepancies up to 27% are observed for some cases with $U_\infty = 0.1$ m/s and $H/\lambda = 1/15$, but apart for them the difference is in general rather small. Better agreement is observed for cases with smaller wave steepness. In particular, for cases in waves only with $H/\lambda = 1/60$, the numerical solver can have a good prediction of both the mean and total force. One possible reason for the large discrepancies in higher sea states is that the developed model is based on linear wave theory. For instance the wave particle velocity, which is important for evaluating the viscous loads on the cage, is assumed constant above

the mean free surface ($z_E = 0$) and equals to the value at $z_E = 0$, and the wave excitation loads of the floater are calculated by linear potential-flow solver, so the numerical model is expected to hold better for waves with smaller wave steepness.

The simplified fish-farm system was also studied numerically by Kristiansen and Faltinsen (2015) based on a similar numerical model (not shown here). Compared with their results, the present numerical results are slightly larger for cases in combined waves and current, but the general trend is consistent. As explained for cases in current only, the most possible reason causing the difference is that the mesh strategy for the net cage in the present work is different from that used by Kristiansen and Faltinsen (2015). This would suggest that present results should be more reasonable, though they are slightly less close than Kristiansen and Faltinsen (2015) solution to the experiments in the high-current region. There are also other differences in the numerical modeling between the two numerical solutions, for instance, in the model by Kristiansen and Faltinsen (2015), the hydrodynamic loads for the floating collar were based on a low-frequency slender-body theory from Li and Faltinsen (2012) and the axial tensions were estimated by the simplified method introduced before, but their influences are expected to be small.

3.3.3 Parameter analysis

In this section, a detailed sensitivity analysis is performed to identify important parameters influencing the total force in the front mooring line. These parameters need to be properly modeled. Regular waves in Table 3.3 with $H/\lambda = 1/30$ and two current velocities $U_\infty = 0$ m/s and 0.1 m/s are chosen. The different parameters examined are shown in Table 3.4. In order to quantify the significance of them and try to identify the important ones, we present condensed results in Figure 3.23. In the figure, each bar represents the percentage difference of the total mooring load with respect to the nominal value, averaged over all the examined wave periods. "Nominal" denotes that basis values of different parameters are used in the simulations. More detailed discussions are presented below.

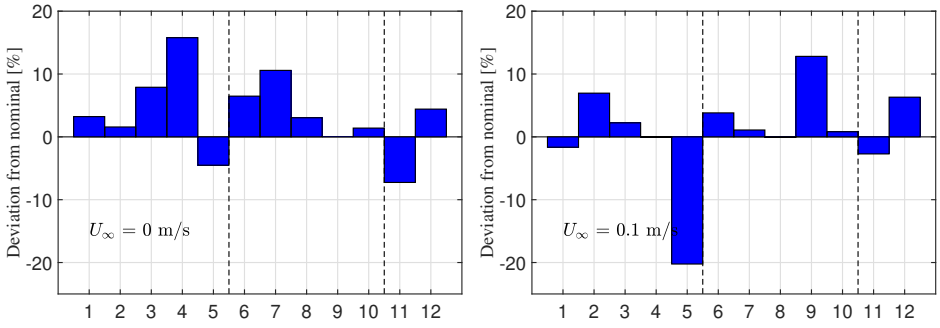

Figure 3.23: Each bar represents the percentage difference of the total load in the front mooring line with respect to the nominal value, averaged over all the examined wave periods. The numbers on the horizontal axis refer to variation numbers as given in Table 3.4. Left: $U_\infty = 0$ m/s. Right: $U_\infty = 0.1$ m/s.

Table 3.4: Parameters that are varied in the sensitivity analysis. $a_{33}^n(0)$ and $a_{11}^n(0)$ denote zero frequency added mass coefficients used for the mode n in vertical and horizontal direction of the floating collar, respectively (No. 3). Nominal number of vertical and radial structural modes for the floating collar are $N_v = N_h = 8$ (No. 5). The mesh used in the nominal simulations is $N_H \times N_V = 24 \times 8$. Parameters that lead to more than 5% difference from the nominal value are marked by "$\times$" in the right two columns. Parameters not investigated are marked by "-".

	No.		Explanation	>5%	
				Wave	Waves and current
Floater	1	$C_D^f = 0$	Floater Drag		
	2	$T_{ax} = 0$	Axial stiffness		$\times$
	3	$a_{33}^n(0)$,$a_{11}^n(0)$	Floater added mass	$\times$	
	4	$f^{\text{Froude Kriloff}} + f^{\text{restoring}}$	Nonlinear model	$\times$	
	5	N_h=1, N_v=2	Rigid body		$\times$
Net	6	$N_H = 32$, $N_V = 12$	Mesh resolution	$\times$	
	7	$N_H = 48$, $N_V = 18$	Mesh resolution	$\times$	
	8	Rn	Reynolds number definition		
	9	r= 0	Reduction factor	-	$\times$
	10	$f_{\text{net-twine}}^{\text{added mass}}$	Net-twine added mass		
Moorings	11	$k_s = 40$ N/m	Spring stiffness	$\times$	
	12	$T_p = 10$ N	Pre-tension		$\times$

First, we analyze some parameters related with the modeling of the floater.

Drag on the floater: The drag force on the floater in the horizontal plane is estimated by the drag term in Morison's equation, see Eq. (2.15). In terms of drag coefficient, in case of no over-topping, the free surface acts like a splitter plate and for a circular cylinder with splitter plate a representative value for the drag coefficient in steady flow is $C_D^f = 0.6$ - 0.8. The actual C_D^f depends on several parameters, as explained in Section 2.2.3 and it is not practical to account for all these influences. A constant C_D^f =0.6 is used in the nominal simulations. Neglecting the drag load on the floater, i.e. $C_D^f = 0$, will increase the total mooring load in waves only and reduce the value in combined waves and current. However, the influence for both cases is small (<4%). In combined waves and current, neglecting the drag force on the floating collar will increase the amplitude of the mooring load but will reduce the mean value, resulting in a reduction of the total value.

Axial stiffness: The different structural modes of the floater are coupled due to the axial terms in the beam equation, see Eq. (2.13). Neglecting the axial stiffness, i.e. axial tension $T_{ax} = 0$, will increase the total mooring load and have more effect when current is present, with an increase of about 7%.

Floater added mass: The sectional non-dimensional added mass and damping coefficients for the first four modes of the floater in horizontal and vertical direction, calculated by the linear potential-flow solver WAMIT are shown in Figure 3.24 and Figure 3.25, respectively. The added mass and damping coefficients for vertical modes, estimated by the low-frequency slender-body theory (LST) proposed by Li (2017) are also shown in Figure 3.24 and good agreement between low-frequency slender theory and WAMIT is observed for the shown wave frequency ($kc_f < 0.25$). Increasing difference is expected with increasing wave frequency. The oscillatory behavior indicated by the figure is due to hydrodynamic interaction on the scale of the floater radius, which can not be captured when two-dimensional strip theory is adopted. Similar discussions for the vertical modes were given by Li (2017). They are repeated here for completeness in understanding the important physical mechanisms.

For the hydrodynamic coefficients in horizontal plane, the damping coefficients are almost zero for small wave frequency ($kc_f < 0.15$) and the corresponding added mass coefficients are almost constant and equal to the value for zero frequency, as shown in Figure 3.25.

Using zero frequency instead of the frequency-dependent added mass for both the horizontal and vertical modes will increase the total mooring load by about 8.5% when $U_\infty = 0$ m/s, but has a negligible influence when $U_\infty = 0.1$ m/s .

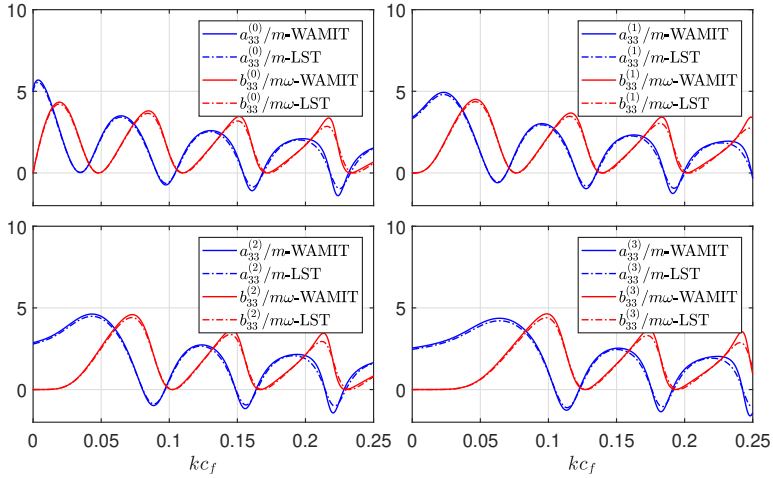

Figure 3.24: Sectional non-dimensional vertical added mass $a_{33}^{(n)}/m$ and damping $b_{33}^{(n)}/m\omega$ coefficients of a floater for the modes number $n = 0$, 1, 2, 3 versus non-dimensional wave number kc_f. Here the subscript "33" denotes vertical direction. $k = \omega^2/g$ is the wave number and c_f the cross-sectional radius of the floater. m is cross-sectional displaced water mass. Solid line: by WAMIT. Dashed line: by the low-frequency slender-body theory (LST) from Li (2017).

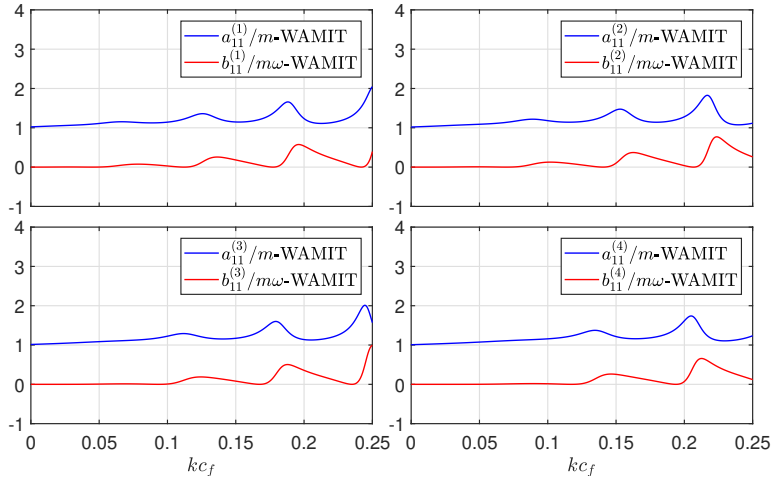

Figure 3.25: Sectional non-dimensional horizontal added mass $a_{11}^{(n)}/m$ and damping $b_{(11)}^{n}/m\omega$ coefficients of a floater for the modes number $n = 1$, 2, 3, 4 by means of WAMIT verus non-dimensional wave number kc_f. Here the subscript "11" denotes horizontal direction. $k = \omega^2/g$ is the wave number and c_f the cross-sectional radius of the floater. m is cross-sectional displaced water mass.

Nonlinear Froude-Kriloff and restoring forces: In the nominal simulations, linear wave excitation and radiation loads, including Froude-Kriloff and restoring forces, are considered. Here, we try to incorporate nonlinear Froude-Kriloff and restoring forces while still keeping the linear diffraction and added-mass and damping forces. The Froude-Kriloff force is connected with the dynamic pressure of the incident waves as the body was not there. Since the considered wavelength is long compared with the cross-sectional diameter of the floater, long wavelength approximation is assumed valid, then the nonlinear Froude-Kriloff and hydrostatic force are given by

$$\begin{aligned} f_r^{\text{nonlin.FK}} &= \rho A_{\text{sub}} \ddot{r}_w \\ f_z^{\text{nonlin.FK}+\text{nonlin.rest}} &= \rho A_{\text{sub}} \ddot{z}_w + \rho g \left(A_{\text{sub}} - 0.5\pi c_f^2 \right) \end{aligned} \tag{3.2}$$

where $\ddot{r}_w$ and $\ddot{z}_w$ are the radial and vertical undisturbed wave particle accelerations at the geometrical center of the submerged floater. A_{sub} is the instantaneous submerged area (see shaded area in Figure 3.26), which is found considering the local vertical displacement of the floater z_f and the local undisturbed incident-wave elevation ζ.

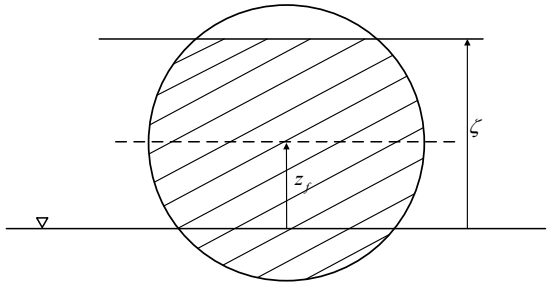

Figure 3.26: Sketch for calculating the submerged cross-sectional area of a circular section. ζ is incident-wave elevation and z_f is vertical displacement of the section.

Considering nonlinear Froude-Kriloff and restoring forces will significantly increase the total mooring load in waves only, by about 16.6%, but has a negligible influence in combined waves and current. The main reason is that the load on the floater is small compared with that on the cage with the presence of current.

Rigid floater: In Section 3.1, numerical results show that considering a rigid instead of an elastic floater will lead to erroneous vertical accelerations along the floater. Here we want to quantify this influence on the mooring load.

From Figure 3.23, modeling the floater as a rigid body will reduce the total mooring loads, in particular for cases in combined waves and current, with an average reduction of about 20%. The reason is that side mooring lines will provide more contribution to balance the load on the net cage when the floater is rigid compared to the case with an elastic floater. However, one must note that this may not be the case for a realistic fish farm with much smaller pre-tension and

different mooring line arrangement.

Next, we discuss some more parameters connected with the modeling of the net cage and of the mooring lines.

Mesh resolution: More refined mesh will increase the total mooring load by about 7% - 10% when $U_\infty = 0$ m/s, but with much smaller effect when $U_\infty = 0.1$ m/s. We are more interested in the case with current, so a relatively coarse mesh with $N_H \times N_V = 24 \times 8$ is enough.

Reynolds number definition: In the nominal simulations, when calculating the drag coefficient for the screen, the relevant Reynolds number is defined according to Eq. (2.39) by the instantaneous relative velocity instead of by the characteristic free-stream velocity including the velocity amplitude from incident waves, see Eq. (2.37).

Numerical results indicate that using the two different definitions will yield similar total mooring load.

Reduction factor: Due to the shading effect of the front net cage, the inflow (steady part) is reduced for the rear part net. Neglecting this effect will increase the total mooring load by about 13% for the examined current velocity.

Net-twine added mass: In the nominal simulations, when evaluating the added-mass force $f_{\text{net-twine}}^{\text{added mass}}$ for the net twines in Eq. (2.18), the added mass of the net twine is assumed equal to the mass of the water displaced by the twine, i.e. sectional added mass $= \rho\pi d_w^2/4$. Increasing the net added mass by 100% will have a negligible influence on the total mooring load.

Moorings: Reducing the spring stiffness in the front and aft mooring lines by 10% will reduce the total mooring load by about 7% and 3 % while changing the pre-tension from 14 N to 10 N will lead to an increase of the total mooring load by 4.4% and 6.3%, for cases without and with current, respectively.

3.3.4 Explicit versus implicit coupling for the fish-farm system

Both the explicit and implicit coupling strategies proposed in Section 2.6 are adopted to deal with the coupling between the different components of the simplified fish-farm system described in Section 3.3. The results shown in the figures are associated with the implicit coupling but they are practically the same as those from the explicit strategy. The two coupling approaches showed instead quite different costs in terms of computational time, as explained in the following. When using them, the matrix of the equations system for truss tensions is sparse and the corresponding sparse patterns are shown in Figure 3.27. A renumbering technique, i.e. reverse Cuthill–McKee algorithm (RCM, see Cuthill and McKee, 1969), is used to reduce the bandwidth of the equation systems for the two strategies.

From the figure, the number of nonzero values in the matrix is significantly reduced when using the explicit coupling strategy and less computational time is needed than for the implicit coupling strategy when the same time-step is used. However, for some cases with higher wave steepness, much smaller time step is needed to reach convergence when using the explicit coupling strategy and greater CPU time is expected than for the implicit method. Because severe and extreme conditions are of interest to draw the operational limits of a fish-farm system, to ensure a better robustness of the solver in the analysis reported in the rest of the thesis, the implicit coupling strategy will be adopted.

A direct sparse matrix solver is used to solve the equations system and a time step in the range of $T/200$ is found enough to reach convergence for all the simulated cases in Section 3.3. In particular, for a simulation in regular waves with wave period $T = 1$ s and wave steepness $H/\lambda = 1/30$, it takes about 1-2 minutes computational time on a 3 GHZ one-core laptop for the simulation lasting for instance 50 s, as physical time. The considered mesh is $N_H \times N_V = 24 \times 8$.

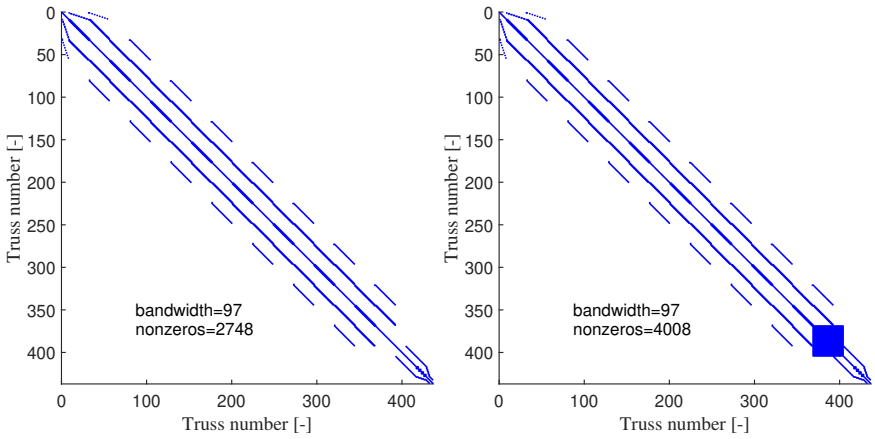

Figure 3.27: Sparse pattern of the equation system for unknown truss tensions with $N_H \times N_V = 24 \times 8$. Left: using the explicit coupling strategy. Right: using the implicit coupling strategy.

Figure 3.28 presents the computational time needed versus number of unknown truss tensions for a given simulation time lasting 50 s, with the same wave condition introduced above. Both the results using the implicit coupling and the explicit coupling are provided. The same time step is used in the simulations. The four symbols in the figure correspond to mesh resolutions $N_H \times N_V = 24 \times 8$, 32×12, 48×18 and 64×24, respectively. The figure shows that the developed solver is quite efficient using both coupling strategies. Also, the explicit approach is more efficient than the implicit approach, with a reduction of the computation time by about 30% - 40%. The former is expected to be even more efficient compared with the latter for the case with more complex fish-farm set up. This denotes that the explicit approach is promising in reducing the computational time, thus deserves more research, although it is not used in the rest of the present thesis.

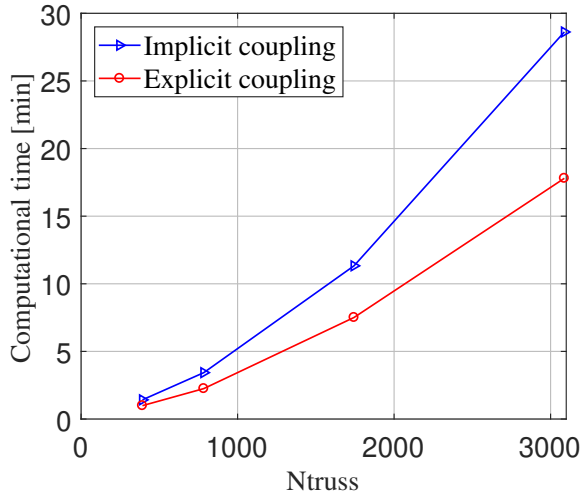

Figure 3.28: Computational time in minute versus number of unknown truss tensions.

3.4 Conclusions and following work

In this chapter, the modeling of each individual component of a fish farm has been validated with available experimental data. First, the modeling of a single isolated torus was examined and nice agreement was observed between the experimental and numerical results of the vertical accelerations along the torus. Numerical results also showed that the elasticity of the torus is important, even if the torus is almost rigid. For the net cage, the screen-type force model could provide a good estimation of the viscous current loads on the cage. A slightly over-estimation tendency was observed and an improved prediction is possible if the effect of the flow around the net cage is considered.

A simplified fish-farm system featuring all the main components of a realistic aquaculture fish farm in current only, waves only and combined waves and current was also investigated. The developed numerical solver could have a good prediction of the mooring load in current only. In combined waves and current, nice agreement of the load in the front mooring line was achieved between the numerical and experimental results for cases with smaller wave steepness. Larger discrepancies (over-estimation) were observed for some cases with higher wave steepness, but the general agreement was still reasonable.

A sensitivity analysis was also performed to identify the influences of the different parameters on the total load in the front mooring line. When current is present, the most important two parameters are the floater elasticity and the flow reduction factor for the rear part of the net cage.

The different validation studies indicate that the proposed numerical model with simplified fish-farm system is reliable and correctly implemented. Although this includes all the necessary components, it is still far from reality in terms of the

floating collar, the net cage, the sinker tube and also the mooring lines arrangement. To provide more practical guidance for fish-farm operations, the developed numerical tool will be used to analyze a realistic fish-farm system as described in Chapter 2 (with single cage) in current only, and in regular and irregular waves in the following chapter.

Chapter 4

Numerical and experimental investigations on mooring loads of a marine fish farm in waves and current

In this chapter, a realistic aquaculture fish-farm system in both regular and irregular waves is investigated by numerical simulations and model tests. The considered fish farm comprises a floating collar with two concentric tubes, a flexible net cage including a cylindrical part and a conical part with a center point weight at the bottom, and a sinker tube attached directly to the net. The system is moored with a complex mooring system with bridle lines, frame lines and anchor lines, supported by buoys. The main purpose is to validate the developed numerical tool for a realistic fish farm and then to use this tool to investigate the survival conditions of the system.

First, a description of the model tests conducted in Marintek (Nygaard, 2013) for a fish farm with realistic set-up is given. Then, theories for generating both regular and irregular waves are introduced. Detailed information for evaluating the hydrodynamic loads on the floating collar is also provided. After that, numerical results are compared with the experimental data for a realistic fish-farm system in current only, regular-waves only, combined regular-waves and current and irregular seas, along with a numerical sensitivity study to identify important parameters influencing the mooring loads. At last systematic simulations for fish farms with different set-ups are performed and the limitations of moving the conventional fish farm to more exposed regions are discussed. Parts of the results in this chapter are documented in Shen et al. (2018) and Faltinsen and Shen (2018).

Dr. Arne Fredheim and Mr. Ivar Nygaard from SINTEF Ocean AS are acknowledged for providing the experimental data for this in-depth analysis.

4.1 Experiments

The model experiments for a realistic fish farm carried out at the Ocean Basin Laboratory of MARINTEK by Nygaard (2013) are considered as reference. All measurements reported hereinafter, relate to full-scale values, unless otherwise specifically indicated.

4.1.1 Model test set up

The physical model used in the experiments featured all the main components presented in a full-scale sea cage system (with single cage) commonly used in Norway, which included two concentric floating tubes, an elastic sinker tube, a cylindrical net cage with a conical bottom, mooring system comprising bridle lines, mooring frame lines, mooring buoys, coupling plates, chains connecting the coupling plates to the buoys and the anchor lines attaching the system to the bottom of the basin, see Figure 4.1. A model test scale of 1:16 was adopted and Froude scaling with geometric similarity except for the net twines was assumed. For the net twines, geometric similarity cannot be applied, as the net twine diameter and net E-module are too small to be realized in model scale if using geometric similarity. So nylon net twines were used in the model tests.

According to the screen model proposed by Kristiansen and Faltinsen (2012), the solidity ratio and the Reynolds number of the twines are two important parameters to estimate the drag force on the cage. Correct solidity ratio was used in the model test while the Reynolds number of the twine in model-scale cage (Rn = 100 - 300) is smaller than that in a full-scale cage (Rn = 500 - 1000). In terms of the drag coefficient C_D of the twine, it is larger in model scale ($C_D \approx$ 1.25-1.35) than in full scale ($C_D \approx$ 1.0-1.1). C_D is estimated with the same formula as for the drag coefficient for a smooth circular cylinder, see Eq. (2.32). To represent a more realistic full-scale value, we should use as large twine diameter as possible in the model tests to keep the twine Reynolds number as high as possible. Two linear springs were inserted in the front two anchor lines where the forces were measured, as shown in the upper part of Figure 4.1. The sinker tube was attached directly to the net in this study, without vertical chains between the floating collar and the sinker tube to avoid chafing between the chain and the net cage. A list of relevant parameters and dimensions of the model-scale and corresponding full-scale values are given in Table 4.1 and Table 4.2. Photos illustrating the general set-up of different components are presented in Figure 4.2.

The instrumentation of the model consisted of a total of 8 linear accelerometers, 14 force measurement devices, three wave gauges (one at the axis origin was used only for wave calibration, not in the model tests). Axial forces were measured in one bridle pair (bridle line-1 and bridle line-2) on the windward side of the floating collar, in the two front two anchor lines (anchor line-1 and anchor line-2), under two buoys (buoy-1 and buoy-2) in the 7 m long chain between the buoy and the coupling plate, and in ropes connecting the sinker tube and the net in positions with $\beta = 0,\ \pi/2,\ 4\pi/5,\ \pi$, where β is defined in Figure 4.1. The positions of the majority of the instruments are shown in Figure 4.1.

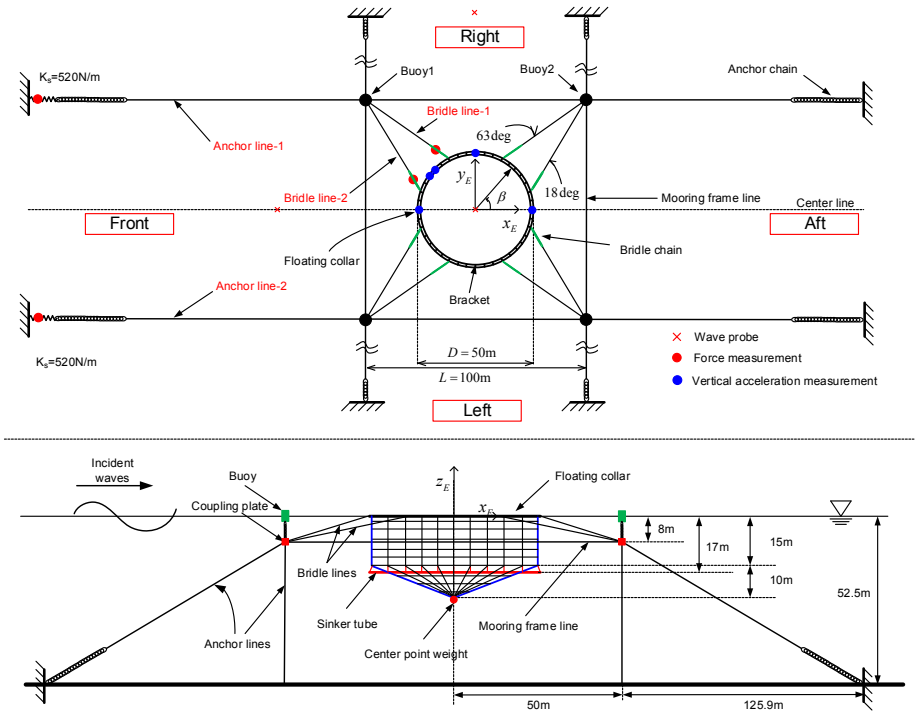

Figure 4.1: Experimental set-up (full-scale). Upper: top view. Lower: side view. Two springs were inserted in the front two anchor lines. The Cartesian coordinate system $O_E x_E y_E z_E$ is located at the center of the floating collar in calm conditions.

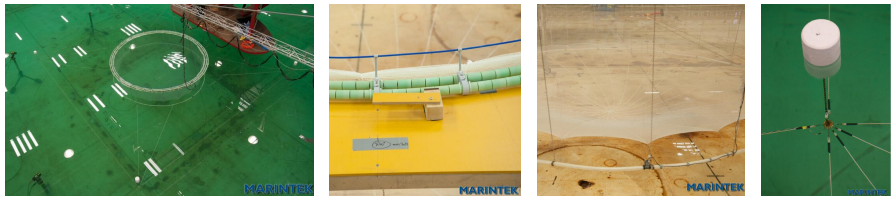

Figure 4.2: Photos of the physical set-up. Left: general set-up including the floating collar, the net cage, the sinker tube and the mooring system. Middle left: detail of the two concentric floating tubes which are combined by 40 brackets. Middle right: details of the sinker tube and the net cage. Right: photography showing the buoy, the coupling plate and the mooring lines.

4.1.2 The models

The floating collar consisted of two floating tubes with outer cross-sectional diameter $d_f = 2c_f = 450$ mm. Selected SDR (SDR = ratio between the floater cross-sectional diameter and the wall thickness of the plastic tube) was 17.6, i.e.

Table 4.1: Parameters of the floating collar, net cage and sinker tube in the model tests. Both model-scale (MS) and full-scale (FS) values are given. Since 'ordinary' nylon ropes were used for the net cage in the model tests, the corresponding full-scale E-module (E_{net}) is larger than that used in full-scale cages. The parameters marked with * are not presented in Nygaard (2013) and are taken from a similar experiment.

Description	Symbol	Model scale	Full scale	Unit
Floating collar				
Number of tubes	-	2	2	-
Diameter inner tube (center)	D_{f1}	3.125	50	m
Diameter outer tube (center)	D_{f2}	3.2375	51.8	m
Distance between tubes	p	56.25	900	mm
Tube section diameter	d_f	28.125	450	mm
Tube bending stiffness	EI_f	0.72	7.72×10^5	Nm^2
Tube mass	m_f	0.124	32.54	kg/m
Net cage				
Diameter	D_c	3.125	50	m
Depth of vertical net	h_u	0.9375	15	m
Depth of cone net	h_l	0.625	10	m
Net twine diameter*	d_w	0.975	3.25	mm
Net mesh-bar length*	l_w	7.5	14.3	mm
Net E-module*	E_{net}	5×10^8	8.2×10^9	N/m^2
Net solidity	Sn	0.26	0.26	-
Center point weight	W_c	0.048	200	kg
Sinker tube				
Tube diameter	D_s	3.2375	51.8	m
Tube section diameter	d_s	17.5	280	mm
Tube depth	h_s	1.0625	17	m
Tube bending stiffness	EI_s	0.195	2.0×10^5	Nm^2
Mass per meter in water	w_s	0.095/0.191	25/50	kg/m

the wall thickness of the plastic tube was 25.6 mm. Floating tubes were modeled with correct outer diameter, horizontal circumference, buoyancy and bending stiffness. The diameter of the center line of the inner tube was $D_{f1} = 50$ m. The outer tube was positioned with a pipe diameter distance (center-to-center distance $p = 0.9$ m), leading to the center line diameter is equal to $D_{f2} = 51.8$ m. The tubes were held together by 40 brackets. The specific fluidity of each of the tubes was 0.2, i.e. the dry weight in relation to the buoyancy of fully submerged pipe, leading to the mass per unit length of the tube to be $m_f = 32.54$ kg/m. Bending stiffness of the tubes was Froude scaled in the model tests to have correct elastic natural frequencies for both horizontal and vertical modes. The bending stiffness (full scale) of each of the tube was $EI_f = 7.715 \times 10^5$ Nm^2.

A sinker tube with center line diameter $D_s = 51.8$ m, cross-sectional diameter $d_s = 2c_s = 280$ mm and bending stiffness $EI_s = 2.0 \times 10^5$ Nm^2 was chosen. Two

Table 4.2: Parameters of the mooring system in the model test. The springs were inserted in the lower end close to the anchor in the front two mooring lines, as shown in Figure 4.1. The stiffness of the anchor lines without spring was 2180 N/m, the inserted spring stiffness $k_s = 520$ N/m, the total line stiffness became about 420 N/m, consistently with the specified value. All values given above are in model scale. The full-scale stiffness of the bridle lines and frame lines are larger than those used in commercial full-scale cages, since 'ordinary' ropes were used in the experiments. All ropes were almost without weight in water and were intended to provide just geometry contribution. The parameters marked with * are not presented in Nygaard (2013) and are taken from a similar experiment.

Description	Model scale	Full scale	Unit
Bridle lines			
Position on cage (bridle-1)	117	117	degrees
Position on cage (bridle-2)	162	162	degrees
Bridle rope diameter*	2.5	40	mm
Bridle chain diameter*	1.4	22.4	mm
Bridle chain length *	0.342	5.47	m
Bridle chain mass *	0.033	8.66	kg/m
Bridle stiffness *	1.85	486.1	kN/m
Frame lines			
Mooring frame length	6.25	100	m
Mooring frame depth	0.5	8	m
Frame rope diameter*	3.2	51.2	mm
Frame stiffness*	3.92	1.03×10^3	kN/m
Anchor lines			
Anchor line length	8.344	133.5	m
Anchor rope length*	6.47	103.5	m
Anchor rope diameter*	3.2	51.2	mm
Anchor chain length*	1.88	30	m
Anchor chain diameter*	2	32	mm
Anchor chain mass*	0.061	16.0	kg/m
Anchor line stiffness (no spring)	2.18	572.0	kN/m
Anchor line stiffness (with spring)	0.42	110.2	kN/m
Buoy system			
Number of buoys (1 at each corner)	4	4	-
Buoy diameter *	0.0965	1.55	m
Buoy length*	0.146	2.34	m
Buoy mass*	0.035	146.9	kg
Buoy Chain length	0.4375	7	m
Buoy chain mass*	0.033	8.66	kg/m
Buoy chain diameter*	1.4	22.4	mm
Coupling plate mass	0.013	55	kg

different submerged masses were adopted with w_s = 25 kg/m and 50 kg/m. A center point weight with W_c = 200 kg submerged mass was attached to the lower end of the net, see Figure 4.1.

A cylindrical net cage with a conical bottom was attached to the floating collar with net-height of the cylindrical part h_u = 15 m and conical part h_l = 10 m and with a typical solidity ratio Sn = 0.26. In the lower edge of the cylindrical part 20 ropes were attached to connect the sinker tube.

The anchor system, consisting of a square 100 m × 100 m frame anchoring, was laid out around the net 8 m deep and was held in place by 4 buoys, one buoy at each corner. At each spar buoy a chain 7 m long hangs, whose lower end was attached to a steel plate. From each steel plate two bridle lines were connected to the floating collar and two anchor lines were connected to the Ocean-Basin bottom. Bottom depth was set to 52.5 m.

4.1.3 Test conditions

A total of 6 irregular waves (long crested), 4 regular waves and two current only cases were considered in the experimental study. The test matrix is presented in Table 4.3. The same test number referred in Nygaard (2013) is adopted here. The 6 irregular waves were generated according to the definition of JONSWAP wave spectrum with spectrum peakedness γ=2. The duration of all irregular waves was 1.5 hour (full-scale). In terms of the significant wave height H_s and peak wave period T_p, the generated irregular waves in the model tests have less than 5% deviation from the corresponding specified values. The actual current speed in the facility was found to be 0.48 ± 0.031 m/s and 0.72 ± 0.046 m/s when it was prescribed to be 0.5 m/s and 0.7 m/s, respectively.

4.1.4 Pre-tension

In order to benchmark numerical results with experimental data, we should know the pre-tension of the system in static configuration. The original report from the experiments does not present the values of the pre-tensions, instead we obtain the pre-tensions from the time histories of the mooring loads in static condition. Results from model tests show that mean pre-tensions (full scale) in anchor line-1 and anchor line-2 are 38.4 kN and 25.3 kN, respectively, which means that the model has asymmetric pre-tensions.

4.2 Theory and numerical model

In this section, we will first give an introduction of theories for generating both regular and long-crested irregular waves. Then we will describe in detail the hydrodynamic loads experienced by the floating collar.

Table 4.3: Test matrix showing prototype (full) scale current velocity, the wave height and wave period (in regular-wave cases) and significant wave height and peak wave period (in irregular-wave cases). CUR, REG and IRR represent current, regular and irregular waves. BR represents mass per unit length of the sinker tube.

Test no.	**Test type**	H_s(m)	T_p(s)	**Current** U_∞(m/s)	**BR**
5010	CUR	-	-	0.5	50 kg/m
5020	CUR	-	-	0.7	25 kg/m
5030	IRR	1.0	4.0	0.5	50 kg/m
5040	IRR	1.5	4.5	0.5	50 kg/m
5050	IRR	2.0	5.0	0.5	50 kg/m
5060	IRR	2.5	6.0	0.5	50 kg/m
5070	IRR	3.0	7.0	0.5	50 kg/m
5080	IRR	4.0	8.0	0.5	50 kg/m
5150	REG	2.5	6.0	-	50 kg/m
5160	REG	2.5	8.0	-	50 kg/m
5170	REG	2.5	6.0	0.5	50 kg/m
5180	REG	2.5	8.0	0.5	50 kg/m

4.2.1 Wave field

The responses of a fish farm system in both regular and irregular waves are to be investigated. Linear potential wave theory is adopted to describe the regular waves. According to Faltinsen (1990), the deep-water wave potential φ_0 for a wave propagating along the positive x_E-axis is given as

$$\varphi_0 = \mathrm{Re}\left\{\frac{ig\zeta_a}{\omega}e^{-i(kx-\omega t)}e^{kz}\right\} \tag{4.1}$$

where Re denotes the real part of a complex value, i is the imaginary unit, x and z are the horizontal and vertical coordinates, respectively, t the time, ζ_a the wave amplitude, g the gravitational acceleration, ω the circular frequency and $k = \omega^2/g$ the wave number. The corresponding wave elevation according to linear wave theory is

$$\zeta(x,t) = \zeta_a \cos(kx - \omega t) \tag{4.2}$$

Using the amplitude spectrum estimated from the time history of generated regular wave in the experiment, small contribution from double frequency 2ω component is observed, but the influence is expected to be small.

For long-crested irregular waves, the surface elevation $\zeta(x,t)$ at a position x and time t is obtained as the superposition of multiple (N) monochromatic waves

$$\zeta(x,t) = \sum_{i=1}^{N} A_i \cos(k_i x - \omega_i t + \varepsilon_i) \tag{4.3}$$

where A_i is the amplitude of the wave associated with the circular frequency ω_i and $k_i = \omega_i^2/g$ is the corresponding wave number. ε_i is the random phase angle for frequency component i and is uniformly distributed between 0 and 2π. The wave amplitude A_i is given as

$$A_i = \sqrt{2S(f_i)\Delta f} \tag{4.4}$$

where $S(f)$ is the wave spectrum, $f_i = \omega_i/2\pi$ is the wave frequency. Δf is the frequency interval. If a constant frequency interval is used, the realization of the wave elevation with respect to time will not be a real random process. The wave elevation will have a return period $T_r = 1/\Delta f$, which means that the wave pattern will repeat in time with period T_r. So, small constant Δf is needed for long time simulation. The solution to this issue is using also random frequency intervals. We can obtain random frequency seed $f_i^{'}$ by

$$f_i^{'} = f_i + \Delta f p_i \tag{4.5}$$

where f_i is obtained with constant frequency interval Δf, p_i is a random stochastic variable evenly distributed between -0.5 and 0.5. In terms of the wave spectrum, the JONSWAP wave spectrum was used in the experiment and defined as

$$S\left(f\right) = \alpha g^2 (2\pi)^{-4} f^{-5} \exp\left(A\right) \gamma^{\exp(B)} \tag{4.6}$$

where

$$\begin{aligned} A &= -1.25(f/f_p)^{-4} \\ B &= -(f-f_p)^2/\left(2\sigma^2 f_p^2\right) \\ \alpha &= 5.061 H_s^2 f_p^4 \left(1.0 - 0.287 \ln \gamma\right) \end{aligned} \tag{4.7}$$

Here f is the frequency in [Hz], $f_p = 1/T_p$ is the frequency of spectral peak in [Hz], H_s is the significant wave height and γ is the spectral peakedness. Finally, σ is the spectral width parameter given as

$$\sigma = \begin{cases} = 0.07 & \text{for } f \leq f_p \\ = 0.09 & \text{for } f > f_p \end{cases} \tag{4.8}$$

A sample of the wave spectrum derived from generated irregular waves in the experiment and that obtained from the JONSWAP wave spectrum with significant wave height H_s= 4 m, peak wave periods T_p = 8 s and spectrum peakedness γ = 2 is shown in Figure 4.3. The corresponding time history of the waves from the experiment is shown in Figure 4.4.

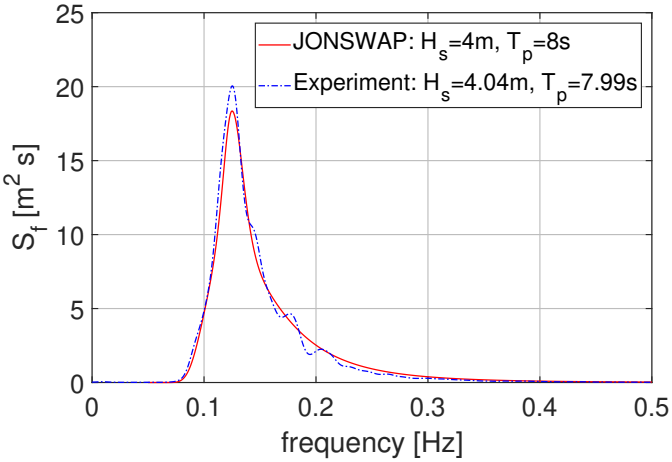

Figure 4.3: Comparison of the wave spectrum from the experiment and from the JONSWAP wave spectrum with significant wave height H_s= 4 m, peak period T_p = 8 s and spectrum peakedness $\gamma = 2$.

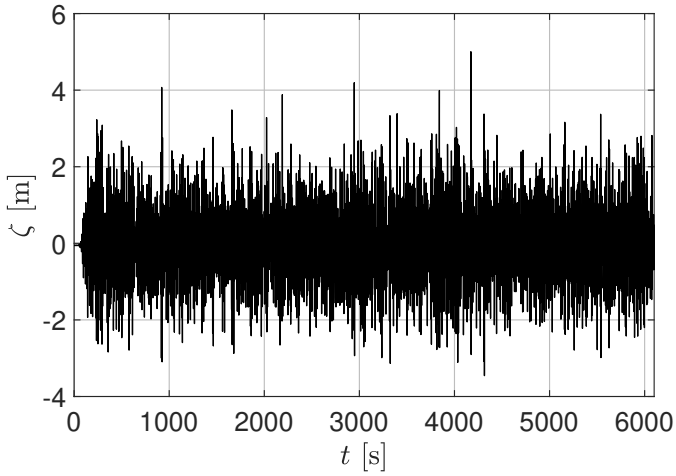

Figure 4.4: Time history of the irregular waves from the experiment with significant wave height H_s= 4 m, peak period T_p = 8 s and spectrum peakedness $\gamma = 2$.

4.2.2 Hydrodynamic loads for the floating collar

The theoretical model for different components of the fish farm has been introduced in detail in Chapter 2 and validated in Chapter 3, so it will not be repeated. Here, just some detailed information regarding the estimation of the hydrodynamic loads for the floating collar will be provided.

Added mass and damping coefficients

For the floating collar examined here with two concentric tubes, the hydrodynamic forces and coefficients are evaluated in a similar way as for a single torus in Chapter 3, i.e. by the frequency-domain potential-flow solver WAMIT, using Higher-order Boundary Element Method (HBEM). Since the incident flow is in the positive x_E direction, only modes symmetric with respect to the x_E-axis, i.e. $\cos(n\beta)$ modes, can be excited. The floating collar is assumed half-submerged when at rest. As an example, the sectional non-dimensional added mass and damping coefficients for the first four modes of the floating collar in vertical and horizontal direction are shown in Figure 4.5 and Figure 4.6, respectively. In Figure 4.5, analytical zero frequency vertical added mass coefficients are also included and are calculated according to the following expression by Faltinsen (2011)

$$a_{33}^{(n)} = f + \rho \frac{16c^2}{\pi} \left[\ln\left(\frac{8R}{c}\right) - K_n \right] \tag{4.9}$$

with

$$\begin{aligned} K_n &= \frac{1}{2\sqrt{2}} \int_0^{2\pi} \frac{1-\cos(n\mu)}{\sqrt{1-\cos(\mu)}} \, \mathrm{d}\mu \\ &= 2\left(1 + \frac{1}{3} + \frac{1}{5} + \ldots + \frac{1}{2n-1}\right), \quad n \geq 1 \end{aligned} \tag{4.10}$$

and

$$\begin{aligned} \frac{f}{\rho c^2} &= 5.74604 - 5.76835\left(\frac{p}{c}\right) + 1.55575\left(\frac{p}{c}\right)^2 \\ &\quad - 0.21295\left(\frac{p}{c}\right)^3 + 0.01128\left(\frac{p}{c}\right)^4 \end{aligned} \tag{4.11}$$

for a floating collar with two tubes and $2.0 < p/c < 6.0$. Here p is the distance between the axes of two semi-submerged circular cylinders, each with radius c. In our case, $p/c = p/c_f = 4.0$, so Eq. (4.9) is applicable. Compared with the results for a single torus (see Figure 3.24), the non-dimensional added mass and damping coefficients for two tubes have stronger oscillatory behavior. In terms of the hydrodynamic coefficients for the examined floating collar in horizontal plane shown in Figure 4.6, similar behavior is observed as that for a single torus (see Figure 3.25), i.e. the damping coefficients are almost zero for small wave frequency and the corresponding added mass coefficients are almost constant and equal to the values for zero frequency.

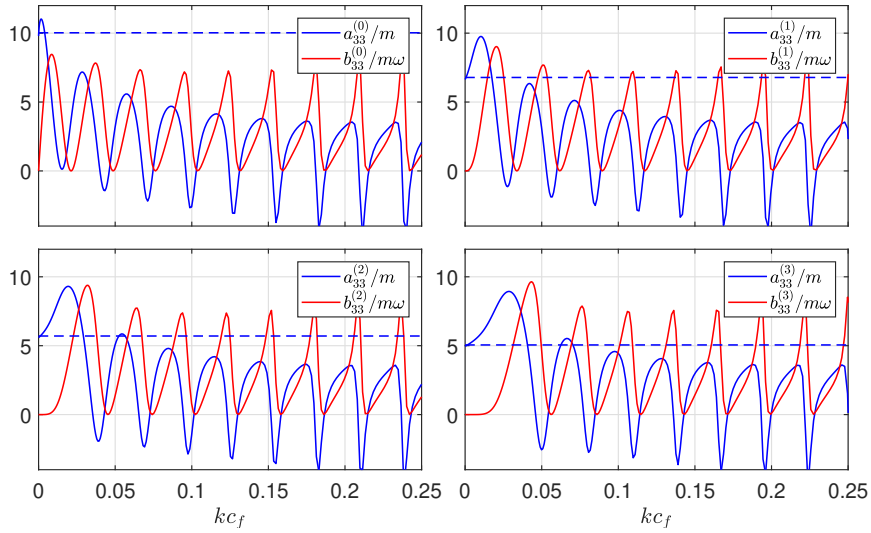

Figure 4.5: Sectional non-dimensional vertical added mass $a_{33}^{(n)}/m$ and damping $b_{33}^{(n)}/m\omega$ coefficients of a floating collar with two tubes for the modes number $n = 0, 1, 2, 3$ versus non-dimensional wave number kc_f. m is cross-sectional displaced water mass (two tubes). Solid line: by WAMIT. Horizontal dashed line: zero frequency analytical added mass coefficients from Faltinsen (2011).

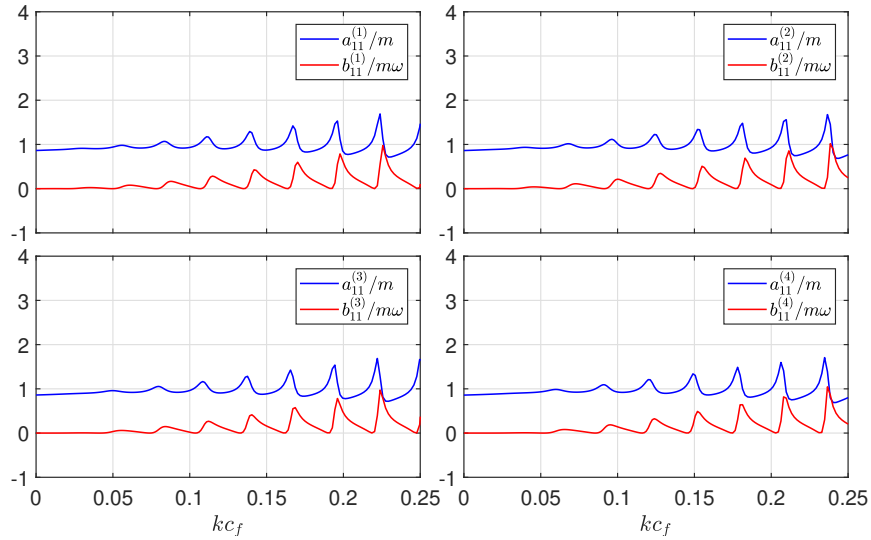

Figure 4.6: Sectional non-dimensional horizontal added mass $a_{11}^{(n)}/m$ and damping $b_{11}^{(n)}/m\omega$ coefficients of a floating collar with two tubes for the modes number $n = 1, 2, 3, 4$ by means of WAMIT versus the non-dimensional wave number kc_f.

Retardation functions

For cases in irregular waves or anyway when transient effects occur, they are considered by including the convolution integrals with retardation functions, see Eq. (2.10). The formula to calculate the retardation function for a vertical mode is shown Eq. (2.11). The retardation functions for some representative vertical and horizontal modes are shown in Figure 4.7 and Figure 4.8, respectively. Their accuracy is verified by observing that the added mass and damping coefficients calculated from the retardation functions agree well with those found directly from WAMIT (not shown here). From the figures, the retardation functions for both the rigid and elastic modes in vertical and horizontal directions become negligible for times larger than about $250\sqrt{R/g}$. We can also see that the retardation functions for vertical modes decay faster than those for horizontal modes. The behavior of the retardation functions for the floating collar is different from that for traditional ocean structures. It is probably connected with the ring shape of the body and very complex frequency-dependent added mass and damping coefficients with several peaks and troughs, and to occurrence of negative added mass (Li et al., 2014).

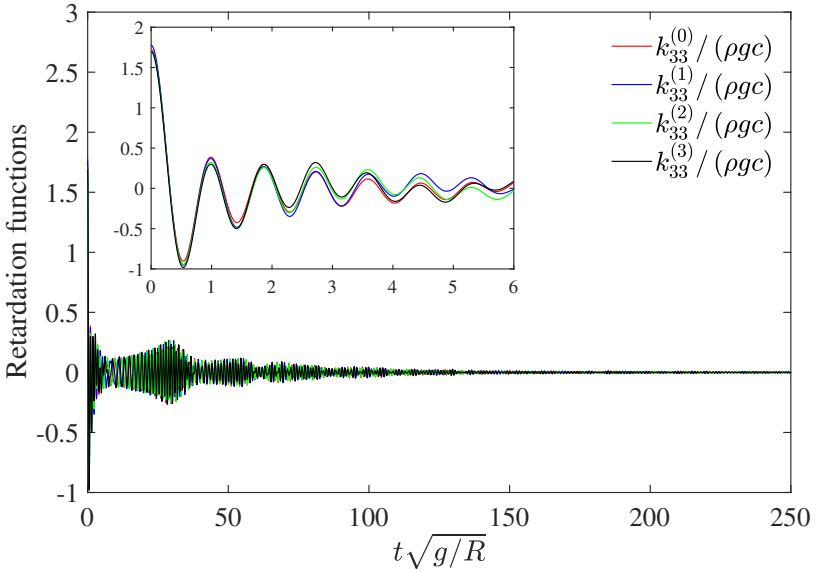

Figure 4.7: Sectional non-dimensional vertical retardation functions $k_{(33)}^{(n)}/\rho g c$ for the modes number $n = 0, 1, 2, 3$ as a function of time. The zoomed view shows the detail of the behavior at small times interval.

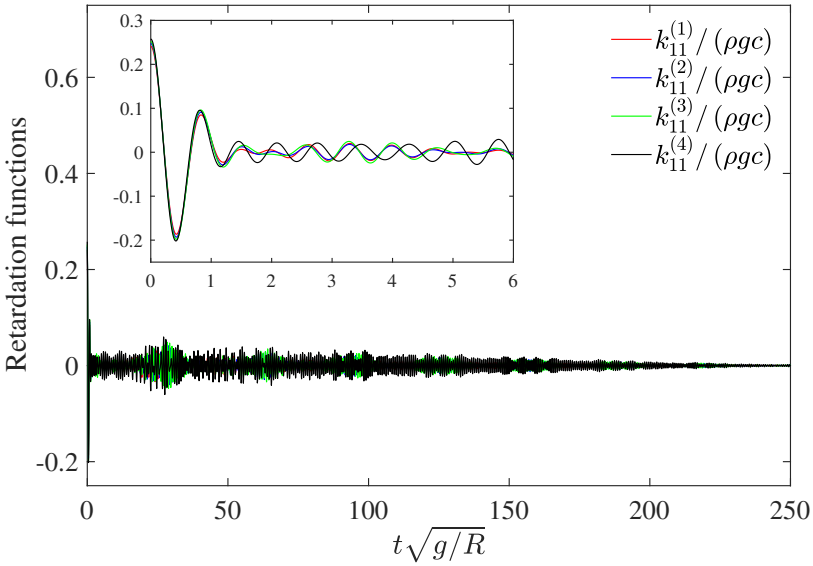

Figure 4.8: Sectional non-dimensional horizontal retardation functions $k_{11}^{(n)}/\rho gc$ for the modes number $n = 1, 2, 3, 4$ as a function of time. The zoomed view shows the detail of the behavior at small times interval.

Drag coefficient for the floating collar

As explained in Section 2.2.3, the drag term in Morison's equation is adopted to model the drag force on the floating collar in the horizontal plane. The drag coefficient depends on several parameters, for instance the Reynolds number, the distance between the two tubes, the Keulegan-Carpenter number (KC) and the ratio between the wave particle amplitude and current velocities in the case of combined waves and current. In the present work, constant drag coefficients for the two cylinders are assumed with $C_{D,1}^f = 0.9$ and $C_{D,2}^f = 0.0$, according to Zdravkovich (1985) for two cylinders in current with relative distance $p/d_f = 2$ (used in the model tests), and neglecting the influence of Reynolds number.

4.3 Results with numerical sensitivity analysis

In this section, we present results from the numerical simulations and the experiments for the realistic fish farm system introduced in section 4.1. The main focus is on the mooring loads in the front two anchor lines and bridle lines. Nominal results from cases in current only are presented in section 4.3.1. "Nominal" denotes that basis values of different parameters are used in the simulations. A detailed sensitivity analysis is also presented. Nominal results from cases in waves only and combined waves and current are presented and discussed in section 4.3.2, together with a sensitivity analysis. Numerical and experimental results for the system in irregular waves are shown in section 4.3.3. Finally systematic simulations of fish

farms with different set-ups in different exposure scenarios are performed in section 4.3.4 to identify the operational limits of the conventional fish-farm system.

4.3.1 Current only

In this section, we present the results of the mooring loads in the front two anchor lines for cases in current only. We will focus on the average value of the loads in the front two anchor lines (hereafter indicated as anchor load). Numerical results are compared with the experimental data. Nominal results with a convergence study are shown at first, then a detailed sensitivity analysis is presented, identifying the dominant parameters influencing the anchor loads.

Nominal results

A convergence study for cases in current only was performed at first and three different meshes were tested. Steady shapes of the net with different mesh resolutions are presented in Figure 4.9. Numerical results indicate that the anchor load is not sensitive to the mesh and a relative coarse mesh is enough to reach convergence. The mesh $N_H \times N_V = 20 \times (8{+}6)$ is adopted as the nominal mesh and to be used in the sensitivity analysis.

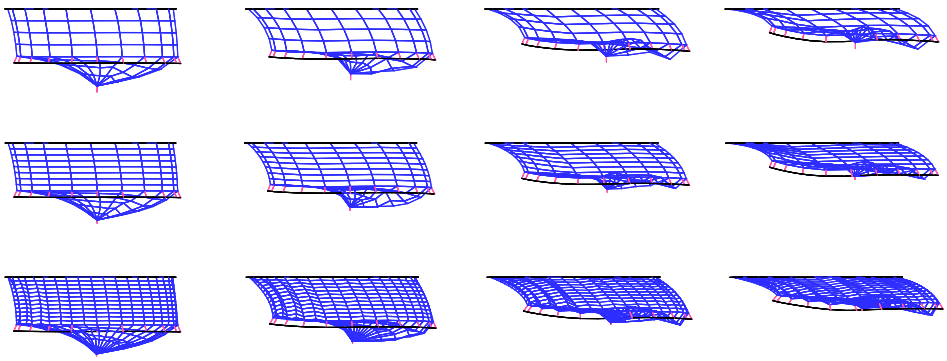

Figure 4.9: Steady-state shapes of a realistic fish farm system (mooring system not shown): convergence study. The weight of the sinker tube is 50 kg/m. From top to bottom: $N_H \times N_V = 20 \times (4{+}4)$, $20 \times (8{+}6)$ and $40 \times (12{+}6)$. N_H and N_V denote the number of trusses in the horizontal and vertical directions. N_V comprises two parts: meshes for cylindrical and conical part. From left to right: $U_\infty = 0.2$, 0.4, 0.6, and 0.8 m/s.

A comparison of the anchor line loads between numerical and experimental results is given in Figure 4.10. Unluckily only two cases were studied in the model tests, with two different current speed and two different sinker tube weights. More current scenarios have been simulated numerically. From the figure we can have the following conclusions: (1) increasing the weight of the sinker tube does not have significant influence on the anchor load for low current velocities, but has

more effect for higher current velocities. The main reason is that the projected area of the net cage in the current direction is important for the anchor load and it is influenced by sinker tube weight and current velocity U_∞; (2) numerical results slightly over-predict the anchor loads, compared to the experimental data, by about 15% and 7.2 % for the case with current velocity $U_\infty = 0.5$ m/s, sinker tube weight $w_s = 50$ kg/m and with $U_\infty = 0.7$ m/s, $w_s = 25$ kg/m, respectively. One of the possible reasons for the over-estimation is that the inflow modifications around the net cage due to the presence of the net cage are not considered. In fact, it is assumed that all the water goes through the net cage in nominal simulations.

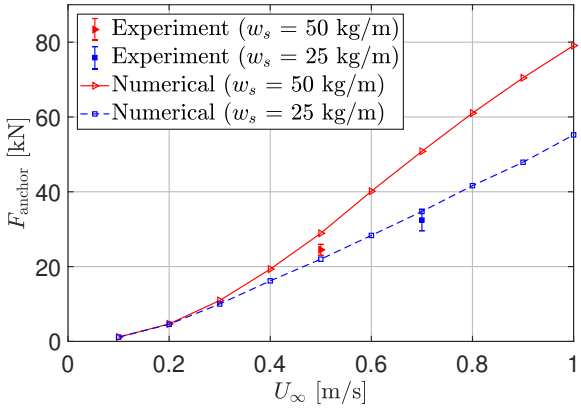

Figure 4.10: Average value of the loads in the front two anchor lines. Pre-tension is subtracted. Filled symbols with error bar: experimental results. In particular, the red triangular symbol represents the case 5010 with current velocity 0.5 m/s and sinker tube weight 50 kg/m while the blue square symbol corresponds to the case 5020 with current velocity 0.7 m/s and sinker tube weight 25 kg/m. Solid line and dashed line: present simulations with sinker tube weight equals 50 kg/m and 25 kg/m, respectively.

Numerical sensitivity analysis

Due to uncertainties in the experiments and lack in the information required to complete the mathematical modeling, we performed a sensitivity analysis. The different parameters examined are shown in Tables 4.4 and 4.5. The parameters are given separately for different components. Some of them are relevant only for cases with waves and are not investigated here. In order to quantify the significance of the different parameters and to try identifying the important ones, we present condensed results in Figure 4.11 and 4.12. Two sinker tube weights are investigated. In Figure 4.11, each bar represents the percentage difference of the anchor force with respect to the nominal value, averaged over all the examined current velocities. Here the anchor force means the average value of the tensions in the front two anchor lines. As seen from the figure, each parameter has different impact on the anchor force.

Table 4.4: Parameters varied in the sensitivity analysis of anchor force for cases in current only, waves only and combined waves and current. Quantities with subscript 0 means nominal values, as given in Table 4.1 and Table 4.2. $a_{33}^n(0)$ means zero frequency added mass coefficients for the floating collar. Nominal number of vertical and radial modes for both the floating collar and the sinker tube are $N_v = N_h = 8$. The flow modification around the net cage is not considered in nominal simulations. Nominal weight of the net in water is zero. Mean pre-tension denotes that the average value of the pre-tensions in the front two anchor lines is adopted. Parameters that impose more than 5% difference from nominal value are marked by "$\times$" in the right three columns. Parameters not investigated are marked by "-".

	No.		Explanation	>5%		
				Current	Wave	Waves and current
Floating collar	1	Nonlinear FK + rest	Froude Kriloff force	-		
	2	$a_{33}^n(0)$	Added mass	-		
	3	$T_{ax} = 0$	Axial stiffness	-		
	4	$C_{D,1}^f$=0, $C_{D,2}^f$=0	Drag force			$\times$
	5	N_h=1, N_v=2	Rigid body motions			
Sinker tube	6	C_D^s=0	Drag force			
	7	$w_s = 0.9w_{s,0}$	Weight in water			
	8	$w_s = 1.1w_{s,0}$	Weight in water			
	9	N_h=1, N_v=2	Rigid body motions		$\times$	
Net	10	r= 0	Flow reduction factor	$\times$	-	$\times$
	11	Flow modification	Flow around net cage	$\times$	-	-
	12	m_{net}= $1.1m_{\text{net},0}$	Mass of net	$\times$		
	13	L_u= $0.9L_{u,0}$	Net depth (cylindrical)	$\times$		
	14	L_u= $1.1L_{u,0}$	Net depth (cylindrical)	$\times$		
	15	D_C= $0.9D_{C,0}$	Diameter (conical part)	$\times$		
	16	D_C= $1.1D_{C,0}$	Diameter (conical part)	$\times$		$\times$
	17	E_{net}=6.25×10^7N/m^2	E-modulus of net twines			
	18	E_{net}=5×10^{10}N/m^2	E-modulus of net twines			

Table 4.5: Continuation of Table 4.4.

	No.		Explanation	>5%		
				Current	Wave	Waves and current
	19	$Sn=0.9Sn_0$	Solidity ratio of net cage	×		×
	20	$Sn=1.1Sn_0$	Solidity ratio of net cage	×		×
	21	$W_c=0.9W_{c,0}$	Center point weight			
	22	$W_c=1.1W_{c,0}$	Center point weight			
Moorings	23	Mean pre-tension	Pre-tension moorings			
	24	$k_s = 0.9k_{s,0}$	Spring stiffness moorings			
	25	$k_s = 1.1k_{s,0}$	Spring stiffness moorings			
	26	$m_{\text{chain}} = 0.9m_{\text{chain},0}$	Anchor chain mass			
	27	$m_{\text{chain}} = 1.1m_{\text{chain},0}$	Anchor chain mass			
	28	$C_D^B=0$	Buoy drag coefficient			
	29	$D_B=0.9D_{B,0}$	Buoy diameter	-	×	
	30	$D_B=1.1D_{B,0}$	Buoy diameter	-	×	

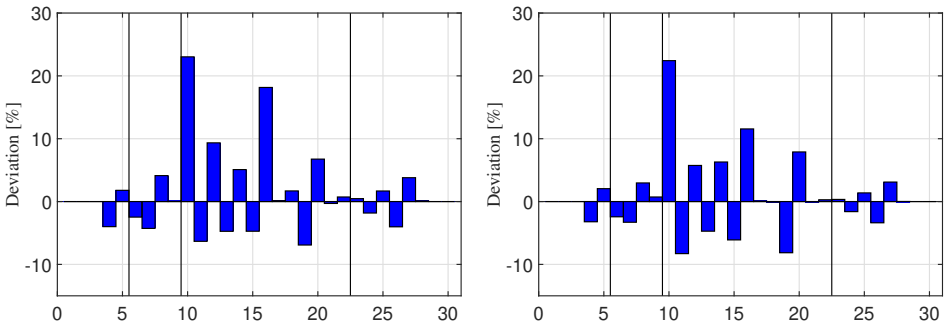

Figure 4.11: Each bar represents the percentage difference of the anchor force with respect to the nominal value, averaged over all the examined current velocities. The numbers on the horizontal axis refer to variation numbers as given in Tables 4.4 and 4.5. Left: sinker tube with weight 25 kg/m. Right: sinker tube with weight 50 kg/m.

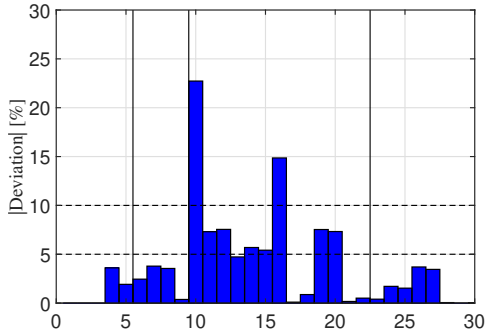

Figure 4.12: The mean of the absolute value of the condensed data presented in Figure 4.11.

Parameters with more than 5% difference with respect to nominal values are marked by "×" in the third last column in in Tables 4.4 and 4.5 for cases in current only, waves only and combined waves and current. In this section, we will just discuss results for current only cases. The others are explained in section 4.3.2. Parameters not considered are marked by "-". One general observation is that the anchor force is more sensitive to the modeling of the net cage than to other components. More detailed discussions are presented in the following.

Floating collar and sinker tube: When the drag forces on the two floating tubes are neglected, namely the drag coefficients for the two tubes are set as $C^f_{D,1}$=0, $C^f_{D,2} = 0$, the anchor force has a 4% reduction which means that the drag on the floating collar is quite moderate compared with the total drag on the system. So it is not necessary to model the drag force on the floating collar in a very accurate and time-consuming way. Modeling the floating collar as a rigid body has a small

effect on the anchor force. Similar conclusions are obtained for the sinker tube.

Net cage: The flow reduction factor r in the rear part of the net cage due to the shadowing effect is the most important parameter for the anchor force and the anchor force will increase up to 22% if the shading effect is neglected.

The inflow modifications due to the presence of the net cage are not considered in the nominal simulations and could be one of the possible reasons why the numerical results tend to overestimate the experimental drag forces on the cage. Applying the Lagally's theorem to model the flow around the net cage will reduce the anchor load by about 7.3%, consequently it will improve the numerical results.

The weight of the net in water is assumed to be zero in nominal simulations, so the weight of the net equals the buoyancy of the net. Archimedes' principle is directly applied to estimate the net buoyancy which maybe problematic since the net is not completely surrounded by water. The weight of the net in water is slightly larger than zero in reality. Increasing the net weight by 10% in the sensitivity analysis changes the anchor load by about 7%.

Detailed variation of the structural modeling of the net is also considered. Changing the net depth (cylindrical part) and the net solidity ratio by 10% lead to a similar deviation from the nominal value between about 5% and 7%. Increasing the net diameter (conical part) by 10% will lead to larger deviation, about 15%. This is due to a big increase of the net volume, leading to larger drag force on the net. The effect of the net elasticity is also investigated. Ordinary ropes were used in the model test for the net cage, however when scaled up using Froude-scaling, the elasticity gives higher stiffness than for nets used in commercial full-scale cages. A model scale Young's modulus of $E_{\text{net}} = 6.25 \times 10^7 \text{N/m}^2$ would conform more to a realistic full-scale value, but could be difficult to realize in a model test set-up. So two different net elasticities are tried in the sensitivity analysis with $E_{\text{net}} = 6.25 \times 10^7 \text{N/m}^2$ and $E_{\text{net}} = 5 \times 10^{10} \text{N/m}^2$, which correspond to a realistic full-scale value and to an almost rigid net. Numerical results show that the net elasticity has a small effect on the anchor force as long as it is in a reasonable region. The point weight that attached to the bottom of the net is also varied and very small deviation is observed.

Mooring system: The pre-tensions in the front two anchor lines are asymmetric with respect to x_E-axis in the model tests, as explained in section 4.1. Asymmetric pre-tensions are used in nominal simulations and negligible difference is observed if the average value of the pre-tensions is applied to the two anchor lines. The anchor load does not seem to be sensitive also to the stiffness of the springs in the anchor lines, to the weight of the anchor chain and to the drag forces on the buoys.

4.3.2 Combined waves and current

In this section, we present the numerical results of the mooring loads in the front two anchor lines and front two bridle lines when the system is exposed to combined waves and current. Experimental data are used to validate the numerical results. Similar as in current cases, nominal numerical results are shown at first, then a detailed sensitivity analysis is conducted, identifying the dominant parameters influencing the mooring loads.

Nominal results

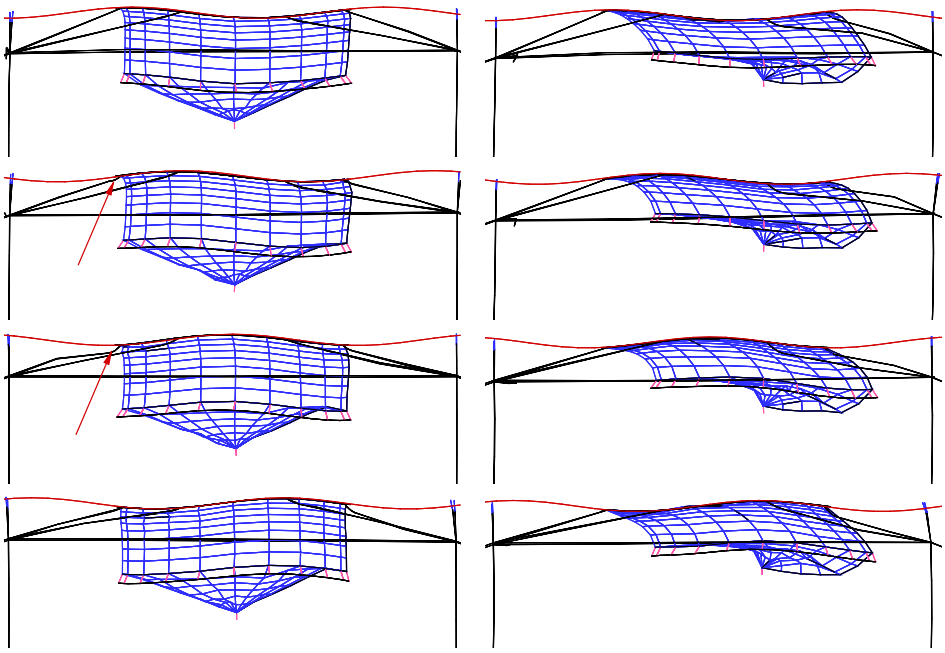

Figure 4.13: Left column: snapshots for different time-steps from numerical simulations with $N_H \times N_V = 24 \times (8+6)$ (wave only). Wave period $T = 6$ s and wave height $H = 2.5$ m. Right column: snapshots for different time-steps from numerical simulations (combined wave and current). Current velocity $U_\infty = 0.5$ m/s, wave period $T = 6$ s and wave height $H = 2.5$ m.

A convergence study has been performed and the mesh $N_H \times N_V = 20 \times (8{+}6)$ is found to be sufficient to reach convergence and is used in nominal simulations. Snapshots showing the floating collar, net cage, sinker tube and mooring lines are given in Figure 4.13 for cases in wave only and in combined wave and current. The linear incident wave profile is included. Since the considered waves are relatively long (wave length-to-floating collar diameter ratio λ/D=1.12), the floating tubes basically follow the waves. Taking a close look at the middle two snapshots in the left, we can see that the front two bridle lines get slack. This means that the bridle

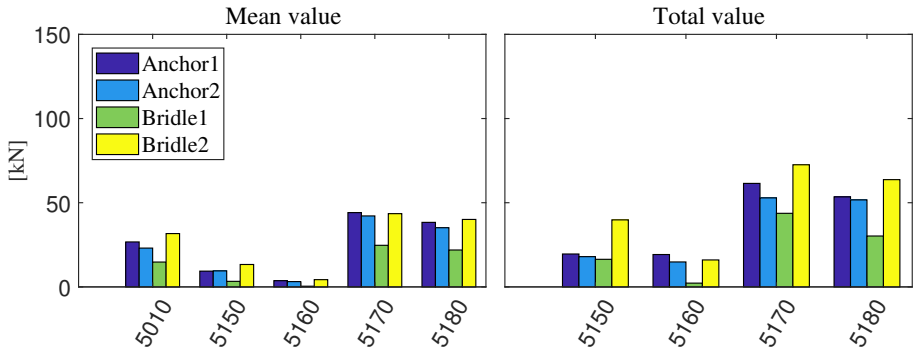

Figure 4.14: Mean and total values of the mooring loads in the front two anchor lines and bridle lines, obtained from experiments. The pre-tension is subtracted. The positions of the anchor lines and bridle lines are illustrated in Figure 4.1. Detailed test information of different test numbers is shown in Table 4.3. Test 5010: current only. Test 5150 and 5160: waves only. Test 5170 and 5180: combined waves and current.

lines may experience snap loads. The latter consequence is not included in the analysis, but needs to be considered in future work in a similar way as done by Bardestani and Faltinsen (2013).

Before going to detailed analysis, we first show the mooring loads in the anchor lines and bridle lines from the model tests, see Figure 4.14. From the figure, we can have the following conclusions: the loads in the two anchor lines are similar if the pre-tensions are subtracted; load in the bridle line-2 is about twice that in the bridle line-1; the forces in the anchor lines and in the bridle line-2 are similar. In the following analysis, we will focus on the average value of the loads in the front two anchor loads (anchor load) and the load in the bridle line-2 (bridle load).

Nominal results for the anchor load and bridle load are presented in Figure 4.15 and 4.16 and are compared with the experimental data. Just the total values are investigated. Two wave steepnesses ($H/\lambda = 1/40$ and $1/22$) and two current velocities (U_∞=0.0 m/s and 0.5 m/s) are considered. In general, the agreement is fair for both the anchor load and the bridle load. Two different sinker tube weights with $W_s = 25$ kg/m and 50 kg/m are investigated and numerical results indicate that the sinker tube weight has a small influence on the mooring loads for wave only cases. For combined waves and current cases, the system with larger sinker tube weight experiences larger mooring loads due to smaller deformations of the net cage.

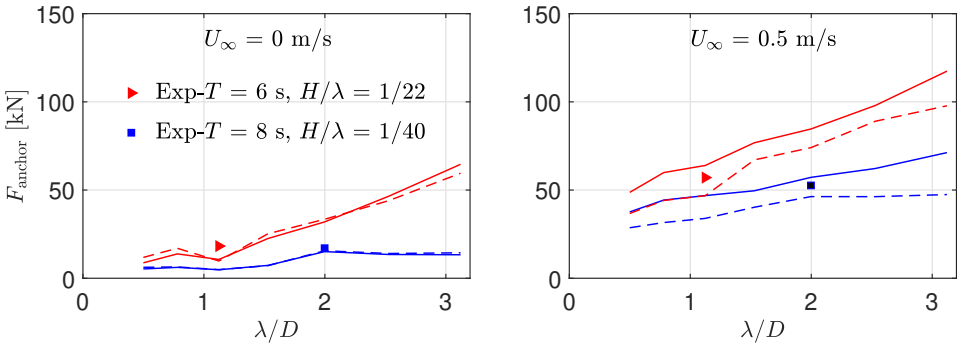

Figure 4.15: Comparison of the total anchor loads from the model tests (solid symbols) and present numerical simulations (solid curves) with sinker tube weight W_s = 50 kg/m. Pre-tension is subtracted. Results are presented versus wave length-to-diameter ratio λ/D. Here $D = (D_{f1} + D_{f2})/2$ is the mean value of the center line diameter of the two tubes of the floating collar. Two wave steepnesses are considered with H/λ = 1/22 and 1/40. Numerical results with sinker tube weight W_s=25 kg/m are also shown (dashed line). Left: wave only. Right: combined waves and current, with current velocity U_∞ = 0.5 m/s.

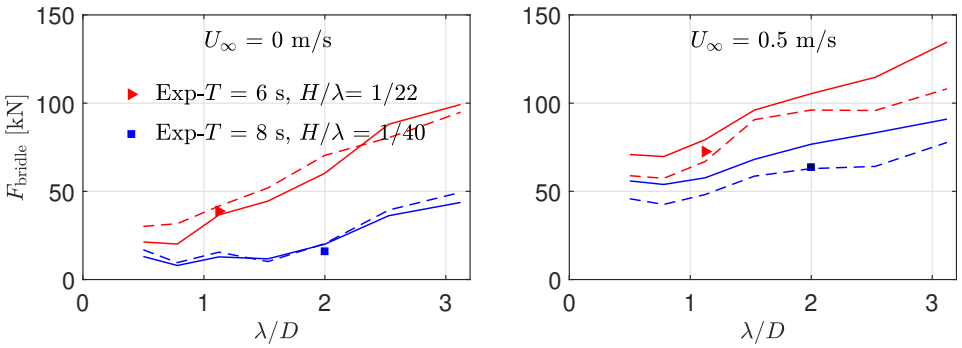

Figure 4.16: Same as in Figure 4.15, but for the bridle line-2.

Numerical sensitivity analysis

A sensitivity analysis is performed for the system in regular waves only and in combined regular waves and current. The focus is on the total values of the mooring loads. The parameters examined are shown in Tables 4.4 and 4.5. The majority of the parameters are the same as for cases in current only, but with some additional wave related parameters. The condensed results for the anchor load are presented in Figure 4.17 and 4.18.

In Figure 4.17, each bar represents the percentage difference of the anchor load with respect to the nominal value, averaged over all the examined wave periods. In Figure 4.18 each bar represents the mean of the absolute value of the condensed data presented in Figure 4.17. Parameters that impose more than 5% difference

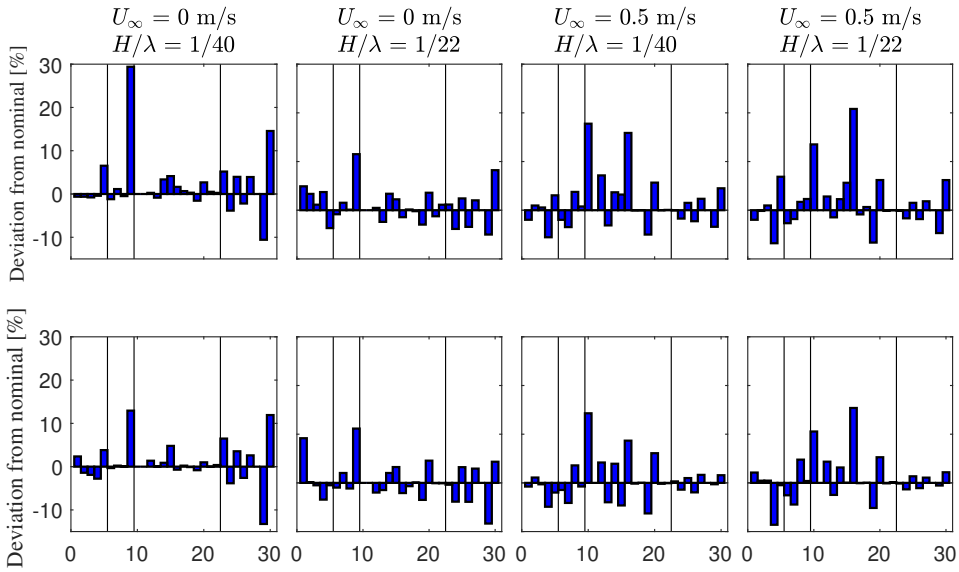

Figure 4.17: Each bar represents the percentage difference of the anchor load with respect to the nominal value, averaged over all the examined wave periods. The numbers on the horizontal axis refer to variation numbers as given in Tables 4.4 and 4.5. Upper row: sinker tube with weight 25 kg/m. Lower row: sinker tube with weight 50 kg/m.

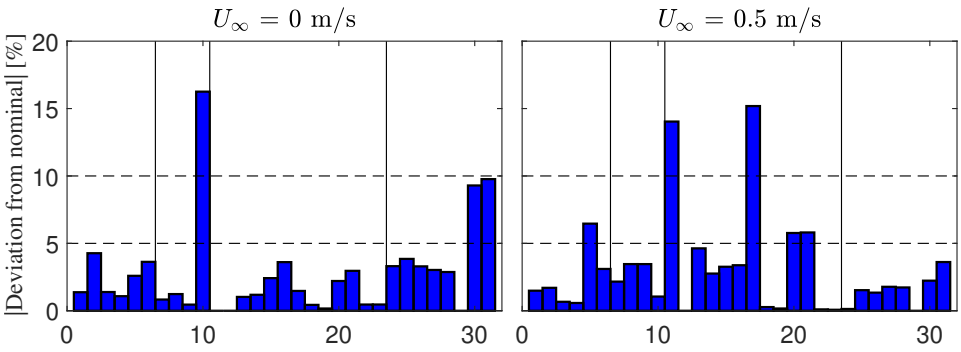

Figure 4.18: The mean of the absolute value of the condensed data presented in Figure 4.17.

with respect to nominal value for waves only cases and combined waves and current cases, are marked by "×" in the last two columns in Tables 4.4 and 4.5. From Figure 4.17, we can see that modeling the sinker tube as a rigid body has the most pronounced effect on the anchor load for cases in waves only. This is maybe because a rigid sinker tube will change the deformation of the net in vertical direction, as a rigid sinker tube cannot deform accordingly with the floating collar, which follows

the wave profile. In combined waves and current cases, the flow reduction factor r in the rear part of the net and the diameter of the net cage (conical part) are the two important parameters. In terms of the modeling of the floating collar, simplifications can be made with limited errors, such as modeling the floating collar as a rigid body, neglecting the axial stiffness due to axial tensions and using zero frequency instead of the frequency-dependent added mass. Also numerical results indicate that considering nonlinear Froude Kriloff and restoring forces for the floating collar is not necessary. In general, the loads on the floating collar are quite moderate compared with those on the whole system.

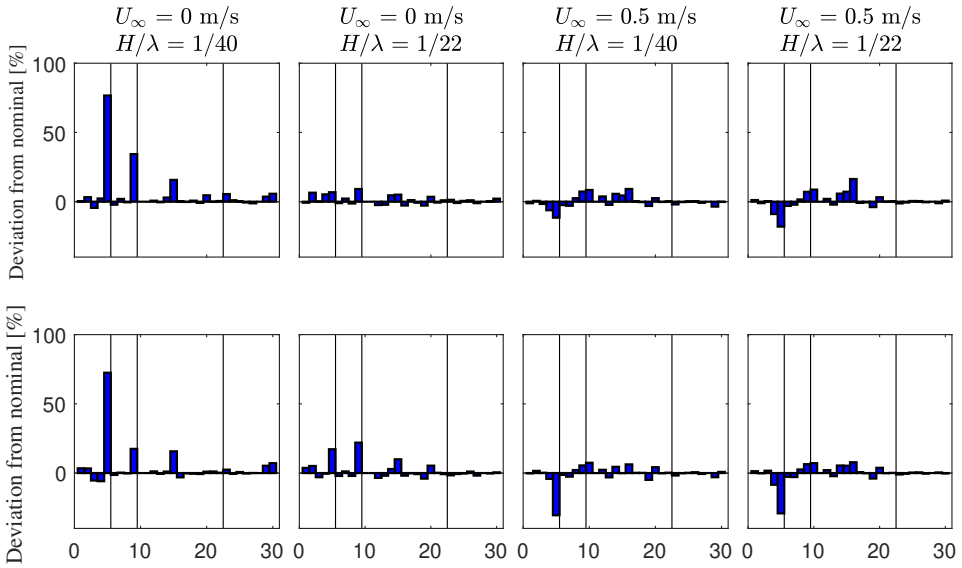

Figure 4.19: Same as in Figure 4.17, but for the bridle load.

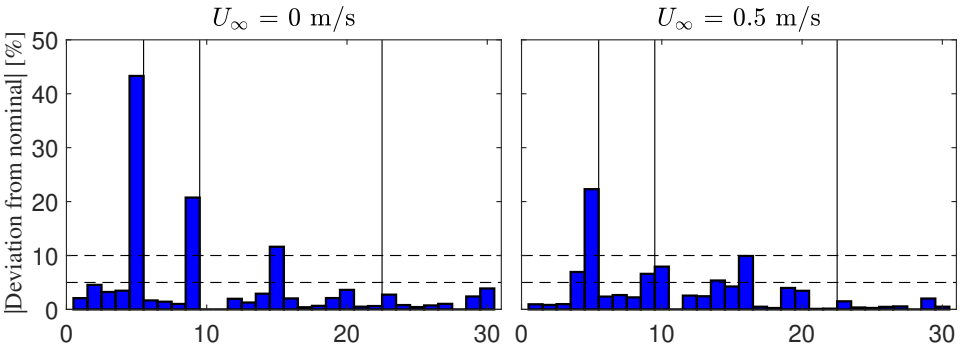

Figure 4.20: The mean of the absolute value of the condensed data presented in Figure 4.19.

Sensitivity analysis for the bridle load is also conducted and results are shown

in Figure 4.19 and 4.20. Figure 4.20 clearly shows that modeling the floating collar as a rigid body has a pronounced effect on the bridle load, this is because rigid floating collar significantly changes the force distribution along the bridle lines.

4.3.3 Irregular sea

In this section, the fish farm system in irregular waves is investigated. In Figure 4.21, we present the mean and maximum values of the mooring loads in the front two anchor lines and front two bridle lines from experiments. The pre-tensions are subtracted. The duration of the irregular waves in the model tests is 1.5 hour. The corresponding time histories of the mooring loads for the case with significant wave height H_s= 4 m and peak period T_p = 8 s are shown in Figure 4.22 for illustration purpose. From Figure 4.21, we can have the following conclusions: the mean values of the mooring loads for cases with different significant wave heights and peak wave periods are similar while there is a big difference in the maximum values; the tension in the bridle line-2 is about twice than that in the bridle line-1; the mean values of the tensions in the bridle line-2 and in the anchor lines are similar, but the maximum tension in the bridle line-2 is much larger. We will focus on the average value of the loads in the front two anchor lines (anchor load) and the load in the bridle line-2 (bridle load) in the following analysis.

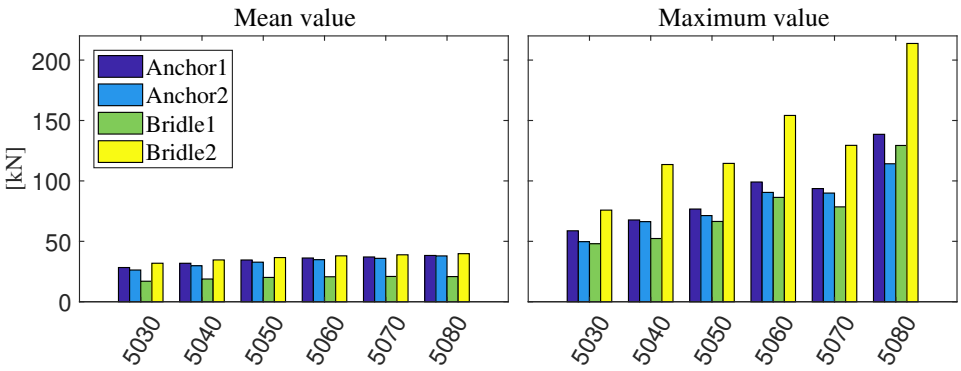

Figure 4.21: Mean and maximum values of the tensions in the front two anchor lines and front two bridle lines, obtained from the experiments for the system in irregular waves. The pre-tension is subtracted. The positions of the anchor lines and bridle lines are illustrated in Figure 4.1. Detailed test information of different test numbers is shown in Table 4.3. The significant wave height and peak wave period increase with increasing test numbers.

Figure 4.23 shows the comparison of the mean, standard deviation and maximum values of the anchor loads from the numerical simulations and the experiments. The same wave duration is considered in the simulations as that in the model tests. From the figure, we can see that general agreement between the numerical (nominal) and experimental results of the mean, standard deviation and maximum values of the anchor loads is fair and numerical results slightly over-

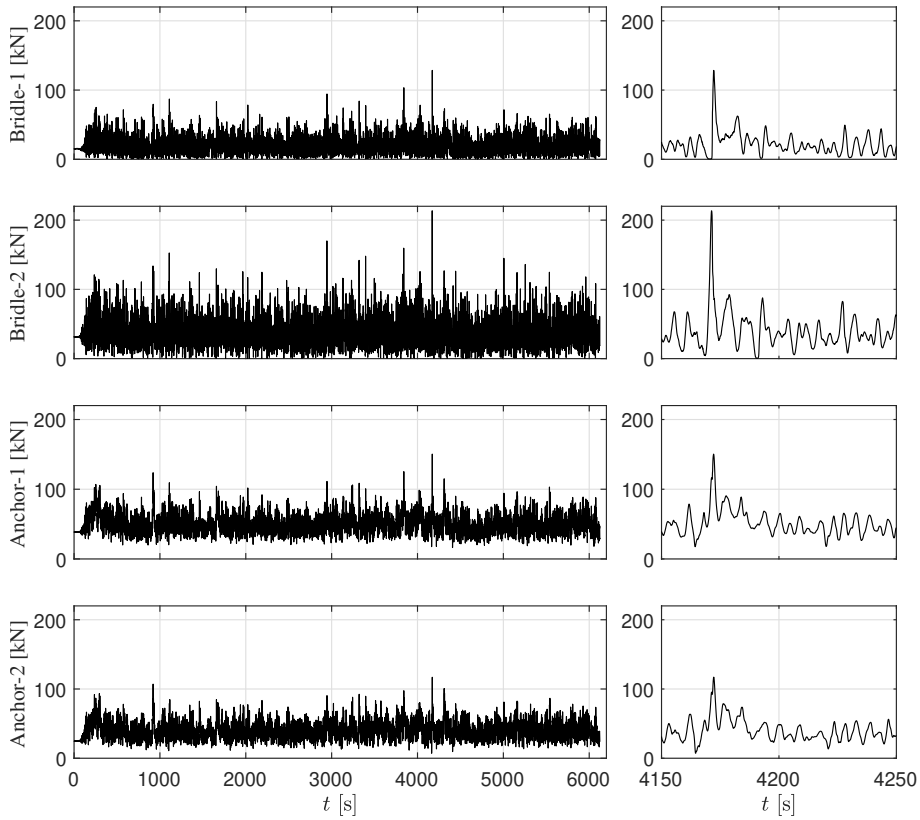

Figure 4.22: Time histories of the tensions in the front two bridle lines and front two anchor lines from the experiment with significant wave height H_s= 4 m and peak period T_p = 8 s. Zoomed views are also given in the right when the tensions reach the maximum values within the studied time histories.

predict the mean values which is similar as for the cases in current only. It should be noted that the random phase seeds used in the experiments to generate the incident irregular waves are different with respect to those used in the simulations.

In the nominal simulations, the hydrodynamic radiation loads for different modes (both rigid and elastic) of the floating collar are expressed in terms of convolution integrals with retardation functions according to linear potential-flow theory. Numerical results using zero frequency added mass for different modes and modeling the floating collar as a rigid body are also shown in Figure 4.23. The comparison indicates that the effect of the elasticity of the floating collar on the anchor load is rather moderate and simplified hydrodynamic model for the floating collar is enough to reach desired accuracy. One should note that the conclusion given here is different from that presented in Section 3.3.3 where a simplified fish-farm system with horizontal mooring lines was studied. There, the conclusion was that the elasticity of the floating collar matters for the mooring loads. The seemingly con-

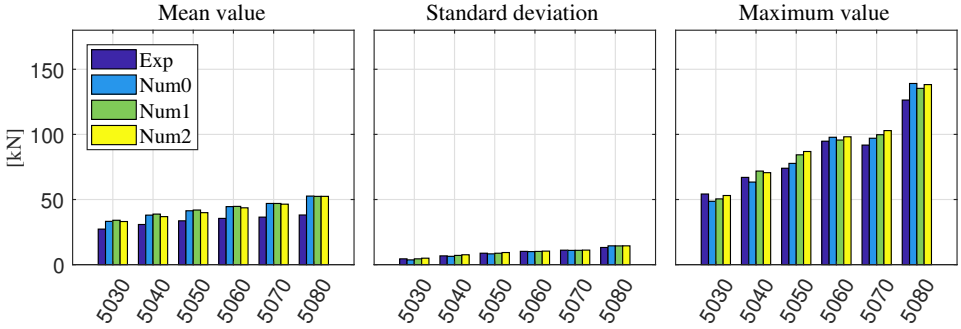

Figure 4.23: Comparison of mean, standard deviation and maximum values of the anchor loads from the model tests and present numerical simulations for the fish farm system in irregular waves. Detailed test information of different test numbers is shown in Table 4.3. Num0, Num1 and Num2 denote nominal results, results using zero frequency added mass for different modes of the floating collar and results considering a rigid floating collar, respectively.

tradictory conclusion is caused by the difference in the mooring-line arrangement. The simplified mooring system adopted in Section 3.3.3 is similar with the bridle lines in the complete mooring system studied here. Relevant sensitivity analysis for the loads in the bridle lines will be given later.

According to the experimental data, the ratio of the maximum anchor load (estimated as the real maximum value minus the mean value) to the standard deviation varies from 4.6 to 6.7 according to the experimental data. The drag load on the net cage has the dominant contribution to the total load, which is expected to be similar with the case when Morison's equation is used to estimate the wave load. So we can have a rough estimation of the probability distribution of the maximum anchor load based on the statistics characteristics of the Morison-type forces for random seas. It is assumed that the wave elevation process is a stationary Gaussian process. Then according to Naess and Moan (2012), in the absence of current, the distribution of the maximum value for Morison-type force depends on the relative importance of the drag and inertial forces. If the inertial force is dominant, then Rayleigh distribution can be used to describe the distribution of the maximum values. Then the most probable largest value (estimated as the real maximum value minus the mean value) can be approximately estimated by four times the standard deviation for a short time description of the wave elevation in the range from 1/2 hour to 10 hour. The actual ratio, i.e. the ratio between the most probable largest value and the standard deviation, depends on the duration of the sea state and the mean wave period. If the drag force is dominant, then exponential distribution can be adopted and higher most probable largest values are expected.

For the fish farm system, the distribution of the maximum values of the anchor load should be a combination of Rayleigh distribution and exponential distribution and the most probable largest value should be larger than four times the standard

deviation, which means that the experimental results are reasonable.

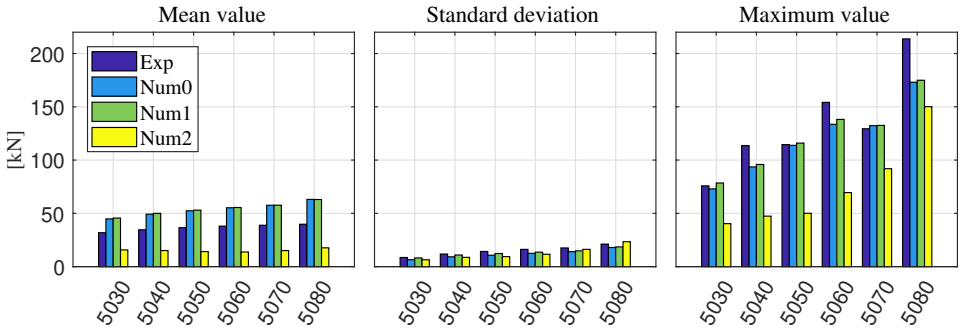

Figure 4.24: Same as in Figure 4.23, but for the bridle line-2.

In Figure 4.24, we present the loads in the bridle line-2 from the numerical simulations and the experiments. Both the nominal numerical results and results using zero frequency added mass for different modes and modeling the floating collar as a rigid body are shown. The figure shows that modeling the floating collar as a rigid body has a significant influence on the bridle load, as it will change the force distribution between bridles.

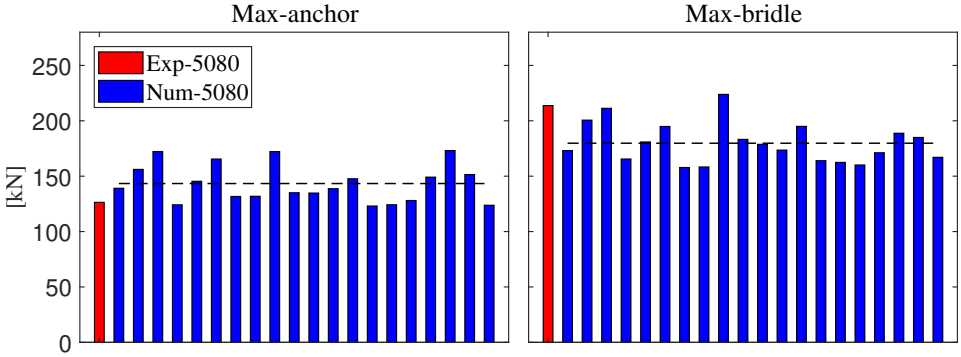

Figure 4.25: Comparison of the mooring loads (maximum value) obtained from the experiments and the numerical simulations for case 5080. The first bar represents the experimental data, the rest are numerical results but with different random phase seeds to generate the incident irregular waves. Dashed line represents the most probable maximum value obtained as mean among the maximum values from numerical simulations. Left: anchor load. Right: bridle load.

Numerical simulations with different random phase seeds (in total 20) to generate the incident irregular waves are performed and the comparison of the maximum values of the mooring loads for the numerical and experimental results for case 5080 is given in Figure 4.25. The figure shows that there is a big variation of the maximum loads in the anchor line and in the bridle line when different random phase

seeds are used in the numerical simulations. The maximum anchor loads from numerical predictions vary from 98% to 136% of that from the experiment and the maximum bridle loads change from 74% to 105% of the experimental data.

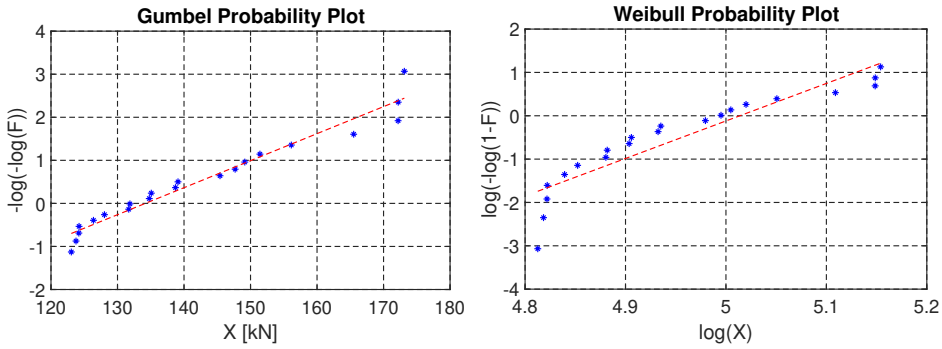

Figure 4.26: Probability distribution for the maximum anchor load with the values described in Figure 4.25. X denotes the maximum load from different realizations and F denotes the cumulative distribution function.

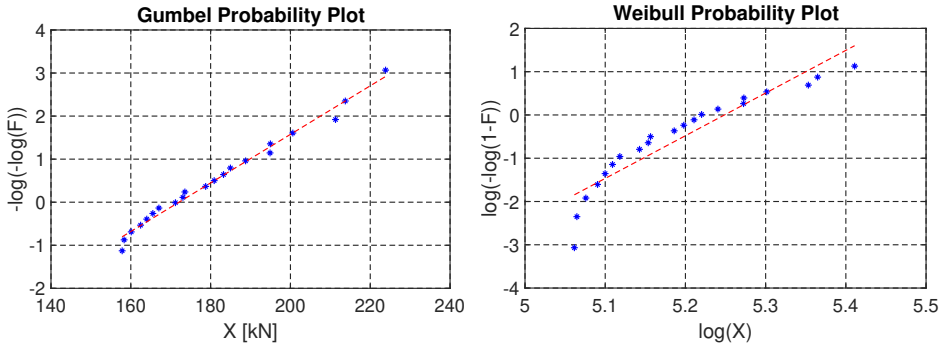

Figure 4.27: Probability distribution for the maximum bridle load with the values described in Figure 4.25. X denotes the maximum load from different realizations and F denotes the cumulative distribution function.

The Gumbel and Weibull probability distribution functions are commonly used to fit the distribution of the maximum values from different independent realizations. Curve fitting the results, as in Figure 4.26 and Figure 4.27, we can see that that the Gumbel distribution is more proper to fit the maximum loads in the mooring lines, especially for the bridle line. We are specifically interested in the Most Probable Maximum Extreme (MPME) value for a given time duration. If the probability distribution for the maximum values is known, then the MPME can be obtained where the probability distribution function reaches the maximum. Alternatively, as an engineering practice, the MPME is taken as the average value of the maximum values from at least 10-20 realizations of the same wave spectrum.

Our results show that MPME estimated by the two methods are similar, with a difference in the range of 4-8%.

In order to have a better comparison of the most probable maximum value between numerical and experimental results, more realizations of the same spectrum in the experiments are needed.

4.3.4 Survival conditions

The aquaculture industry is trying to move the fish farms from nearshore to more exposed sea regions. However, a question remains to be answered: is it feasible to use the conventional fish farm concept to operate in exposed area and how exposed it can operate. In this section, the proposed numerical method is used to examine the responses of a conventional floating collar fish farm system in different exposure scenarios and in this respect to determine the survival conditions of the system.

First, we should choose proper criteria to determine the survival conditions. From the structural perspective, the major components should be strong enough to withstand the environmental loads in exposed regions. For the mooring system, the maximum load in the mooring line should not yield its breaking limit. In terms of the floating collar, it basically follows the waves and may experience large deformations in severe sea states, so we should guarantee that it will not collapse. Since the sinker tube is attached directly to the net in the present study, we can avoid the possible chafing between the vertical chains and the net (dominant cause for fish escape). Also, the force acting on the sinker tube is quite moderate, so both the net cage and the sinker tube should not be of a major concern. In addition, enough net cage volume is required for the welfare of the fish. In summary, from

Table 4.6: Environmental matrix used in the simulations, showing current velocity, regular wave steepness and wave period ranges. The different combinations of the sinker tube weight (or discrete sinker weights) and point weight (attached to the bottom of the net cage) are also shown in the lower table. If discrete sinker weights instead of the sinker tube are adopted, the discrete sinker weights are chosen to have the same total submerged weight as that of the sinker tube.

Current U_∞ [m/s]	Wave steepness H/λ		
	1/60	1/30	1/15
0.0	4-10s	4-10s	4-10s
0.3	4-10s	4-10s	4-10s
0.5	4-10s	4-10s	4-10s
0.7	4-10s	4-10s	4-10s
0.1-1.2	-	-	-

Sinker tube weight (w_s)	25 kg/m	50 kg/m	80 kg/m	93 kg/m
Discrete sinker weights (W_s)	203 kg	407 kg	651 kg	757 kg
Center point weight (W_c)	200 kg	500 kg	1000 kg	1500 kg

the perspective of fish welfare and structural integrity, three criteria are proposed to determine the survival conditions, i.e. maximum forces in the mooring lines; maximum stress in the floating collar and maximum reduction of net cage volume.

The simulation matrix is shown in Table 4.6. The different fish farm set-ups considered are also shown in the table. Detailed information of the wave conditions and the corresponding wave classes according to the Norwegian Standard are given in Table 4.7.

Table 4.7: Detailed information of the wave conditions described in Table 4.6. The corresponding wave class according to the Norwegian Standard (see Table 1.2) for regular waves is given in the lower table.

T [s]	λ [m]	λ/D [m]	$H/\lambda = 1/60$	1/30	1/15
			H[m]		
4	25.0	0.50	0.42	0.83	1.66
5	39.0	0.78	0.65	1.30	2.60
6	56.2	1.12	0.94	1.87	3.75
7	76.5	1.53	1.27	2.55	5.10
8	99.9	2.00	1.66	3.33	6.66
9	126.4	2.53	2.10	4.21	8.43
10	156.0	3.12	2.60	5.20	10.40

Wave	Exposure	$H = 1.9H_s$
A	Small	H <1.0 m
B	Moderate	1.0 m< H <1.9 m
C	Heavy	1.9 m< H <3.8 m
D	High	3.8 m< H <5.7 m
E	Extreme	5.7 m< H

Current only

First, we present results for cases in current only. The current velocity is chosen from small exposure to high exposure. The anchor loads and the net cage volume reductions in different current velocities are shown in Figure 4.28.

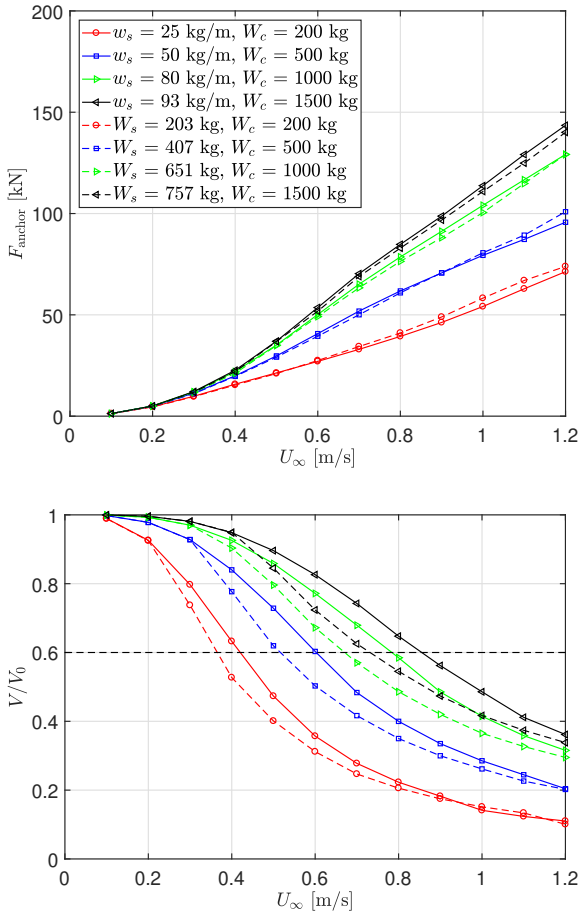

Figure 4.28: Numerical predictions of the mean load in the front two anchor lines (upper) and the net volume reductions (lower) for cases in current only with different fish farm set-ups, see Table 4.6. Solid line: sinker tube (w_s). Dashed line: discrete sinker weights (W_s). Lower: V_0 is the initial volume of the net cage, V the net volume in steady-state. Horizontal dashed line represents the fish-farm operational limit in terms of volume reduction.

The net cage volume is estimated by

$$V = -\iint_{S_c} n_1 x dS = -\iint_{S_c} n_2 y dS = -\iint_{S_c} n_3 z dS \tag{4.12}$$

where V is the net cage volume, $\mathbf{n} = (n_1, n_2, n_3)$ the normal vector of the cage surface S_c and is pointing outwards. The net volume is taken as the average value of the volumes estimated numerically with the three formulas in Eq. (4.12). From the figure we can see that the difference is small in the anchor loads when we use

the sinker tube or the discrete sinker weights to reduce the net-cage deformation. However, relatively big difference in the net cage volume reduction is observed between the two options, especially for medium current velocities. The numerical results demonstrate that the sinker tube is more suitable to be used to reduce the net-cage deformation. The maximum cage volume reduction is set to be 60% as a operational limit for the sake of fish welfare. The figure shows that the fish farm with sinker tube weight $w_s = 93$ kg/m and center point weight $W_c = 1500$ kg can operate in current velocity up to 0.85 m/s, which is in the region of high exposure.

Combined waves and current

The numerical results for the anchor forces for cases in combined waves and current are given in Figure 4.29. Just the total values are shown. Four current velocities and three wave steepnesses are considered, covering the range of wave class from small exposure to extreme exposure.

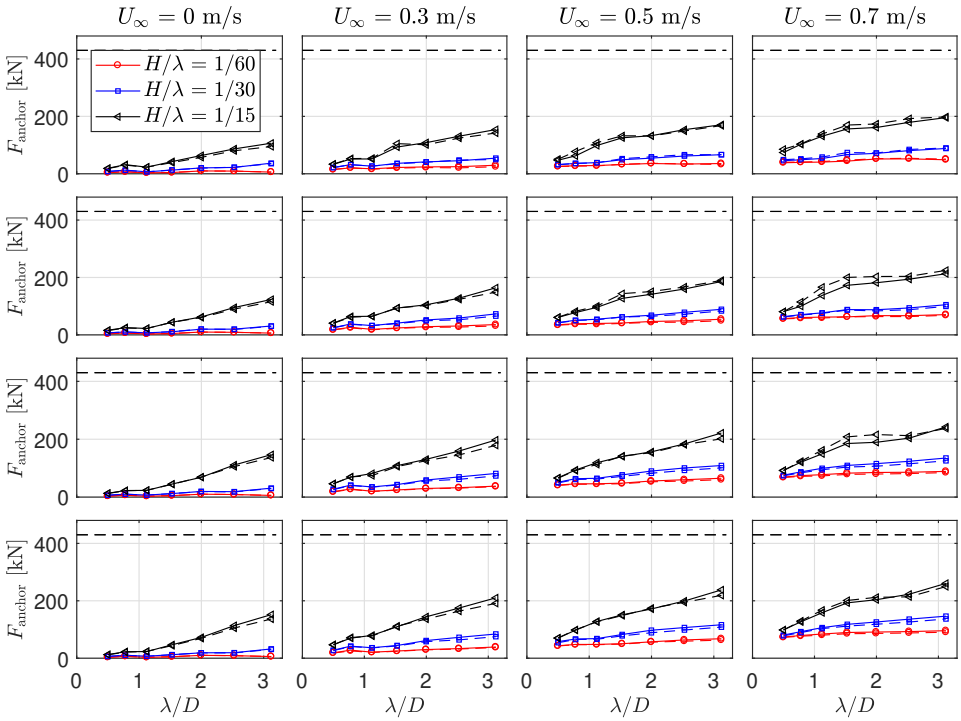

Figure 4.29: Mean load in the front two anchor lines for cases in combined regular waves and current with different fish farm set-ups. Results are presented versus wave length-to-diameter ratio λ/D. Solid line with symbols: sinker tube. Dashed line with symbols: discrete sinker weights. From left to right: current velocities $U_\infty = 0$ m/s, 0.3 m/s, 0.5 m/s, 0.7 m/s. From top to bottom: sinker tube weights $w_s = 25$ kg/m, 50 kg/m, 80 kg/m and 93 kg/m. Horizontal dashed line represents the minimum breaking force (polysteel, 3 strand, diameter 52 mm).

The figure shows that the difference of the anchor force is small when the sinker tube and the discrete sinker weights are used, respectively, similarly as in the cases in current only. The minimum breaking force for the considered anchor polysteel ropes is about 430 kN, which is larger than the maximum force experienced by the anchor lines, so the anchor loads are not the main concern for the fish farm system to operate in exposed regions.

Figure 4.30 shows the numerical predictions of the loads in the bridle line-2. In general, the load in the bridle line-2 is slightly larger than that in the anchor lines. However the bridle lines are weaker than the anchor lines in reality. Therefore, special attention should be paid to this during the design. The maximum force in the bridle line may exceed its breaking limit in high to extreme exposure sea states. It should be noted that the loads in the bridle lines are strongly dependent on the arrangement of the bridle lines, so the load distribution between bridle lines may be totally different from the present set-up if a new mooring system is considered.

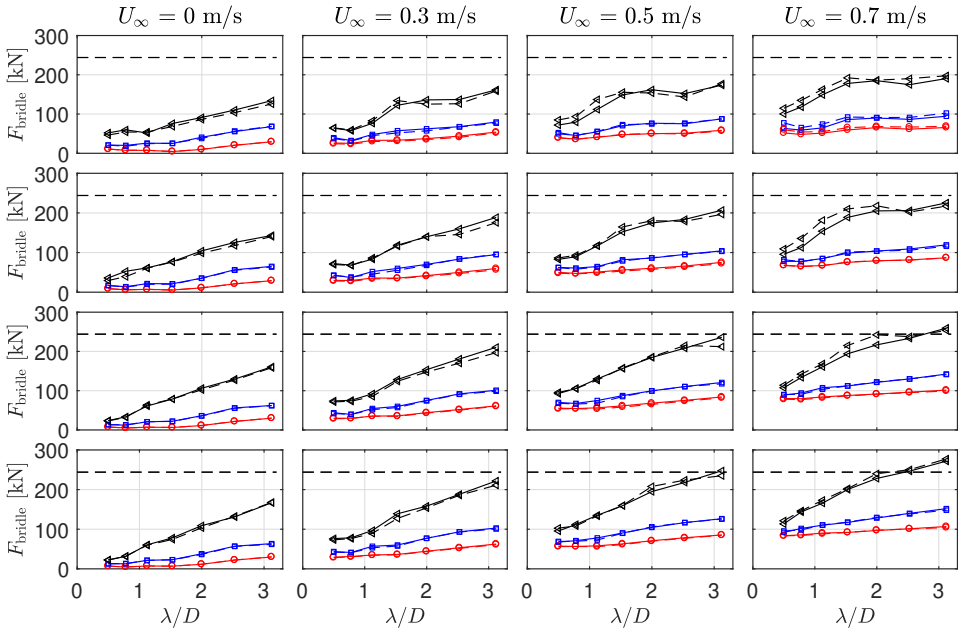

Figure 4.30: Same as that in Figure 4.29, but for the bridle line-2. Horizontal dashed line represents the minimum breaking force (polysteel, 3 strand, diameter 40 mm).

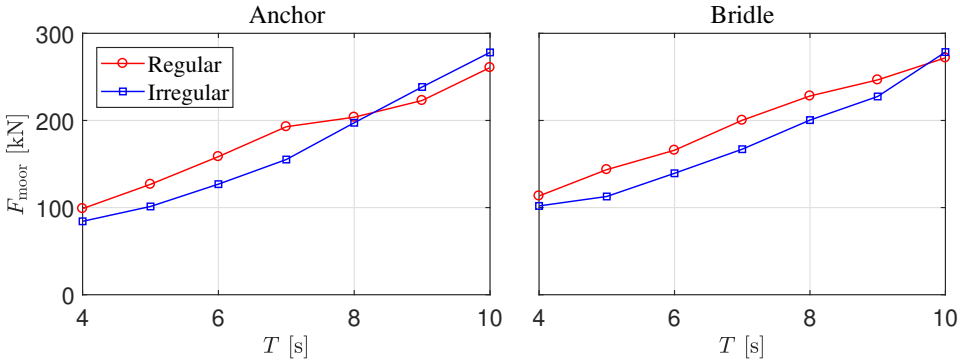

Figure 4.31: Comparison of the maximum loads in the anchor line (left) and bridle line (right) by numerical calculations in irregular waves and equivalent regular waves. The considered regular wave steepness $H/\lambda = 1/15$, current velocity $U_\infty = 0.7$ m/s.

In order to see how irregular waves are represented by regular waves according to the standard in Table 1.2, we present the maximum values of the anchor loads and the bridle loads in Figure 4.31 for the system in both irregular and equivalent regular waves. The figure shows that the maximum mooring loads are similar for the considered two wave types and results from regular waves are generally more conservative, which coincides with the conclusion from Berstad and Tronstad (2005). It should be noted that just one realization is considered for the irregular sea scenario and actual results in irregular sea are realization dependent.

The results of the net volume reductions for the system in combined waves and current are also investigated and are not shown here. The general conclusion is that the cage volume reduction is dominated by the current in mild wave conditions, however in cases with high wave steepness, current and waves will have similar contributions.

Finally, we show the numerical predictions of the stress distributions along the floating collar. The maximum bending stress due to horizontal deformations in a position $x = R\cos\beta$ along the floater is given as

$$\sigma(\beta, t) = \frac{M(\beta, t)}{I} r_{\max} = \frac{E r_{\max}}{R^2} \sum_{n=2}^{\infty} n^2 b_n(t) \cos n\beta \tag{4.13}$$

where E is the Young's modulus, I is the area moment of the cross section in horizontal plane and $r_{\max} = 3c_f$ with c_f the cross-sectional radius of the floating collar which comprises two tubes placed with center-to-center distance $4c_f$. Similar expression can be obtained for the stress due to vertical deformations. One should note that the cross-sectional area moment in the horizontal plane is about ten times that in the vertical plane. The stress distributions along the floating collar due to horizontal and vertical deformations are given in Figure 4.32. The figure shows that the stress due to vertical deformations are small compared with the contribution from horizontal deformations and the maximum stress occurs at the positions β

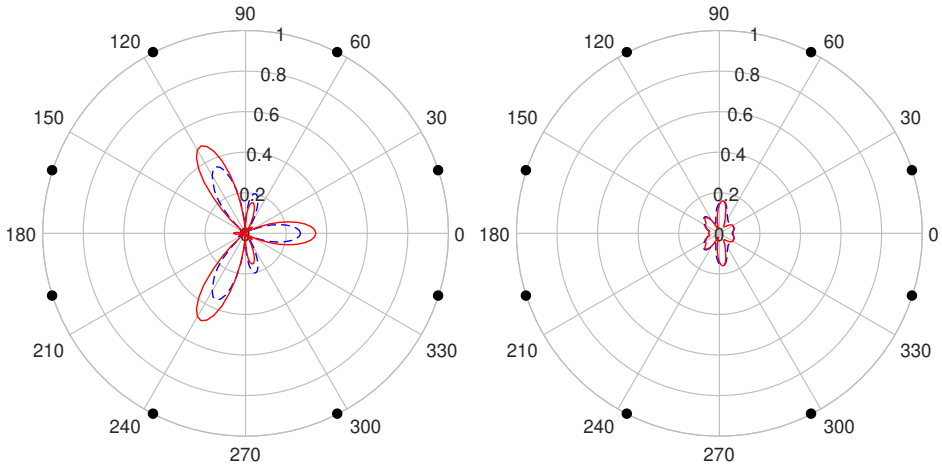

Figure 4.32: Stress distributions along the floating collar for cases with U_∞=0.7 m/s, H/λ =1/15 and T=8 s (dashed dot line) and T=10 s (solid line). The stress is made non-dimensional by the yield stress (high-density polyethylene). Left: stress due to horizontal deformations. Right: stress due to vertical deformations. Solid circle symbols represent the positions where bridle lines are attached.

= 117^0 and 243^0 where bridle lines are attached. The maximum stress along the floating collar will not exceed the yield stress for the considered sea states.

4.4 Conclusions and following work

We presented a study on a realistic fish farm system with single cage exposed to current, regular and irregular waves. The system comprises a floating collar with two concentric tubes, a flexible net cage and a sinker tube attached directly to the net, moored by a complex mooring system with anchor lines, bridle lines and frame lines. Loads in the anchor lines and in the bridle lines were investigated in detail and satisfactory agreement between numerical and experimental results was demonstrated for the system in both regular and irregular waves. One thing interesting was that the load in one of the bridle lines was larger than the rest of the mooring loads for most of the cases.

A systematic sensitivity analysis was performed to identify the dominant factors when modeling the fish farm in regular waves and current. The main focus is on the mooring loads. In total 30 parameters from different components were analyzed separately. The study suggested that the mooring loads in the anchor lines and in the bridle lines were not sensitive to the majority of the variations. The most important parameter for the anchor loads is the flow reduction factor in the rear part of the net cage. Modeling the floating collar as a rigid body has a moderate effect on the anchor loads, but the bridle loads may differ by more than 20% as a rigid collar will change the force distribution along bridles. The mooring loads are not sensitive to the wave load model for the floating collar and hydrodynamic

forces on the floating collar are quite moderate compared with the total loads on the system for cases in both regular and irregular waves.

Finally, fish farms with different set-ups in different exposure scenarios were investigated numerically. The considered wave periods, wave steepness and current velocities cover the sea states from light exposure to extreme exposure, according to the Norwegian standard for regular waves. The main target was to figure out the main constraint for the conventional fish farms to operate in exposed areas and how exposed they can operate. Three criteria were proposed: maximum net cage volume reduction, maximum loads in the mooring lines and maximum stress in the floating collar. Numerical results showed that the net volume reduction was the dominant limit. The maximum stress in the floating collar was moderate compared with the yield stress of the floating collar, even for extreme sea states. In terms of the mooring system, the existing mooring system can be applied in offshore area if the bridle lines are properly designed.

The studies in survival conditions only examined the most critical scenario with aligned long crested waves and current. It means that the conclusions may be a bit conservative. The fish farm system in more general sea states should also be studied and possibly three-dimensional waves should be accounted for; this is left for a future work. Their implementation in the present method is relatively straightforward within the assumption of linear superposition principle. The influence of the arrangement of the bridle lines on the mooring loads should also be considered. The numerical solver proposed in this paper is applicable to any net-based fish farm concept and can be used to analyze fish farms, for instance, with submersible net cages or square net cages. However, how to account for the effect of upstream cages on current in case with multiple cages needs to be further studied.

Up to now we have focused on the study of the fish-farm as isolated. However, for fish farms operating in more exposed sea areas the probability of well-boat routine operations to occur in severe weather conditions will also increase. During the loading/offloading phase, the well boat is moored directly to the fish farm, which may significantly increase the mooring loads and the floating collar deformations and thus endanger the structural integrity of the fish farm. So there is a need to have a detailed investigation of the influence of the well boat on the fish farm and identify the operational conditions for performing such load/offloading operation, as shown in the following two chapters.

Chapter 5

Numerical modeling of a well boat operating at a fish farm

In this chapter, theoretical models of a well boat operating at a fish farm in current only and in long-crested irregular waves and current are introduced. A modern design well boat and a realistic fish-farm set-up (with single cage) including a floating collar, an elastic sinker tube, a flexible-closed net cage and a complex mooring system are examined.

For the coupled system in current only, transverse viscous current loads on the well boat are estimated using the cross-flow principle. The drag coefficients are obtained empirically by considering cross-sectional details, free surface and three-dimensional (3D) flow effects. The drag force is experimentally validated. The strategy used for the well boat-fish farm coupling is also explained, together with the method to measure the contact force between them.

For the coupled system in long-crested irregular waves and current, the modeling of the motions of the well boat when the well boat operates at the weather side of the fish farm is explained in detail. The approaches to estimate the slow-drift excitation force and slow-drift damping (wave-drift damping and eddy-making damping) are given. The cross-flow principle is assumed valid for evaluating the transverse viscous loads and the needed cross-sectional drag coefficients are estimated empirically and validated against available experiments. The system coupling with well-boat bow against the inflow is also outlined as it will be examined for selected cases in the next chapter.

In the following, a description of the numerical set-up of the coupled well boat-fish farm system is given at first. Then, numerical modeling of the coupled well boat-fish farm system in current only is briefly introduced. The strategy used for their coupling is also explained. Finally, the modeling of well-boat motions in long-crested irregular waves and current is provided. In terms of the fish farm, a realistic set up and a simplified set up (fish farm represented as a linear spring) are considered. Parts of the results in this chapter are documented in Shen et al. (2016), Shen et al. (2018a) and Shen et al. (2018b).

5.1 Numerical set-up

The main arrangement and dimensions of the coupled fish farm-well boat system are described in this section.

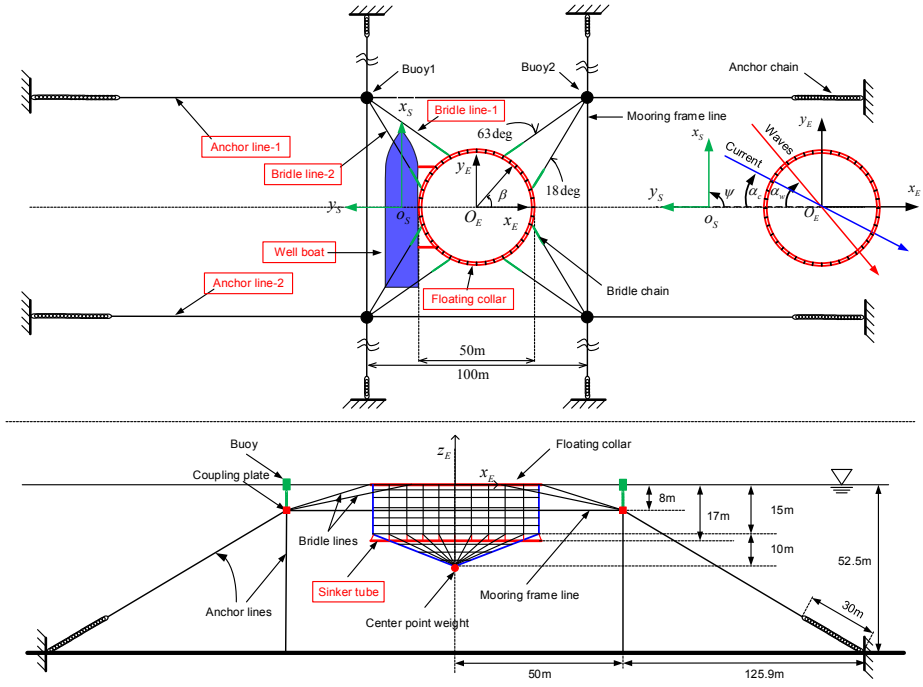

Figure 5.1: Configurations of the coupled well boat-fish farm system with definitions of the inertial Earth-Fixed coordinate systems $O_E x_E y_E z_E$ and $O_S x_S y_S z_S$ used in this study. Upper: top view. The floating collar is duplicated in the right part of the sketch to define current direction α_c, wave direction α_w and boat heading angle ψ. Lower: side view. The well boat is not shown.

For the fish farm, similar set-up used in Chapter 4 is adopted here, including two concentric floating tubes, an elastic sinker tube, a cylindrical net cage with a conical bottom, a mooring system comprising bridle lines, mooring frame lines, mooring buoys, coupling plates, chains connecting the coupling plates to the buoys and the anchor lines attaching the system to the sea bed, see Figure 5.1. The parameters and dimensions of different components are given in Tables 5.1 and 5.2. All the values given are in full scale. Some of the parameters are different from those given in Chapter 4, to represent more realistic values. The parameters used in Chapter 4 were derived based on the experimental data from Nygaard (2013). Since 'ordinary' ropes were used in the experiments, the corresponding full-scale stiffness of the bridle lines and frame lines are larger than those used in commercial full-scale cages. So instead, we use realistic full-scale values in this study. Also,

the stiffness of the front two anchor lines was about 110 kN/m in Nygaard (2013), as specified value in the experiments, while in the present case the corresponding value is about 55 kN/m, based on the realistic length, diameter and Young's module for the anchor lines.

Table 5.1: Parameters of the floating collar, net cage and sinker tube. The position of the center point weight W_c is shown in Figure 5.1.

Description	**Symbol**	**Value**	**Unit**
Floating collar			
Number of tubes	-	2	-
Diameter inner ring	D_{f1}	50	m
Diameter outer ring	D_{f2}	51.8	m
Tube section diameter	d_f	450	mm
Tube bending stiffness	EI_f	7.72×10^5	Nm^2
Tube mass	m_f	32.54	kg/m
Net cage			
Diameter	D_c	50	m
Depth of vertical net	h_u	15	m
Depth of cone net	h_l	10	m
Net twine diameter	d_w	2.7	mm
Net mesh-bar length	l_w	19.3	mm
Net E-module	E_{net}	5×10^8	N/m^2
Net solidity ratio	Sn	0.26	-
Center point weight	W_c	200	kg
Sinker tube			
Tube diameter	D_s	51.8	m
Tube section diameter	d_s	280	mm
Tube depth	h_s	17	m
Tube bending stiffness	EI_s	2.0×10^5	Nm^2
Sectional mass in water	w_s	50	kg/m

Table 5.2: Parameters of the mooring system. All ropes are almost without weight in water. All ropes Young's module $E_{\text{rope}} = 1.8$ GPa and the chain Young's module $E_{\text{chain}} = 105$ GPa. Positions where the two bridle lines are attached to the floating collar are defined in the coordinate system $O_E x_E y_E z_E$.

Description	Value	Unit
Bridle lines		
Position (bridle-1)	117	degrees
Position (bridle-2)	162	degrees
Rope diameter	48	mm
Rope length	44.2	m
Chain diameter	19	mm
Chain length	5.47	m
Chain mass	8.66	kg/m
Bridle line stiffness	72.7	kN/m
Anchor lines		
Line length	133.5	m
Rope length	103.5	m
Rope diameter	64	mm
Chain length	30	m
Chain diameter	36	mm
Chain mass	28.73	kg/m
Anchor line stiffness	55.1	kN/m
Frame lines		
Length	100	m
Depth	8	m
Diameter	64	mm
Frame line stiffness	57.9	kN/m
Buoys system		
Number of buoys	4	-
Buoy diameter	1.55	m
Buoy length	2.34	m
Buoy mass	146.9	kg
Chain diameter	19	mm
Chain length	7	m
Chain mass	8.66	kg/m
Coupling plate mass	55	kg

In terms of the well boat, a modern design well boat from Rolls-Royce Marine, is used in the study. The three-dimensional (3D) numerical panel model employed in the potential-flow calculations together with the body plan are shown in Figure 5.2. The principal dimensions are given in Table 5.3.

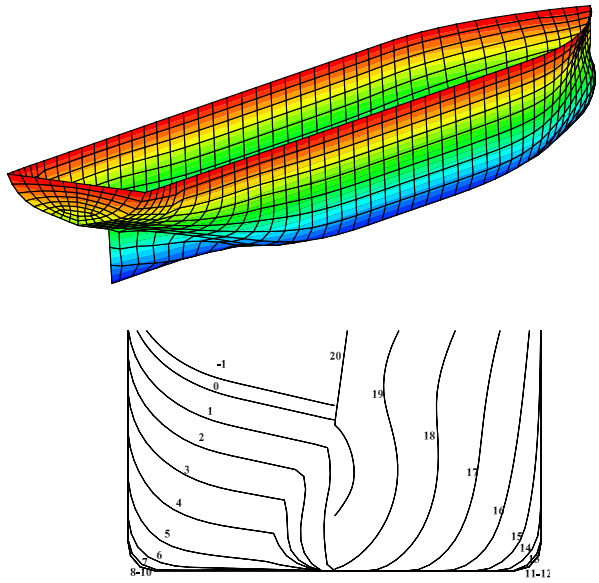

Figure 5.2: Submerged geometry of the well boat. Upper: panel model. Lower: body plan. Numbering of sections is also given with section 1 in the aft part of the boat.

Table 5.3: Principal dimensions of the well boat.

Length between perpendiculars (L)	70 m
Breadth (B)	15 m
Draft (D)	6.7 m
Displacement volume (∇)	5145 m^3
Block coefficient (C_b)	0.75
Mid-ship coefficient (C_m)	0.99
Height of center of gravity (KG)	$0.75D$
$OG = KG - D$	$-0.25D$
Roll gyration radius	$0.35B$
Pitch gyration radius	$0.28L$
Yaw gyration radius	$0.28L$
Transverse metacentric height (GM)	1.6 m
Bilge-keel length (l_{bk})	$0.3L$
Bilge-keel breadth (b_{bk})	$0.02B$

Two different inertial and Earth-fixed coordinate systems are used in the simulations and are defined in Figure 5.1. One is the Cartesian right-handed coordinate system $O_E x_E y_E z_E$ with the vertical z_E-axis positive upwards through the center of the floating collar in calm water (also defined in Chapter 4). The other is the

seakeeping coordinate system $O_S x_S y_S z_S$ with origin in the undisturbed free surface z_E=0. The vertical z_S-axis is positive upwards through the center of gravity (COG) of the boat in the mean-ship configuration and the horizontal x_S-axis points towards the bow. The incident wave angle α_w and current angle α_c are defined in the figure. $\alpha_w = 0^o$ means that the waves propagate in positive x_E direction and $\alpha_c = 0^o$ denotes that the current direction coincides with the positive x_E direction. The heading angle of the boat ψ is also defined in Figure 5.1 and $\psi = 0^o$ means that the bow of the boat points towards the positive x_E-axis.

The well boat can be moored in different positions relative to the fish farm. No thruster action is considered, which is common practice in order to avoid possible net suction. Assuming a scenario with main inflow direction along positive x_E, three relevant well-boat set-ups are given in Figure 5.3. Set-up A: at the weather side of the floating collar; set-up B: at the leeward side; set-up C: with the well-boat bow against the inflow. Each set-up has pros and cons. It will be difficult for the boat to detach from the fish farm with set-up A in severe sea conditions and this set-up is expected to be the most critical in terms of mooring loads and floating collar stresses. In sea regions with strong current, the well boat should avoid connecting to the fish farm with set-up B as there is a risk of the net drifting into the propeller. The system with set-up C can significantly reduce the external loads from the boat and therefore is not so critical. Here we will mainly investigate the coupled system with set-up A, and the results for the system with the other two set-ups will be just briefly discussed.

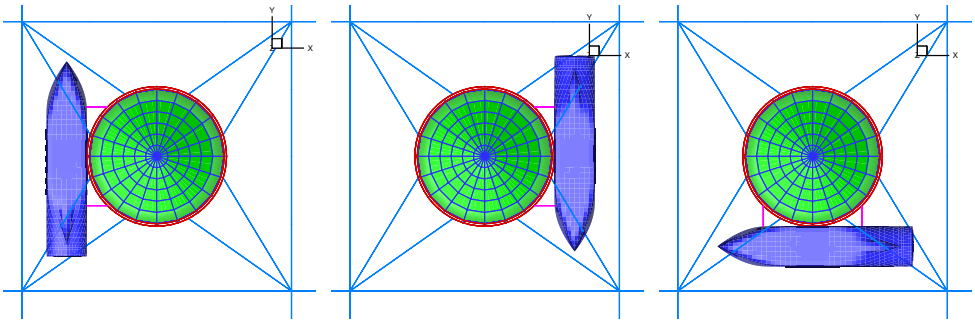

Figure 5.3: Different set-ups with the well boat moored to the fish farm. The inflow is in the positive x_E-direction. Left: set-up A, heading angle of the boat $\psi = 90^o$ (weather side). Middle: set-up B, $\psi = 270^o$ (leeward side). Right: set-up C, $\psi = 180^o$ (bow against inflow).

5.2 Theoretical and numerical model: in current

In this section, the modeling of the coupled well boat-fish farm system in current only is presented. A time-domain solution is used to find the steady configuration and response. Since the theoretical model for different components of the fish farm has been introduced in Chapter 2, here the main attention is paid to the modeling of

well-boat loads. An empirical way to estimate the cross-sectional drag coefficients of the well boat in current is proposed. The way to evaluate the damping coefficient for roll motion is also presented. In the end, the strategy used for the well boat-fish farm coupling is explained and the method to measure the contact force between them is introduced.

5.2.1 The well boat

The transient motions of the well boat are solved in the seakeeping coordinate system $O_S x_S y_S z_S$. Transient linear potential-flow effects as proposed by Cummins (1962) are included and the motion equations are given by

$$\sum_{k=1}^{6}\left[\left(M_{jk}+A_{jk}(\infty)\right)\ddot{\eta}_k+\int_0^t K_{jk}\left(\tau\right)\cdot\dot{\eta}_k\left(t-\tau\right)\,\mathrm{d}\tau+C_{jk}\eta_k\right] = F_j\left(t\right)\ \left(j=1,2,...,6\right) \tag{5.1}$$

where η_k, $\dot{\eta}_k$ and $\ddot{\eta}_k$ are the motion, velocity and acceleration for ship rigid mode k and $k = 1,...,6$ represents surge, sway, heave, roll, pitch and yaw, respectively. M_{jk}, $A_{jk}\left(\infty\right)$ and C_{jk} are components of the generalized ship mass matrix, infinite-frequency added-mass matrix and the restoring matrix of the boat. $\int_0^t K_{jk}\left(\tau\right)\cdot\dot{\eta}_k\left(t-\tau\right)\,\mathrm{d}\tau$ is the convolution integral connected with the free-surface memory effects and $K_{jk}\left(t\right)$ is the retardation function connected with rigid modes j and k. It provides a radiation load in j direction acting on the vessel at the actual time t as a consequence of an impulse velocity in k direction experienced by the ship at a previous time instant $t-\tau$. $K_{jk}\left(t\right)$ can be estimated in a similar way as shown in Eq. (2.11), so it is not repeated here. The transient motions will decay after a short time in the simulations when only viscous current loads are considered. $F_j\left(t\right)$ is the generalized force in the j_{th} degree of freedom. Due to coupling with the fish farm, apart from the current loads, $F_j\left(t\right)$ will also have other external loads with respect to those of a single ship. These may include contact forces and connection-line forces. In the following we will mainly pay attention to the estimation of steady-state viscous current loads, the estimations of the others are given in section 5.2.2.

The boat interaction with a current, with generic direction relative to the boat, will lead to viscous loads. In principle, these loads can be affected by the presence and coupling with the fish farm, but this can be neglected as a first approximation. Under these assumptions, to estimate the current loads on the boat, dedicated model tests or Computational Fluid Dynamics (CFD) simulations could be used. The former involve a cost and will have the issue of Reynolds number scaling; the latter become more and more popular because less costly but require suitable validation and can be time consuming for performing converged simulations at high Reynolds numbers. An argument against CFD is also that the well boat is a subsystem and numerical tools for the different subsystems must be balanced in

complexity. The many meshes of the netting of a fish cage prohibit the use of CFD and complete structural modelling.

For a more efficient and still physically-sound estimation of current loads, here we follow the procedure documented by Faltinsen (1990). We assume that the current loads can be decomposed in transverse and longitudinal loads caused, respectively, by the transverse and by the longitudinal component of the current velocity with respect to the ship main axis. The transverse loads are mainly connected with flow separation along the vessel as long as the angle between the current direction and the longitudinal ship direction is not small and can be estimated with the cross-flow principle. They lead in general to a 3D transverse force and to a yaw moment. In addition a potential-flow Munk yaw moment is also caused by the current. The longitudinal force is mainly connected with frictional stresses. In particular, the 3D transverse (Y_F) and longitudinal (X_F) forces can be written as

$$\begin{aligned} Y_F &= -0.5\rho \int_L \left[C_D\left(x\right) V_F \left|V_F\right| D\left(x\right)\right] dx \\ X_F &= -0.5\rho C_F U_F \left|U_F\right| S \end{aligned} \tag{5.2}$$

Here ρ is the water density, $C_D(x)$ is the drag coefficient for cross-flow past an infinitely long cylinder with uniform cross-section equal to the ship cross-section at the longitudinal coordinate x, modified by 3D effects due to flow separation around the ship ends. V_F is the transverse current component and $D(x)$ is the sectional draft. Similarly, C_F is the frictional coefficient, U_F is the longitudinal current component and S is the wetted surface area of the ship hull. $V_F = U_\infty \sin\beta_c$ and $U_F = U_\infty \cos\beta_c$ with β_c the angle between the current velocity U_∞ and the positive longitudinal x_S-axis. It means that empirical load coefficients, C_D and C_F, are needed and they are estimated using available data from the literature. Information on the applicability and limits of this decomposition approach and cross-flow principle can be found e.g. in Faltinsen (1990).

Transverse viscous force

Within the cross-flow principle, the 2D transverse viscous current force is a drag force. In order to have a reliable prediction of it, we need a reliable estimation of the drag coefficient at the different ship cross-sections. Faltinsen (1990) showed that cross-flow drag coefficient for ship cross-sections is mainly influenced by the section geometry (beam-to-draft ratio, bilge radius, bilge keel presence and dimensions), Reynolds number, free-surface and three-dimensional (3D) effects. We will briefly explain the different parameters in the present context.

Flow regimes: If the cross-section has no sharp corners, the value of the cross-sectional drag coefficient depends on the flow regime in the boundary layer upstream of flow separation (depending on the Reynolds number and surface roughness), i.e. laminar or turbulent boundary layer flow. The two flow regimes are associated with different locations of the flow separation points, so the corresponding drag coefficient will be different (Aarsnes et al., 1985).

Three-dimensional (3D) effects: The 3D effects due to the flow around the ship ends tend to reduce the total drag force compared with pure strip theory approach because they tend to reduce locally the inflow velocity at the cross-sections towards the ship ends (Aarsnes et al., 1985).

Free surface: The free surface has a significant influence on the drag coefficient and can be approximated as an infinitely long splitter plate, as long as the boundary layer effect due to the splitter plate is negligible. It will change the flow pattern behind the body and cause a reduction of the drag coefficient. More detailed explanation is given by Faltinsen (1990, 2005).

Cross-sectional shape: The effect of the cross-sectional shape upon the drag coefficient for typical midship sections is mainly due to the bilge radius r, beam-to-draft ratio B/D and bilge keels. An increase in bilge radius will lead to a reduction of the drag coefficient. The beam-to-draft ratio will have influence, but only when $B/(2D) < 0.8$. The presence of the bilge-keels will make the drag coefficient less scale dependent when transforming model values to full scale (Faltinsen, 1990, 2005). The reason is that the flow separation points are at the bilge keels and not determined by the boundary layer flow. The position of the flow-separation points will significantly influence the drag coefficients.

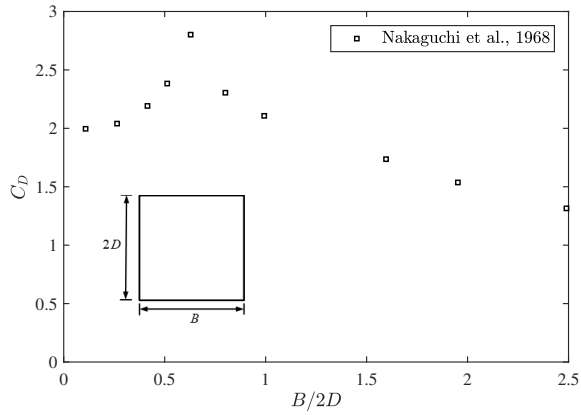

Figure 5.4: Drag coefficient C_D as a function of aspect ratio $B/(2D)$ for a rectangular two-dimensional cylinder with sharp corners in steady incident flow parallel to the rectangular side with length B (Nakaguchi et al., 1968). Reynolds number $\mathrm{Rn} = 2U_\infty D/\nu = 2 \sim 6 \times 10^4$ with U_∞ the inflow velocity and ν the kinematic viscosity.

The next step is to account for the influences of all the above mentioned parameters and give an estimation of the drag coefficient for the different cross-sections. In terms of the flow regime, the cross-flow for different cross-sections of a full-scale well boat should be turbulent, so drag coefficients for turbulent flow should be adopted. We start with the midship section (section 10). For this, the aspect ratio

$B/(2D)$=1.12. According to the experimental data from Nakaguchi et al. (1968), see Figure 5.4, the drag coefficient C_D for a rectangular section with $B/(2D)$=1.12 and bilge radius r=0 in infinite fluid is about 2.0. Faltinsen (1990) documented that the drag coefficient depends strongly on the bilge radius. As r increases, the drag coefficient decreases because the vortex shedding becomes less intense and the dependency can be written as

$$C_D = C_1 e^{-kr/D} + C_2 \tag{5.3}$$

where C_1 and C_2 are constants of similar magnitude. By fitting the experimental data from Delany (1953), Faltinsen (1990) showed that k may be 6 and $C_D = 0.8e^{-6r/D} + 1.2$ for the case with $B/(2D)$=1. As similar $B/(2D)$ is considered for our midship section, the same C_D expression is assumed. For the midship section, r/D= 0.149, then the drag coefficient C_D= 1.53.

The free surface will reduce the drag coefficient. In order to have an idea of this reduction effect, we examined the drag coefficients for different cross-section geometries with and without free surface (or splitter plate behind) effect, using data available from the literature. Blevins (2003) showed that the drag coefficient for a sharp-edged square section reduces from 2.0 to 1.45 (Reynolds number = 5×10^4) due to a splitter plate behind the section, with about 27.5% reduction. The length of the splitter plate was equal to $20D$ and can be roughly seen as infinitely long. Similarly, the drag coefficient for cross-flow past a thin flat plate reduces from 1.9 to 1.38 due to a splitter plate behind, with about 27.3% reduction. The drag coefficient for a circular section with infinity long splitter plate in the middle changes from 1.1 to 0.8 (Reynolds number = 10^4), with about 27.3% reduction. It is interesting to see that the free surface exerts similar influence on the drag coefficient for different cross-sectional shapes. In the present study, we assume the free surface will reduce the drag coefficient of the midship section by 27.3%, then the drag coefficient for the midship section will be $C_D = 1.53 - 1.53 \cdot 0.273 = 1.11$. The same procedure is applied to estimate the drag coefficient for the midship section of the hull presented in Aarsnes et al. (1985) and nice agreement was achieved with their numerically predicted value.

In the above analysis, the influence of bilge keels is not considered, which may have a big importance. According to the experimental results from Mercier and Huijs (2005), the lateral drag coefficient increases from 0.6 to 0.9 $\sim$ 1.0 when bilge keels are included. This means that the bilge keels increase the lateral drag coefficient by at least 50%. A simple explanation of the influence of bilge keels is that the flow will be forced to separate at the sharp corner of the bilge keel, which makes the flow field around the corner resembles that for a sharp-edged rectangular section, as shown in Figure 5.5. So for the midship section with bilge keels, the drag coefficient for a rectangular section with r=0 is proposed, which means using C_D = 2 instead of C_D = 1.53 as basic drag coefficient. Here we neglect the influence of the bilge keel breadth. Considering the free surface effect, the drag coefficient for the midship section becomes $C_D = 2 - 2 \cdot 0.273 = 1.45$. The bilge keels exist from section 7 to section 13, so for simplicity drag coefficient C_D = 1.45 is used for all

these cross-sections.

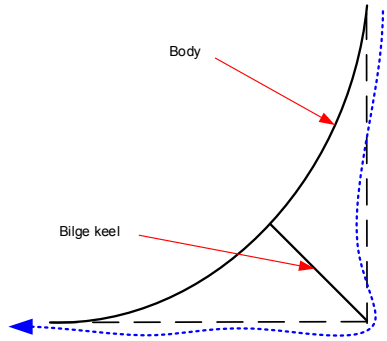

Figure 5.5: Sketch for flow around the cross-section with bilge keel. Dotted line: sketch of the flow streamline.

For the other ship sections, with geometry close to rectangular, the same procedure introduced above has been followed. The well boat sections near the ship ends present shapes not studied experimentally or numerically. A rough estimation of their drag coefficients has been obtained by interpolating the drag coefficients of ship sections with closest geometries studied numerically in the turbulent-flow regime by Aarsnes et al. (1985). This is an error source but has a limited influence on the average drag coefficient for the well boat, as discussed below in the text. The 2D drag coefficient for different sections needs to be lowered as consequence of 3D effects. Since no other study on 3D effects is available, but for the one by Aarsnes et al. (1985), the 3D reduction factor for the cross-section drag coefficient from such research work has been adopted here. The drag coefficients for different sections with and without considering the 3D reduction factor are shown in Figure 5.6. The average drag coefficient with and without considering the reduction effect are 0.9 and 1.06, respectively. The obtained ship average C_D is reasonable compared with that shown in Mercier and Huijs (2005) for a tanker-based FPSO with bilge keels.

From our results, the average drag coefficient for the well boat is not much sensitive to the specific value of the drag coefficients for cross-sections close to the ship ends, which are those potentially more connected with estimate errors. In fact, a change in these C_D of 10% would cause a change of about 3% for the average well-boat drag coefficient. In order to assess the method introduced, we applied the same procedure to estimate the transverse drag coefficient for a tanker (without bilge keels) presented by Faltinsen et al. (1979) in loaded condition and we compared the results against their experimental data. The results are shown in Figure 5.7. The empirically estimated average drag coefficient ($C_D = 0.69$) agrees well with that from the model tests ($C_D = 0.68$). This suggests a fair reliability of the followed approach for the C_D prediction. The well-boat scenarios examined in this thesis will not lead to important yaw excitation, therefore the viscous and Munk current yaw moments will not be discussed; details can be found in e.g.

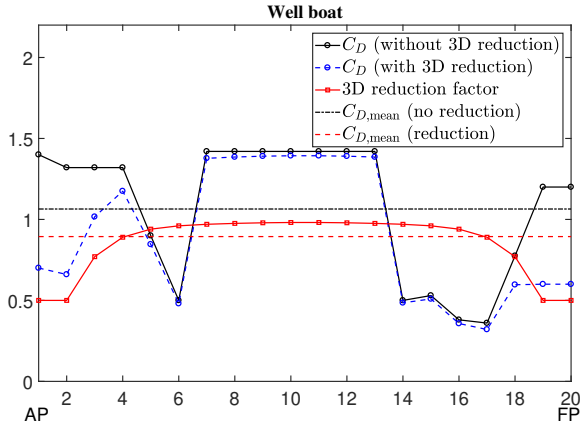

Figure 5.6: Sectional transverse drag coefficient C_D for different sections of the present well boat. The 2D drag coefficients with and without the 3D reduction effects are shown. The corresponding average drag coefficients are also given.

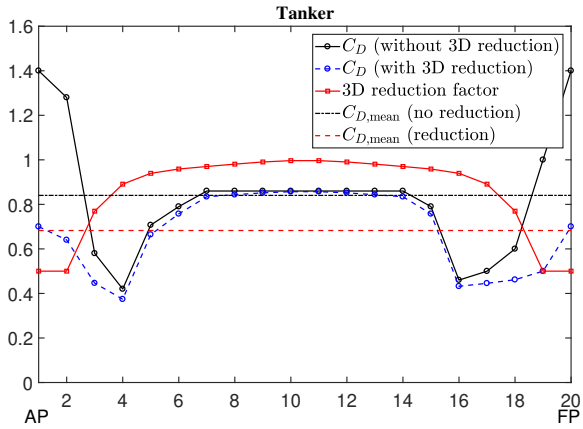

Figure 5.7: Sectional transverse drag coefficient C_D for different sections of the tanker documented by Faltinsen et al. (1979).

Faltinsen (1990).

Longitudinal viscous force

The viscous force in longitudinal direction is mainly due to the friction force on the wetted ship hull. Pressure drag and roughness effects are not considered as first approximation. The frictional coefficient C_F is estimated according to the ITTC'57 guidelines as the value for a smooth flat plate in turbulent flow conditions (see Faltinsen, 1990) and given as

$$C_F = 0.075/(\log_{10}^{\text{Rn}} - 2)^2 \tag{5.4}$$

where Reynolds number $\mathrm{Rn} = U_F L/\nu$, with L the length between perpendiculars of the well boat.

Roll damping coefficient due to bilge keels

According to Himeno (1981), the ship roll damping for zero forward speed can be divided into several components, that are, friction, eddy and wave damping for a naked hull, and bilge-keel damping, involving normal-force damping, hull-pressure damping and wave damping. Here, the different components of the roll damping are approximated using a simplified formula proposed by Kawahara et al. (2011), obtained as best-fitting of the Ikeda's method from Ikeda et al. (1977). This formula is convenient compared with the direct use of the Ikeda's method because the involved parameters are limited to the general ship features. Detailed results are not shown here.

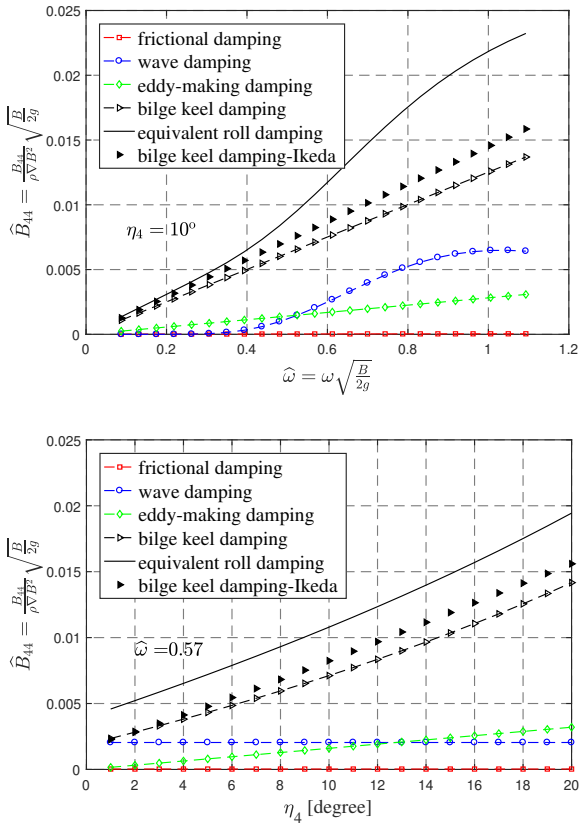

Figure 5.8: Non-dimensional equivalent roll damping coefficient predicted with the simplified formula proposed by Kawahara et al. (2011). Solid symbols: bilge-keel damping estimated by Ikeda's method from Ikeda et al. (1977). The results are presented versus non-dimensional wave frequency (upper) and roll amplitude (lower).

The non-dimensional equivalent roll damping coefficient estimated by the simplified method is shown in Figure 5.8. The figure also shows the prediction of each individual damping component. The friction damping coefficient is negligible for a full-scale ship, as shown in the figure. The damping due to the bilge keels has the dominant contribution to the roll damping, approximately 70%-80%. It should be noted that the damping due to the waves generated by the ship rolling is already estimated by the potential flow theory and therefore not included in the final calculation in order to avoid redundancy. For the bilge-keel damping, the bilge-keel dimensions are needed and for the simplified formula validity, the following conditions should be satisfied: $0.01 \leq b_{bk}/B \leq 0.06$, $0.05 \leq l_{bk}/L \leq 0.4$ and $-0.2 \leq OG/D \leq 1.5$. All the mentioned symbols are defined in Table 5.3. In our case, the OG/D = -0.25 is slightly out of the applicability region. So the bilge-keel damping predicted by the original Ikeda's formula is also provided in the figure. From the figure, we can see that there is a difference between the two methods especially for cases with higher wave frequency and larger roll amplitude, but it is quite moderate, about 10%. So the simplified method will be used in the analysis.

5.2.2 Contact force estimation

The well boat is coupled with the fish farm system in two ways: it is connected to the floating collar by two ropes and has also direct contact with the floating collar. This represents a typical connection scenario for well-boat operations at fish farm. For each rope, the connection force is estimated as a linear spring force directed along the connection line and given by the product between the rope spring stiffness and the rope elongation. The latter is easily estimated when the well-boat position and the floating-collar configuration are known. The force is taken as zero if the elongation is negative.

The contact force F_c is normal to the surface of the boat when contact with the floating collar happens. Here a simplified method (named indirect method) is proposed to deal with the contact between the well boat and the floating collar. Before estimating the contact force, we need to determine whether the contact happens or not. If the distance Δ_c between the center line of the floating-collar outer tube and the boat surface is smaller than the tube's cross-sectional radius $d_f/2$, then the floating collar gets in contact with the boat. The reason to use the center line in this contact criterion is that the motions of the floating collar center line can be readily obtained in the simulations.

If the floater gets in contact with the boat, the contact force F_c is assumed to be proportional to $d_f/2 - \Delta_c$ and expressed as $F_c = k_c(d_f/2 - \Delta_c)$ with k_c the contact stiffness and $d_f/2 - \Delta_c$ the normal distance between the floating collar outer surface and the boat surface. This means that we model the contact effect like a spring (or multiple springs) with stiffness k_c between the well boat and the floating collar, see Figure 5.9. The next step is to determine the contact stiffness k_c. Ideally, the contact stiffness should be close to infinity to well represent the stiffness of the boat surface, but very small time-step is then needed to guarantee the convergence of the simulations. Practically, we should choose a sufficiently high k_c to ensure correct global response of the coupled system while still reasonable

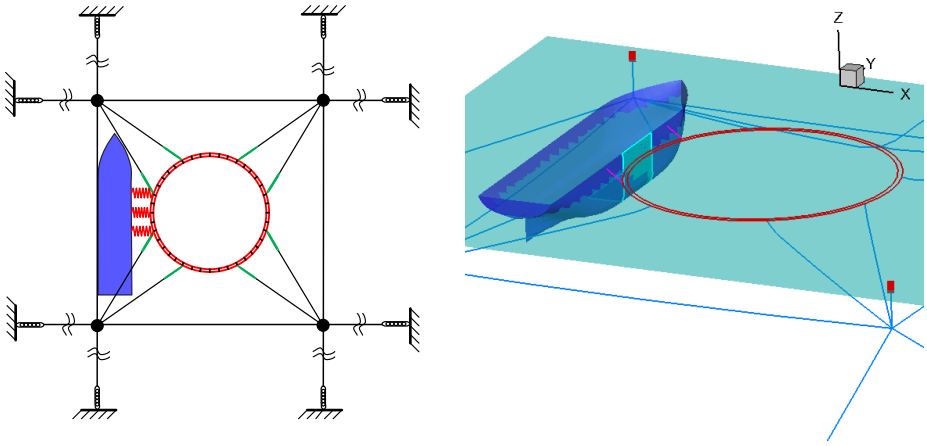

Figure 5.9: Sketch for explaining the estimation of the well boat-fish farm contact force by very soft springs. Left: bird view. Right: three-dimensional view.

time-steps can be used in the simulations.

For the well boat, the fish farm acts like a spring, preventing the boat from drifting away. The inserted spring stiffness (or contact stiffness) k_c is determined on the basis that the restoring stiffness of the fish farm (with well boat) k_g will not change from its original value (without well boat) k_f, namely $k_g = 1/(1/k_c + 1/k_f) \approx k_f$. This means that the inserted spring stiffness $k_c \gg k_f$.

To estimate a suitable value for k_c, one must establish a realistic value for k_f. Let us assume that the well boat is placed at the fish farm according to set-up A (defined in Figure 5.3). Then the equivalent fish-farm stiffness k_f to be compared with k_c can be defined as $k_f = dF_x/dx$. Here F_x is the horizontal force, along the x_E-axis, acting at position $\beta = 180^o$ of the floating collar and pointing towards the positive x_E-axis while x is the corresponding horizontal displacement along x_E-axis. Figure 5.10 shows the equivalent stiffness k_f of the fish farm without well boat as a function of the pretension force and floating collar stiffness. The figure shows that k_f is not constant when subjected to sufficiently small external force. This is due to the catenary shape of the chains in the lower end of the anchor lines. As the load exerted on the system increases, k_f is almost constant and about 24 kN/m. In this case, there is no anchor chain laying on the seabed and the stiffness of the mooring system is mainly determined by the mooring line stiffness. Larger pretension forces in the anchor lines will increase k_f when small external force is exerted on the system. If we increase the floating collar stiffness, k_f increases, as expected. If we consider a rigid floating collar, then k_f reaches a maximum value and the maximum stiffness k_{fmax} is about 40 kN/m. So it is fairly safe for us to set the contact stiffness between the well boat and the floating collar $k_c = 100k_{fmax}$ = 4000 kN/m to ensure correct global restoring stiffness for the well boat.

In order to see how the contact stiffness will influence the mooring forces, time histories of the contact force F_c and the load in anchor line-1 (see Figure 5.1) with

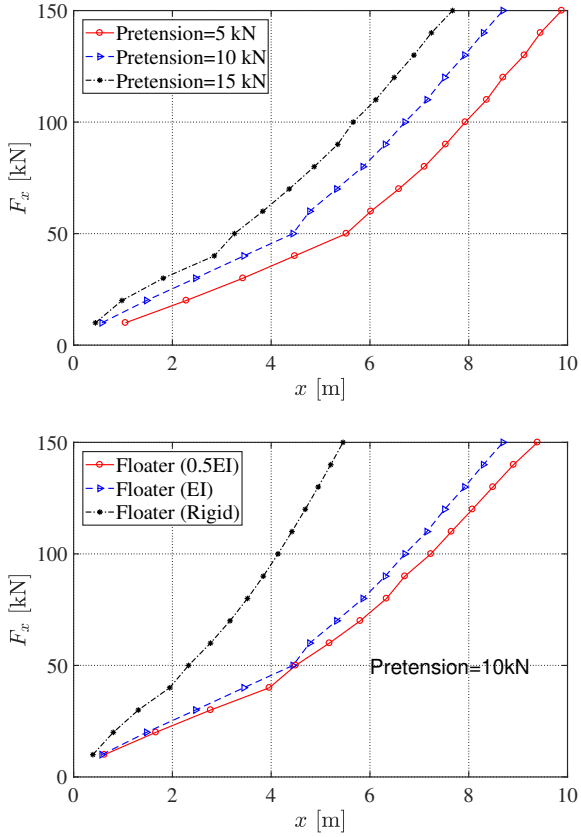

Figure 5.10: The equivalent stiffness k_f of the fish farm without well boat is represented by the slope of the curve F_x. Upper: with different pretension forces in the anchor lines. Lower: with different floating collar stiffnesses. $EI = 7.27 \times 10^6$ Nm^2 is the cross-sectional bending stiffness of the floating collar in the horizontal plane with E the Young's modulus (high-density polyethylene) and I the area moment of the cross-section with two tubes.

three different values of the contact stiffness, i.e. k_c = 400 kN/m, 4000 kN/m and 40000 kN/m, are shown in Figure 5.11. Regular waves in the x_E direction and set-up A are considered in the analysis. By using regular waves, we can analyze the influence of the contact stiffness on both the mean value and oscillation amplitude of the anchor force. The mean value is relevant for the study in current while the oscillation amplitude is important for the investigation of the coupled system in irregular waves examined in Section 5.3. From the figure, larger high-frequency oscillations are observed when larger contact stiffness is adopted, which is reasonable. However, for the anchor force, relatively small difference is observed for the three examined values of the contact stiffness. This indicates that we can have a reasonable prediction of the global response of the coupled system as long

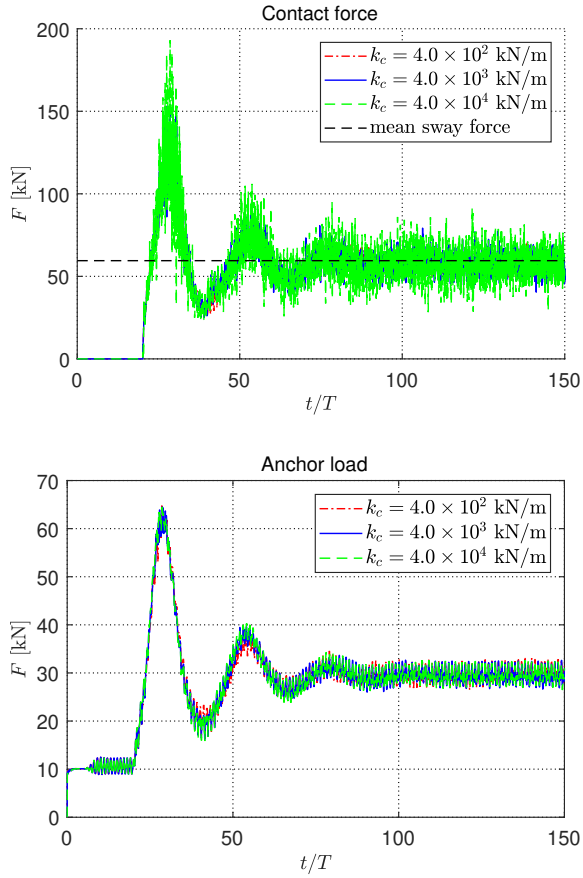

Figure 5.11: Time histories, during transient and steady-state phases, of the well boat-floating collar contact force (upper) and of the loads in anchor line-1 (lower) in beam-sea regular waves, i.e. along x_E-axis when set-up A is used, with wave period $T = 6$ s and wave height-to-wavelength ratio $H/\lambda = 1/60$. Three different contact stiffnesses k_c are considered.

as a reasonably high contact stiffness is assumed, while locally the contact force may be more sensitive to the actual stiffness. The time histories of the loads in anchor line-1 show that the total anchor load comprises two components: (1) wave frequency component that oscillates with the incident wave period and (2) slowly varying decaying component that oscillates with the natural period ≈ 150 s of the coupled fish farm-well boat system. The slowly varying resonant oscillation may be excited by nonlinear wave loads when the coupled system is exposed to irregular waves and can significantly increase the mooring loads and floating collar stresses. More discussions for the coupled system in irregular waves can be found in Section 5.3.

An alternative method (named direct method) to estimate the contact force is

given by Shen et al. (2016) and is just briefly mentioned here for completeness. The essence of this method is that the contact force is estimated directly by satisfying the condition that the floater and the boat share the same normal velocity at a given contact point. The method is physically sound, but difficult to implement in actual scenario. For a simplified coupled system in waves, numerical results show that the two contact methods give the same contact forces and mooring forces if sufficiently high contact stiffness k_c is used in the above introduced indirect method, see Appendix C.

In general when contact happens, also a tangential force F_s will act on the ship, directed to the opposite direction of the relative tangential velocity between the well boat and the floating collar and estimated as $F_s = \mu F_c$, with μ the frictional coefficient between the well boat (steel) and the floating collar (high-density polyethylene). According to the experimental results from Dhouibi et al. (2013), the frictional coefficient μ is in the range $\mu = 0.09 - 0.15$. $\mu = 0.12$ will be used in numerical simulations.

5.3 Theory and numerical model: in long-crested irregular waves and current

The modeling of the coupled well boat-fish farm system in current has been documented in Section 5.2. There, the modeling of the well boat in current and the strategy used for the well boat-fish farm coupling was explained. In this section, we will mainly deal with the modeling of the coupled system in long-crested irregular waves and current. For the fish-farm system in irregular waves, the numerical modeling was introduced in Chapter 4 and is not repeated here. In terms of the well-boat response, apart from the first-order wave-induced motions, the slow-drift resonant oscillations of the well boat may also be excited by non-linear interaction effects between incident waves and body motions.

The well boat can be moored in different positions relative to the fish farm, as shown in Figure 5.3. Assuming a scenario with main inflow direction along positive x_E-axis, two well-boat set-ups are modeled in this section, i.e. set-up A: with the well boat at the weather side of the floating collar and set-up C: with the well-boat bow against the inflow. The coupled system with set-up A is expected to be more critical in terms of mooring loads and floating collar stresses and will be our research focus in the next chapter. Results for set-up C will be considered in selected cases, for comparison.

Irregular long-crested waves and current in positive x_E direction are assumed in the analysis. The modeling of the irregular waves is described in section 5.3.1. For the coupled system with set-up A (see Figure 5.3) with the well boat placed at the weather side of the fish farm, the slow-drift surge motion and yaw motion of the well boat are expected to be small and therefore neglected, i.e. only the slow-drift sway motion is considered. Detailed explanation of how to estimate the motion is provided in section 5.3.2. For the coupled system with set-up C (see Figure 5.3), the slow-drift sway and yaw motions are expected to be far less important than the slow-drift surge motion, so we will only consider the slow-drift surge motion in

the simulations and its modeling is briefly discussed in Section 5.3.3.

5.3.1 Irregular waves

The Norwegian standard for design of aquaculture fish farms operating in the sea (NS9415, 2009) requires that the JONSWAP spectrum with $\gamma = 2.5$ for wind-generated seas shall be used for calculations of response in irregular waves, where γ is the spectral peakedness parameter. As an example, Figure 5.12 provides the wave spectra for two sea states that will be investigated in the numerical simulations in next chapter. They are with $H_s = 2$ m and $T_p = 6$ s, and with $H_s = 1$ m and $T_p = 5$ s, corresponding to moderate exposure and to heavy exposure sea conditions (see Table 1.2), respectively.

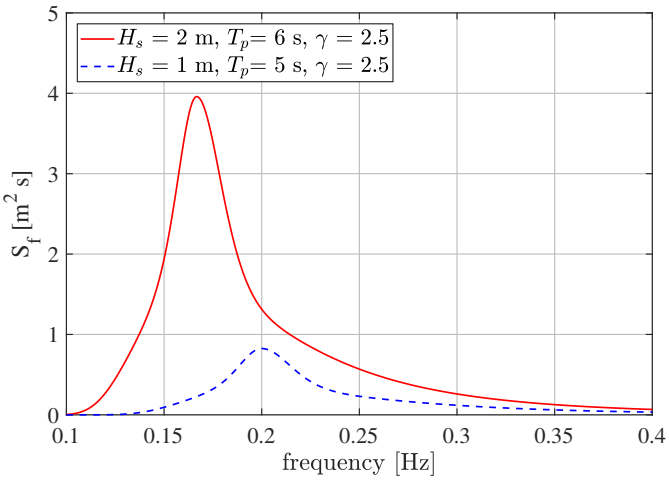

Figure 5.12: JONSWAP wave spectrum as a function of wave frequency. Solid line: significant wave height $H_s = 2$ m and peak period $T_p = 6$ s. Dashed line: $H_s = 1$ m and $T_p = 5$ s.

The definition of the JONSWAP wave spectrum and detailed procedure to generate the long-crested irregular waves were given in Chapter 4. Here only the main information on the numerical strategy for estimating the well-boat slow-drift motions is provided. In particular, when generating the incident irregular waves, the frequency is evenly distributed into N_f components between $f_{\min} = 0.7/T_p$ and $f_{\max} = 2.0/T_p$ with the length of each interval $\Delta f = (f_{\max} - f_{\min})/N_f$. Here $f_{\min}$ and $f_{\max}$ are the minimum and maximum frequency in Hz of the range where the wave spectrum has energy. The selection of the number of wave components N_f requires some care. We must require that Δf is a small fraction of the smallest natural frequency f_n of the relevant slow-drift response in order to model numerically wave components with frequency sufficiently close to f_n and, therefore, able to excite a resonance condition. In the simulations, $N_f = 500$ is used. Within each frequency interval, a frequency value f_i is randomly selected and, there, the wave

spectrum is evaluated, i.e. $S(f_i)$. The random selection of frequencies avoids that the incident-wave time history shows a periodic behavior.

5.3.2 Coupled well boat-fish farm system in set-up A

In this section, we will focus on the modeling of the coupled system in set-up A. Special attention is paid to the modeling of the slow-drift sway motion of the well boat. The governing equation of the sway motion is introduced at first by solving the first-order motion and the slow-drift motion simultaneously. The modelings of the slow-drift excitation force and slow-drift damping are introduced. The damping terms may include eddy-making damping and wave-drift damping. The coupling between the well boat and the fish farm is also included.

To reduce complexity and for validation purpose, a simplified model of the coupled system is also proposed, with the fish farm represented by a linear spring and neglecting the influence of the first-order motion. The damping from the fish farm is also neglected, as it is not straightforward to be incorporated in a simple way. In this way, frequency-domain solutions for the slow-drift sway motion can be obtained, using a technique to linearize the eddy-making damping.

Well-boat sway-motion equation

By neglecting the coupling with other rigid-body motions, the sway motion of the well boat η_2 in beam-sea irregular waves and collinear current with speed U_∞ can be described by the following one-degree-of-freedom equation

$$\begin{aligned}&\left[M + A_{22}\left(\infty\right)\right]\ddot{\eta}_2 + \int_0^t K_{22}\left(\tau\right)\dot{\eta}_2\left(t-\tau\right)d\tau + B_{22}^{SD}\dot{\eta}_2 \\ &+ B_D\left(\dot{\eta}_2 - u_w - U_\infty\right)\left|\dot{\eta}_2 - u_w - U_\infty\right| = F_2^{Excit} + F_2^{Ext}\end{aligned} \tag{5.5}$$

Here $\ddot{\eta}_2 = d^2\eta_2/dt^2$, $\dot{\eta}_2 = d\eta_2/dt$ and F_2^{Excit} are the acceleration, velocity and excitation force in sway, including both the first-order and slow-drift components. M is the mass of the well boat. $A_{22}\left(\infty\right)$ and K_{22} are the infinite-frequency added mass and the retardation function in sway, respectively. B_{22}^{SD} is the wave-drift damping in sway. B_D is the quadratic damping coefficient connected with the eddy-making damping and can be expressed as $0.5\rho C_D A_Y$ with ρ the water density, A_Y the projected area of the submerged hull in the direction of the sway motion and C_D the corresponding ship averaged drag coefficient. u_w is the transverse component of incident-wave velocity, estimated at $0.5D$ below the mean free surface, with D the mean draft of the well boat. F_2^{Ext} contains possible external forces in sway due to coupling with the fish farm, which may include contact force and connection-line forces. The reason to solve the first-order motion and slow-drift motion simultaneously is because the first-order velocity may matter when evaluating the eddy-making damping. This effect will be examined in the next chapter.

The first-order excitation force is calculated by the linear potential-flow solver WAMIT. The evaluation of the external forces from the fish farm has been given

in Section 5.2.2. In the following, we will explain how to find the remaining terms introduced in Eq. (5.5), i.e. slow-drift excitation force (F_2^{SV}), wave-drift damping (B_{22}^{SD}) and eddy-making damping (B_D).

Slow-drift excitation force

The slow-drift excitation loads are generally much lower than linear wave loads, but relatively large slow-drift response amplitudes may occur if resonance is excited and the slow-drift damping, involving wave-drift and eddy-making damping in our application, is small. Slow-drift excitation loads can be explained in a similar way as mean wave loads, detailed derivation process can be found in Faltinsen (1990), here we will just recall the main formulas for sway motion. In general, such loads are caused by the interaction of a body with irregular long-crested waves. If we can split the incident waves in N regular-wave components, a generic slow-drift second-order load oscillates with a circular frequency μ equal to the difference of two incident-wave frequencies, i.e. $\mu = \omega_k - \omega_j$ $(k, j = 1, .., N)$. In particular, the slow-drift second-order force in sway F_2^{SV} can be formally written as

$$F_2^{SV} = \sum_{j=1}^{N}\sum_{k=1}^{N} A_j A_k \left\{ \begin{array}{c} T_{jk}^{2c} \cos\left[(\omega_k - \omega_j)\, t + (\varepsilon_k - \varepsilon_j)\right] \\ + \\ T_{jk}^{2s} \sin\left[(\omega_k - \omega_j)\, t + (\varepsilon_k - \varepsilon_j)\right] \end{array} \right\} \tag{5.6}$$

Here A_k, ω_k and ε_k and A_j, ω_j and ε_j, are the amplitude, circular frequency and random-phase angle for wave k and wave j, respectively. The coefficients T_{jk}^{2s} and T_{jk}^{2c} are second-order transfer functions of the cosine and sine contribution to the force, respectively. By their definition in eq. Eq. (5.6), they are independent of the wave amplitudes A_j and A_k, but a function of wave frequency ω_j and ω_k, as well as of the heading angle of the waves and of the body geometry. One should note that Eq. (5.6) includes also the mean loads associated with the wave-body interaction. An approximate way to calculate F_2^{SV} is to use the Newman's approximation (Newman, 1974), which implies that

$$\begin{aligned} T_{jk}^{2c} &= T_{kj}^{2c} = 0.5\left(T_{jj}^{2c} + T_{kk}^{2c}\right) \\ T_{jk}^{2s} &= T_{kj}^{2s} = 0 \end{aligned} \tag{5.7}$$

The approximation is less good if T_{jk}^{2c} shows maxima or minima in the vicinity of the line $\omega_j = \omega_k$, or if the natural period of the studied body motion is not sufficiently large, or in shallow-water conditions, but neither of these cases should occur in the present study. The direct calculation of Eq. (5.6), including approximation Eq. (5.7), is still time consuming. Newman (1974) proposed to approximate Eq. (5.6) further by substituting the double summation with the square of a single series. This can be done by adding high-frequency terms that have no physical meaning but do not excite any relevant response if body resonance conditions are in the low-frequency range. The simplified expression of the slow-drift force is given as

$$F_2^{SV} = 2\left[\sum_{j=1}^{N} A_j \sqrt{T_{jj}^{2c}} \cos\left(\omega_j t + \varepsilon_j\right)\right]^2 \tag{5.8}$$

According to Pinkster (1975), the spectral density for the low-frequency part of the force, i.e. not including the mean-drift force, can be expressed in terms of the wave spectrum as

$$S_F(\mu) = 8 \int_0^\infty S(\omega) S(\omega + \mu) \left[\frac{\bar{F}_2(\omega + \mu/2)}{\zeta_a^2} \right]^2 d\omega \tag{5.9}$$

where S is the incident wave spectrum, $\bar{F}_2$ is the mean wave load in sway for frequency $\omega + \mu/2$.

Wave-drift damping

The wave-drift damping for the horizontal motions of a structure is connected with the structure's ability to generate waves and is a potential flow effect that neglects interaction with flow separation. In fact, this damping is caused by second-order effects in the wave-body interactions and therefore is proportional to the square of the incident-wave amplitude. However it is a linear damping load in terms of the body slowly-varying speed. The presence of the wave-drift damping can be seen by comparing free decay model tests in surge or sway of a large-volume structure in still water and in regular waves. The wave-drift damping in surge or sway can be explained by interpreting the slow-drift surge or sway speed, caused by the wave-body interaction, as a quasi-steady forward and backward speed of the structure (Zhao and Faltinsen, 1988). This "steady" speed can for an observer on the structure be interpreted as an incident steady flow, i.e. a fictitious current with equal and opposite speed, say U_∞. The interaction with the body causes a mean force in the inflow direction that depends on U_∞. For the slowly oscillating body, this force acts as a damping and to a leading order is linearly dependent on U_∞. For example, in case of slowly varying motion in sway, the wave-drift damping coefficient is therefore $B_{22}^{WD} = \frac{\partial \overline{F_2}}{\partial U_\infty}\Big|_{U_\infty=0}$, with $\bar{F}_2$ the mean-wave force in sway direction, and assuming implicitly that the body interacts only with waves, i.e., without a real current. Within this approach, to estimate B_{22}^{WD}, the dependence on U_∞ of the $\bar{F}_2$ experienced by the body must be estimated. In particular, this can be done by examining the structure in regular waves without current and with current (1) in the same and (2) in opposite direction of the incident waves, and then using the approach by Zhao and Faltinsen (1988) to approximate $\frac{\partial \overline{F_2}}{\partial U_\infty}\Big|_{U_\infty=0}$.

Left plot of Figure 5.13 presents the effect of a current on the mean sway force on the well boat. Regular beam sea waves and three different current velocities are considered with U_∞ = -0.5 m/s, 0 m/s and 0.5 m/s. The positive current is in the wave direction. The potential-flow solver HydroStar (BureauVeritas, 2016) is adopted to estimate the mean-wave loads, considering the wave-current interaction and neglecting the flow separation. The results indicate that, for the well boat in beam sea, a current in the wave direction will significantly increase the mean sway force, especially for cases in short waves. In the HydroStar formulation, only the first-order term in the parameter $\tau = U_\infty \omega_e / g$, being $\omega_e = \omega + kU_\infty$ the encounter frequency with ω the incident wave frequency and $k = \omega^2/g$ the wave number, is

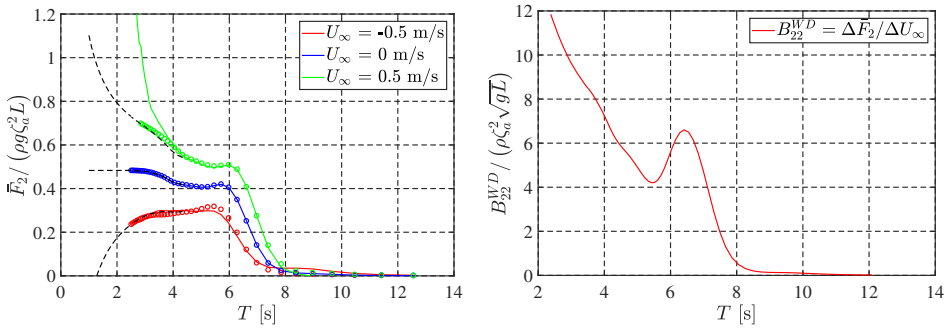

Figure 5.13: Left: the effect of current on the mean sway force based on potential flow. From the lowest to the highest curve: U_∞= -0.5 m/s to 0.5 m/s. $\bar{F}_2$ is the mean sway force, ξ_a the wave amplitude, ρ the water density, g the gravity acceleration, L the boat length. Solid lines: results from the potential-flow solver HydroStar considering wave-current interactions. Empty circles: results according to formula from Aranha (1994). Dashed lines: results from our simplified analysis by the direct pressure-integration method. Right: wave-drift damping B_{22}^{WD} as a function of wave period T.

kept in the simplified free-surface boundary condition when considering the wave-current interactions. It means that the results in Figure 5.13 are reliable for small τ. So for very short waves ($T = 2\pi/\omega \leq 4$ s), the results from HydroStar are questionable. In order to characterize the effect of current in high wave frequency, we examined also the results based on the formula proposed by Aranha (1994). This formula is commonly used in engineering practice and there are some disputes about its accuracy. According to Aranha (1994), the mean sway force is influenced by the current velocity as

$$\bar{F}_2(\omega, U_\infty) = \bar{F}_2(\omega_e)(1 + 4U_\infty\omega/g) \tag{5.10}$$

This expression is formally similar to that given in the short wavelength asymptotic theory by Faltinsen et al. (1980). The results based on Eq. (5.10) are also shown in Figure 5.13. From the figure, reasonable agreement is observed between them and those from HydroStar for wave period $T \geq 4$ s. We also carried out a simplified analysis by using the direct pressure integration method for cases with very high frequency, i.e. $\omega \to \infty$, see Appendix D. It is assumed that the waterline of the well boat near the free surface acts like a vertical wall and that the incoming wave is totally reflected. For the effect of current, only the encounter frequency effect is considered, then we can obtain similar formula as that from Aranha (1994) and given as

$$\bar{F}_2(\omega, U_\infty) = \bar{F}_2(\omega)(1 + 4U_\infty\omega/g) \tag{5.11}$$

It should be noted that only the incident wave frequency ω is involved in this formula. Since the applicability of the formula is for very high wave frequency, the difference between ω and ω_e is expected to be small, so the mean wave load predicted, respectively, by Eq. (5.10) and Eq. (5.11) should be similar. The

obtained results according to Eq. (5.11) are also shown in the left plot of Figure 5.13 and indicate a consistency with the formula by Aranha for small values of incident-wave periods. Therefore, the HydroStar's predictions of the mean-drift force in sway have been substituted by the Aranha's formula for T <4 s. The resulting mean-drift force in sway was used to estimate the wave-drift damping presented in non-dimensional form in the right plot of Figure 5.13.

$B_{22}^{WD}(\omega)/\zeta_a^2$ represents the second-order transfer function of the mean wave-drift damping and can be used to estimate the mean wave-drift damping $\bar{B}_{22}^{SD}$ in irregular long-crested waves as follows

$$\bar{B}_{22}^{SD} = 2\int_0^\infty S(\omega)\left(\frac{B_{22}^{WD}(\omega)}{\zeta_a^2}\right)d\omega \tag{5.12}$$

Faltinsen and Zhao (1989) argued that there also ought to be a slowly-varying wave-drift damping if there is a slowly-varying excitation force. It can be expressed in a similar way as the slow-drift excitation force and reads

$$B_{22}^{SD} = \sum_{j=1}^{N}\sum_{k=1}^{N} A_j A_k \frac{\partial}{\partial U}\left\{\begin{array}{c} T_{jk}^{2c}\cos\left[\left(\omega_k-\omega_j\right)t+\left(\varepsilon_k-\varepsilon_j\right)\right] \\ + \\ T_{jk}^{2s}\sin\left[\left(\omega_k-\omega_j\right)t+\left(\varepsilon_k-\varepsilon_j\right)\right] \end{array}\right\}_{U=0} \tag{5.13}$$

The formula can be further simplified in a similar way as for the slow-drift excitation force shown in Eq. (5.8) to increase computational efficiency.

Eddy-making damping

Eddy-making damping is usually also important for the estimation of slow-drift sway motion. Here, this is calculated by strip theory assuming valid the cross-flow principle. In order to have a reliable prediction of its value, we need a reliable estimation of the drag coefficient at the different ship cross-sections. Detailed procedures to estimate the cross-sectional drag coefficients for cases in oscillatory flow only and in combined oscillatory flow and current are presented in the following. The oscillatory flow is mono-chromatic and associated with the natural sway period. The 3D flow effects are also accounted for and estimated by using a reduction factor in a similar way as it was done in estimating transverse current forces in Section 5.2.1.

Cross-sectional drag coefficient in oscillatory flow

Faltinsen (1990) showed that the cross-flow drag coefficient for ship cross-sections in mono-chromatic oscillatory flow depends on the section geometry (beam-to-draft ratio, bilge radius, bilge keel presence and dimensions), the Keulegan-Carpenter number KC=$U_M T/D$ (with U_M = amplitude of oscillatory relative velocity between the body and the ambient flow, T = oscillatory period, D = sectional draft), the free-surface and three-dimensional (3D) effects. A brief explanation of the different parameters will be given in the following.

Free surface: For the slow-drift oscillation in sway, relevant characteristic KC number is expected to be less than 10. Then the free surface will have little influence on the drag coefficient, according to Faltinsen (1990).

Cross-sectional shape: The effect of the cross-sectional shape on the drag coefficient for typical midship sections is mainly due to the bilge radius r, beam-to-draft ratio B/D and bilge keels. Increasing the bilge radius means decreasing the drag coefficient. The beam-to-draft ratio will have influence, but only when $B/(2D) < 1$. In terms of the bilge keels, the drag coefficient depends strongly on the bilge-keel breadth.

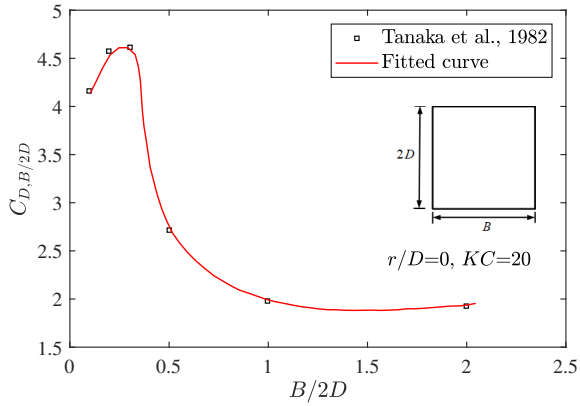

Figure 5.14: Drag coefficient C_D as a function of aspect ratio $B/2D$ for a rectangular cylinder with sharp corners at KC = 20 (Tanaka et al., 1982).

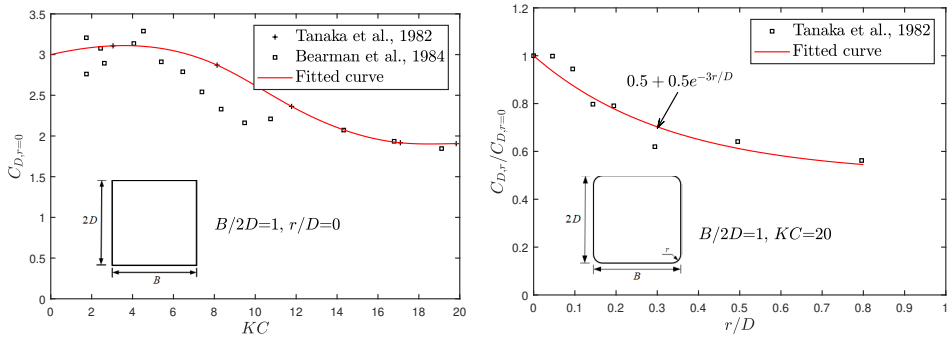

Figure 5.15: Left: drag coefficient C_D as a function of KC for a sharp-edged square cylinder from Tanaka et al. (1982) and Bearman et al. (1984). Right: drag coefficient C_D as a function of r/D at KC = 20. Experimental results are from Tanaka et al. (1982). The fitted curves are used in present analysis.

For a rectangular cross-section, the drag coefficient will be obtained by adjusting the value for a sharp-edged square cross-section, considering the influence of aspect

ratio and bilge radius. The reason is that relevant information of the drag coefficient for a square cross-section is more readily available. Detailed procedure used here is explained below. The dependence of the drag coefficient C_D on the aspect ratio $B/(2D)$ for a sharp-edged rectangular cross-section at KC = 20 is shown in Figure 5.14 (see Tanaka et al., 1982). The dependence is assumed to be applicable also for KC¡ 20. If the drag coefficient for a square section is known, then the value for a general rectangular section can be obtained, considering the aspect ratio influence. So our main attention is paid to the estimation of C_D for a square section.

The drag coefficient $C_{D,r=0}$ for a sharp-edged square section as a function of KC number is shown in the left plot of Figure 5.15 (see Tanaka et al., 1982 and Bearman et al., 1984). A fitted curve of the experimental data is also provided in the figure and will be used in the analysis. On the other hand, experimental results by Tanaka et al. (1982) show that there is a strong effect of the bilge radius on the drag coefficient, see the right plot of Figure 5.15. Similarly as shown in Eq. (5.3) for a section in steady flow, a best fit of these experimental data is estimated, giving

$$C_{D,r}/C_{D,r=0}|_{\mathrm{KC}=20} = 0.5 + 0.5e^{-3r/D}. \tag{5.14}$$

The examined KC is 20, but the bilge-radius influence on the C_D is assumed applicable also for KC< 20, as we do not have, to author's knowledge, experiments for KC lower than 20. This is an error source in the numerical results. This means that $C_{D,r}$ for a given KC can be evaluated by

$$C_{D,r} = C_{D,r=0} \cdot (0.5 + 0.5e^{-3r/D}) \tag{5.15}$$

with $C_{D,r=0}$ given by the fitted curve in the left plot of Figure 5.15 as a function of KC number. Once $C_{D,r}$ for a square section is obtained, by accounting for the influence of aspect ratio $B/(2D)$, the drag coefficient C_D for a generic rectangular section at different KC numbers can be estimated by

$$C_D = C_{D,r} \cdot C_{D,(B/2D)}/C_{D,(B/2D=1)} \tag{5.16}$$

with $C_{D,B/2D}$ provided by the fitted curve in Figure 5.14.

Next, we will show how the drag coefficients for different cross-sections of the well boat are predicted. For the ship sections without bilge keels and with geometry close to a rectangle (sections 4-6, 14-18, see Figure 5.2), the same procedure as the one described for a rectangular cross-section has been followed. For sections with bilge keels (sections 7-13), the above introduced procedure cannot be applied, as the drag coefficient depends strongly on the breadth of the bilge keels. Instead, we estimate the drag coefficient based on the experimental data from Faltinsen and Sortland (1987). In these experiments, $B/(2D) = 1.35$, $r/D = 0.22$ and three bilge-keel breadth-to-draft ratio $b/D = 0$, 0.03 and 0.06 were examined. In our case, for the considered well-boat sections, $B/(2D) = 1.12$, $r/D = 0.15 - 0.23$ and $b/D = 0.0448$. The drag coefficient is expected to be mainly determined by the parameter b/D, so its value can be obtained through interpolating the experimental data in terms of b/D, see Figure 5.16. There are differences of $B/(2D)$ and r/D between the well-boat sections with bilge keels and the sections studied experimentally and

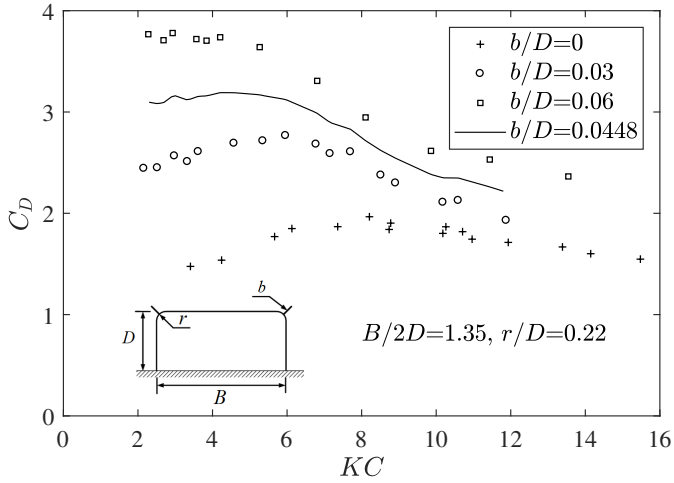

Figure 5.16: The effect of bilge keels on the drag coefficient C_D at small KC numbers. Symbols: experimental data from Faltinsen and Sortland (1987). Solid curve: interpolated value for the cross-section of the well boat equipped with bilge keels.

given in the figure, but their effect is expected to be small, based on the results shown in Figures 5.14 and 5.15.

The well-boat sections near the ship ends (section 1-3, 19-20, see Figure 5.2) present shapes not studied experimentally or numerically. A rough estimation of their drag coefficients has been obtained by assuming that the flow around one of these cross-sections resembles that around a flat plate and C_D= 8.0 $\mathrm{KC}^{-1/3}$ is assumed for small KC, as documented in Faltinsen (1990). The reasons to apply C_D for a flat plate to these sections are: (1) the drag coefficients for these sections in steady flow are close to that for a flat plate (2) some of these sections are characterized with small beam-to-draft ratio. This is an error source but has a limited influence on the average drag coefficient for the well boat, as explained in Section 5.2.1. Similarly as shown in Section 5.2.1 in steady flow, the 2D drag coefficient for different sections needs to be lowered as consequence of three-dimensional (3D) effects and the same reduction factor as the one for steady flow is adopted here because no study on 3D effects for oscillatory flow is available in literature.

Figure 5.17 shows the estimated drag coefficients for different sections of the well boat at KC=8 (left plot) and KC=4 (right plot). From the figure, the ship averaged drag coefficients are about 2.2 and 2.5 for KC=8 and KC=4, respectively, which indicates that the average drag coefficient is not so sensitive to the change of KC number, in the KC range relevant for our application. In order to assess the method proposed here, we applied it to estimate the average transverse drag coefficient for a ship for which experimental data are available in Faltinsen et al. (1986). The results are shown in Figure 5.18. From them, the empirically estimated average drag coefficients agree well with the experimental data at different KC numbers.

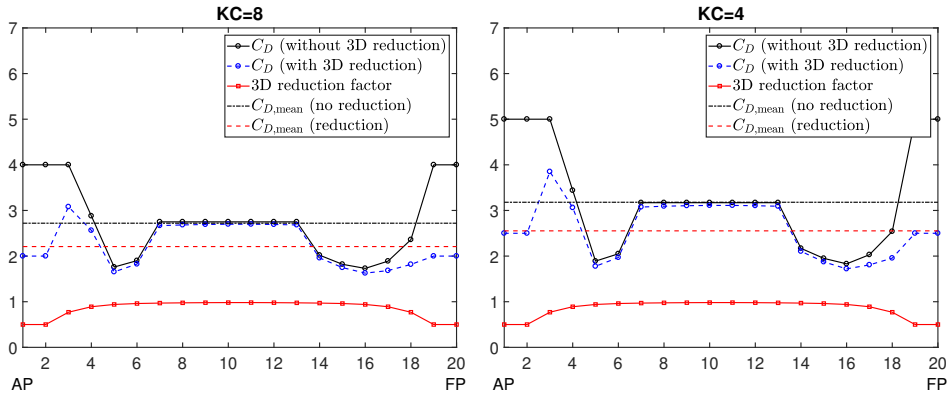

Figure 5.17: Sectional transverse drag coefficient $C_D(x)$ for different sections of the examined well boat. Left: KC=8. Right: KC=4. The 2D drag coefficients with and without the 3D reduction effects are shown. The corresponding ship averaged drag coefficients are also given.

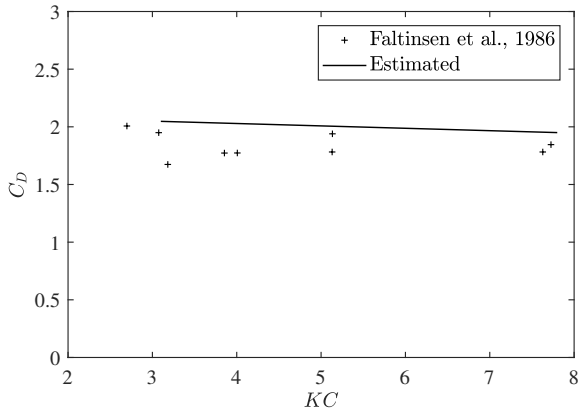

Figure 5.18: Drag coefficient for slow-drift sway motion of the well boat as a function of KC number. Symbols: experimental data from Faltinsen et al. (1986). Solid line: drag coefficient estimated with the empirical approach proposed here.

This suggests a fair reliability of the approach proposed for the C_D prediction in oscillatory flow.

Cross-sectional drag coefficient in combined oscillatory flow and current

Current may have an important effect on the eddy-making damping and its influence on wave-drift damping and slow-drift excitation force should also be considered. Sarpkaya and Storm (1985) conducted experiments with circular cylinders moving with constant velocity in a sinusoidally oscillating flow to determine the drag and inertial coefficients and found that, in general, the drag and inertia

coefficients obtained for coexisting waves and current (both when following the waves and when in opposite direction) were found to be much smaller than the drag and inertia coefficients derived in waves alone for small KC number. They pointed out that the force coefficients were governed by Keulegan-Carpenter number KC=$U_M T/D$, Reynolds number Rn=$U_M D/\nu$, alternatively expressed by their ratio β=Rn/KC=$D^2/\nu T$, and by the reduced velocity VK=$U_\infty T/D$. Here the involved parameters are defined as above in this section and ν is the kinematic viscosity coefficient of water.

Hamel-Derouich (1993) carried out experiments for smooth sharp-edged rectangular cylinders. The cylinders were horizontally submerged and tested in wavy flow and in combined steady and wavy flows, corresponding to low KC numbers up to a value of 8. Three different reduced velocities were considered, i.e., VK=8, 12, 16. The experiments showed that the drag coefficient measured in conditions without current overestimated the measured wave-current induced non-dimensional forces and the drag coefficient under combined waves and current was quite close to the value in steady flow and was less KC-number dependent, especially for larger reduced velocity. The phenomenon can be explained by the fact that when $U_c/U_M > 1$, the returning vorticity due to the oscillatory part of the flow has a small influence on the inflow velocity to the body, so the influence of KC on C_D is small. In the present analysis, $U_c/U_M \geq 1$ for the cases relevant for determining the operational conditions of the well boat. Therefore, the drag coefficient for steady flow will be adopted for cases with waves and current. A sensitivity analysis will be performed to investigate the influence of the variation of the drag coefficient.

Slow-drift sway motion of the well boat with simplified fish-farm coupling

To better explain and verify the numerical modeling of the slow-drift sway motion of the well boat, a simpler model is proposed. In this case, the loads in sway from the fish-farm system are simplified as a linear spring, neglecting the damping due to the net cage and the mooring lines. Moreover the influence of the first-order response is neglected when formulating the eddy-making damping. Then the slow-drift sway motion $\eta_2^{(2)}$ of the well boat can be described by the following equation

$$\left[M + A_{22}\left(0\right)\right]\ddot{\eta}_2^{(2)} + B_{22}^{SD}\dot{\eta}_2^{(2)} + B_D\left(\dot{\eta}_2^{(2)} - U_\infty\right)\left|\dot{\eta}_2^{(2)} - U_\infty\right| + C_{22}\eta_2^{(2)} = F_2^{SV} \tag{5.17}$$

where $\ddot{\eta}_2^{(2)} = d^2\eta_2^{(2)}/dt^2$ and $\dot{\eta}_2^{(2)} = d\eta_2^{(2)}/dt$ are the slow-drift acceleration and velocity in sway, $A_{22}(0)$ is the zero frequency added mass in sway, F_2^{SV} is the slow-drift excitation force (including mean value) in sway, C_{22} is the equivalent restoring stiffness from the fish farm including the mooring-line and the floating-collar effects.

If only the mean value and the standard deviation of the sway response are targeted, the time-varying feature of the wave-drift damping can be neglected (see e.g. Faltinsen, 1990). It means that only the mean wave-drift damping can be considered, i.e. $B_{22}^{SD} \approx \bar{B}_{22}^{SD}$. If then the nonlinear eddy-making damping is approximated with an equivalent linear damping, Eq. (5.17) can be solved in the frequency domain. Relative to a time-domain solution, this is a very robust and

time-efficient way to obtain the mean value and standard deviation of the motion. In particular, the nonlinear eddy-making damping term is linearized through an equivalent stochastic linearization, see Price and Bishop (1974) and Roberts and Spanos (2003). By assuming a Gaussian response, which is not strictly true, we can obtain an equivalent linear damping coefficient, in the form

$$B_{22}^{e} = B_D \left[\frac{4}{\sqrt{2\pi}} \sigma_{\dot{\eta}_2^{(2)}} \exp\left(-0.5 U_\infty^2 / \sigma_{\dot{\eta}_2^{(2)}}^2 \right) + 2 U_\infty \Phi \left(\frac{U_\infty}{\sqrt{2}\sigma_{\dot{\eta}_2^{(2)}}} \right) \right] \tag{5.18}$$

where $\sigma_{\dot{\eta}_2^{(2)}}$ is the standard deviation of the slow-drift sway velocity and Φ is the error function

$$\Phi = \frac{2}{\sqrt{\pi}} \int_0^x e^{-t^2} dt \tag{5.19}$$

We can approximate $\sigma_{\dot{\eta}_2^{(2)}}$ as $\mu_n \sigma_{\eta_2^{(2)}}$, where $\sigma_{\eta_2^{(2)}}$ is the standard deviation of slow-drift sway motion and $\mu_n = \sqrt{C_{22} / \left[M + A_{22}(0) \right]}$ is the natural undamped circular frequency in sway. For zero current velocity, i.e. $U_\infty = 0$ m/s, $B_{22}^{e} = 4 B_D \sigma_{\dot{\eta}_2^{(2)}} / \sqrt{2\pi}$. This is consistent with the expression documented in Faltinsen (1990). Eq. (5.17) can then be written as

$$\left[M + A_{22}(0) \right] \ddot{\eta}_2^{(2)} + B_{22} \dot{\eta}_2^{(2)} + C_{22} \eta_2^{(2)} = F_2^{SV} \tag{5.20}$$

with $B_{22} = \left(\bar{B}_{22}^{SD} + B_{22}^{e} \right)$ the sum of mean wave-drift and linearized eddy-making damping coefficients. The variance of $\eta_2^{(2)}$ can be written as (see e.g. Faltinsen, 1990)

$$\sigma_{\eta_2^{(2)}}^2 = \int_0^\infty \frac{S_F(\mu)\, d\mu}{\left\{ C_{22} - \left[M + A_{22}(0) \right] \mu^2 \right\}^2 + B_{22}^2 \mu^2} \tag{5.21}$$

Here S_F is the spectral density for the slow-drift excitation force, B_{22} is also a function of $\sigma_{\eta_2^{(2)}}$, so the unknown $\sigma_{\eta_2^{(2)}}$ is on both the left- and right-hand side of Eq. (5.21) and iteration is needed to obtain $\sigma_{\eta_2^{(2)}}$.

If the damping B_{22} is small, the major contribution to the variance comes from the resonance, then $S_F(\mu)$ can be approximated as $S_F(\mu_n)$ and set outside the integral. By small damping, we mean small relative to the critical damping $2\left[M + A_{22}(0) \right] \mu_n$. It follows that

$$\sigma_{\eta_2^{(2)}} = \sqrt{\frac{S_F(\mu_n)\, \pi}{2 C_{22} B_{22}}} \tag{5.22}$$

If the mean wave-drift damping $\bar{B}_{22}^{SD}$ is not considered and the current velocity is zero, then $B_{22} = B_{22}^{e} = 4 B_D \sigma_{\dot{\eta}_2^{(2)}} / \sqrt{2\pi} \approx 4 B_D \mu_n \sigma_{\eta_2^{(2)}} / \sqrt{2\pi}$. $\sigma_{\eta_2^{(2)}}$ from Eq. (5.22) can then be expressed as

$$\sigma_{\eta_2^{(2)}} = \left[\frac{S_F(\mu_n)\, \pi \sqrt{2\pi}}{4 \mu_n C_{22} \rho A C_D} \right]^{1/3} \tag{5.23}$$

This equation shows that $\sigma_{\eta_2^{(2)}}$ is proportional to $C_D^{-1/3}$. This implies low sensitivity between $\sigma_{\eta_2^{(2)}}$ and C_D.

5.3.3 Coupled well boat-fish farm system with set-up C

In set-up C, the slow-drift surge motion of the well boat is excited and needs to be estimated. By neglecting the coupling with other rigid-body motions, the surge motion η_1 of the well boat in head-sea irregular waves and collinear current with speed U_∞ can be described by the following equation

$$\begin{aligned}&[M + A_{11}(\infty)]\,\ddot{\eta}_1 + \int_0^t K_{11}(\tau)\,\dot{\eta}_1(t-\tau)\,d\tau + B_{11}^{SD}\dot{\eta}_1 \\ &+ C_X(\dot{\eta}_1 - u_u - U_\infty)\,|\dot{\eta}_1 - u_u - U_\infty| = F_1^{Excit} + F_1^{Ext}\end{aligned} \tag{5.24}$$

Here $\ddot{\eta}_1 = d^2\eta_1/dt^2$, $\dot{\eta}_1 = d\eta_1/dt$ and F_1^{Excit} are the acceleration, velocity and excitation force in surge, including both the first-order and slow-drift components. $A_{11}(\infty)$ and K_{11} are the infinite-frequency added mass and the retardation function in surge, respectively. B_{11}^{SD} is the wave-drift damping in surge. C_X is the quadratic damping coefficient. u_u is the longitudinal component of incident-wave velocity, estimated at $0.5D$ below the mean free surface, with D the mean draft at the middle section of the well boat. F_1^{Ext} contains possible external forces in surge due to coupling with the fish farm, which may include contact force and connection-line forces. The slow-drift excitation force F_1^{SV} in surge can be estimated in a similar way as done for F_2^{SV}. Here we just outline the approach to find the slow-drift damping in surge, including wave-drift damping (B_{11}^{SD}) and viscous hull damping (C_X).

Wave-drift damping

Left plot of Figure 5.19 shows the effect of current on the mean wave force in surge for the well boat. Different from the beam-sea condition (see Figure 5.13), the current presence will have a small influence on the mean surge force in shorter waves (wave period $T \leq 6s$). For very short waves ($T \leq 4s$), the results from HydroStar are not reliable, as explained in section 5.3.2. Aranha's formula is also employed to account for the current influence (not shown here), but poor agreement is observed compared with the results from HydroStar. This indicates that such formula is applicable for beam-sea waves and current, but not for head-sea scenario. Results from short wavelength asymptotic theory by Faltinsen et al. (1980) are also given and are used to estimate the wave-drift damping for shorter waves, to overcome the limitations of the HydroStar predictions in this wave-frequency range. The requirement by the asymptotic theory that the ship hull surface at the mean waterline should be vertical is not exactly satisfied by the examined well boat and is regarded as an error source. The wave-drift damping for slow-drift surge motion obtained with this approach is shown in the right plot of Figure 5.19 as a function of the wave period. From the figure, the wave-drift damping is small especially

for shorter waves ($T \leq 6$ s). This suggests that, for the sea states relevant in our analysis (peak period $T_p \leq 6s$), the wave-drift damping is expected to be not so important.

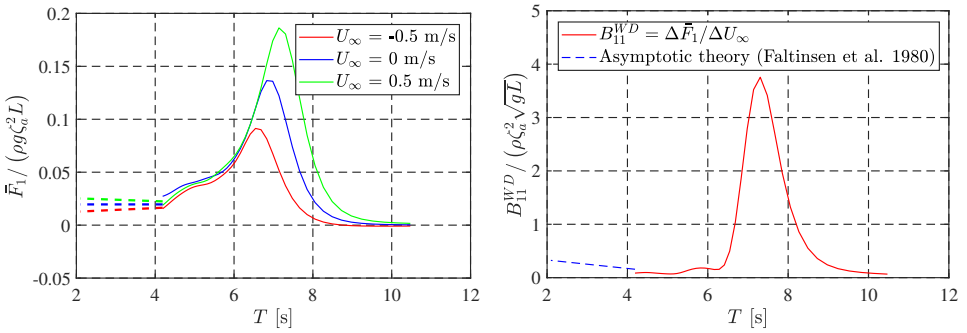

Figure 5.19: Left: the effect of current on the mean surge force. From the lowest to the highest curve: U_∞ = -0.5 m/s to 0.5 m/s. $\bar{F}_1$ is the mean surge force. Solid lines: results from the potential-flow solver HydroStar considering wave-current interactions. Dashed lines: results from short-wavelength asymptotic theory (Faltinsen et al., 1980). Right: wave-drift damping in surge B_{11}^{WD} for the well boat as function of the wave period T. The solid line indicates the part predicted with HydroStar and the dashed line the part predicted with the short-wavelength asymptotic theory.

Viscous damping

The prediction of the viscous surge force on the well boat in non-separated oscillatory flow is addressed here. The boundary-layer flow can be turbulent or laminar depending on the characteristic Reynolds number. The flow is likely to be turbulent in full scale. Jonsson (1980) proposed empirical formulas for the shear stress that apply to turbulent flow along fixed-plane surfaces. Outside the boundary layer, the flow oscillates harmonically. Jonsson defines the Reynolds number as

$$\mathrm{Rn} = \mathrm{U_M^2}/\omega\nu = \omega \mathrm{A_0^2}/\nu \tag{5.25}$$

where ω is the oscillatory circular frequency and A_0 the oscillatory amplitude. For the slow-drift surge motion, ω and A_0 are taken, respectively, as the resonance frequency and the standard deviation of the motion. Rn=10^5 is proposed as an engineering criterion for transition to turbulent boundary-layer flow for a smooth surface. When the surface is smooth, Jonsson writes the maximum wall shear stress τ_{wm} as

$$2\tau_{wm}/\frac{1}{2}\rho U_M^2 = 0.09\mathrm{Rn}^{-0.2} \tag{5.26}$$

However, when considering the viscous force in surge on the well boat connected with the non-separated turbulent boundary-layer flow, it is not sufficient to account for the shear stresses. Since the ship surface has a finite curvature, it follows that

there is an in/out flow through the boundary layer (Faltinsen and Timokha, 2009). The in/out flow is associated with pressure gradient. It means that there is also a pressure drag force. We write the total drag force in the longitudinal ship direction as

$$F_{D,x} = \frac{1}{2}\rho\left(0.09\mathrm{Rn}^{-0.2}S_w + C_p A_X\right)\dot{\eta}_1^{(2)}\left|\dot{\eta}_1^{(2)}\right| = C_X\dot{\eta}_1^{(2)}\left|\dot{\eta}_1^{(2)}\right| \tag{5.27}$$

Here $\dot{\eta}_1^{(2)}$ is the slow-drift velocity in surge, S_w is the mean wetted-surface area, C_p and A_X are the drag coefficient and the mean-wetted projected area in the longitudinal ship plane. Projected area A_X can be approximated as $B \times D$. By applying Eq. (5.27) to the ship presented in Faltinsen et al. (1986) and comparing with their experimentally obtained C_X from free-decay test, we have $C_p = 0.59$ for their ship, once substituted in the C_X expression of Eq. (5.27) the values for Rn, S_w and A_X. Since the geometry of the ship examined by Faltinsen et al. (1986) is quite close to the present well boat, the same C_p will be used for the well boat.

5.4 Conclusions and following work

The numerical modelings of a well boat operating at a fish farm in current only and in combined long-crested irregular waves and current have been introduced. A modern design well boat and a realistic fish farm were adopted. Both the well boat and the fish farm were modeled with state-of-the-art theoretical and numerical formulations. In particular, the transverse viscous loads on the boat were estimated by the cross-flow principle and the cross-sectional drag coefficients were estimated empirically and validated against available experiments. Important parameters are section geometry, Reynolds number and three-dimensional flow at the ship ends, and in addition, reduced velocity and Keulegan-Carpenter number with the presence of waves. The strategy used for the coupling between the well boat and fish farm was also introduced and the approach to measure the contact force between them was explained.

For the coupled system in long-crested irregular waves and current, the numerical modeling of the sway motion (including the first-order motion and slow-drift motion) of the well boat when operating at a realistic fish farm in setup A, was introduced. The approach to estimate the slow-drift excitation force and slow-drift damping (wave-drift damping and eddy-making damping) was given. The motion equation of the slow-drift sway motion of the well boat was also provided by simplifying the influence of the net cage as a restoring term and neglecting the influence of the first-order motion. The simplified analysis involves an analytically-oriented approach and will serve in the next chapter as a verification of the complete time-domain analysis of the coupled well boat-fish farm system. The complete coupling with well boat in setup C has been also outlined as it will be examined for selected cases in the next chapter.

The proposed numerical model will be used to analyze the coupled well boat-fish farm system in the time domain in the following chapter and the operational conditions of the well boat will be determined through systematic simulations.

Chapter 6

Numerical investigation of a well boat operating at a fish farm

The dynamic responses of a well boat operating at a fish farm in current and in long-crested irregular waves and current are analyzed numerically in the time domain using the numerical model proposed in Chapter 5. The main target is to quantify the influence of the well boat on the fish farm and to determine the operational conditions of the well boat. The most critical scenario with the well boat placed at the weather side of the fish farm is analyzed in detail. Special attention is paid to two critical response variables, i.e. maximum anchor-line loads and maximum floating-collar stresses.

Numerical response of the coupled system in current is presented at first. The influence of the well boat on the fish farm is addressed. A detailed sensitivity analysis is also performed and the effects of different parameters on the two critical response variables are discussed. The most important parameters for determining the operational conditions of the well boat are identified.

The coupled system in long-crested irregular waves and current is investigated afterwards. The slow-drift sway motion of the well boat is studied at first by simplifying the fish farm as a linear spring. The modeling of the slow-drift motions of the well boat is verified by comparing the mean value and standard deviation of the motion from the time domain with those from frequency domain when equivalent linearized drag damping is incorporated. Then the coupled system with a realistic fish farm is analyzed in detail, together with a sensitivity analysis to identify the important parameters influencing the two critical response variables. Lastly, the operational conditions of the well boat are determined through systematic simulations. Parts of the results in this chapter are documented in Shen et al. (2016), Shen et al. (2018a) and Shen et al. (2018b).

6.1 Physical investigation of the coupled system in current

In this section, we present a physical investigation of a coupled well boat-fish farm system in current using the numerical model proposed in Section 5.2. Relevant arrangement and dimensions of the system are described in Section 5.1. The main focus is on how the presence of the well boat will influence the fish farm. Based on the previous description of the proposed numerical model, we expect that the numerical results for the coupled system are reliable. Unfortunately, no experimental data are available for a quantitative validation of our numerical model including the well boat and the fish farm. Performing such model tests is challenging due to the scaling of different components. The coupled system with set-up A (see Figure 5.3), with the well boat placed at the weather side of the floating collar, is our research focus. Results for the other two set-ups presented in Figure 5.3 will be considered in selected cases, for comparison. Current with zero incident angle are considered in nominal simulations. "Nominal" denotes that basis values are used in the simulations. First, nominal results are shown in section 6.1.1. Special attention is paid to the load in anchor line-1 (defined in Figure 5.1) and to the floating-collar stresses, which are two important parameters for the fish-farm integrity. Then a detailed sensitivity analysis is performed in section 6.1.2 to identify important parameters affecting the anchor loads and the maximum stress in the floating collar. Finally, the operational conditions of the well boat are discussed and the most important parameters for determining them are proposed in section 6.1.3.

6.1.1 Nominal results

Time histories of the loads in anchor line-1 in current are shown in Figure 6.1. In the simulations, the isolated fish farm is investigated first, then, after about 280

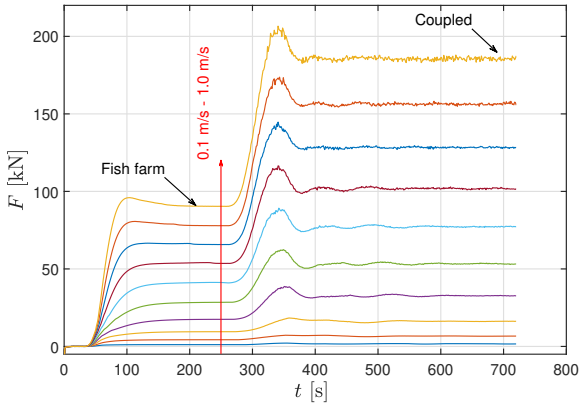

Figure 6.1: Time histories of loads in anchor line-1 in current only. The pre-tension is subtracted. Current velocity varies from 0.1 m/s to 1.0 m/s.

s, the well boat is connected with the fish farm. The considered current velocity varies from 0.1 m/s to 1.0 m/s, covering the scenario from small exposure to high exposure, according to the Norwegian Standard (see Table 1.2). The figure shows that the mean steady-state anchor loads increase strongly due to the viscous current loads on the well boat.

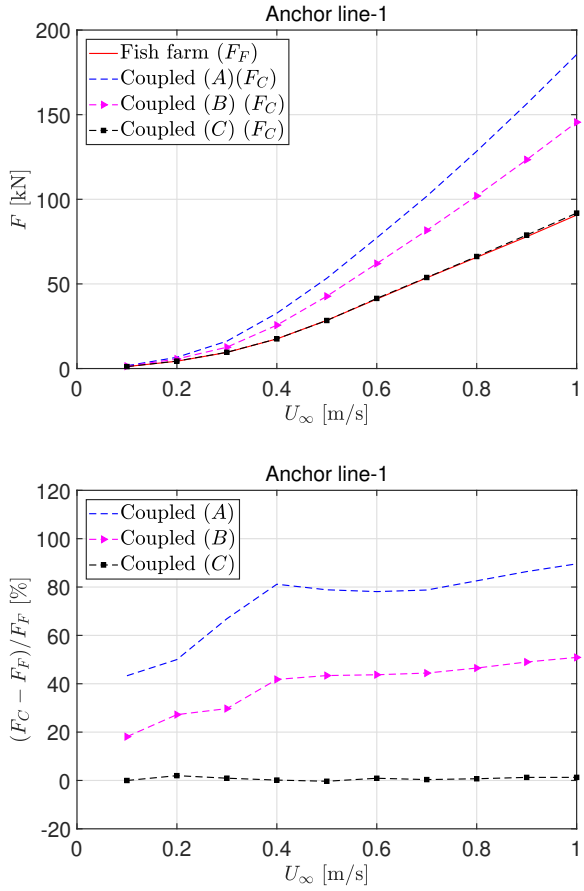

Figure 6.2: The effect of the well boat on the mean steady-state anchor loads. Results for set-up B and set-up C (see Figure 5.3) are also provided. F_F and F_C represent the anchor loads for the fish farm only and for the coupled system, respectively.

In Figure 6.2, the steady-state anchor loads with and without the well boat are shown. The figure highlights that the anchor load increases by more than 40% in small current velocities and up to 90% in high current velocities due to the well boat. Results for the other two set-ups with boat heading angle $\psi = 270^o$ and $\psi = 180^o$ are also given. It is not surprising that the well boat has a small influence on the anchor loads for set-up C with boat heading angle $\psi = 180^o$, as the loads on the boat mainly come from the hull friction in this case. The anchor loads for

set-up B are about 20% smaller than that for set-up A. This is because the shading effect of the net cage on the ambient flow is considered when estimating the viscous loads on the boat for set-up B. Apart from the flow reduction due to the front part netting, an additional reduction after the flow go through the aft part of the net is also considered for set-up B. The flow reduction factor is estimated according to Eq. (2.38). Steady shapes of the coupled system with different set-ups are shown in Figure 6.3.

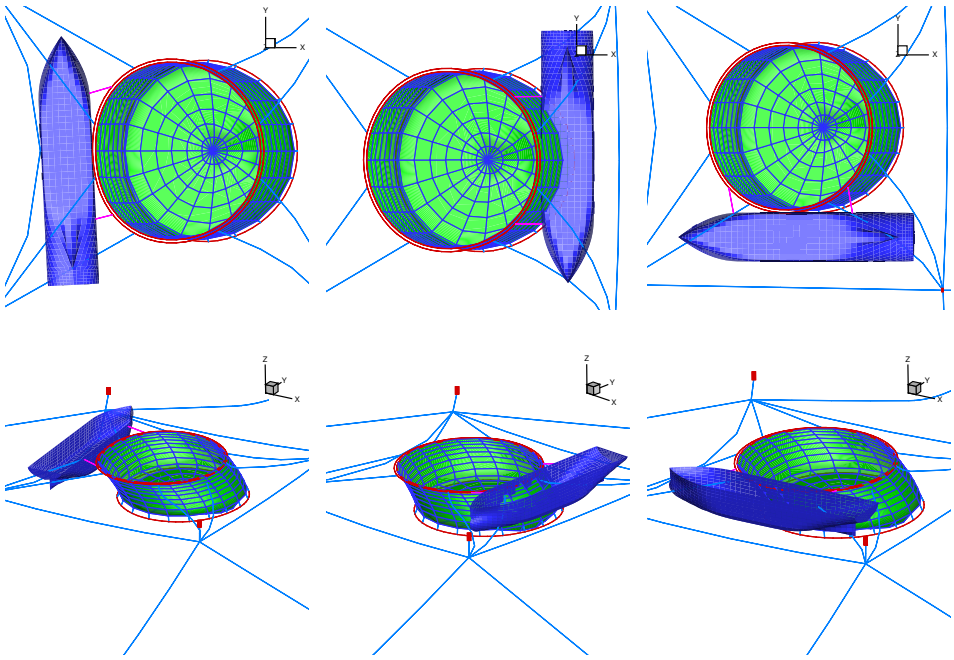

Figure 6.3: Steady configurations of the coupled system in current. Current velocity $U_\infty = 0.5$ m/s along the x-axis. Left: set-up A. Middle: set-up B. Right: set-up C. Upper: bird view. Lower: three-dimensional view.

Figure 6.4 and Figure 6.5 examine the influence of the well boat on the horizontal deformations of the floating collar. In Figure 6.4, time histories of the first seven horizontal mode amplitudes are provided for current velocity U_∞=0.5 m/s. Both the results for the fish farm only and for the coupled system are included. From the figure, the first four horizontal modes are the most important and there is a big increase of both rigid-body surge mode (c_1) and other elastic $\cos(n\beta)$ modes due to the well boat. Structural modes that are asymmetric about the x_E-axis, i.e. $\sin(n\beta)$ are also included in the simulations, but they are relatively small, so they are not presented here. The influence of the well boat on the steady values of the first four horizontal mode amplitudes of the floating collar versus current velocity is shown in Figure 6.5. Numerical results indicate that the well boat will strongly increase these mode amplitudes. Considering the current speed U_∞=0.5 m/s, the well boat will increase the first four mode amplitudes by about 41%, 99%, 73.7%

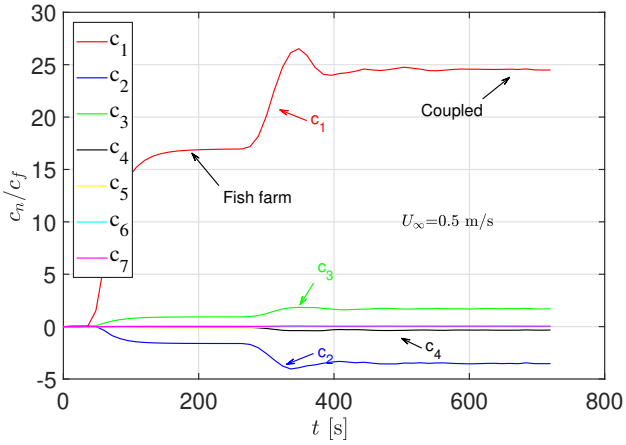

Figure 6.4: Time histories of non-dimensional horizontal floating collar Fourier mode amplitudes c_n in current with set-up A (see Figure 5.3). Current velocity $U_\infty = 0.5$ m/s. The different mode amplitudes are made non-dimensional by the cross-sectional radius of the floating collar tubes $c_f = d_f/2$.

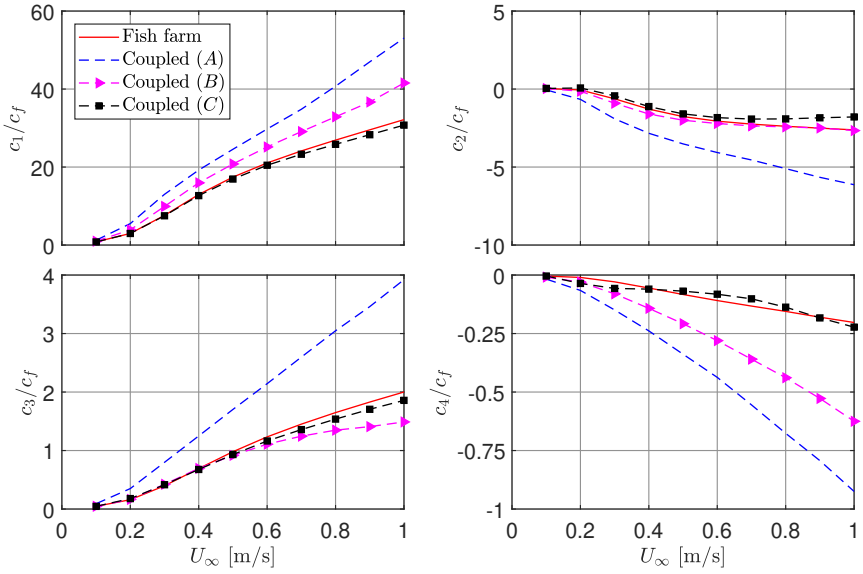

Figure 6.5: The effect of the well boat on the steady values of surge and first three elastic horizontal mode amplitudes versus current speed. The different mode amplitudes are made non-dimensional by c_f. Current velocity varies from 0.1 m/s to 1.0 m/s. Results for cases with set-up B and set-up C are also provided.

and 360%, respectively. Numerical results for the system with set-up B and set-up C are also shown in the figure. Negligible difference is observed in the floating

collar deformations with and without the well boat for set-up C. For cases with set-up B, the presence of the well boat will mainly affect the surge motion c_1 and the third elastic mode c_4. The main reason is that there is no contact between the well boat and the floating collar in this scenario and the loads from the well boat are transferred to the fish farm through the connection lines.

To see more clearly how the well boat will influence the floating collar, the stress distribution along the floating collar due to horizontal deformations without and with the well boat are shown in Figure 6.6.

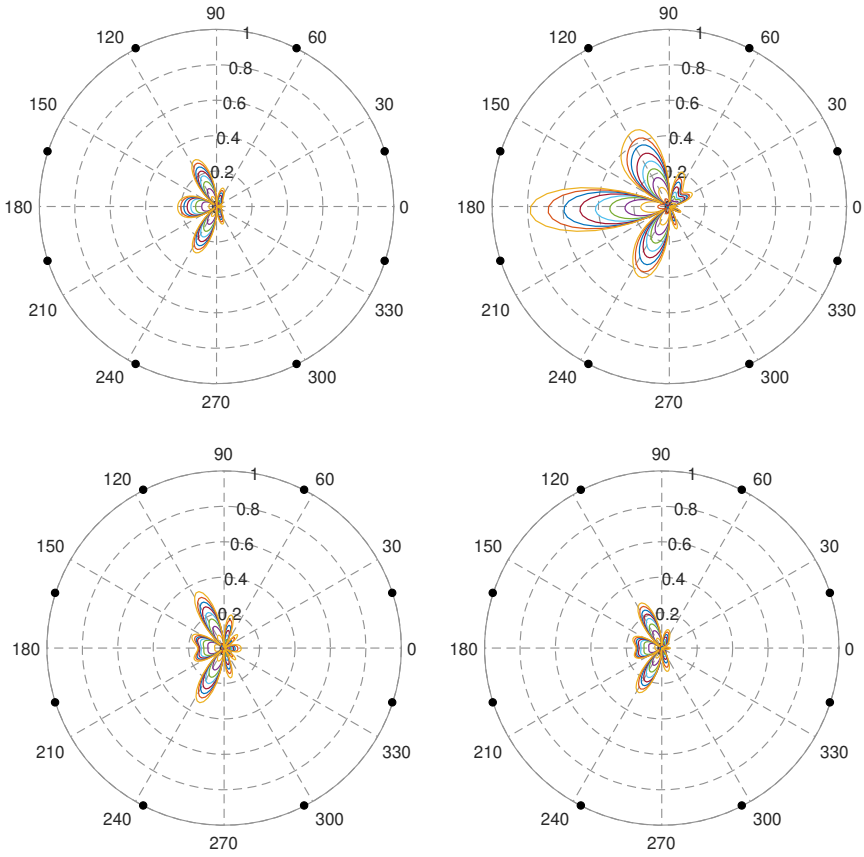

Figure 6.6: Stress distribution along the floating collar due to horizontal deformations. The stress is made non-dimensional by the yield stress (high-density polyethylene). The labels 0° - 360° represent the radial angle β (position) along the floating collar. Upper left: fish farm system only. Upper right: coupled system with set-up A. Lower left: set-up B. Lower right: set-up C. Different lines correspond to different current velocities and from inner to outer they correspond to current velocity $U_\infty = 0.1$ m/s - 1.0 m/s. The 8 solid circles in each plot represent the positions where bridle lines are attached to the floating collar.

The maximum stress due to horizontal deformations at a position $x = R\cos\beta$ along the floating collar is given as

$$\sigma(\beta,t) = \frac{M(\beta,t)}{I} r_{\max} = \frac{E r_{\max}}{R^2} \sum_{n=2}^{\infty} n^2 [c_n(t)\cos n\beta + d_n(t)\sin n\beta] \tag{6.1}$$

where $r_{\max} = 3c_f$ with $c_f = d_f/2$ the cross-sectional radius of the floating collar, which comprises two tubes, $R = (D_{f1}/2 + D_{f2}/2)/2$ is the mean value of the center line radius of the two tubes. Results are provided for all the three coupling set-ups in Figure 5.3. From Figure 6.6, the maximum stress for set-up A occurs at the region where the well boat is in contact with the floating collar while the maximum stress for the two other set-ups occurs at the positions $\beta = 117^{\circ}$ and $\beta = 243^{\circ}$ where bridle lines are attached. Moreover, the maximum stress for set-up A is much larger than those for the other two set-ups and for the fish farm only. By examining the loads in anchor line-1 and stresses along the floating collar for set-up A and set-up B, we can see that it is more favorable to place the well boat in the leeward side of the fish farm, if one accepts to face higher probability of sucking the net into the well-boat propeller.

6.1.2 Sensitivity analysis

Due to uncertainties in the mathematical modeling and system set-up, we performed a sensitivity analysis for the coupled system in current. The main focus is on the loads in anchor line-1 (defined in Figure 5.1) and the maximum stresses in the floating collar. As explained before, the well boat is implicitly assumed to be placed at the weather side of the fish farm (set-up A). The different parameters examined are shown in Table 6.1. In order to quantify the significance of them and try to identify the important ones, we present condensed results in Figure 6.7 and Figure 6.12 for the two parameters, respectively. Each bar represents the percentage difference of the load in anchor line-1 (Figure 6.7) and the maximum floating collar stress (Figure 6.12) with respect to the nominal value, averaged over all the considered current velocities. From the figures, we can see that each parameter has different impact on the examined two parameters. Parameters that lead to more than 5% difference are marked by "×" in the right two columns in Table 6.1. More detailed discussions are presented below.

Table 6.1: Parameters that are varied in the sensitivity analysis for cases in current only. Quantities with subscript 0 mean nominal values. Parameters that lead to more than 5% difference from the nominal value of the anchor load and the maximum floating collar stress are marked by "×" in the right two columns. Parameters not investigated are marked by "-".

	No.	Value	Explanation	>5% Anchor load	>5% Stress
Environment	1	$\alpha_c = -15^{\circ}$	Current direction	×	×
	2	$\alpha_c = 15^{\circ}$	Current direction		
Wellboat	3	$C_D = 1.1C_{D0}$	Drag coefficient		×
	4	$C_D = 0.9C_{D0}$	Drag coefficient		×
Floating collar	5	N_h=1, N_v=2	Rigid body		-
	6	$\beta_1 = 90^{\circ}$ and $\beta_2 = 270^{\circ}$	Boat connection positions		
Sinker tube	7	$h_s = 0.5h_{s0}$	Sinker tube depth	×	
	8	$w_s = 80$kg/m, $W_c = 1000$ kg	Weight in water	×	
	9	$w_s = 93$kg/m, $W_c = 1500$ kg	Weight in water	×	
Net	10	$U_1 = 1.1U_{\infty}$	Current velocity (shading effect)	×	
	11	$U_1 = 1.3U_{\infty}$	Current velocity (shading effect)		
Moorings	12	Pretension = 5 kN	Pretension	×	×
	13	Pretension = 15 kN	Pretension		×
	14	$k_s = 2.0k_{s,0}$	Anchor line stiffness		
	15	$m_{\text{chain}} = 0.5\ m_{\text{chain},0}$	Anchor chain weight		
	16	$m_{\text{chain}} = 2.0\ m_{\text{chain},0}$	Anchor chain weight	×	×

Loads in anchor line-1

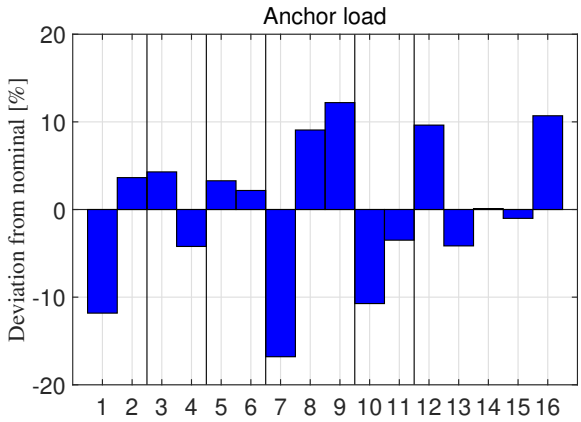

Figure 6.7: Each bar represents the percentage difference of the anchor load with respect to the nominal value, averaged over all the examined current velocities. The numbers on the horizontal axis refer to the variation numbers as given in Table 6.1.

Environment: In the nominal simulations, zero current direction $\alpha_c = 0^o$ is assumed. $\alpha_c = -15^o$ and $\alpha_c = 15^o$ are considered in the sensitivity analysis to account for the influence of possible change of current direction. Changing the current direction to $\alpha_c = -15^o$ will reduce the anchor load by about 12%. There are two reasons for the reduction. One is that the current loads on the boat are reduced due to the change of current direction. The other is that the anchor line provides less support to the fish-farm system in the considered current direction. Small difference is observed with respect to the nominal value for the case with $\alpha_c = 15^o$. This is because smaller load is exerted on the well boat while more load is absorbed by the anchor line, so the joint effects tend to balance each other leading to a small change of the anchor load.

Well boat: The cross-sectional drag coefficients C_D for the well boat in current are estimated empirically (see Section 5.2.1), so an error in the boat drag coefficient is expected. In the nominal simulations, the ship averaged drag coefficient equals to 0.9. Changing the value by 10% leads to about 4% change of the anchor load with respect to the nominal value.

In the following, we will discuss the influence of the fish farm related parameters on the anchor load.

Floating collar: The influence of the floating collar elasticity on the anchor load is studied and numerical results indicate that modeling the floating collar as rigid or as flexible has a small influence on the anchor load. Similar conclusion was drawn for the fish farm without well boat when exposed to current in Chapter 4.

In the nominal simulations, the well boat is connected to the floating collar by two ropes at positions $\beta_1 = 135^o$ and $\beta_2 = 225^o$, as shown in Figure 5.1, while in the sensitivity study $\beta_1 = 90^o$ and $\beta_2 = 270^o$ are examined. Negligible difference is observed when changing the positions where the well boat is connected to the floating collar.

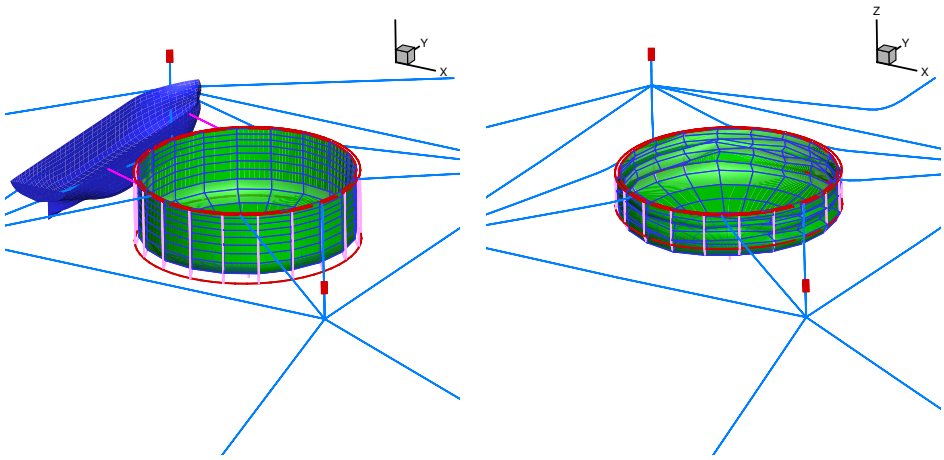

Figure 6.8: Sketch showing the lifting of the sinker tube up during the loading/offloading operation. Left: initial shape. Right: sinker tube is lifted up (well boat not shown).

Sinker tube: During the loading/offloading operation, the sinker tube may be lifted up for sake of operational convenience and this is not considered in nominal simulations. Lifting the sinker tube up to half of its original depth will reduce the anchor load by 16.8%. To lift the sinker tube, additional 20 ropes between the floating collar and the sinker tube are added, see Figure 6.8, using similar lift-up configuration as in Nygaard (2013).

A larger weight of the fish-farm bottom is expected to limit the reduction of net-cage volume when the fish farm operates in exposed regions. To investigate quantitatively this effect, two additional bottom weights have been examined and related results are compared with those of the nominal fish-farm set-up. These bottom weights correspond, respectively, to a sinker tube weight w_s=80 kg/m with center point weight W_c= 1000 kg, and w_s=93 kg/m with center point weight W_c= 1500 kg. The choices are motivated by expected practical set-ups for fish farms operating in exposed regions. Numerical results show that the anchor load increases by about 9% and 12.2%, respectively, with the two new bottom weights.

Net cage: In the nominal simulations, the shading effects of the well boat on the net incoming flow is not considered when evaluating the loads on the net cage. In reality, the presence of the well boat will change the incoming flow and will

consequently alter the loads on the net cage. Only the ship wake effect on the front part of the net cage is assessed. To quantify the influence, we need to have a reasonable estimation of the flow distribution behind different sections of the boat.

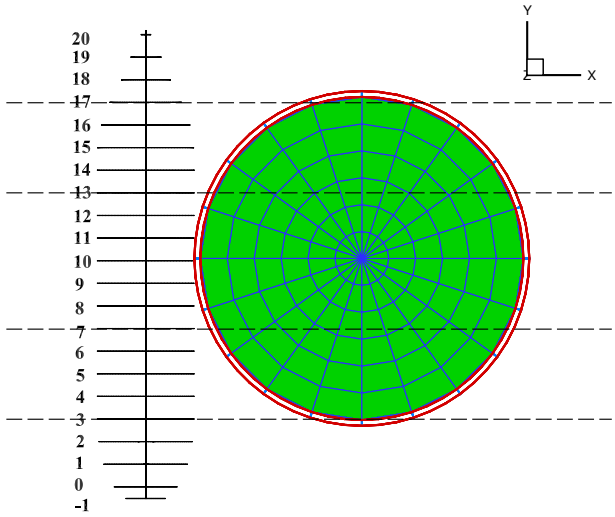

Figure 6.9: Positions of the different sections of the well boat relative to the net cage from bird view.

The relative positions of the different well-boat sections to the net cage are shown in Figure 6.9. The net cage is in the wake of section 3 to section 17. Since we do not have available information on the flow behind each section individually, we divide all the considered sections into two types: with and without bilge keels. For sections with bilge keels (section 7-13), the flow will separate at the leading edge (i.e. at the sharper corner in the weather side) and the flow behind the body is assumed to be similar to that behind a two-dimensional (2D) rectangular body (a block), see the left plot in Figure 6.10. The center line of the free shear layer z_m is given according to the experimental results from Baker (1977) for the flow behind a 2D block on a wall. Baker (1977) showed that the distribution of mean horizontal velocity in free shear layer behind the 2D block resembles that of a plane mixing layer flow. According to White (2006), the mean velocity profile $\bar{u}$ in a plane mixing layer between parallel streams, with the upper stream moving with mean velocity U_2 and the lower stream with mean velocity U_1 can be written as

$$\frac{\bar{u}-U_1}{U_2-U_1}=\frac{1}{2}\left[1+\Phi\left(\frac{13.5z}{x}\right)\right] \tag{6.2}$$

where Φ is the error function, see Eq. (5.19). Eq. (6.2) is for the flow with the center line of the free shear layer at z=0. For cases with curved shear layer, as in

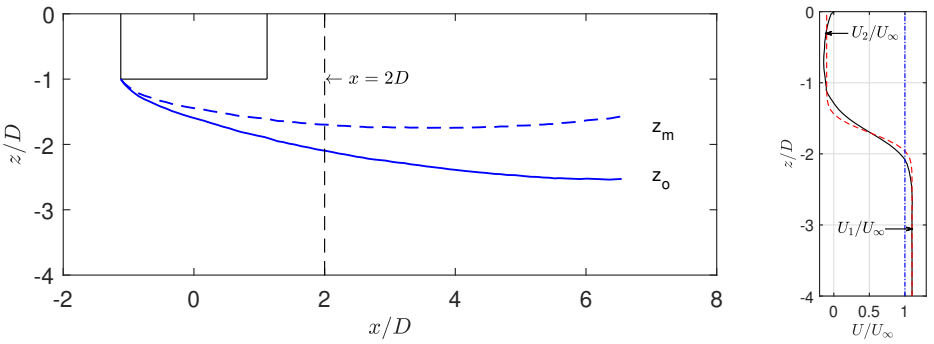

Figure 6.10: Left: sketch showing important lines for the free shear layer around a section with bilge keels. z_m represents the center line of the free shear layer and z_0 the outer boundary of the turbulent separated flow. Both x and z coordinates are made non-dimensional by the draft D. Right: distribution of mean horizontal velocity. Solid line: experimental data from Baker (1977). Dashed line: theoretical value for plane mixing layer flow. Dash-dot line: undisturbed inflow velocity.

Figure 6.10, we need to express the formula in a curved coordinate as

$$\frac{\bar{u} - U_1}{U_2 - U_1} = \frac{1}{2}\left[1 + \Phi\left(13.5\frac{z_s - z_m}{x_s}\right)\right] \tag{6.3}$$

where z_m is the center line of the shear layer, x_s is a curved coordinate along z_m with $x_s = 0$ at the separation point and z_s is a coordinate perpenticular to x_s and pointing downwards. The half thickness of the free shear layer is given by $\tan(7^o)x_s$ (White, 2006), using this, we can identify the outer boundary of the turbulent shear layer z_o, as shown in Figure 6.10. If we can have a reasonable estimation of U_1 and U_2, then the flow distribution behind these sections can be obtained. In the right plot of Figure 6.10, a comparison of the mean velocity distribution in free shear layer from the experimental data by Baker (1977) and the theoretical plane mixing layer flow is given. To fit the experimental data, mean lower stream velocity U_1 = 1.1 U_∞ and mean upper stream velocity U_2 = -0.1 U_∞ are used in the theoretical calculation and good agreement between the experimental and theoretical results is observed. This demonstrates that the plane mixing layer flow can be used to describe the flow behind a 2D block. $U_1 = 1.1\,U_\infty$ means that the flow is accelerated outside the boundary of turbulent flow compared with the incident flow U_∞. U_2 = -0.1 U_∞ denotes that there is a small mean reverse flow behind the section.

The obtained free shear layer region is quite similar to the experimental measurements by Chauhan et al. (2017) for the flow past a square prism with a splitter plate attached behind. The Particle Image Velocimetry (PIV) technique is adopted in their measurement. Their experimental results also show that the horizontal velocity is almost constant outside the turbulent layer with U_1 equal to about $1.2U_\infty$ at $x = 2D$ and for z between -4D and -2.2D. The main reason for the difference in U_1 from the two experiments is that the tests from Chauhan et al. (2017) were

performed in water while the tests from Baker (1977) were conducted in air. There exists a very thick boundary layer of the inflow in the front region of the 2D block in Baker (1977), so the inflow mass flux is reduced compared with that in Chauhan et al. (2017). The value of U_1 from Chauhan et al. (2017) is believed to be more accurate for our case.

As U_2 is small compared with U_1, the load on the front upper part of the net cage is expected to have a small contribution to the total net cage load, for simplicity U_2 = -0.1U_∞ from Baker (1977) is used in the sensitivity analysis. In terms of U_1, two U_1 values with $U_1 = 1.1U_\infty$ and $1.3U_\infty$ are investigated. The chosen two U_1 values are consistent with the minimum and maximum values of the horizontal velocity at $x = 2D$ with $-4D \leq z \leq -D$, obtained from potential-flow calculation for the section in steady flow. Considering the deformation of the net cage, the velocity profile at position $x = 2D$ is used as the incident flow for the front part of the net cage.

For sections without bilge keels, the flow will separate at the cross-section backward corner in turbulent flow and we assume that the flow behind the body can be described by the flow behind a backward facing step (beam-to-draft ratio $B/D \geq 1$), see Figure 6.11. The center line of the free shear layer in the figure is given according to the experimental results from Baker (1977). According to Baker (1977), the flow behind a backward facing step can also be seen as a plane mixing layer flow. A comparison of the mean horizontal velocity distribution between experimental data and theoretical results (plane mixing layer flow) is shown in the right plot of Figure 6.11. $U_1 = U_\infty$ and $U_2 = 0$ m/s are used in the theoretical model. Reasonable agreement is observed. $U_2 = 0$ m/s means that negligible reverse flow is found in the region right behind the cross- section, this is intuitively reasonable because the flow separation is not intense.

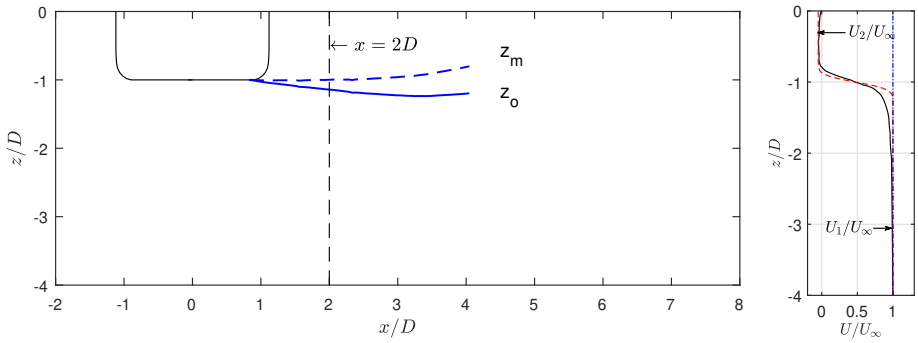

Figure 6.11: Same as in Figure 6.10, but for flow around a section without bilge keels.

The flow is expected to be accelerated below the cross-section with respect to the undisturbed inflow, according to the law of mass conservation. However, the obtained U_1 value seems to indicate that this is not the case, see Figure 6.11. The main reason is that the inflow mass flux is reduced due to a very thick boundary

layer of the inflow in the experiments. Larger U_1 value should be used for our case. In the sensitivity analysis, $U_2 = 0$ m/s is assumed. For U_1, since the flow separates at the backward corner, U_1 should be close to the potential-flow solution, from which U_1 is between $1.1U_\infty$ and $1.3U_\infty$ at $x = 2D$ with z between -4D and -D. This means that we can use the same upper limit and lower limit of U_1 both for sections with and for sections without bilge keels. It should be noted that the flow distributions around sections with and without bilge keels can be totally different, even if similar U_1 and U_2 values are assumed. This is because the length of the free-shear-layer center line x_s is also very important, as shown in Eq. (6.3).

Numerical results show that considering the shading effect of the well boat will reduce the anchor loads by 10.7% with $U_1 = 1.1U_\infty$ and 3.5% with $U_1 = 1.3U_\infty$, respectively. The results denote that the increment of the load on the lower part of the net cage due to the accelerated inflow can not compensate the reduction of the load on the upper part and larger U_1 will cause a smaller reduction of the anchor loads.

Mooring system: In the nominal simulations, the pretension force in the anchor line is 10 kN, two alternative values of the pretension force are considered in the sensitivity study, i.e. 5 kN and 15 kN, respectively. They correspond to a 50% reduction and a 50% increase of the pretension force, respectively. Relatively large increase of the anchor loads, about 9.6%, is observed when pretension force equal to 5 kN is adopted. The pretension force is subtracted during the comparison.

Increasing the stiffness of the anchor lines by 100% and reducing the anchor chain weight by 50% has negligible influence on the anchor loads. However, increasing the anchor chain weight by 100% will increase the anchor loads by about 10.5%. This is due to that with larger anchor chain weight, the side anchor lines will have smaller stiffness, so the front two anchor lines will provide more contribution to balance the load on the fish farm.

Maximum stress in the floating collar

From Figure 6.12, the maximum stress in the floating collar is in general sensitive to parameters that are important for estimating the viscous current loads on the well boat. For example, changing the current direction α_c from 0^o to $+15^o$ and -15^o will reduce the maximum stress by about 6.7% and 3.3%, respectively, due to the reduction of the current loads on the boat. Increasing the ship averaged drag coefficient will increase the maximum stress and a variation of the former by 10 % will lead to about 7% change of the latter. The maximum stress is also sensitive to parameters that are closely related with the stiffness of the floating collar, like the pretension force in the anchor line. Larger floating collar stiffness is expected when higher pretension force is applied. Numerical results show that increasing the pretension force in the anchor line from 10 kN to 15 kN will reduce the maximum stress by about 10.7% while reducing the value from 10 kN to 5 kN will increase the maximum stress by about 14.7%. The maximum stress is not so sensitive to parameters associated with the evaluation of the loads on the net cage, like the

weight system including sinker tube depth, sinker tube weight and center point weight as well as the shading effect on the incident current field due to the well boat.

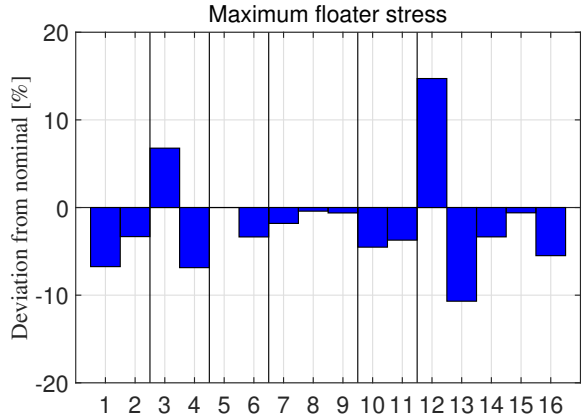

Figure 6.12: Each bar represents the percentage difference of the maximum floating collar stress with respect to the nominal value, averaged over all the examined current velocities. The numbers on the horizontal axis refer to the variation numbers as given in Table 6.1.

6.1.3 Operational conditions in current

Operating fish farms in exposed regions will increase the probability of routine well boat operations in severe weather conditions. Nowadays the decision on when performing the operation is mainly dependent on the captain. So it is valuable to have a decision-support tool to give guidance for safe well-boat operations. In this section, we will discuss how to determine the operational conditions of the well boat when operating at the fish farm during the loading/offloading operation. The well boat is moored at the weather side of the fish farm. The operational conditions are determined based on the criteria that the structural integrity of the fish farm system is not endangered. The loads on the well boat are transferred to the fish farm through direct contact with the floating collar, so the floating collar should be able to withstand the loads. Moreover, the floating collar is moored to the seabed through the mooring system, so the mooring lines should be strong enough. Therefore, two operational criteria are proposed, connected, respectively, with maximum forces in the mooring lines and maximum stress in the floating collar.

In this section, we mainly focus on the coupled system in current only. Results of the loads in anchor line-1 and floating collar stresses were shown in Figure 6.2 and Figure 6.6. The considered current velocity varies from small exposure to high exposure. The minimum breaking force for the considered anchor polysteel rope is about 628 kN, which is much larger than the maximum force experienced by the anchor line, about 185 kN, so the anchor load is not the main concern when

determining the operational conditions. The loads in the two bridle lines are also examined, the maximum loads are slightly smaller than that in anchor line-1 and will also not exceed the breaking limit for the considered sea states. The maximum stress in the floating collar occurs in the region where the well boat is in contact with the floating collar with a value about 80% of the yield stress for the considered current velocities. Although the maximum stress does not exceed the yield stress in the present study, the results indicate that this response variable is of concern in current and it is expected to be even more critical in combined waves and current.

To represent more realistic scenario and provide practical guidance for well-boat operation, the coupled system in irregular waves has to be examined. This will be done in the following section.

6.2 Physical investigation of the coupled system in long-crested irregular waves and current

In this section, the dynamic response of a coupled well boat-fish farm system in irregular long-crested waves and current is analyzed numerically in the time domain. Free decay tests in x_E direction for the coupled system with set-up A (see Figure 5.3) in calm water are performed at first to have an idea of the natural period of the system and the damping contributions from different components of the system, in particular from the net cage. Then, a numerical study of slow-drift sway motion of the well boat is performed, with the fish farm represented by a linear spring. The main purpose of this study is to verify the modeling of the slow-drift motion of the well boat. Finally, the coupled system with the well boat placed at the weather side of the fish farm is analyzed in detail, using a realistic fish-farm set up. The operational conditions of the well boat are also determined through systematic simulations.

6.2.1 Free decay tests

A free decay test for the coupled system with set-up A in still water is performed. The well boat is assumed to experience only sway motion. The motion can be described by Eq. (5.5) but with zero wave-drift damping and zero wave excitation force, i.e. $B_{22}^{SD} = 0$ and $F_2^{Excit} = 0$. A ship averaged drag coefficient $C_D = 2.2$ is used for estimating the eddy-making damping. The way to estimate the viscous hydrodynamic loads on the fish farm, including the net cage, has been shown in Chapter 2.

Time history of the sway motion of the well boat during the free decay is shown in the upper row of Figure 6.13. The linear and quadratic damping coefficients are found according to Faltinsen (1990). The natural period of the coupled system is $T_n = 153.8$ s. A free decay test without the net cage is also conducted and the corresponding results are shown in the lower row in Figure 6.13. The quadratic damping coefficient due to the mooring lines is expected to be small, so the obtained value mainly comes from the well boat. By comparing the drag coefficients from

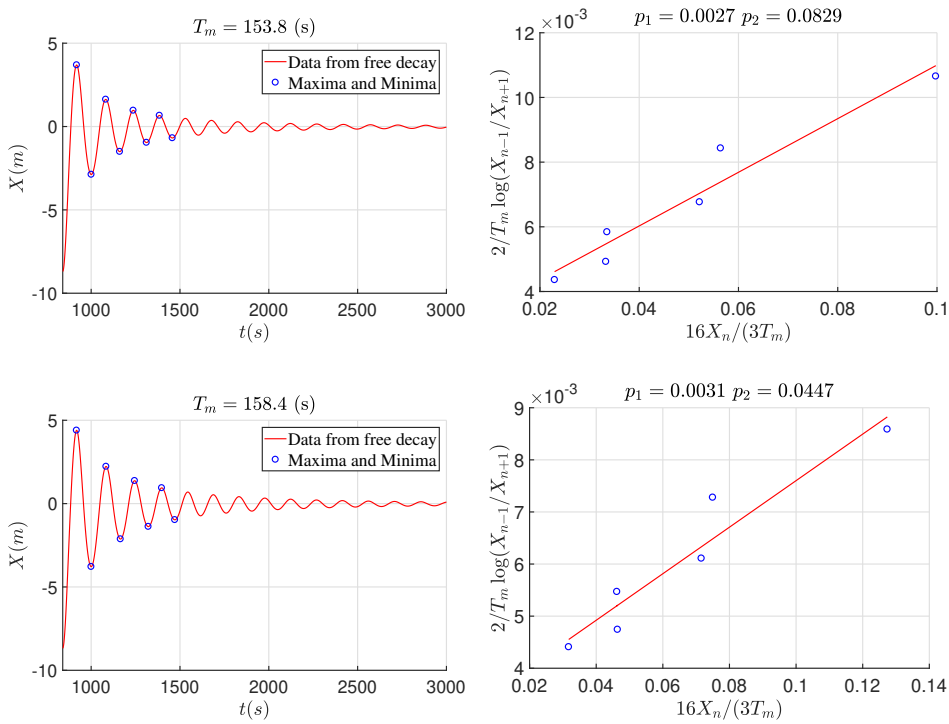

Figure 6.13: Left: time histories of sway motion of the well boat from free decay tests for the coupled system in calm water. Right: illustration of how to obtain linear damping coefficient p_1 and quadratic damping coefficient p_2 (see e.g. Faltinsen, 1990). Upper: fish farm with net cage. Lower: fish farm without net cage. X_n is the amplitude of the nth oscillation. T_m is the mean natural period.

the two cases, we can see that the net cage contributes about 50% to the quadratic damping, but has negligible contribution to the linear damping. It should be noted that the restoring stiffness provided by the fish farm is not constant and also that the quadratic damping coefficient from the net cage is response-amplitude dependent, so the estimated drag coefficient can just serve as a guidance value for the coupled system in oscillatory flow. A free decay test for the coupled system in current has been also examined and numerical results indicate that the system is overdamped.

6.2.2 Slow-drift response of the well boat

In this part, we present numerical results of the slow-drift sway motion of the well boat, with the load on the well boat from the fish-farm system represented by a linear spring. The damping from the fish farm is neglected, as it is not straightforward to be considered, although it may have important contribution, as shown from the free-decay tests. The main purpose of this study is to verify

the modeling of the slow-drift motion and investigate the influence of different parameters on the motion. This will serve as a guidance for the study of the coupled well boat-fish farm system in section 6.2.3.

The slow-drift motion is estimated here by solving Eq. (5.17) in the time domain. A stiffness coefficient in sway from the fish farm $C_{22} = 24$ kN/m is assumed, corresponding to the restoring stiffness provided by the fish farm when there is no anchor chain laying on the seabed, as obtained from Figure 5.10. The importance of different slow-drift damping terms is discussed and the necessity of considering the first-order motion when calculating the eddy-making damping is also studied. In addition, different statistic approaches are used to examine the extreme values obtained from time-domain simulations with different time durations.

Wave-drift damping

Figure 6.14 shows the time histories of the slow-drift sway motion of the well boat, considering in Eq. (5.17) the mean wave-drift damping and the mean plus slowly-varying wave-drift damping, respectively. The eddy-making damping is not included. Two wave conditions with $H_s = 2$ m, $T_p = 6$ s and with $H_s = 1$ m, $T_p = 5$ s, respectively, are considered. The figure shows that considering the slowly-varying wave-drift damping will reduce the maximum motion for $H_s = 2$ m and $T_p = 6$ s, while negligible influence is observed for $H_s = 1$ m and $T_p = 5$ s. Detailed analysis is given below.

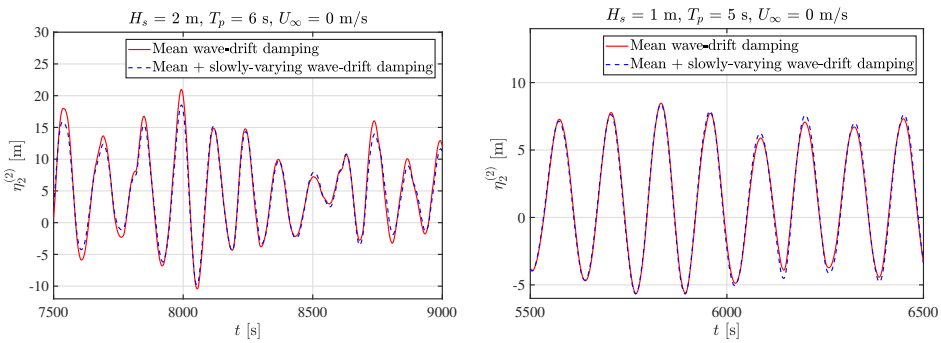

Figure 6.14: Time histories of the slow-drift motion in sway. Just a short time interval when the motion reaches the largest maximum in the performed simulation is shown. The duration of the simulations is 3 hours. Solid line: numerical solution of Eq. (5.17) with mean wave-drift damping. Dashed line: numerical solution of Eq. (5.17) with mean plus slowly-varying wave-drift damping. Left: $H_s = 2$ m and $T_p = 6$ s. Right: $H_s = 1$ m and $T_p = 5$ s.

- Irregular waves with $H_s = 2$ m, $T_p = 6$ s:

  The expected mean value $\bar{\eta}_2^{(2)}$, the standard deviation $\sigma_{\eta_2^{(2)}}$ and the maximum value $\eta_{2,\max}^{(2)}$ of the slow-drift motion from time-domain simulations are presented

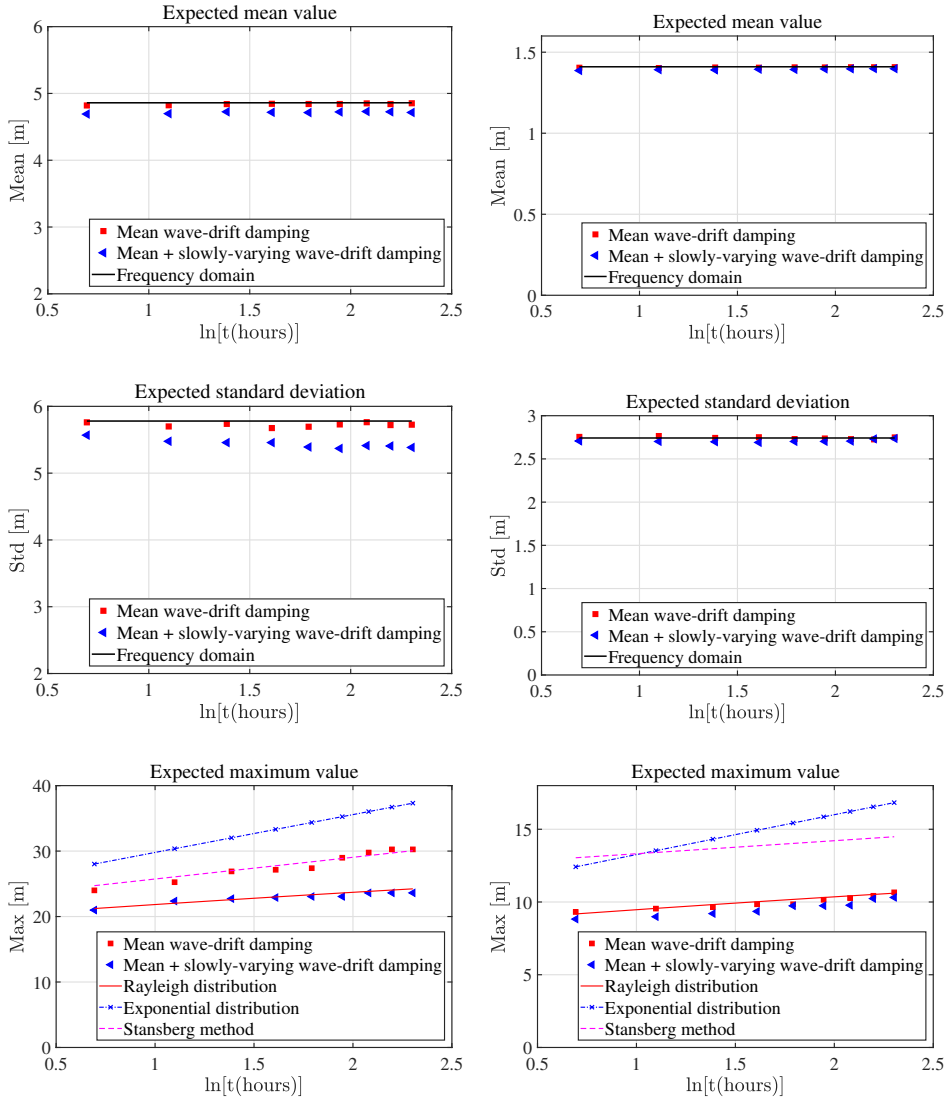

Figure 6.15: Expected mean value (upper), standard deviation (middle) and maximum value (lower) of the slow-drift sway motion. Only the wave-drift damping is included. Left: $H_s = 2$ m, $T_p = 6$ s, $U_\infty = 0$ m/s. Right: $H_s = 1$ m, $T_p = 5$ s, $U_\infty = 0$ m/s. The predicted maximum values based on Rayleigh distribution (including only the mean wave-drift damping), exponential distribution and Stansberg's method (including only the mean wave-drift damping, see Stansberg, 1991) are also shown.

in the left column of Figure 6.15 as a function of simulated time (from 2 hours up to 10 hours). Ten different realizations are considered and the simulated

time of each realization is 10 hours. In the analysis, portions of each realization are considered, with duration varying from 2 hours to 10 hours, and treated as individual realizations to see the effect of the simulated time. Each value in the figure is taken as the mean value from ten different realizations. From the figure, the expected mean value and standard deviation are almost independent from the simulated time. Including the slowly-varying wave-drift damping will reduce the mean value, the standard deviation and the maximum value, with the maximum value the most affected. The frequency-domain solutions of the standard deviation from Eq. (5.21) and the mean sway motions caused by the mean wave loads are also provided. In this case the slowly-varying wave-drift damping cannot be accounted for. The figure shows that the expected mean value and the standard deviation from the time-domain analysis agree nicely with those from the frequency-domain solution. The mean value and the standard deviation from frequency domain are 4.86 m and 5.78 m, respectively. In terms of the damping level, the considered mean wave-drift damping is $\xi = 7.86\%$ of the critical damping.

- Irregular waves with $H_s = 1$ m, $T_p = 5$ s:

  The expected mean value, the standard deviation and the maximum value of the slow-drift motion are presented in the right column of Figure 6.15. Also in this case nice agreement is observed for the mean value and the standard deviation between the time-domain and the frequency-domain results. The mean value and the standard deviation from frequency domain are 1.41 m and 2.74 m, respectively. The mean wave-drift damping is $\xi = 2.22\%$ of the critical damping. Including the slowly-varying wave-drift damping has negligible influence on the motion due to the small damping level.

Three different statistical approaches are used to examine the expected largest sway motion from the time-domain simulations. One is based on the use of the Rayleigh distribution. This is theoretically sound when the damping is linear, time-independent and asymptotically small. So only the mean wave-drift damping can be included. The expected largest value $\eta^{(2)}_{2,\max}$ can then be written as

$$\eta^{(2)}_{2,\max}(t_s) \approx \sigma_{\eta^{(2)}_2}\sqrt{2\ln N} + \bar{\eta}^{(2)}_2 \tag{6.4}$$

where t_s is the simulated time, N is the number of slow-drift oscillations during t_s. This can be estimated as $N = t_s/T_n$ with T_n the natural period of the slow-drift motion. The standard deviation $\sigma_{\eta^{(2)}_2}$ can be obtained from frequency-domain or time-domain analysis.

The second approach is to use exponential distribution as a rough approximation to estimate the extreme slow-drift response. This was suggested by Naess (1989). In this case, the expected maximum value takes the form

$$\eta^{(2)}_{2,\max}(t_s) = \sigma_{\eta^{(2)}_2}\ln N + \bar{\eta}^{(2)}_2 \tag{6.5}$$

Eq. (6.5) is generally on the conservative side and the smaller is the damping the more it is conservative.

The third approach is based on a simple statistical model proposed by Stansberg (1991). A critical point in the use of such model is the determination of the relative spectral bandwidth parameter, defined as the ratio between the width of the wave group spectrum and the width of the slow-drift response spectrum. Detailed formulas will not be shown here. More accurate estimation procedure is possible (Naess, 1986), but the quadratic transfer function (QTF) of the wave-drift force on the well boat must be known and the estimation of this is not attempted in the present work.

Detailed comparison of the expected largest values obtained directly from the time-domain simulations and using the three theoretical statistical approaches for the considered two sea states are shown in the lower plots of Figure 6.15. From the figure, the exponential distribution clearly overestimates the extreme values for both cases. The Rayleigh distribution can well-predict the extreme values for H_s = 1 m and T_p = 5 s, when the damping is small, but will underpredict the extreme values for H_s = 2 m and T_p = 6 s associated with relatively large damping (> 3-4% of the critical damping). The Stansberg's method has a nice prediction of the extreme values for cases with H_s = 2 m and T_p = 6 s but overpredicts the results for cases with H_s = 1 m and T_p = 5 s.

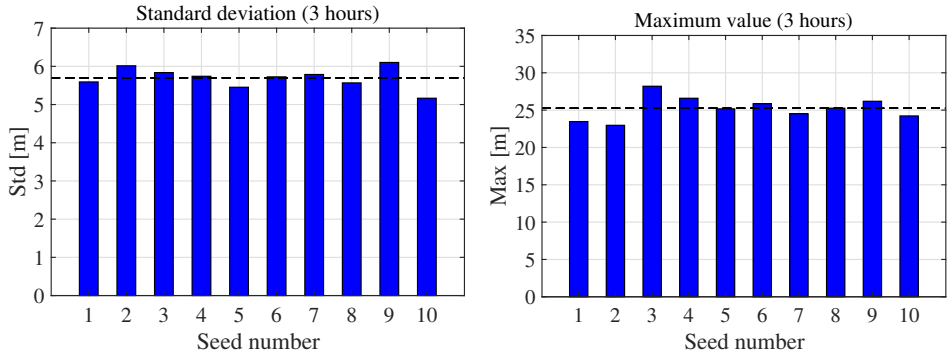

Figure 6.16: Standard deviation (left) and maximum value (right) of the slow-drift sway motion from different realizations with only mean wave-drift damping considered. The considered H_s = 2 m, T_p = 6 s, U_∞ = 0 m/s. The numbering along the horizontal axis represents the use of different random-phase seeds to generate the incident irregular waves. In each plot, the dashed line represents the expected value, taken as the mean value from different realizations.

Figure 6.16 presents the standard deviation and maximum value of the slow-drift motion from ten different realizations with H_s = 2 m and T_p = 6 s. The first 3-hour simulation of each realization is considered. The corresponding mean standard deviation and mean maximum value are shown in Figure 6.15. Figure

6.16 shows that both the standard deviation and the maximum value are realization dependent. At least 10-20 realizations are needed to have a robust estimation of the two examined variables.

Eddy-making damping

In this section, the analysis of the slow-drift sway motion is carried out assuming that the slow-drift damping is only associated with the eddy-making damping. Figure 6.17 presents the influence of the ship averaged drag coefficient on the expected standard deviation and on the largest value of the slow-drift motion in irregular waves. Two different wave conditions are considered with $H_s = 2$ m, $T_p = 6$ s (left column) and with $H_s = 1$ m, $T_p = 5$ s (right column), respectively. Two different ship averaged drag coefficients $C_D = 2.2$ and 0.9 are examined, corresponding to the value for oscillatory flow (KC =8) and for steady flow, respectively. The main purpose to use two different C_D is to examine the sensitivity of the slow-drift motion to C_D. Detailed explanations are given below.

- Irregular waves with $H_s = 2$ m, $T_p = 6$ s:

  The expected standard deviations obtained from both time-domain and frequency-domain solutions are provided and agree for the two C_D values, see the upper plot in Figure 6.17. The eddy-making damping is linearized according to Eq. (5.18) in the frequency-domain solution. The ratio between the linearized damping and the critical damping is $\xi = 16.2\%$ and 8.89%, respectively, when $C_D = 2.2$ and 0.9 are used. For 3-hour simulated time, the expected standard deviations are 4.08 m and 5.65 m, respectively, for the two values of the C_D, indicating approximatively a dependence on C_D as $C_D^{-1/3}$, consistently with that shown in Eq. (5.23). In terms of the expected largest values, the Rayleigh distribution underpredicts while the exponential distribution overpredicts them for both C_D values. The predictions by Stansberg's method agree well with the time-domain values, see the lower two plots in the figure.

- Irregular waves with $H_s = 1$ m, $T_p = 5$ s:

  In this case, the ratio between the linearized eddy-making damping and the critical damping is $\xi = 6.48\%$ and 3.54%, respectively, when $C_D = 2.2$ and 0.9 are used. The exponential distribution and the Stansberg's method tend to overpredict the expected largest value while the Rayleigh distribution can well predict this value especially when the damping is small (i.e., $C_D = 0.9$ for which $\xi = 3.54\%$).

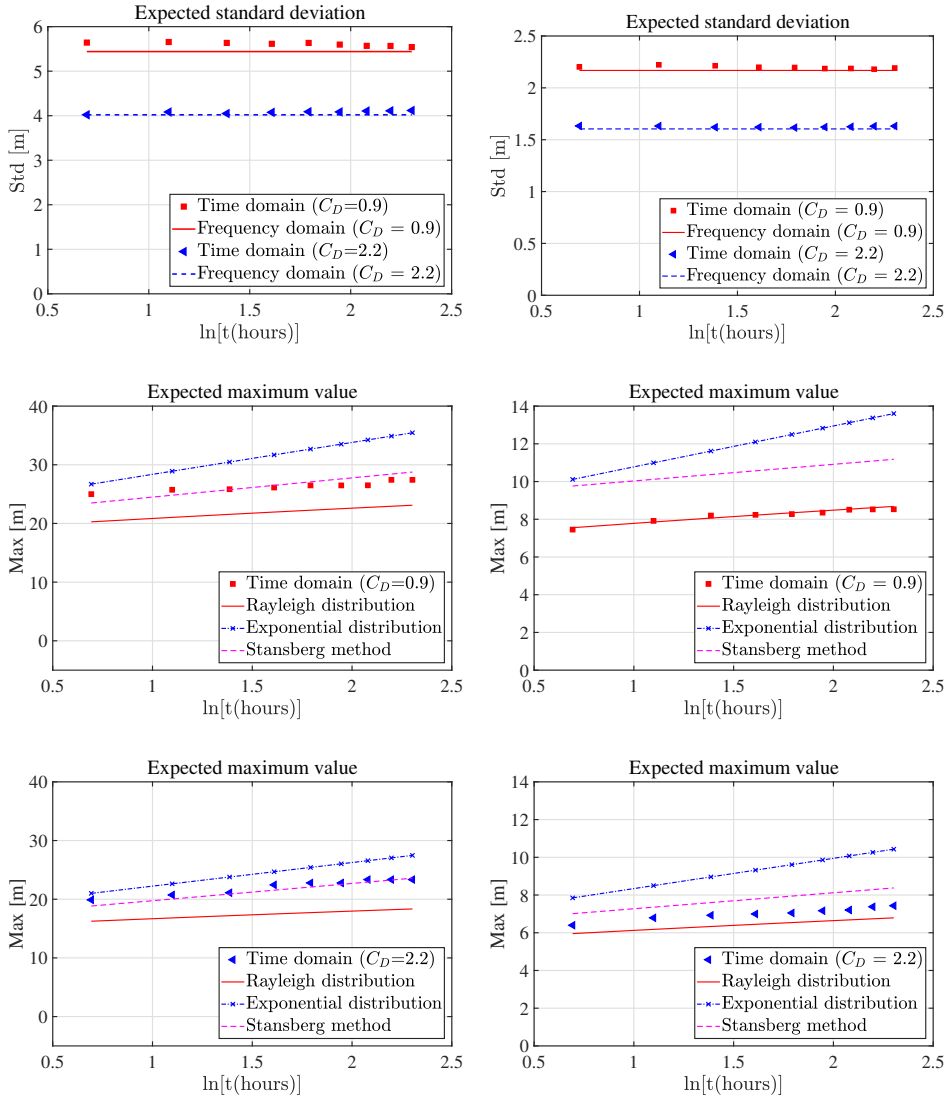

Figure 6.17: Expected standard deviation (upper) and maximum value (middle with $C_D = 0.9$ and lower with $C_D = 2.2$) of the slow-drift sway motion. Only the eddy-making damping is included. Full symbols: time-domain results. Left: $H_s = 2$ m, $T_p = 6$ s, $U_\infty = 0$ m/s. Right: $H_s = 1$ m, $T_p = 5$ s, $U_\infty = 0$ m/s. The expected maximum values predicted by Rayleigh distribution, exponential distribution and Stansberg's method are also provided.

The influence of current on the slow-drift motion is also examined. In particular, a current velocity $U_\infty = 0.3$ m/s leads to the results shown in Figure 6.18. The considered current velocity corresponds to a small to moderate current condition,

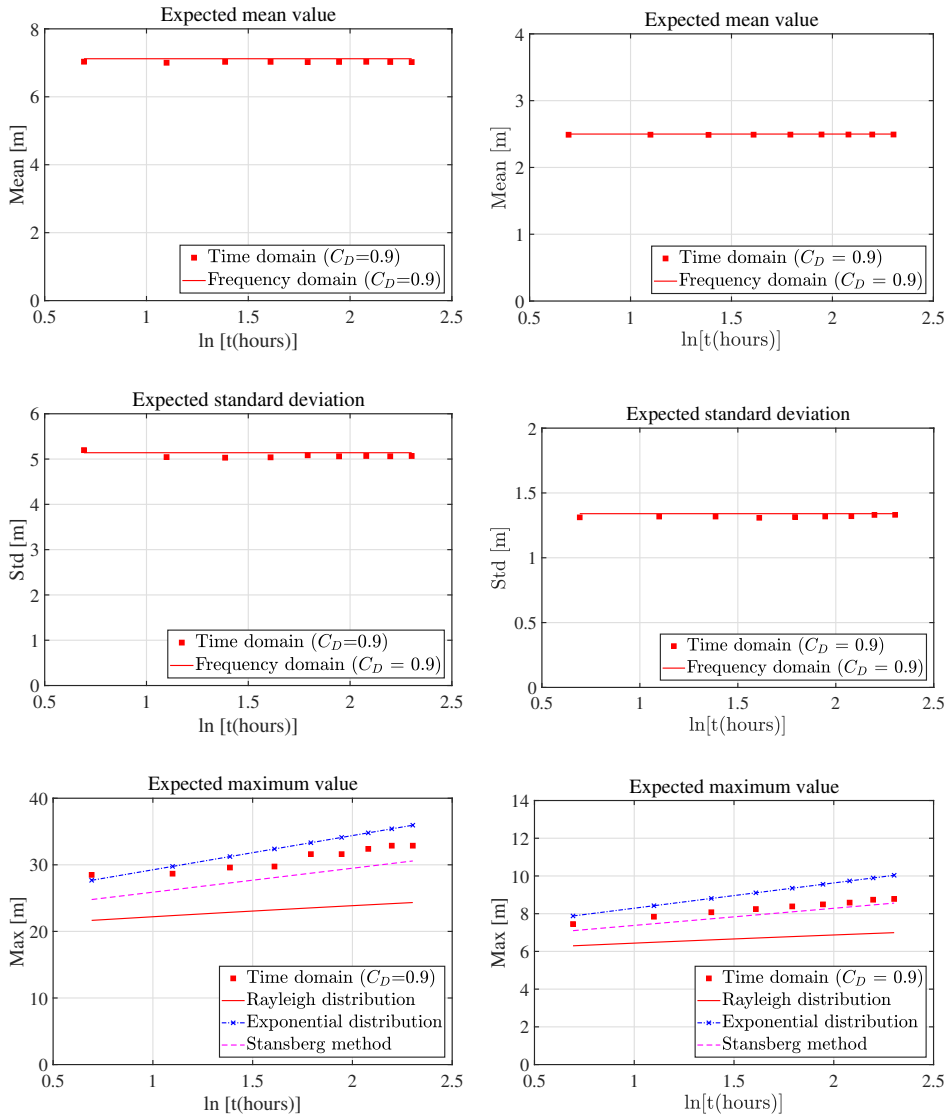

Figure 6.18: Expected mean value (upper), standard deviation (middle) and maximum (lower) value of the slow-drift sway motion of the well boat. Only the eddy-making damping is included. Upper: $H_s = 2$ m, $T_p = 6$ s, $U_\infty = 0.3$ m/s. Lower: $H_s = 1$ m, $T_p = 5$ s, $U_\infty = 0.3$ m/s. The predicted maximum value based on Rayleigh distribution, exponential distribution and Stansberg's method are also shown.

see Table 1.2. As explained in section 5.3.2, the steady-flow drag coefficient should be used for cases in combined oscillatory flow and current when estimating the eddy-making damping. Therefore, a ship averaged drag coefficients $C_D = 0.9$ is adopted

following the analysis in steady current documented in Chapter 5. From the figure, the expected mean values and standard deviations from frequency domain match nicely with the time-domain results for both examined sea states. The eddy-making damping is linearized according to Eq. (5.18) in the frequency-domain solution and the ratio between the equivalent linearized damping and the critical damping is $\xi = 13.86\%$ and 12.69% for cases with $H_s = 2$ m and 1 m, respectively. Compared with the value without current, we can see that the presence of current significantly increases the ratio ξ, changing ξ from 8.89% to 13.86% for $H_s = 2$ m and $T_p = 6$ s and from 3.54% to 12.69% for $H_s = 1$ m and $T_p = 5$ s. When estimating the mean value of the sway motion in frequency domain, apart from the contribution from mean-wave load, the influence of current in connection with mean-drag force in sway should be also considered and written as

$$\begin{aligned} &\frac{1}{T_N}\int_0^{T_N} B_D\left(\dot{\eta}_2^{(2)} - U_\infty\right)\left|\dot{\eta}_2^{(2)} - U_\infty\right| dt \\ &\approx \frac{1}{T_N}\int_0^{T_N} B_D\left[\dot{\eta}_{2a}^{(2)}\cos\left(\mu_N t\right) - U_\infty\right]\left|\dot{\eta}_{2a}^{(2)}\cos\left(\mu_N t\right) - U_\infty\right| dt \end{aligned} \tag{6.6}$$

Here T_N is the damped natural period of the slow-drift motion considering linearized eddy-making damping, $\dot{\eta}_{2a}^{(2)} \approx \sqrt{2}\sigma_{\dot{\eta}_2^{(2)}} \approx \sqrt{2}\mu_N\sigma_{\eta_2^{(2)}}$ is the characteristic velocity amplitude of the slow-drift motion, $\mu_N = 2\pi/T_N$ is the natural wave frequency. $\sigma_{\dot{\eta}_2^{(2)}}$ and $\sigma_{\eta_2^{(2)}}$ are the standard deviation of the slow-drift velocity and motion in sway, respectively. There exists also theoretical solution for the expected mean-drag force (Price and Bishop, 1974), given as

$$B_D\left\{-\frac{2U_\infty\sigma_{\dot{\eta}_2^{(2)}}}{\sqrt{2\pi}}\exp\left(-\frac{1}{2}\frac{U_\infty^2}{\sigma_{\dot{\eta}_2^{(2)}}^2}\right) - \left(\sigma_{\dot{\eta}_2^{(2)}}^2 + U_\infty^2\right)\Phi\left(\frac{U_\infty}{\sqrt{2}\sigma_{\dot{\eta}_2^{(2)}}}\right)\right\} \tag{6.7}$$

Here Φ is the error function, see Eq. (5.19). The mean-drag forces predicted by Eq. (6.6) and Eq. (6.7) are quite close.

For the expected largest value, when current is present, the exponential distribution can provide a reasonable prediction of this variable, especially for sea state with $H_s = 2$ m and $T_p = 6$ s, while Stansberg's solution yields better results for cases with $H_s = 1$ m and $T_p = 5$ s.

Influence of the first-order motion on the slow-drift sway response

When evaluating the eddy-making damping, it is not common to account for the first-order velocity. However, this may matter for the slow-drift sway motion. To include the first-order velocity, we need to solve the first-order motion and slow-drift motion simultaneously, see Eq. (5.5). Time histories of the sway motion of the well boat without and with including the first-order motion are shown in Figure 6.19. For the slow-drift damping, only the eddy-making damping is considered to

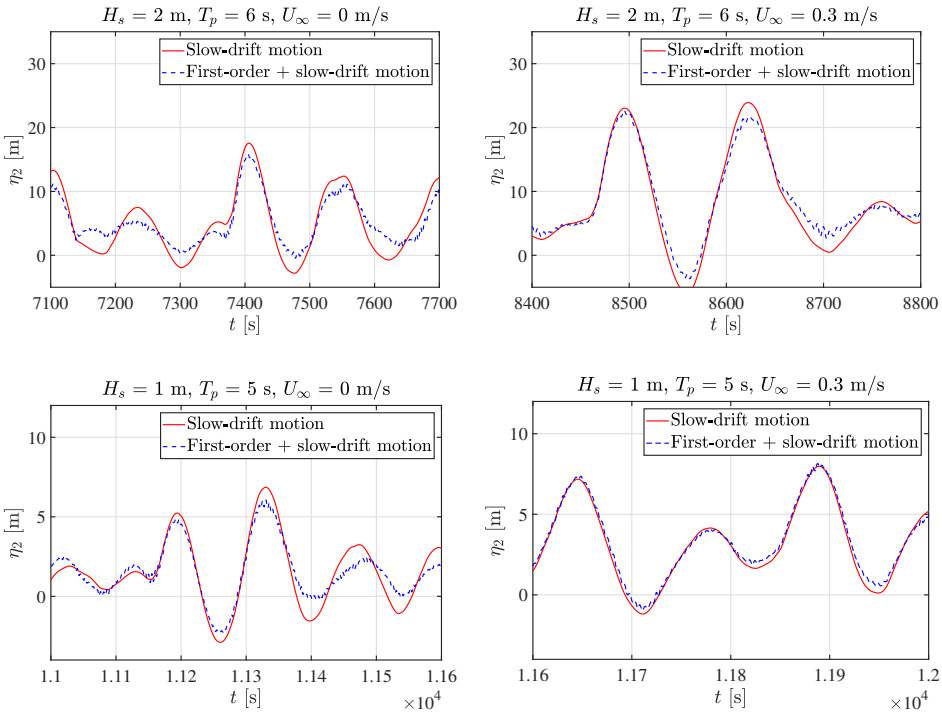

Figure 6.19: Time histories of the slow-drift sway motion of the well boat without and with considering the first-order motion. Upper: $H_s = 2$ m, $T_p = 6$ s. Lower: $H_s = 1$ m, $T_p = 5$ s. Left: irregular waves only ($U_\infty = 0$ m/s). Right: irregular waves and current ($U_\infty = 0.3$ m/s).

reduce complexity, which means that B_{22}^{SD} in Eq. (5.5) is set to zero. The figure shows that considering the first-order motion will reduce the maximum value of the slow-drift motion when $U_\infty = 0$ m/s (left plot), but will have a much smaller influence when $U_\infty = 0.3$ m/s (right plot). The presented results also show that the first-order motion is small compared with the slow-drift component for the considered sea states.

6.2.3 Dynamic response of the coupled well boat-fish farm system

In this part, we present a numerical investigation of the coupled well boat-fish farm system in irregular waves and current. The main purpose is to see how the presence of the well boat will influence the behavior of the fish farm and in this respect to determine the operational conditions of the well boat. The slow-drift sway motion of the well boat with a simplified mooring system has been studied and verified in section 6.2.2. The numerical model for the fish-farm system has been validated against experimental data in Chapter 4. This suggests that the numerical results

of the coupled system can be reasonable and suitable for the analysis of well-boat operational limits in waves and current. Long-crested irregular waves and current in positive x_E direction (see Figure 5.1) are assumed. As shown in Section 6.1, the coupled system with set-up A (see Figure 5.3), with the well boat placed at the weather side of the floating collar, is the most critical in terms of anchor-line loads and floating collar stresses, so this set-up is also our research focus here. Results for set-up C, also shown in Figure 5.3, will be considered in selected cases for comparison. Nominal results are first shown. The main attention is paid to the load in anchor line-1 (defined in Figure 5.1) and to the floating-collar stresses, which are two important parameters for the structural integrity of the fish farm. Then a sensitivity analysis is carried out to identify important parameters affecting the maximum anchor loads and floating-collar stresses. Lastly, systematic simulations are performed to determine the operational conditions of the well boat.

Nominal results

In the nominal simulations, we try to model the coupled system as complete as possible. For the well boat, both the first-order motions and the slow-drift motions are included. The first-order motions are solved by the classical linear potential-flow theory, including all the six-degree-of-freedom motions shown in Eq. (5.1). In terms of the slow-drift motions, the slow-drift surge, sway and yaw motions can be considered. For the coupled system with set-up A, the well boat is placed at the weather side of the fish farm, the slow-drift surge and yaw motions are expected to be small, therefore they are not considered in the simulations, i.e. only the slow-drift sway motion is included. Concerning the wave-drift damping, both the mean and the slowly-varying wave-drift damping are included. When formulating the eddy-making damping, both the first-order velocity and slow-drift velocity are accounted for. This means that the first-order motions and slow-drift motions need to be solved simultaneously. In terms of the fish farm, a realistic set-up (with single cage) is considered, including a floating collar, an elastic sinker tube, a flexible-closed net cage and a complex mooring system. The final motion equations of the well boat are similar to Eq. (5.5), but for the six rigid degrees of freedom. The restoring provided by the fish farm is represented by contact and connect-line forces, as explained in Chapter 5.

Time histories of the sway motion of the well boat in irregular waves and in combined irregular waves and current are shown, respectively in the left and right plot of Figure 6.20. The duration of the simulations is 3 hours. The considered environmental parameters are: significant wave height $H_s = 1$ m and peak period $T_p = 5$ s for the waves, and current velocity $U_\infty = 0$ m/s and 0.3 m/s. The ship averaged drag coefficients $C_D = 2.2$ and 0.9 are adopted, respectively, for $U_\infty = 0$ m/s and $U_\infty = 0.3$ m/s. From the figure, the presence of current increases the maximum sway motion from 6.33 m to 8.03 m, with an increment of about 26.4%. The figure also shows that the slow-drift motion dominates over the wave-frequency component for both cases, similarly to the results for the simplified system in Figure 6.19. The coupled system in sea state with $H_s = 2$ m and $T_p = 6$ s is also investigated and numerical results (not shown here) indicate that the maximum

sway motion increases with similar magnitude due to the current. In particular, the increment is about 22%, with a change from 14.12 m to 17.23 m.

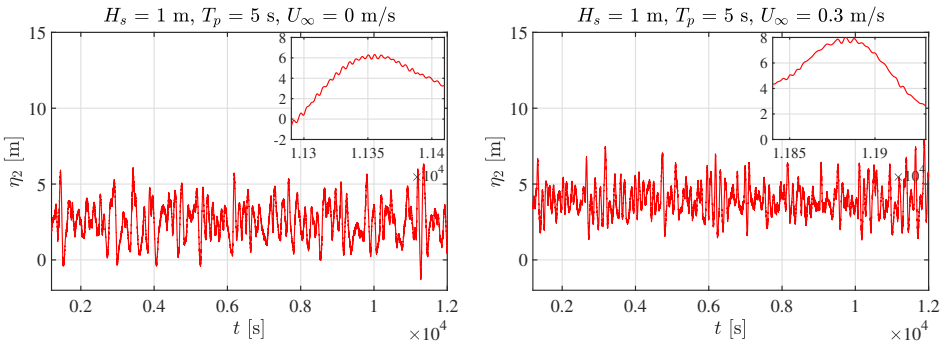

Figure 6.20: Time histories of the sway motion of the well boat when placed at the weather side of a fish farm (set-up A). A zoomed view is also given when the motion reaches the largest maximum within the examined simulated time (3 hours). Left: $H_s = 1$ m, $T_p = 5$ s and $U_\infty = 0$ m/s. Right: $H_s = 1$ m, $T_p = 5$ s and $U_\infty = 0.3$ m/s.

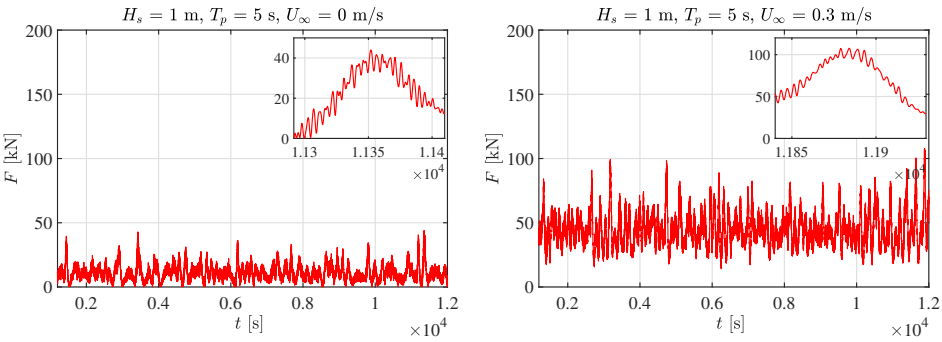

Figure 6.21: Same as in Figure 6.20, but for the loads in anchor line-1.

Figure 6.21 shows the time histories of the loads in anchor line-1 for the coupled system in sea state with $H_s = 1$ m and $T_p = 5$ s. From the figure, the wave-frequency component is small compared with the total anchor load, especially for the case with current. The time instant when the anchor load reaches the largest maximum coincides with that when the largest sway motion occurs within the examined simulated time (see Figure 6.20). The presence of current increases the maximum anchor load significantly, from 44 kN to 107.5 kN. There are two reasons: (1) the maximum sway motion of the well boat increases due to the current and (2) viscous loads on the net cage increase due to the current. Without the well boat, the maximum anchor loads are about 10 kN and 29 kN for $U_\infty = 0$ m/s and 0.3 m/s, respectively. It means that the well-boat presence increases the maximum anchor load by more than 300% both without and with current. When the coupled

system is exposed to more severe sea states with $H_s = 2$ m and $T_p = 6$ s, the maximum anchor loads are 167 kN and 300 kN, respectively, for $U_\infty = 0$ m/s and 0.3 m/s. Without the well boat, much smaller maximum values are obtained, approximately 16.2 kN and 44 kN, respectively.

Next, we show the results of the bending stresses in the floating collar due to its horizontal deformations. The stresses are estimated according to Eq. (6.1). The maximum stress is expected to occur at $\beta = 180^o$ where the well boat is in contact with the floating collar, see Figure 6.6. Time histories of the stress at $\beta = 180^o$ in the floating collar are shown in Figure 6.22 for $H_s = 1$ m and $T_p = 5$ s. The largest maximum stress occurs at the time when the sway motion of the well boat reaches the largest maximum value within the examined simulated time. The maximum stresses are 0.48 σ_0 and 0.7 σ_0, respectively, for $U_\infty = 0$ m/s and 0.3 m/s. Here σ_0 is the yield stress (high-density polyethylene) for the floating collar. The obtained maximum stress for $U_\infty = 0.3$ m/s is close to the yield stress. This indicates that the examined sea conditions are of relevance when determining the operational conditions of the well boat.

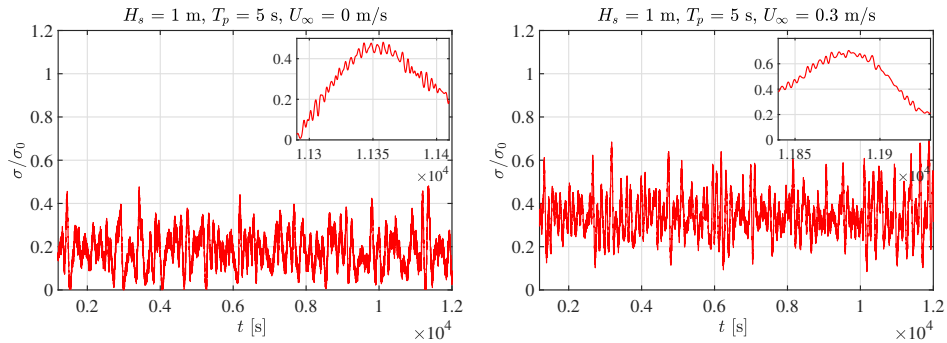

Figure 6.22: Same as in Figure 6.20, but for the stresses at $\beta = 180^o$ in the floating collar. The stress is made non-dimensional by the yield stress (high-density polyethylene).

To see more clearly how the well boat will influence the floating collar, the stress distributions along the floating collar due to horizontal deformations without and with the well boat are shown in Figure 6.23. Results for the coupled system with set-up C (see Figure 5.3) are also given for comparison. Two wave conditions with $H_s = 1$ m, $T_p = 5$ s and with $H_s = 2$ m, $T_p = 6$ s, respectively, are considered. Each wave condition is combined alternatively with two current velocities, $U_\infty = 0$ m/s and 0.3 m/s. From the figure, the presence of the well boat will change the stress distribution along the floating collar. For fish farm only, there are several peak values with similar amplitude along the floating collar. For the coupled system, the maximum stress occurs at the region where the well boat is in contact with the floating collar, respectively, at $\beta = 180^o$ for set-up A and at $\beta = 270^o$ for set-up C. For cases with $H_s = 1$ m and $T_p = 5$ s, without the well boat, the maximum stresses are about 0.08 σ_0 and 0.17 σ_0, respectively, for $U_\infty = 0$ m/s and 0.3 m/s while for the coupled system, with set-up A the corresponding values are 0.48 σ_0

and 0.7 σ_0 and with set-up C the corresponding values are 0.27 σ_0 and 0.35 σ_0. The results show that the maximum stresses increase significantly due to the well boat and that the coupled system with set-up A is more critical, as expected.

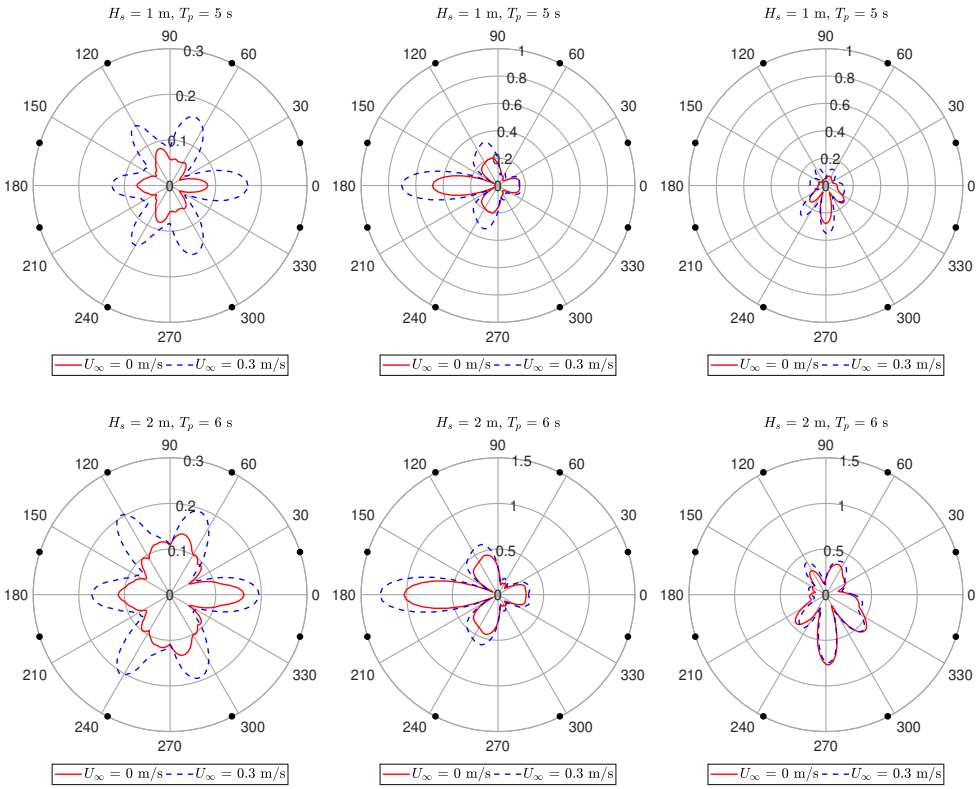

Figure 6.23: Maximum stress distribution along the floating collar due to horizontal deformations. The stress is made non-dimensional by the yield stress (high-density polyethylene). Left: fish-farm system only. Middle: coupled system with set-up A. Right: coupled system with set-up C. Upper: H_s = 1 m and T_p = 5 s. Lower: H_s = 2 m and T_p = 6 s. Solid lines: U_∞ = 0 m/s. Dashed lines: U_∞ = 0.3 m/s. The 8 solid circles in each plot represent the positions where bridle lines are attached to the floating collar.

For cases with H_s = 2 m and T_p = 6 s without the well boat, the maximum stresses are about 0.162 σ_0 and 0.195 σ_0 for U_∞ = 0 m/s and 0.3 m/s, respectively, while for set-up A the corresponding values are 1.03 σ_0 and 1.3 σ_0 and for set-up C the corresponding values are 0.74 σ_0 and 0.76 σ_0. The results show that the maximum stress for the coupled system with set-up A will exceed the yield stress for the considered H_s sea state even without current. One should note that, for the coupled system with set-up C, the well boat will have a pendulum motion relative to the floating collar, see Figure 6.24. If one more rope is used to connect the well boat and the floating collar, inserted between the two existing ropes and with

connecting position at the floating collar $\beta = 270^{o}$, a significant reduction of the maximum stress ($\approx 30\% - 40\%$) with respect to the original value is observed.

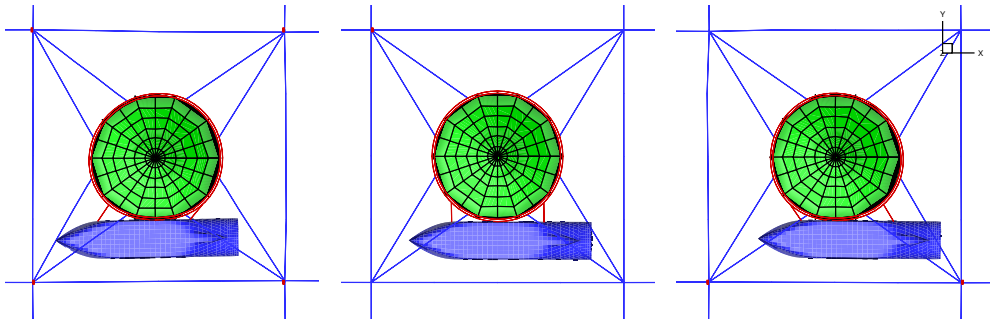

Figure 6.24: Sketch for the coupled system with set-up C in three different time instants showing the pendulum motion of the well boat relative to the floating collar.

6.2.4 Sensitivity analysis

Due to uncertainties in the mathematical modeling and system set-up, we performed a sensitivity analysis for the coupled system in irregular waves and current. The main focus is on the maximum loads in anchor line-1 (defined in Figure 5.1) and the maximum stresses in the floating collar. The inflow is in the positive x_E direction ($\alpha_c = 0^{o}$, $\alpha_w = 0^{o}$). The well boat is assumed to be placed at the weather side of the fish farm (set-up A).

For the irregular waves, $H_s = 1$ m and $T_p = 5$ s, are considered, combined with two current conditions, i.e. $U_\infty = 0$ m/s and 0.3 m/s. The different parameters examined are shown in Table 6.2. In order to quantify their significance and try to identify the critical ones, we present condensed results in Figure 6.25 for the maximum load in anchor line-1 and in Figure 6.27 for the maximum stress in the floating collar. Each bar represents the percentage difference with respect to the corresponding nominal value. Parameters that lead to more than 5% difference from the nominal value are considered to be important. More detailed discussions are presented below for the anchor loads and the floating collar stresses, respectively.

Table 6.2: Parameters varied in the sensitivity analysis for cases in irregular waves and current. $C_{D,0}$ and $k_{s,0}$ are, respectively, the ship averaged drag coefficient and the anchor-line stiffness used in the nominal simulations. $C_{D,0} = 2.2$ and 0.9 for cases without and with current, respectively. N_h and N_v are the number of structural modes used for the floating collar, respectively, in horizontal and vertical directions and $N_h = 7$ and $N_v = 8$ are found from convergence studies and used in the nominal simulations. The shading effect of the well boat on the floating collar is not considered in the nominal simulations. The nominal value of the pretension force in the anchor line is 10 kN.

	No.	Value	Explanation
Wellboat	1	$C_D = 1.2C_{D,0}$	Drag coefficient
	2	$C_D = 0.8C_{D,0}$	Drag coefficient
	3	$\bar{B}_{22}^{SD}$	Mean wave-drift damping
	4	Zero frequency	Added mass
	5	$\eta_2^{(2)} + \eta_2^{(1)}$	First-order + slow-drift motion, cage neglected
	6	$\eta_2^{(2)}$	Slow-drift motion, with cage
	7	$\eta_2^{(2)}$	Slow-drift motion, cage neglected
Floating collar	8	$N_h = 3$, $N_v = 4$	Less modes
	9	$f^{\text{exc}} = 0$	Excitation force (shading effect)
Moorings	10	Pretension = 5 kN	Pretension
	11	Pretension = 15 kN	Pretension
	12	$k_s = 2.0k_{s,0}$	Anchor line stiffness

Loads in anchor line-1

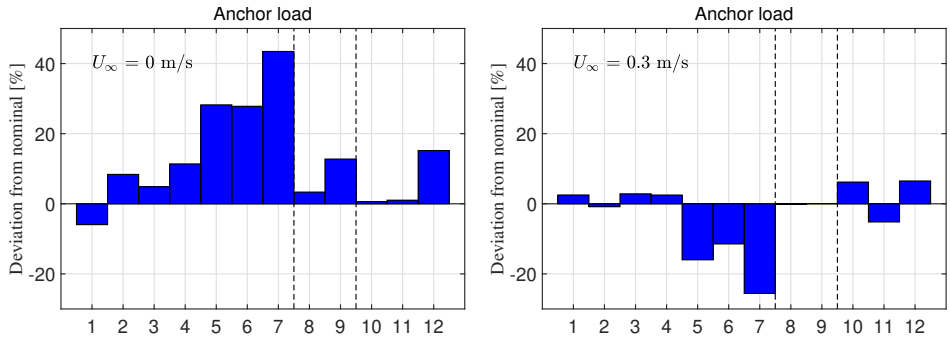

Figure 6.25: Each bar represents the percentage difference of the anchor load (maximum value) with respect to the nominal value. The considered $H_s = 1$ m and $T_p = 5$ s. The numbers on the horizontal axis refer to the variation numbers as given in Table 6.2. Left: $U_\infty = 0$ m/s. Right: $U_\infty = 0.3$ m/s.

Well boat: The maximum anchor load is closely connected with the slow-drift sway motion of the well boat, so the main attention in the sensitivity analysis is paid to parameters that may be important for the slow-drift motion.

First we examine the influence of the ship averaged drag coefficient. The cross-sectional drag coefficients C_D for the well boat are estimated empirically and assumed KC-number independent in the nominal simulations. In reality, C_D may slightly vary with KC for small KC number. Furthermore, the influence of first order motions on C_D is not considered. So an error in the boat drag coefficient is expected. Changing the ship averaged drag coefficient by 20% will lead to about 6%-8% change of the maximum anchor load with respect to the nominal value when $U_\infty = 0$ m/s. Negligible influence is observed for the case with current.

For the wave-drift damping, considering the mean wave-drift damping instead of the time-varying wave-drift damping will lead to a moderate increase of the maximum anchor load, by about 5% and 3%, respectively, for cases without and with current. This indicates that considering only the mean wave-drift damping is sufficient for the examined wave condition.

Next, we want to quantify how the maximum anchor load will be influenced when simplified modeling of the coupled system is adopted. The main purpose of simplifying the modeling is to increase the computational efficiency.

In the nominal simulations, for sea state with $H_s = 1$ m and $T_p = 5$ s, a time step in the range of 0.03 s is needed to reach convergence and it takes about 4.8-5 hours computational time on a 3.0 GHZ one-core laptop for a simulated time $t_s = 3$ hours. For more severe sea states, smaller time step is needed and greater computational time is expected. Although the developed numerical solver is efficient

enough compared with available commercial softwares, it is still interesting to see whether it is possible to increase the computational efficiency by simplifying the numerical modeling, while still preserving reasonable accuracy. In the following analysis, in terms of the wave-drift damping, only the mean wave-drift damping is considered in the simulations.

Net cage: Modeling the net cage is challenging in the simulations and the latter may more easily break down with the presence of net cage due to the occurrence of unphysical negative tensions, especially in irregular waves with higher H_s. Neglecting the net cage, i.e. modeling the fish-farm effect only in terms of the mooring lines and the floating collar, will increase the maximum anchor load by about 28% when $U_\infty = 0$ m/s, but will reduce the value by about 15.9% when $U_\infty = 0.3$ m/s. The maximum sway motion of the well boat will increase if the net cage is neglected, this will tend to increase the maximum anchor load, but neglecting the net cage means that the loads on the net cage are not included, this will tend to reduce the maximum anchor load. So the actual change of the maximum anchor load with respect to its nominal value depends on the joint effects of these two factors. The fact that the maximum anchor load increases without current will then mean that in this case the increase of sway motion dominates with respect to the net-cage loads not included, while the opposite occurs in current. Neglecting the net cage will reduce the computational time by about 20%.

First-order motion: To predict the first-order motions of the well boat, transient effects are included in the motion equations. This is time consuming.

Neglecting the transient effects and using zero-frequency added mass coefficients for the well boat will lead to an increase of the maximum anchor load by 11.4% when $U_\infty = 0$ m/s. For the case with current, negligible influence is observed. The computational time will reduce by about 23%.

Neglecting the first-order response, i.e., only considering the slow-drift motions for the well boat and the fish farm, will increase the maximum anchor load by about 28 % when $U_\infty = 0$ m/s, but will reduce the value by about 11.5% when $U_\infty = 0.3$ m/s. The computational time will be reduced by about 50% when only the slow-drift motions are considered.

First-order motion + net cage: If both the first-order motion and the net cage are neglected, the maximum anchor load will increase by about 43% when $U_\infty = 0$ m/s but will reduce by about 26% when $U_\infty = 0.3$ m/s. The computational time will be reduced by about 90%.

Selected fish-farm related parameters are also examined and detailed results are given in the following.

Floating collar: The influence of the number of modes used for the floating collar is studied and numerical results indicate that modeling the floating collar

with less modes in both the lateral and vertical directions will have small influence on the maximum anchor load.

The shading effect of the well boat on the floating collar is not considered in the nominal simulations and is investigated here. Only the case with $U_\infty = 0$ m/s is examined. As an example, the wave excitation forces of the floating collar in heave and surge directions with and without the presence of the well boat are shown in Figure 6.26. The hydrodynamic loads for both cases are estimated by the linear potential-flow solver WAMIT. From the figure, the excitation forces of the floating collar are significantly reduced due to the presence of the well boat in shorter waves ($T < 6$ s), which is relevant for the present study. Therefore, for simplicity, to account for the shadowing effect we assume the excitation forces of the floating collar to be zero for all wave periods in the sensitivity analysis and a 12.7% increase of the anchor load is observed with respect to the nominal value. WAMIT simulations showed that the hydrodynamic loads on the well boat are instead almost not influenced by the floating collar (not shown here).

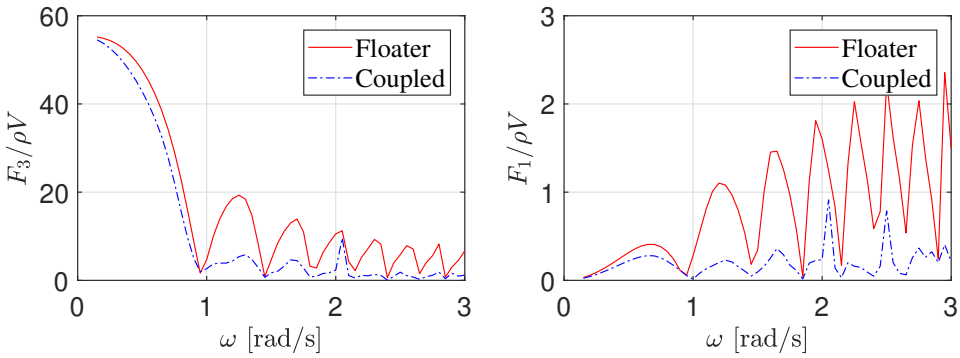

Figure 6.26: The effect of the well boat on the wave excitation forces of the floating collar. Solid line: the floating collar only. Dash-dotted line: the well boat placed at the weather side of the floating collar. Left: heave force. Right: surge force. Forces are made non-dimensional by the displacement of the floating collar. V is the displacement volume of the floating collar when half submerged.

Mooring system: In the nominal simulations, the pretension force in the anchor line is 10 kN. Increasing the pretension force by 50% or reducing the value by 50% will lead to a moderate influence on the maximum anchor load. Increasing the stiffness of anchor lines by 100% will increase the maximum anchor load by 15% when $U_\infty = 0$ and a smaller increment, i.e. about 6.5%, is observed when $U_\infty = 0.3$ m/s.

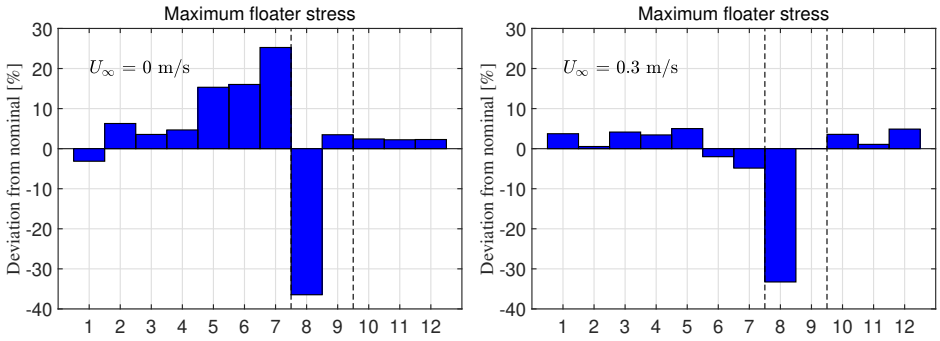

Figure 6.27: Same as in Figure 6.25, but for the maximum stress in the floating collar at the position $\beta = 180^o$.

Maximum stress in the floating collar

The sensitivity of the maximum stress to the different parameters is similar to that of the maximum anchor load when $U_\infty = 0$ m/s, but when $U_\infty = 0.3$ m/s the maximum stress is not sensitive to the majority of the examined parameters, with a maximum variation of about 5% with respect to the nominal value (see Figure 6.27). The only exception is parameter No.7 (see definition in Table 6.2), when less modes are used to model the floating collar. In nominal simulations, $N_h = 7$ and $N_v = 8$ are found sufficient for convergence purpose. If less modes are used with $N_h = 3$ and $N_v = 4$, a significant reduction of the maximum stress, about 35%, is observed. It implies that the elasticity of the floating collar must be properly modeled to have a reliable prediction of the maximum floating-collar stress.

6.2.5 Operational conditions

In this section, we will discuss how to determine the operational conditions of the well boat when at the fish farm for the loading/offloading operation. The well boat is moored at the weather side of the fish farm. As explained in Section 6.1.3, two operational criteria are proposed connected, respectively, with maximum forces in the mooring lines and maximum stresses in the floating collar.

In the present context, we mainly focus on the coupled well boat-fish farm system in irregular waves and current. The simulation matrix is shown in Table 6.3, covering the scenario from small exposure to high exposure, according to the Norwegian Standard (see Table 1.2). For sea states with $H_s = 2$ m, only irregular waves are considered ($U_\infty = 0$ m/s). The ship averaged drag coefficient $C_D = 2.2$ and 0.9 are adopted, respectively, for $U_\infty = 0$ m/s and $U_\infty > 0$ m/s. The duration of each simulation is 3 hours.

Numerical results of the force in anchor line-1 are given in Figure 6.28. Mean value, standard deviation and maximum value are provided. The maximum force experienced by the anchor line for the considered sea states is about $0.42F_0$ with $F_0 = 628$ kN the minimum breaking force for the considered anchor polysteel rope.

Table 6.3: Environmental matrix used in the simulations for determining the operational conditions, showing current velocity U_∞ and significant wave height H_s, respectively, in the first column and first row. Four current velocities and three significant wave heights are considered. The remaining cells give the examined peak-period T_p ranges. For each examined T_p range, an interval $\Delta T_p = 1$ s is used.

Current U_∞ [m/s]	H_s [m]		
	0.5	1	2
0.0	2-3 s	2-5 s	3-6 s
0.1	2-3 s	2-5 s	-
0.3	2-3 s	2-5 s	-
0.5	2-3 s	2-5 s	-

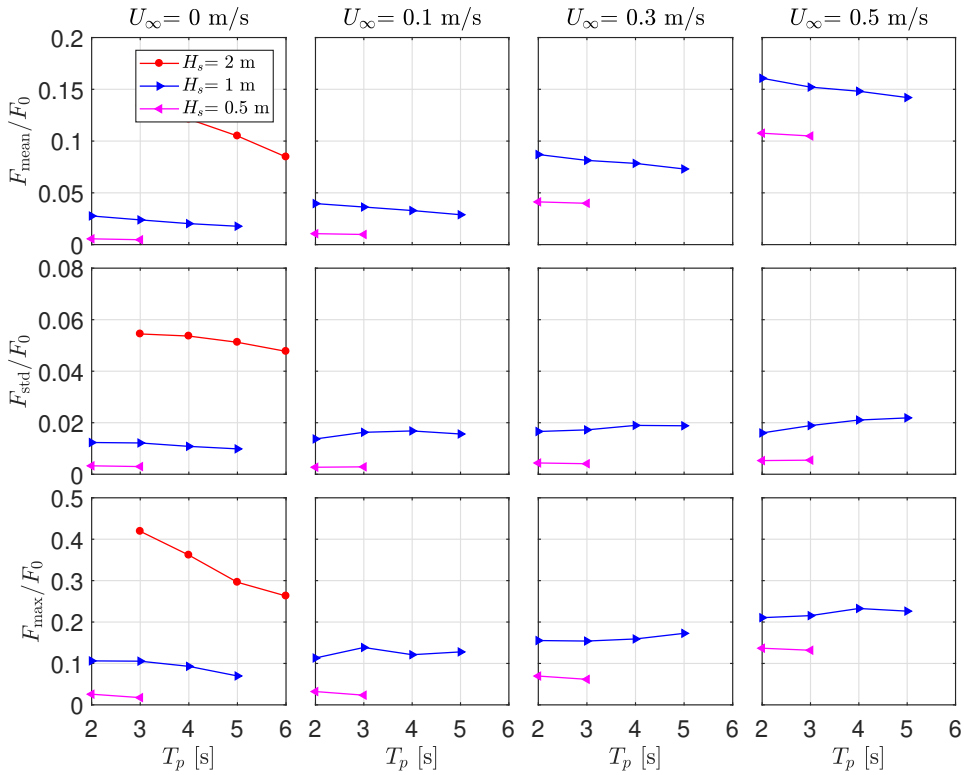

Figure 6.28: Mean value (upper row), standard deviation (middle row) and maximum value (lower row) of the force in anchor line-1. The force is made non-dimensional by the minimum breaking force F_0, which is 628 kN for polysteel rope with 3 strands and a diameter 64 mm. From left to right: current velocities U_∞ = 0 m/s, 0.1 m/s, 0.3 m/s, 0.5 m/s.

The maximum anchor load for the considered sea states is less than 50% of the breaking limit, so it should not be of concern. For a given H_s without current, all the three examined parameters decrease with increasing peak period T_p. For a given H_s with current, the mean anchor load decreases while the standard deviation and maximum value of the anchor load tend to increase with increasing T_p. For a given T_p and H_s, the maximum anchor load tends to increase with increasing U_∞.

The coupled system in regular waves and current is also examined. The main purpose is to check whether it is possible to use equivalent regular waves to represent the irregular waves, as done for the fish farm in Section 4.3.4. The results for the maximum force in anchor line-1 as a function of wave height are shown in Figure 6.29. Two wave steepness $H/\lambda = 1/60$ and $1/30$, two current velocity $U_\infty = 0$ m/s and 0.5 m/s, and nine wave period $T = 3$ - 7 s with an interval $\Delta T = 0.5$ s are considered. For the irregular waves with $H_s = 1$ m, the equivalent regular wave height will be $H = 1.9$ m, according to Table 1.2. The maximum anchor loads in regular waves with $H = 1.9$ m are $0.24F_0$ and $0.52F_0$ for the case with $U_\infty = 0$ m/s and 0.5 m/s, respectively. The corresponding values in irregular waves are $0.07F_0$ - $0.1F_0$ when $U_\infty = 0$ m/s and $0.21F_0$ - $0.22F_0$ when $U_\infty = 0.5$ m/s. The obtained values in regular waves are much higher than those in irregular waves because of unrealistic high mean wave-drift loads exerted on the boat. This implies that the technique to use equivalent regular waves is not applicable for the coupled system, although performing such simplified study is valuable in understanding some basic features of the system, as shown in Shen et al. (2016).

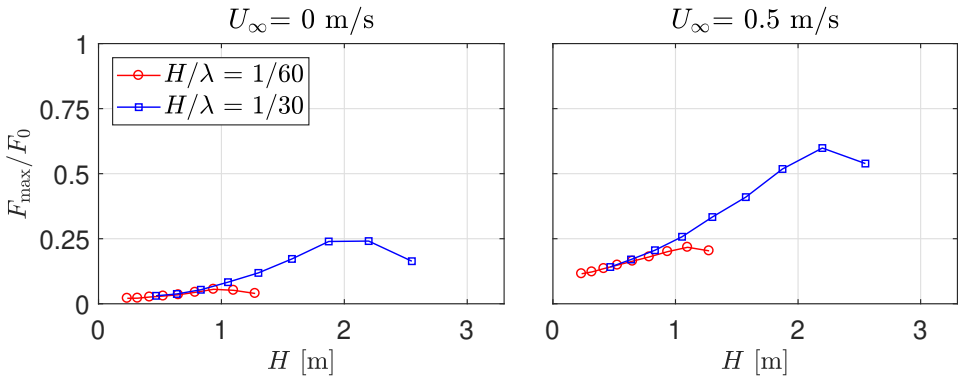

Figure 6.29: Maximum value of the force in anchor line-1 in regular waves and current versus wave height.

Finally, we show the numerical predictions of the maximum stress in the floating collar due to its horizontal deformations. The results for cases in current only in Section 6.1 showed that the maximum stress due to horizontal deformations occurs at the position $\beta = 180^o$ (defined in Figure 5.1) where the well boat is in contact with the floating collar. In Figure 6.30, we present the predicted maximum stresses at the position $\beta = 180^o$. From the figure, the maximum stress is influenced by the different environmental parameters in a similar way as for the maximum anchor

load. For a given H_s without current, the maximum stress tends to decrease with increasing T_p, especially for higher H_s, while an opposite trend is observed in current. One possible reason for the difference is that the presence of current changes the standard deviation's dependency on T_p, as shown in Figure 6.30. For given H_s and T_p, a higher current velocity will lead to larger maximum stress. The maximum stress will exceed the yield stress σ_0 of the floating collar for sea states with $H_s = 2$ m. For cases with $H_s = 1$ m, the maximum stress predicted for the examined sea states is about $0.82\sigma_0$. This indicates that $H_s = 1$ m is relevant for determining the operational conditions of the well boat. It should be noted that just one realization is considered in the analysis and actual results in irregular waves are realization dependent for the considered simulated time, nevertheless they can still provide a valuable guidance for determining the operational conditions of the well boat. Also, we just examine the coupled system in the most critical scenario with long-crested irregular waves and current aligned. The coupled system in more general sea states should also be studied and possibly three-dimensional waves should be accounted for. This is left for future investigations.

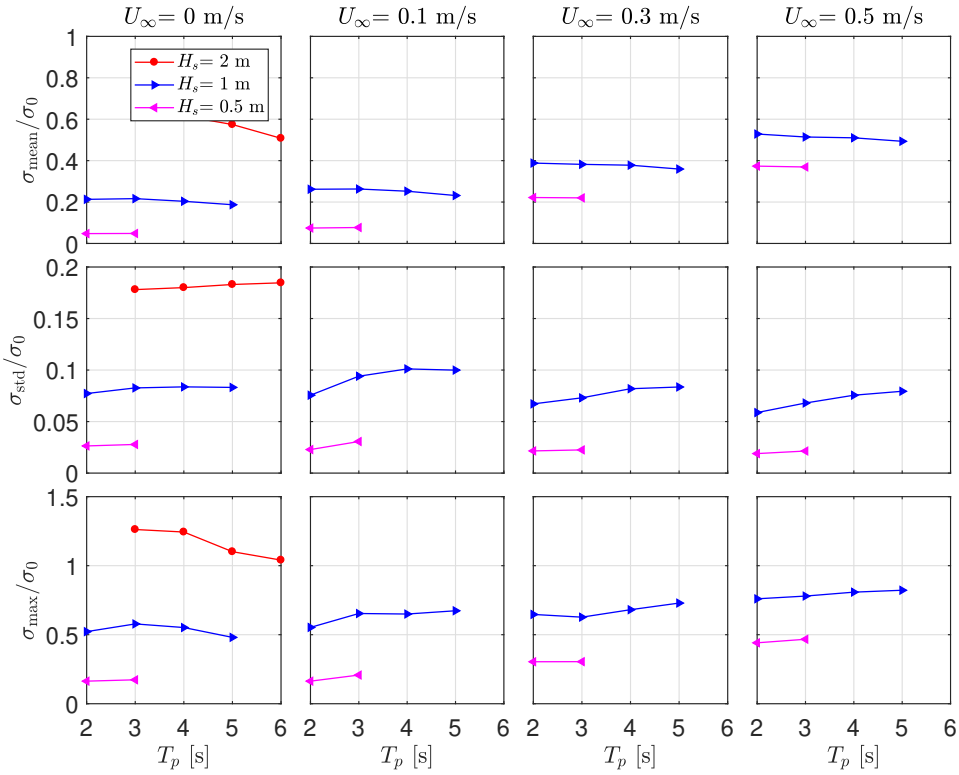

Figure 6.30: Same as in Figure 6.28, but for the stress in the floating collar at position $\beta = 180^o$. The stress is made non-dimensional by the yield stress (high-density polyethylene).

6.3 Conclusions

Numerical studies of a well boat operating at a fish farm in current only and in irregular long-crested waves and current have been performed. The main target was to assess the influence of the well-boat presence on the fish farm and to determine the operational conditions of the well boat. A modern design well boat and a realistic fish farm (with a single cage) were considered in the analysis. Both the well boat and the fish farm were modeled with state-of-the-art theoretical and numerical formulations.

- The coupled system in current:

  The viscous cross-flow loads on the well boat without the net cage and mooring loads on the net cage without the well boat are numerically predicted with experimentally validated methods. However, there is a need for model tests with the coupled system.

  Detailed analysis of the load in one of the front anchor lines and of the floating collar motions performed when the well boat is moored at the weather side of the fish farm. The current transverse viscous loads on the boat were estimated by the cross-flow principle and the cross-sectional drag coefficients were estimated empirically. Numerical results showed that the anchor load increases significantly due to the viscous forces on the boat. A big increase of the floating collar horizontal deformations (both rigid and elastic modes) was also observed and the maximum stress due to the horizontal deformations occurs at the region where the well boat is in contact with the floating collar.

  Due to uncertainties in mathematical modeling and system parameters, a systematic sensitivity analysis was performed, to identify the dominant factors when modeling the coupled system. The main focus was on the load in anchor line-1 and the maximum stress in the floating collar. In order to have a more reliable prediction of the anchor load, we should know more accurate values of the environment related parameters (current direction); the fish-farm related parameters (weight system including sinker tube depth, sinker tube weight and center point weight) and the mooring system properties (pretension load, anchor chain weight). In particular, lifting the sinker tube up to half of its original depth would lead to a significant reduction of the anchor load, by about 16.8%. Accurate estimation of the cross-sectional drag coefficients for the well boat and of the shading effect on the net inflow due to the well boat are not straightforward. However the sensitivity analysis showed that they have moderate effect on the anchor loads. In terms of the maximum floating collar stress, it is more sensitive to well-boat loads related parameters (current direction, cross-sectional drag coefficient) and pretension load in the anchor lines; less sensitive to parameters associated with the loads on the net cage (sinker tube depth, sinker tube weight, etc).

  Lastly, the operational conditions of the well boat when it operates at the fish farm were investigated. Two criteria were chosen: maximum loads in the mooring lines and maximum stresses in the floating collar. Numerical results showed

that the mooring system could withstand the loads transferred from the well boat for the considered current velocities. The maximum stresses in the floating collar reached values close to the yield stress for the examined maximum current velocity and should be a major concern.

- The coupled system in long-crested irregular waves and current:

  The slow-drift sway motion of the well boat was investigated at first by simplifying the influence of the net cage in terms of a restoring term. Hydrodynamic and statistical theories of the motion were presented. Numerical results indicated that both the mean and the slowly-varying wave-drift damping are important, especially for cases with larger significant wave height. When estimating the eddy-making damping, both first-order and slow-drift velocities should be included. The results also showed that Rayleigh distribution can be used to predict the extreme values when the damping is small (i.e. linearized damping $<$ 3-4% of the critical damping). For cases in combined irregular waves and current, both exponential distribution and Stansberg's method can have a reasonable prediction of the extreme values. The former is on the conservative side while the latter gives a slight underestimate. The simplified analysis involved an analytically-oriented approach and served as a verification of the complete time-domain analysis of the coupled well boat-fish farm system.

  A physical investigation of a coupled well boat-fish farm system was also performed, with the well boat moored at the weather side of the fish farm. Detailed analysis of the maximum load in one of the front anchor lines and of the maximum stress in the floating collar was given. Numerical results showed that both of them increase significantly due to the well boat. The increment can be more than 300% when the system operates in moderate exposure sea states.

  A sensitivity analysis was also performed to identify important factors influencing the maximum load in anchor line-1 and the maximum stress in the floating collar. The study showed that the examined two variables were in general more sensitive to the variation of different parameters for cases without current than with current. The cross-sectional drag coefficients for the well boat and the fish-farm related parameters, like the pretension load in the anchor lines and anchor-line stiffness, have moderate influence on the two variables. Sufficient number of structural modes for the floating collar should be used for a reliable prediction of the maximum floating-collar stress. Simplifying the modeling of the coupled system, for instance, neglecting the net cage and the first-order motion has more effect on the maximum anchor load than on the maximum floating-collar stress and smaller influence on the maximum floating-collar stress was observed when current is present.

  Lastly, the operational conditions of the well boat were investigated through systematic simulations. Two criteria were examined based on the limit for the maximum loads in the mooring lines and for the maximum stress in the floating collar, respectively. Numerical results showed that the maximum anchor load will not exceed the anchor-line breaking limit even in high exposure sea conditions and thus it should not be of concern. The maximum stress in the floating collar

would be close to the yield stress when the system operates in moderate exposure sea states, and should be used to determine the operational conditions of the well boat. The conclusions are similar to those in current only. However, in the same current condition, the presence of aligned irregular waves would significantly increase, for instance, the maximum floating-collar stress, due to the slow-drift motion of the well boat.

Although we studied a typical floating-collar fish farm, the numerical solver proposed is applicable to any net-based fish farm concept and can also be used to analyze the operational condition of the well boat when operating in novel open cage fish-farm designs. The effect of short-crested sea as well as the presence of several near-by fish cages should be investigated in the future. Furthermore, the approaching and leaving phases of the well boat need to be studied. The presence of fish inside the net cage matters (see He et al., 2018) and represents an uncertainty in our analysis. More detailed description of the future work will be presented in the following chapter.

Chapter 7

Conclusions and further work

7.1 Conclusions

Present investigations for a fish farm and for a coupled well boat-fish farm system are summarized in Section 7.1.1 and Section 7.1.2, respectively.

7.1.1 Fish-farm system

Dynamic responses of a realistic marine fish farm (with single cage) in current, regular waves and long-crested irregular waves have been investigated through numerical simulations and their comparison against available model tests. The examined fish-farm system comprises a floating collar with two concentric tubes, a flexible net cage and a sinker tube attached directly to the net, moored by a complex mooring system with anchor lines, bridle lines and frame lines. Important parameters influencing the mooring loads have been identified and survival conditions of the system have also been determined through systematic simulations. More detailed summary is given below.

A time-domain numerical solver has been developed, with the different components modeled with the state-of-the-art theoretical and numerical formulations. The motions of the floating collar and the sinker tube are described by a curved beam equation with consideration of axial stiffness and curvature effects. The linear potential-flow solver WAMIT, using a high-order Boundary Element Method, calculates the hydrodynamic loads on the floating collar. The many meshes in a net cage make Computational Fluid Dynamics (CFD) and complete structural modeling impracticable. A hydrodynamic screen model and structural truss elements are instead used to represent the hydrodynamic loading and the structural deformation of the net. The screen-force model implicitly accounts for hydrodynamic net-shadow and Reynolds number effect. In addition, the wake inside the net due to current is considered and the inflow modification due to the net-cage presence

is also modeled. The ropes and chains, elements of the mooring lines, are modeled as elastic trusses and the corresponding hydrodynamic forces are estimated by a modified Morison's equation. An implicit strategy was adopted for the coupling between the different components. An original explicit strategy was also suggested. This needs more attention in terms of robustness but can be more easily applied to other net-based fish-farm concepts. For these two strategies a solution algorithm, with a criterion to prevent unphysical net tensions, was also proposed.

The modeling of the different components was assessed by comparing against experiments available in literature. These validation studies involved simplifications of the various components. Three cases were chosen: (CA1) vertical accelerations along a single circular torus in deep-water regular waves, considering a flexible torus and a nearly rigid torus; (CA2) viscous current loads on a rigid-circular cage, a flexible-bottomless circular cage and a deformable, closed net cage; (CA3) mooring loads for a simplified fish-farm with horizontal mooring lines in current only and in combined waves and current. Reasonable agreement between the numerical and experimental results was observed for all the three examined cases. Numerical studies also indicated that: (CA1) the elasticity of the torus is important for the vertical accelerations, even if the torus is almost rigid; (CA2) the screen-type force model tends to slightly overestimate the viscous current loads on the cage and an improved prediction is expected if the flow around the net cage is considered by applying Lagally's theorem; (CA3) the numerical solver gives better results for cases with smaller wave steepnesses.

A sensitivity analysis was also performed for the scenario CA3 to examine the importance of different parameters on the mooring loads. When current is present, the following conclusions were drawn: (1) the two most important parameters are the floater elasticity and the flow reduction for the rear part of the net cage; (2) neglecting the drag force on the floater, avoiding the axial stiffness due to the axial tension, using zero frequency instead of the frequency-dependent added mass for the floater, considering nonlinear Froude-Kriloff and restoring forces, adopting relatively coarse mesh, defining the Reynolds number by the characteristic free stream velocity instead of the instantaneous relative velocity and doubling the net-twine added mass, have all moderate influence on the mooring loads.

The validated numerical tool was used to analyze a realistic aquaculture fish-farm system (with single cage) in current only, and in regular and long-crested irregular waves. The obtained numerical results were compared with available experimental data. Loads in the anchor lines and in the bridle lines were investigated in detail and satisfactory agreement between numerical and experimental results was demonstrated for the system in both regular and irregular waves.

A systematic sensitivity analysis was also performed to identify important parameters influencing the mooring loads. Similarly as for the simplified fish farm, CA3, the most important parameter for the anchor loads is the flow reduction in the rear part of the net cage. Modeling the floating collar as a rigid body has a moderate effect on the anchor loads, but the bridle loads may differ by more than 20% as a rigid collar will change the force distribution along bridles. It is worth to note that the bridle lines in the complete mooring system are similar to the mooring system adopted in CA3. Other parameters such as net elasticity, net weight,

flow modification around the net cage, and drag forces on the floating collar, sinker tube and buoys, have moderate influence on the mooring loads. Neglecting the transient effects and using zero-frequency added mass for the floating collar would lead to negligible error in irregular waves. There is a big variation of the maximum loads in the anchor line and in the bridle line when different random phase seeds are used to generate the incident irregular waves in the numerical simulations. Gumbel distribution is found proper to fit the maximum loads in the mooring lines from different realizations, especially for the loads in bridle lines.

The operational limits of the fish farm have been determined through systematic simulations. Regular waves and current were examined. Numerical results indicated that the main constraint for operating the floating-collar fish farm in more exposed sea regions is the net volume reduction. The maximum floating-collar stress and mooring loads are moderate, even in extreme sea states. Moreover, the sinker tube is more suitable to be used to reduce the net-cage deformation, compared with the discrete sinker weights. Numerical results showed that mooring loads in equivalent regular waves are of similar magnitude, but generally more conservative than those in irregular waves.

7.1.2 Coupled well boat-fish farm system

Dynamic response of a well boat operating at a fish farm in current and in long-crested irregular waves and current has been analyzed numerically in the time domain. The most critical scenario with the well boat placed at the weather side of the fish farm has been analyzed in detail. The influence of the well boat on the fish farm has been quantified and the operational conditions of the well boat have been determined. A detailed summary is given below.

A time-domain numerical solver has been developed to investigate the response of the coupled system. The transverse viscous loads on the boat in current only and in oscillatory flow and current are evaluated based on the cross-flow principle. A systematic approach is proposed to estimate the corresponding drag coefficients, using available empirical formulas. The Reynolds number, rigid free-surface condition, three-dimensional flow at ship ends, Keulegan-Carpenter number and the ratio between current velocity and a characteristic wave velocity are accounted for. The approach has been validated by experiments available in literature. The strategy for the coupling between the well boat and the fish farm is also introduced and the method to measure the contact force between them is given. The well-boat shading effect on the net inflow is approximated by assuming that the flow behind the boat acts like a plane mixing flow with curved shear layer. The numerical modeling of the slow-drift motions of the well boat, in particular the slow-drift sway motion, is explained. The approaches to estimate the slow-drift excitation force and slow-drift damping (wave-drift damping and eddy-making damping) are provided, together with the technique to linearize the eddy-making damping.

Using the developed numerical solver, the coupled system in current only was studied at first. Numerical results showed that both the anchor loads and the floating-collar horizontal deformations increase significantly due to presence of the well boat. Moreover, the floating-collar maximum stress due to the horizontal

deformations occurs at the region where the well boat is in contact with the floating collar. A sensitivity analysis was also performed, showing that the anchor loads are more sensitive to the net-cage related parameters (e.g. sinker tube depth, sinker tube weight), while the maximum floating-collar stress is more sensitive to well-boat loads related parameters (e.g. cross-sectional drag coefficient).

Before analyzing the complete well boat-fish farm system in long-crested irregular waves and current, the slow-drift sway motion of the well boat was studied as a simplified one-degree-of-freedom system for verification purpose. In particular, the fish farm was simplified as a linear spring, neglecting the damping due to the net cage and the mooring lines. The modeling of sway motion was verified by comparing the mean value and standard deviation of the motion from the time-domain solution with those from the frequency-domain solution. The importance of different slow-drift damping terms was examined, leading to the following conclusions: (1) both the mean and the slowly-varying wave-drift damping are important for cases with larger significant wave height; (2) when estimating the eddy-making damping, both the first-order and slow-drift velocities should be included; (3) the first-order motion is small compared with the slow-drift component for the examined sea states; (4) Rayleigh distribution can be used to predict the extreme values when the damping (both wave-drift damping and eddy-making damping) is small; (5) for cases in combined irregular waves and current, both exponential distribution and Stansberg's method (Stansberg, 1991) can have a reasonable prediction of the extreme values. The former is on the conservative side while the latter gives a slight underestimate.

A physical investigation of the coupled system was then performed, with the well boat moored at the weather side of the fish farm. Both the maximum anchor load and the maximum floating-collar stress increase significantly due to the well boat, e.g. increasing more than 300% in moderate exposure sea states. Numerical results indicated that sufficient number of structural modes for the floating collar should be used for a reliable prediction of the maximum floating-collar stress. Simplifying the modeling of the coupled system, for instance, neglecting the net cage and the first-order motion has more effect on the maximum anchor load than on the maximum floating-collar stress. Smaller influence on the maximum floating-collar stress was observed when current is present.

The operational conditions of the well boat were investigated through systematic simulations. Numerical results showed that the maximum anchor load would not exceed the anchor-line breaking limit even in high exposure sea conditions. The maximum stress in the floating collar would be close to the yield stress when the system operates in moderate exposure sea states, and should be used to determine the operational conditions of the well boat. For the anchor loads, using equivalent regular waves to represent irregular waves is not applicable for the coupled well boat-fish farm system due to unrealistic high mean wave-drift loads.

7.2 Recommendations for further work

This thesis provides a good understanding of the response of a realistic floating-collar fish farm (with single cage), without and with the well-boat presence. Many studies can be pursued as a continuation of the present work.

7.2.1 Fish-farm system

- In this work, a realistic fish farm with single cage was examined. However, in reality many net cages operate in close vicinity, arranged in mooring grid in single or double rows. This raises questions about spatial variations of the current and wave environment, as well as about hydrodynamic interaction between the net cages.

- Snap loads were observed in the bridle lines and in the upper part of the net cage. Occurrence of snap events could lead to unexpected high loads, thus they deserve more research.

- The studies in survival conditions for the fish farm just examined the most critical scenario with aligned regular waves and current. It means that the conclusions may be a bit conservative. The fish-farm system in more general sea states should also be studied and possibly three-dimensional waves should be accounted for. Their implementation in the present method is relatively straightforward within the assumption of linear superposition principle of incident wave components. More detailed statistical analysis is needed, e.g. performing fatigue analysis for the mooring lines and the net cage.

- The numerical solver developed in this thesis is applicable to any net-based fish-farm concept, so it can be used to analyze novel open cage fish-farm designs.

7.2.2 Coupled well boat-fish farm system

- The slow-drift motions of the well boat without the net cage and mooring loads on the net cage without the well boat were numerically predicted and carefully validated. This suggests that the numerical results of the coupled system should be reasonable. However, there is still a need of model tests to better validate the modeling of the coupled system.

- The studies in operational conditions for the well boat just considered the most critical scenario with the well boat placed at the weather side of the fish farm in aligned long-crested irregular waves and current. More generic sea states should be examined.

- In this work, a fish-farm system with single cage was included. To represent more realistic scenario, a well boat operating at a fish farm with multiple cages should be checked.

- A typical well-boat operation can be categorized into three phases: approaching, loading/offloading and leaving. Here, just the loading/offloading phase was investigated. However, the approach and departure phases of a well boat need also to be studied. Maneuvering in waves becomes then an issue. Possible contact with the mooring lines, suction of the net into the propeller and collision with the floating collar need to be prevented when choosing the maneuvering strategy.

Bibliography

Aarsnes, J. V., Faltinsen, O. M. and Pettersen, B. (1985), Application of a vortex tracking method to current forces on ships, *in* 'Proceedings of Proc. Conf. Separated Flow around Marine Structures, Trondheim', pp. 309–346.

Aranha, J. (1994), 'A formula for 'wave damping'in the drift of a floating body', *Journal of Fluid Mechanics* **275**, 147–155.

Baker, S. (1977), Regions of recirculating flow associated with two-dimensional steps, PhD thesis, University of Surrey.

Bardestani, M. and Faltinsen, O. M. (2013), A two-dimensional approximation of a floating fish farm in waves and current with the effect of snap loads, *in* 'Proceedings of the ASME 2013 32nd International Conference on Ocean, Offshore and Arctic Engineering', Vol. 9, Nantes, France. OMAE2013-10487.

Bearman, P. W., Graham, J. M. R., Obasaju, E. D. and Drossopoulos, G. M. (1984), 'The influence of corner radius on the forces experienced by cylindrical bluff bodies in oscillatory flow', *Applied Ocean Research* **6**(2), 83–89.

Berstad, A. and Tronstad, H. (2005), 'Response from current and regular/irregular waves on a typical polyethylene fish farm', *Proceedings from Maritime Transportation and Exploitation of Ocean and Coastal Resources (IMAM)* .

Bi, C.-W., Zhao, Y.-P., Dong, G.-H., Zheng, Y.-N. and Gui, F.-K. (2014), 'A numerical analysis on the hydrodynamic characteristics of net cages using coupled fluid–structure interaction model', *Aquacultural Engineering* **59**, 1–12.

Blevins, R. D. (2003), *Applied Fluid Dynamics Handbook*, Krieger Publishing Company, Florida, USA.

BureauVeritas (2016), 'Hydrostar for experts user manual', *Research Department of Bureau Veritas* .

Chauhan, M. K., More, B. S., Dutta, S. and Gandhi, B. K. (2017), Effect of attached type splitter plate length over a square prism in subcritical reynolds number, *in* 'Fluid Mechanics and Fluid Power–Contemporary Research', Springer, pp. 1283–1292.

Cummins, W. (1962), 'The impulse response function and ship motions', *Schiffstechnik* **9**, 101–109.

Cuthill, E. and McKee, J. (1969), Reducing the bandwidth of sparse symmetric matrices, *in* 'Proceedings of the 1969 24th national conference', ACM, pp. 157–172.

Delany, N. K. (1953), 'Low-speed drag of cylinders of various shapes', *NACA Tech. Note* **3038**.

Dhouibi, S., Boujelbene, M., Kharrat, M., Dammak, M. and Maalej, A. (2013), 'Friction behavior of high density polyethylene (hdpe) against 304l steel: An experimental investigation of the effects of sliding direction, sliding history and sliding speed', *Journal of Surfaces and Interfaces of Materials* **1**(1), 71–76.

Dong, G.-H., Xu, T.-J., Zhao, Y.-P., Li, Y.-C. and Gui, F.-K. (2010), 'Numerical simulation of hydrodynamic behavior of gravity cage in irregular waves', *Aquacultural Engineering* **42**(2), 90 – 101.

Faltinsen, O. M. (1990), *Sea Loads on Ships and Offshore Structures*, Cambridge University Press, Cambridge, England.

Faltinsen, O. M. (2005), *Hydrodynamics of High-Speed Marine Vehicles*, Cambridge University Press, Cambridge, England.

Faltinsen, O. M. (2011), Hydrodynamic aspects of a floating fish farm with circular collar, *in* 'Proceedings of the 26th International Workshop on Water Waves and Floating Bodies', Athens, Greece.

Faltinsen, O. M., Dahle, L. A. and Sortland, B. (1986), Slowdrift amping and response of a moored ship in irregular waves, *in* 'Proceedings of the Fifth International Symposium on Offshore Mechanics and Arctic Engineering', American Society of Mechanical Engineers, pp. 297–303.

Faltinsen, O. M., Kjaerland, O., Liapis, N. and Walderhaug, H. (1979), Hydrodynamic analysis of tankers at single point mooring systems, *in* 'Proceedings of the 2nd International Conference Behaviour of Offshore Structures', Vol. 2, pp. 177–206.

Faltinsen, O. M., Minsaas, K. J., Liapis, N. and Skjørdal, S. O. (1980), Prediction of resistance and propulsion of a ship in a seaway, *in* 'Proceedings of the 13th symposium on naval hydrodynamics, Tokyo, Japan', pp. 505–229.

Faltinsen, O. M. and Shen, Y.-G. (2018), 'Wave and current effects on floating fish farms', *Journal of Marine Science and Application* **18**(1).

Faltinsen, O. M. and Sortland, B. (1987), 'Slow drift eddy making damping of a ship', *Applied ocean research* **9**(1), 37–46.

Faltinsen, O. M. and Timokha, A. N. (2009), *Sloshing*, Cambridge University Press, Cambridge, England.

Faltinsen, O. M. and Zhao, R. (1989), 'Slow-drift motions of moored two-dimensional body in irregular waves', *Journal of ship research* **33**(2), 93–106.

FAO (2005), National aquaculture sector overview: Norway, Technical report, Food and Agriculture Organization of the United Nations, Rome, Italy.

FAO (2006), The state of world fisheries and aquaculture, Technical report, Food and Agriculture Organization of the United Nations, Rome, Italy.

FAO (2010), The state of world fisheries and aquaculture, Technical report, Food and Agriculture Organization of the United Nations, Rome, Italy.

FAO (2015), Aquaculture operations in floating hdpe cages: A field handbook, Technical report, Food and Agriculture Organization of the United Nations, Rome, Italy.

FAO (2016), The state of world fisheries and aquaculture, Technical report, Food and Agriculture Organization of the United Nations, Rome, Italy.

FAO (2017), The future of food and agriculture – trends and challenges, Technical report, Food and Agriculture Organization of the United Nations, Rome, Italy.

Field, C. B., Behrenfeld, M. J., Randerson, J. T. and Falkowski, P. (1998), 'Primary production of the biosphere: Integrating terrestrial and oceanic components', *Science* **281**(5374), 237–240.

Goldstein, S. (1965), *Modern Developments in Fluid Dynamics*, Dover Publications, New York, USA.

Hamel-Derouich, D. (1993), Hydrodynamic forces on rectangular cylinders horizontally submerged in waves and currents at low kc numbers, *in* 'The Third International Offshore and Polar Engineering Conference', International Society of Offshore and Polar Engineers, pp. 168–175.

He, Z., Faltinsen, O. M., Fredheim, A. and Kristiansen, T. (2015), The influence of fish on the mooring loads of a floating fish farm, *in* 'Proceedings of the 7th International Conference on Hydroelasticity in Marine Technology', Split, Croatia.

He, Z., Faltinsen, O. M., Fredheim, A. and Kristiansen, T. (2018), 'The influence of fish on the mooring loads of a floating net cage', *Journal of Fluids and Structures* **76**, 384–395.

Himeno, Y. (1981), Prediction of ship roll damping-a state of the art, Technical report, University of Michigan.

Huang, C. C., Tang, H. J. and Liu, J. Y. (2006), 'Dynamical analysis of net cage structures for marine aquaculture: Numerical simulation and model testing', *Aquacultural Engineering* **35**(3), 258–270.

Ikeda, Y., Himeno, Y. and Tanaka, N. (1977), 'On eddy making component of roll damping force on naked hull', *Journal of the society of Naval Architects of Japan* **1977**(142), 54–64.

Jia, H., Moan, T., Jensen, Ø. et al. (2012), Coupled hydrodynamic analysis between gravity cage and well boat in operation, *in* 'The Twenty-second International Offshore and Polar Engineering Conference', International Society of Offshore and Polar Engineers.

Jonsson, I. G. (1980), 'A new approach to oscillatory rough turbulent boundary layers', *Ocean Engineering* **7**, 109–152.

Kawahara, Y., Maekawa, K. and Ikeda, Y. (2011), A simple prediction formula of roll damping of conventional cargo ships on the basis of ikeda's method and its limitation, *in* 'Contemporary Ideas on Ship Stability and Capsizing in Waves', Springer, pp. 465–486.

Kristiansen, D. (2010), Wave induced effects on floaters of aquaculture plants, Phd thesis, Department of Marine Technology, Norwegian University of Science and Technology, Trondheim, Norway.

Kristiansen, D. and Faltinsen, O. M. (2009), 'Non-linear wave-induced motions of cylindrical-shaped floaters of fish farms', *Proceedings of the Institution of Mechanical Engineers, Part M: Journal of Engineering for the Maritime Environment* **223**(3), 361–375.

Kristiansen, T. (2013), A numerical parameter study on current forces on circular aquaculture net cages, *in* 'ASME 2013 32nd International Conference on Ocean, Offshore and Arctic Engineering', American Society of Mechanical Engineers, pp. V009T12A035–V009T12A035.

Kristiansen, T. and Faltinsen, O. M. (2012), 'Modelling of current loads on aquaculture net cages', *Journal of Fluids and Structures* **34**, 218–235.

Kristiansen, T. and Faltinsen, O. M. (2015), 'Experimental and numerical study of an aquaculture net cage with floater in waves and current', *Journal of Fluids and Structures* **54**, 1–26.

Lee, C. H. and Newman, J. N. (2013), *WAMIT user manual, version 7.0*, WAMIT, Inc., Chestnut Hill, USA.

Li, P. (2017), A Theoretical and Experimental Study of Wave-induced Hydroelastic Response of a Circular Floating Collar, Phd thesis, Department of Marine Technology, Norwegian University of Science and Technology, Trondheim, Norway.

Li, P. and Faltinsen, O. M. (2012), Wave induced response of an elastic circular collar of a floating fish farm, *in* 'Proceedings of 10th International Conference on Hydrodynamics', Vol. 2, St. Petersburg, Russia, pp. 58–64.

Li, P., Faltinsen, O. M. and Greco, M. (2014), Wave-induced accelerations of a fish-farm elastic floater: experimental and numerical studies, *in* 'Proceedings of the ASME 2014 33rd International Conference on Ocean, Offshore and Arctic Engineering', Vol. 7, San Francisco, California, USA. OMAE2014-23302.

Li, P., Faltinsen, O. M. and Greco, M. (2018), 'Wave-induced accelerations of a fish-farm elastic floater: Experimental and numerical studies', *Journal of Offshore Mechanics and Arctic Engineering* **140**(1), 011201.

Li, P., Faltinsen, O. M. and Lugni, C. (2016), 'Nonlinear vertical accelerations of a floating torus in regular waves', *Journal of Fluids and Structures* **66**, 589–608.

Løland, G. (1991), Current forces on and flow through fish farms, Phd thesis, Division of Marine Hydrodynamics, the Norwegian Institute of Technology, Trondheim, Norway.

Lovatelli, A., Aguilar Manjarrez, J. and Soto, D. (2013), Expanding mariculture farther offshore: Technical, environmental, spatial and governance challenges, Technical report, Food and Agriculture Organization of the United Nations, Orbetello, Italy.

Loverich, G. F. and Gace, L. (1997), 'The effect of currents and waves on several classes of offshore sea cages', *Charting the Future of Ocean Farming* pp. 131–144.

Marichal, D. (2003), Cod-end numerical study, *in* 'Third International Conference on Hydroelasticity in Marine Technology', Oxford, UK.

Mercier, R. S. and Huijs, F. A. (2005), *Steady Current Forces On Tanker-based FPSOs*, Vol. 84, WIT Press.

Naess, A. (1986), 'The statistical distribution of second-order slowly-varying forces and motions', *Applied Ocean Research* **8**(2), 110–118.

Naess, A. (1989), Effects of correlation on extreme slow-drift response, *in* 'Proc 8th Int Offshore Mechanics and Arctic Engineering Symposium, Hague, Netherlands', Vol. 2, pp. 465–474.

Naess, A. and Moan, T. (2012), *Stochastic dynamics of marine structures*, Cambridge University Press.

Nakaguchi, H., Hashimoto, K. and Muto, S. (1968), 'An experimental study on aerodynamic drag of rectangular cylinders', *The Journal of the Japan Society of Aeronautical Engineering* **16**(168), 1–5.

Newman, J. N. (1974), Second-order slowly varying forces on vessels in irregular waves, *in* 'Proceedings of the international symposium on dynamics of marine vehicles and structures in waves. London, UK, 1974'.

NS9415 (2009), Marine fish farms - requirements for site survey risk, analysis, design, dimensioning, production,installation and operation, Norwegian standard.

Nygaard, I. (2013), Merdforsøk. kapasitets-tester. interaksjon mellom not og utspilingssystem, Technical report, Tech. rep., Norsk Marinteknisk Forskningsinstitutt AS.

Pinkster, J. A. (1975), 'Low-frequency phenomena associated with vessels moored at sea', *Society of Petroleum Engineers Journal* **15**(06), 487–494.

Pinkster, J. A. and Van Oortmerssen, G. (1977), Computation of the first and second order wave forces on oscillating bodies in regular waves, *in* 'Proceedins of the 2nd International Conference on Numerical Ship Hydrodynamics, Berkeley, CA, USA, 19-21 Sept 1977', pp. 136–156.

Price, W. G. and Bishop, R. E. D. (1974), *Probabilistic theory of ship dynamics*, Chapman and Hall, London, England.

Roberts, J. B. and Spanos, P. D. (2003), *Random vibration and statistical linearization*, Dover Publications, New York, USA.

Rudi, H., Løland, G. and Furunes, L. (1988), Model tests with net enclosures. forces on and flow through single nets and cage systems, Technical report, Technical report, MARINTEK.

Ryan, J. (2004), Farming the deep blue, Technical report, Bord Iascaigh Mhara, Dublin, Ireland:BIM.

Sarpkaya, T. and Storm, M. (1985), 'In-line force on a cylinder translating in oscillatory flow', *Applied Ocean Research* **7**(4), 188–196.

Schubauer, G. B., Spangenberg, W. G. and Klebanoff, P. S. (1950), Aerodynamic characteristics of damping screens, Technical report, NACA Technical Note 2001.

Shainee, M., Leira, B. J., Ellingsen, H. and Fredheim, A. (2014), 'Investigation of a self-submersible spm cage system in random waves', *Aquacultural engineering* **58**, 35–44.

Shen, Y.-G., Greco, M. and Faltinsen, O. M. (2016), Numerical study of a coupled well boat-fish farm system in waves and current during loading operations, *in* 'Proceedings of 12th International Conference on Hydrodynamics', Egmond aan Zee, The Netherlands.

Shen, Y.-G., Greco, M. and Faltinsen, O. M. (2018a), 'Numerical study of a well boat operating at a fish farm in current', *Journal of Fluids and Structures, submitted* .

Shen, Y.-G., Greco, M. and Faltinsen, O. M. (2018b), 'Numerical study of a well boat operating at a fish farm in long-crested irregular waves and current', *Journal of Fluids and Structures, submitted* .

Shen, Y.-G., Greco, M., Faltinsen, O. M. and Nygaard, I. (2018), 'Numerical and experimental investigations on mooring loads of a marine fish farm in waves and current', *Journal of Fluids and Structures* **79**, 115–136.

Stansberg, C. T. (1991), A simple method for estimation of extreme values of non-gaussian slow-drift responses, *in* 'The First International Offshore and Polar Engineering Conference', International Society of Offshore and Polar Engineers, pp. 442–451.

Tanaka, N., Ikeda, Y. and Nishino, K. (1982), Hydrodynamic viscous force acting on oscillating cylinders with various shapes, *in* 'Proceedings of 6th Symposium on Marine Technology, Society of Naval Architecture of Japan'.

Trude, O., Ulf, W., Yngvar, O. and Skjermo, J. (2012), Value created from productive oceans in 2050, Technical report, Trondheim, Norway.

White, F. M. (2006), *Viscous Fluid Flow*, Vol. 3, McGraw-Hill, Boston, USA.

Xu, T. J., Zhao, Y. P., Dong, G. H., Li, Y. C. and Gui, F. K. (2013), 'Analysis of hydrodynamic behaviors of multiple net cages in combined wave-current flow', *Journal of Fluids and Structures* **39**, 222–236.

Yao, Y.-m., Chen, Y.-l., Zhou, H. and Yang, H.-y. (2016), 'Numerical modeling of current loads on a net cage considering fluid–structure interaction', *Journal of Fluids and Structures* **62**, 350–366.

Zdravkovich, M. M. (1985), Forces on pipe clusters, *in* 'Proc. Conf. on Separated Flow Around Marine Structures, Norwegian Institute of Technology', Trondheim, Norway, pp. 201–226.

Zhan, J. M., Jia, X. P., Li, Y. S., Sun, M. G., Guo, G. X. and Hu, Y. Z. (2006), 'Analytical and experimental investigation of drag on nets of fish cages', *Aquacultural engineering* **35**(1), 91–101.

Zhao, R. and Faltinsen, O. M. (1988), 'Interaction between waves and current on a two-dimensional body in the free surface', *Applied Ocean Research* **10**(2), 87–99.

Zhao, Y.-P., Bi, C.-W., Dong, G.-H., Gui, F.-K., Cui, Y. and Xu, T.-J. (2013), 'Numerical simulation of the flow field inside and around gravity cages', *Aquacultural engineering* **52**, 1–13.

Appendices

Appendix A

Mode shape plots

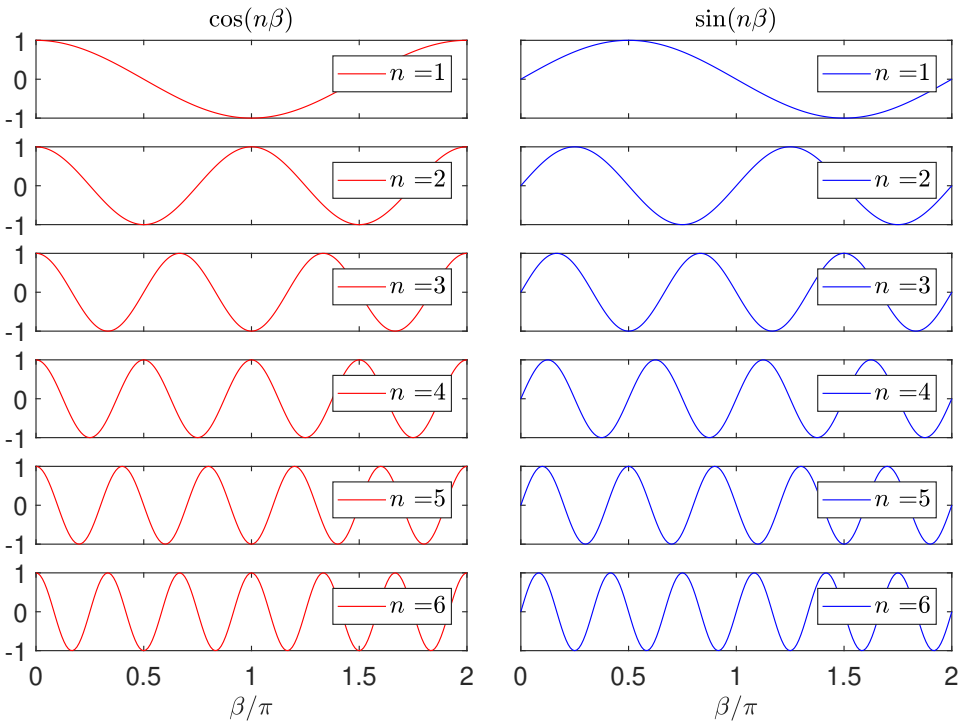

Figure A.1: Normal deformation modes from 1-6. Left: $\cos(n\beta)$. Right: $\sin(n\beta)$.

Appendix B

Analytical integration for axial stiffness

The integration terms in Eq. (2.14) are given analytically by

$$\begin{aligned}
\int \cos(n\beta)\cos(m\beta)\ \mathrm{d}\beta &= \frac{1}{2}\frac{\sin\left[(m+n)\,\beta\right]}{m+n} + \frac{1}{2}\frac{\sin\left[(m-n+\varepsilon)\,\beta\right]}{m-n+\varepsilon} \\
\int \sin(n\beta)\cos(m\beta)\ \mathrm{d}\beta &= -\frac{1}{2}\frac{\cos\left[(m+n)\,\beta\right]}{m+n} + \frac{1}{2}\frac{\left[\cos(m-n+\varepsilon)\,\beta\right]}{m-n+\varepsilon}
\end{aligned} \tag{B.1}$$

here ε is a infinitely small value (10^{-15}). The main purpose to add ε in denominator is to deal with the case when $m = n$.

Appendix C

Contact force between the well boat and the floating collar

Accurate prediction of the contact force between the fish farm and the well boat is important for the response of the coupled system.

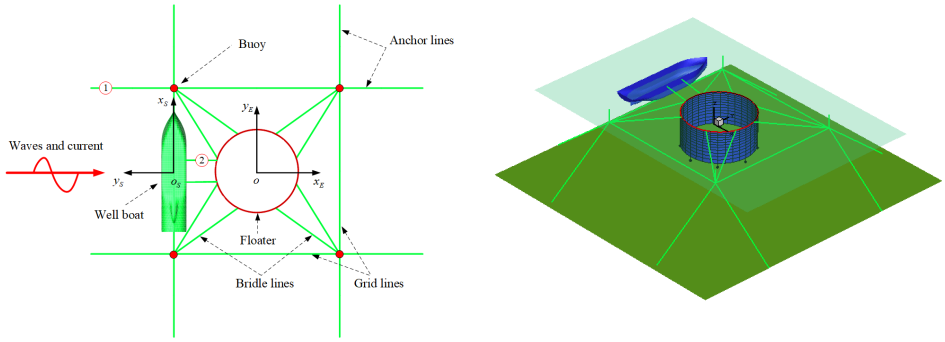

Figure C.1: Configuration of the well boat and the moored fish-farm system with definitions of coordinate systems and wave and current directions. Left: birds eye view. Right: three-dimensional view.

The indirect method, used in the present thesis for this estimation, is described in Section 5.2.2. A different strategy, named as direct method, has been compared against the indirect method by Shen et al. (2016). The results are repeated here for completeness, because the consistency of these independent methods confirms the applicability of the indirect approach. In the direct method, the contact force is evaluated based on the condition that the floater and the boat share the same normal velocity at a given contact point. The direct method is physically sound, but difficult to implement in a general scenario. A simplified case is examined

where the well boat used in this thesis can move only in sway and is coupled with a simplified fish-farm system involving an isolated rigid floater and a bottomless net cage, see Figure C.1. Detailed parameters of the simplified fish farm can be found in Shen et al. (2016). The comparisons of the contact forces and mooring forces are shown in Figure C.2. Two results are shown from the indirect method using two values of the contact stiffness. Increasing further the k_c (not shown here) gives the same predictions as with $k_c = 1.6 \times 10^6$N/m for which the two methods provide consistent results. This indicates that the indirect method is reliable as long as sufficiently high contact stiffness k_c is adopted.

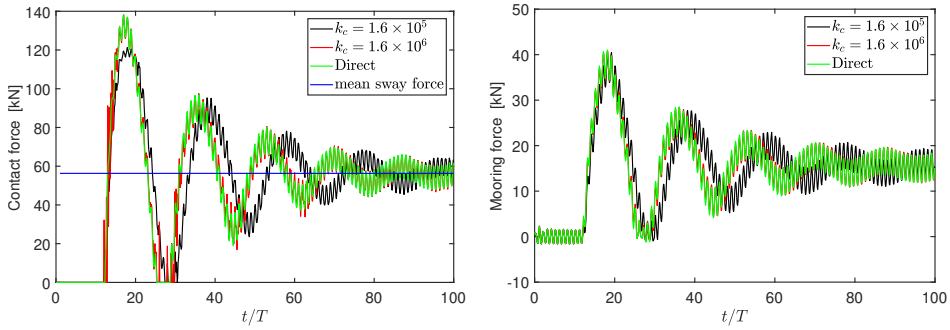

Figure C.2: Time histories of the contact forces (left) and the mooring tensions (right) in waves with wave period $T = 6$ s and wave height-to-wavelength ratio $H/\lambda = 1/60$.

Appendix D

Mean wave forces in very short waves and current

The direct pressure integration method (Pinkster and Van Oortmerssen, 1977) is adopted to estimate the mean wave (second-order) forces on a structure with vertical side at the water plane in very short waves and current. Similar procedure as shown in Faltinsen (1990) is followed. We show the method by analyzing incident regular deep-water waves on a two-dimensional free-surface-piercing body, see Figure D.1.

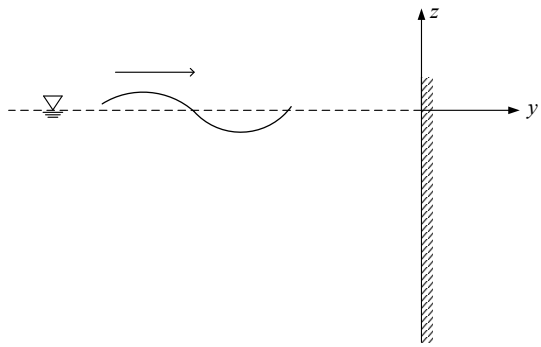

Figure D.1: Incident waves and drift forces on a vertical wall.

The incident wave potential + diffraction potential

$$\phi_{I'} = \phi_I + \phi_D = U_\infty y + \frac{g\zeta_a}{\omega} e^{kz} \cos(\omega_e t - ky) + \left[-U_\infty y + \frac{g\zeta_a}{\omega} e^{kz} \cos(\omega_e t + ky) \right]$$
$$= \frac{2g\zeta_a}{\omega} e^{kz} \cos(\omega_e t) \cos(ky) \tag{D.1}$$

satisfying the body boundary condition. For the effect of current, only the encounter frequency effect is considered. The wave elevation at the wall

$$\zeta = -\frac{1}{g}\frac{\partial \phi_{I'}}{\partial t}\bigg|_{y=0,z=0} = \frac{2\zeta_a \omega_e}{\omega}\sin(\omega_e t) \tag{D.2}$$

We start out with Bernoulli's equation,

$$p = -\rho g z - \rho\frac{\partial \phi_{I'}}{\partial t} - \frac{1}{2}\rho\left[\left(\frac{\partial \phi_{I'}}{\partial y^2}\right)^2 + \left(\frac{\partial \phi_{I'}}{\partial z^2}\right)^2\right] \tag{D.3}$$

We will calculate the mean drift force correct to second order in wave amplitude. The contribution from the two first terms in Eq. (D.3) can be written as

$$\overline{-\rho g\int_0^{\zeta} z dz} - \overline{\rho\frac{\partial \phi_{I'}}{\partial t}\bigg|_{z=0}\zeta} = \rho g\frac{\omega_e^2}{\omega^2}\zeta_a^2 \tag{D.4}$$

The third term in Eq. (D.3) results in the following contribution

$$\overline{-\frac{1}{2}\rho\int_{-\infty}^{0}\left[\left(\frac{\partial \phi_{I'}}{\partial y^2}\right)^2 + \left(\frac{\partial \phi_{I'}}{\partial z^2}\right)^2\right]dz} = -\frac{1}{2}\rho g\zeta_a^2 \tag{D.5}$$

The total sum is

$$\begin{aligned}
\overline{F_2}(\omega, U_\infty) &= \rho g\frac{\omega_e^2}{\omega^2}\zeta_a^2 - \frac{1}{2}\rho g\zeta_a^2 = \frac{1}{2}\rho g\zeta_a^2\left(\frac{2\omega_e^2}{\omega^2} - 1\right) \\
\overline{F_2}(\omega, U_\infty) &= \overline{F_2}(\omega)\left[1 + \frac{4\omega U_\infty}{g} + 2\left(\frac{\omega U_\infty}{g}\right)^2\right]
\end{aligned} \tag{D.6}$$

Let us define $\tau = \omega U_\infty / g$, then the last two terms in the right-hand side of Eq. (D.6) are equal when $\tau = 2$. If τ is small, e.g. $\tau < 0.1$, then the second-order term of τ can be neglected and Eq. (D.6) can be rewritten as

$$\overline{F_2}(\omega, U_\infty) \approx \overline{F_2}(\omega)\left(1 + \frac{4\omega U_\infty}{g}\right) \tag{D.7}$$

Previous PhD theses published at the Department of Marine Technology (earlier: Faculty of Marine Technology) NORWEGIAN UNIVERSITY OF SCIENCE AND TECHNOLOGY

Report No.	Author	Title
	Kavlie, Dag	Optimization of Plane Elastic Grillages, 1967
	Hansen, Hans R.	Man-Machine Communication and Data-Storage Methods in Ship Structural Design, 1971
	Gisvold, Kaare M.	A Method for non-linear mixed -integer programming and its Application to Design Problems, 1971
	Lund, Sverre	Tanker Frame Optimalization by means of SUMT-Transformation and Behaviour Models, 1971
	Vinje, Tor	On Vibration of Spherical Shells Interacting with Fluid, 1972
	Lorentz, Jan D.	Tank Arrangement for Crude Oil Carriers in Accordance with the new Anti-Pollution Regulations, 1975
	Carlsen, Carl A.	Computer-Aided Design of Tanker Structures, 1975
	Larsen, Carl M.	Static and Dynamic Analysis of Offshore Pipelines during Installation, 1976
UR-79-01	Brigt Hatlestad, MK	The finite element method used in a fatigue evaluation of fixed offshore platforms. (Dr.Ing. Thesis)
UR-79-02	Erik Pettersen, MK	Analysis and design of cellular structures. (Dr.Ing. Thesis)
UR-79-03	Sverre Valsgård, MK	Finite difference and finite element methods applied to nonlinear analysis of plated structures. (Dr.Ing. Thesis)
UR-79-04	Nils T. Nordsve, MK	Finite element collapse analysis of structural members considering imperfections and stresses due to fabrication. (Dr.Ing. Thesis)
UR-79-05	Ivar J. Fylling, MK	Analysis of towline forces in ocean towing systems. (Dr.Ing. Thesis)
UR-80-06	Nils Sandsmark, MM	Analysis of Stationary and Transient Heat Conduction by the Use of the Finite Element Method. (Dr.Ing. Thesis)
UR-80-09	Sverre Haver, MK	Analysis of uncertainties related to the stochastic modeling of ocean waves. (Dr.Ing. Thesis)
UR-81-15	Odland, Jonas	On the Strength of welded Ring stiffened cylindrical Shells primarily subjected to axial Compression
UR-82-17	Engesvik, Knut	Analysis of Uncertainties in the fatigue Capacity of

		Welded Joints
UR-82-18	Rye, Henrik	Ocean wave groups
UR-83-30	Eide, Oddvar Inge	On Cumulative Fatigue Damage in Steel Welded Joints
UR-83-33	Mo, Olav	Stochastic Time Domain Analysis of Slender Offshore Structures
UR-83-34	Amdahl, Jørgen	Energy absorption in Ship-platform impacts
UR-84-37	Mørch, Morten	Motions and mooring forces of semi submersibles as determined by full-scale measurements and theoretical analysis
UR-84-38	Soares, C. Guedes	Probabilistic models for load effects in ship structures
UR-84-39	Aarsnes, Jan V.	Current forces on ships
UR-84-40	Czujko, Jerzy	Collapse Analysis of Plates subjected to Biaxial Compression and Lateral Load
UR-85-46	Alf G. Engseth, MK	Finite element collapse analysis of tubular steel offshore structures. (Dr.Ing. Thesis)
UR-86-47	Dengody Sheshappa, MP	A Computer Design Model for Optimizing Fishing Vessel Designs Based on Techno-Economic Analysis. (Dr.Ing. Thesis)
UR-86-48	Vidar Aanesland, MH	A Theoretical and Numerical Study of Ship Wave Resistance. (Dr.Ing. Thesis)
UR-86-49	Heinz-Joachim Wessel, MK	Fracture Mechanics Analysis of Crack Growth in Plate Girders. (Dr.Ing. Thesis)
UR-86-50	Jon Taby, MK	Ultimate and Post-ultimate Strength of Dented Tubular Members. (Dr.Ing. Thesis)
UR-86-51	Walter Lian, MH	A Numerical Study of Two-Dimensional Separated Flow Past Bluff Bodies at Moderate KC-Numbers. (Dr.Ing. Thesis)
UR-86-52	Bjørn Sortland, MH	Force Measurements in Oscillating Flow on Ship Sections and Circular Cylinders in a U-Tube Water Tank. (Dr.Ing. Thesis)
UR-86-53	Kurt Strand, MM	A System Dynamic Approach to One-dimensional Fluid Flow. (Dr.Ing. Thesis)
UR-86-54	Arne Edvin Løken, MH	Three Dimensional Second Order Hydrodynamic Effects on Ocean Structures in Waves. (Dr.Ing. Thesis)
UR-86-55	Sigurd Falch, MH	A Numerical Study of Slamming of Two-Dimensional Bodies. (Dr.Ing. Thesis)
UR-87-56	Arne Braathen, MH	Application of a Vortex Tracking Method to the Prediction of Roll Damping of a Two-Dimension Floating Body. (Dr.Ing. Thesis)

UR-87-57	Bernt Leira, MK	Gaussian Vector Processes for Reliability Analysis involving Wave-Induced Load Effects. (Dr.Ing. Thesis)
UR-87-58	Magnus Småvik, MM	Thermal Load and Process Characteristics in a Two-Stroke Diesel Engine with Thermal Barriers (in Norwegian). (Dr.Ing. Thesis)
MTA-88-59	Bernt Arild Bremdal, MP	An Investigation of Marine Installation Processes – A Knowledge - Based Planning Approach. (Dr.Ing. Thesis)
MTA-88-60	Xu Jun, MK	Non-linear Dynamic Analysis of Space-framed Offshore Structures. (Dr.Ing. Thesis)
MTA-89-61	Gang Miao, MH	Hydrodynamic Forces and Dynamic Responses of Circular Cylinders in Wave Zones. (Dr.Ing. Thesis)
MTA-89-62	Martin Greenhow, MH	Linear and Non-Linear Studies of Waves and Floating Bodies. Part I and Part II. (Dr.Techn. Thesis)
MTA-89-63	Chang Li, MH	Force Coefficients of Spheres and Cubes in Oscillatory Flow with and without Current. (Dr.Ing. Thesis
MTA-89-64	Hu Ying, MP	A Study of Marketing and Design in Development of Marine Transport Systems. (Dr.Ing. Thesis)
MTA-89-65	Arild Jæger, MH	Seakeeping, Dynamic Stability and Performance of a Wedge Shaped Planing Hull. (Dr.Ing. Thesis)
MTA-89-66	Chan Siu Hung, MM	The dynamic characteristics of tilting-pad bearings
MTA-89-67	Kim Wikstrøm, MP	Analysis av projekteringen for ett offshore projekt. (Licenciat-avhandling)
MTA-89-68	Jiao Guoyang, MK	Reliability Analysis of Crack Growth under Random Loading, considering Model Updating. (Dr.Ing. Thesis)
MTA-89-69	Arnt Olufsen, MK	Uncertainty and Reliability Analysis of Fixed Offshore Structures. (Dr.Ing. Thesis)
MTA-89-70	Wu Yu-Lin, MR	System Reliability Analyses of Offshore Structures using improved Truss and Beam Models. (Dr.Ing. Thesis)
MTA-90-71	Jan Roger Hoff, MH	Three-dimensional Green function of a vessel with forward speed in waves. (Dr.Ing. Thesis)
MTA-90-72	Rong Zhao, MH	Slow-Drift Motions of a Moored Two-Dimensional Body in Irregular Waves. (Dr.Ing. Thesis)
MTA-90-73	Atle Minsaas, MP	Economical Risk Analysis. (Dr.Ing. Thesis)
MTA-90-74	Knut-Aril Farnes, MK	Long-term Statistics of Response in Non-linear Marine Structures. (Dr.Ing. Thesis)
MTA-90-75	Torbjørn Sotberg, MK	Application of Reliability Methods for Safety Assessment of Submarine Pipelines. (Dr.Ing.

		Thesis)
MTA-90-76	Zeuthen, Steffen, MP	SEAMAID. A computational model of the design process in a constraint-based logic programming environment. An example from the offshore domain. (Dr.Ing. Thesis)
MTA-91-77	Haagensen, Sven, MM	Fuel Dependant Cyclic Variability in a Spark Ignition Engine - An Optical Approach. (Dr.Ing. Thesis)
MTA-91-78	Løland, Geir, MH	Current forces on and flow through fish farms. (Dr.Ing. Thesis)
MTA-91-79	Hoen, Christopher, MK	System Identification of Structures Excited by Stochastic Load Processes. (Dr.Ing. Thesis)
MTA-91-80	Haugen, Stein, MK	Probabilistic Evaluation of Frequency of Collision between Ships and Offshore Platforms. (Dr.Ing. Thesis)
MTA-91-81	Sødahl, Nils, MK	Methods for Design and Analysis of Flexible Risers. (Dr.Ing. Thesis)
MTA-91-82	Ormberg, Harald, MK	Non-linear Response Analysis of Floating Fish Farm Systems. (Dr.Ing. Thesis)
MTA-91-83	Marley, Mark J., MK	Time Variant Reliability under Fatigue Degradation. (Dr.Ing. Thesis)
MTA-91-84	Krokstad, Jørgen R., MH	Second-order Loads in Multidirectional Seas. (Dr.Ing. Thesis)
MTA-91-85	Molteberg, Gunnar A., MM	The Application of System Identification Techniques to Performance Monitoring of Four Stroke Turbocharged Diesel Engines. (Dr.Ing. Thesis)
MTA-92-86	Mørch, Hans Jørgen Bjelke, MH	Aspects of Hydrofoil Design: with Emphasis on Hydrofoil Interaction in Calm Water. (Dr.Ing. Thesis)
MTA-92-87	Chan Siu Hung, MM	Nonlinear Analysis of Rotordynamic Instabilities in Highspeed Turbomachinery. (Dr.Ing. Thesis)
MTA-92-88	Bessason, Bjarni, MK	Assessment of Earthquake Loading and Response of Seismically Isolated Bridges. (Dr.Ing. Thesis)
MTA-92-89	Langli, Geir, MP	Improving Operational Safety through exploitation of Design Knowledge - an investigation of offshore platform safety. (Dr.Ing. Thesis)
MTA-92-90	Sævik, Svein, MK	On Stresses and Fatigue in Flexible Pipes. (Dr.Ing. Thesis)
MTA-92-91	Ask, Tor Ø., MM	Ignition and Flame Growth in Lean Gas-Air Mixtures. An Experimental Study with a Schlieren System. (Dr.Ing. Thesis)
MTA-86-92	Hessen, Gunnar, MK	Fracture Mechanics Analysis of Stiffened Tubular Members. (Dr.Ing. Thesis)

MTA-93-93	Steinebach, Christian, MM	Knowledge Based Systems for Diagnosis of Rotating Machinery. (Dr.Ing. Thesis)
MTA-93-94	Dalane, Jan Inge, MK	System Reliability in Design and Maintenance of Fixed Offshore Structures. (Dr.Ing. Thesis)
MTA-93-95	Steen, Sverre, MH	Cobblestone Effect on SES. (Dr.Ing. Thesis)
MTA-93-96	Karunakaran, Daniel, MK	Nonlinear Dynamic Response and Reliability Analysis of Drag-dominated Offshore Platforms. (Dr.Ing. Thesis)
MTA-93-97	Hagen, Arnulf, MP	The Framework of a Design Process Language. (Dr.Ing. Thesis)
MTA-93-98	Nordrik, Rune, MM	Investigation of Spark Ignition and Autoignition in Methane and Air Using Computational Fluid Dynamics and Chemical Reaction Kinetics. A Numerical Study of Ignition Processes in Internal Combustion Engines. (Dr.Ing. Thesis)
MTA-94-99	Passano, Elizabeth, MK	Efficient Analysis of Nonlinear Slender Marine Structures. (Dr.Ing. Thesis)
MTA-94-100	Kvålsvold, Jan, MH	Hydroelastic Modelling of Wetdeck Slamming on Multihull Vessels. (Dr.Ing. Thesis)
MTA-94-102	Bech, Sidsel M., MK	Experimental and Numerical Determination of Stiffness and Strength of GRP/PVC Sandwich Structures. (Dr.Ing. Thesis)
MTA-95-103	Paulsen, Hallvard, MM	A Study of Transient Jet and Spray using a Schlieren Method and Digital Image Processing. (Dr.Ing. Thesis)
MTA-95-104	Hovde, Geir Olav, MK	Fatigue and Overload Reliability of Offshore Structural Systems, Considering the Effect of Inspection and Repair. (Dr.Ing. Thesis)
MTA-95-105	Wang, Xiaozhi, MK	Reliability Analysis of Production Ships with Emphasis on Load Combination and Ultimate Strength. (Dr.Ing. Thesis)
MTA-95-106	Ulstein, Tore, MH	Nonlinear Effects of a Flexible Stern Seal Bag on Cobblestone Oscillations of an SES. (Dr.Ing. Thesis)
MTA-95-107	Solaas, Frøydis, MH	Analytical and Numerical Studies of Sloshing in Tanks. (Dr.Ing. Thesis)
MTA-95-108	Hellan, Øyvind, MK	Nonlinear Pushover and Cyclic Analyses in Ultimate Limit State Design and Reassessment of Tubular Steel Offshore Structures. (Dr.Ing. Thesis)
MTA-95-109	Hermundstad, Ole A., MK	Theoretical and Experimental Hydroelastic Analysis of High Speed Vessels. (Dr.Ing. Thesis)
MTA-96-110	Bratland, Anne K., MH	Wave-Current Interaction Effects on Large-Volume Bodies in Water of Finite Depth. (Dr.Ing. Thesis)
MTA-96-111	Herfjord, Kjell, MH	A Study of Two-dimensional Separated Flow by a Combination of the Finite Element Method and

		Navier-Stokes Equations. (Dr.Ing. Thesis)
MTA-96-112	Æsøy, Vilmar, MM	Hot Surface Assisted Compression Ignition in a Direct Injection Natural Gas Engine. (Dr.Ing. Thesis)
MTA-96-113	Eknes, Monika L., MK	Escalation Scenarios Initiated by Gas Explosions on Offshore Installations. (Dr.Ing. Thesis)
MTA-96-114	Erikstad, Stein O., MP	A Decision Support Model for Preliminary Ship Design. (Dr.Ing. Thesis)
MTA-96-115	Pedersen, Egil, MH	A Nautical Study of Towed Marine Seismic Streamer Cable Configurations. (Dr.Ing. Thesis)
MTA-97-116	Moksnes, Paul O., MM	Modelling Two-Phase Thermo-Fluid Systems Using Bond Graphs. (Dr.Ing. Thesis)
MTA-97-117	Halse, Karl H., MK	On Vortex Shedding and Prediction of Vortex-Induced Vibrations of Circular Cylinders. (Dr.Ing. Thesis)
MTA-97-118	Igland, Ragnar T., MK	Reliability Analysis of Pipelines during Laying, considering Ultimate Strength under Combined Loads. (Dr.Ing. Thesis)
MTA-97-119	Pedersen, Hans-P., MP	Levendefiskteknologi for fiskefartøy. (Dr.Ing. Thesis)
MTA-98-120	Vikestad, Kyrre, MK	Multi-Frequency Response of a Cylinder Subjected to Vortex Shedding and Support Motions. (Dr.Ing. Thesis)
MTA-98-121	Azadi, Mohammad R. E., MK	Analysis of Static and Dynamic Pile-Soil-Jacket Behaviour. (Dr.Ing. Thesis)
MTA-98-122	Ulltang, Terje, MP	A Communication Model for Product Information. (Dr.Ing. Thesis)
MTA-98-123	Torbergsen, Erik, MM	Impeller/Diffuser Interaction Forces in Centrifugal Pumps. (Dr.Ing. Thesis)
MTA-98-124	Hansen, Edmond, MH	A Discrete Element Model to Study Marginal Ice Zone Dynamics and the Behaviour of Vessels Moored in Broken Ice. (Dr.Ing. Thesis)
MTA-98-125	Videiro, Paulo M., MK	Reliability Based Design of Marine Structures. (Dr.Ing. Thesis)
MTA-99-126	Mainçon, Philippe, MK	Fatigue Reliability of Long Welds Application to Titanium Risers. (Dr.Ing. Thesis)
MTA-99-127	Haugen, Elin M., MH	Hydroelastic Analysis of Slamming on Stiffened Plates with Application to Catamaran Wetdecks. (Dr.Ing. Thesis)
MTA-99-128	Langhelle, Nina K., MK	Experimental Validation and Calibration of Nonlinear Finite Element Models for Use in Design of Aluminium Structures Exposed to Fire. (Dr.Ing. Thesis)
MTA-99-	Berstad, Are J., MK	Calculation of Fatigue Damage in Ship Structures.

129		(Dr.Ing. Thesis)
MTA-99-130	Andersen, Trond M., MM	Short Term Maintenance Planning. (Dr.Ing. Thesis)
MTA-99-131	Tveiten, Bård Wathne, MK	Fatigue Assessment of Welded Aluminium Ship Details. (Dr.Ing. Thesis)
MTA-99-132	Søreide, Fredrik, MP	Applications of underwater technology in deep water archaeology. Principles and practice. (Dr.Ing. Thesis)
MTA-99-133	Tønnessen, Rune, MH	A Finite Element Method Applied to Unsteady Viscous Flow Around 2D Blunt Bodies With Sharp Corners. (Dr.Ing. Thesis)
MTA-99-134	Elvekrok, Dag R., MP	Engineering Integration in Field Development Projects in the Norwegian Oil and Gas Industry. The Supplier Management of Norne. (Dr.Ing. Thesis)
MTA-99-135	Fagerholt, Kjetil, MP	Optimeringsbaserte Metoder for Ruteplanlegging innen skipsfart. (Dr.Ing. Thesis)
MTA-99-136	Bysveen, Marie, MM	Visualization in Two Directions on a Dynamic Combustion Rig for Studies of Fuel Quality. (Dr.Ing. Thesis)
MTA-2000-137	Storteig, Eskild, MM	Dynamic characteristics and leakage performance of liquid annular seals in centrifugal pumps. (Dr.Ing. Thesis)
MTA-2000-138	Sagli, Gro, MK	Model uncertainty and simplified estimates of long term extremes of hull girder loads in ships. (Dr.Ing. Thesis)
MTA-2000-139	Tronstad, Harald, MK	Nonlinear analysis and design of cable net structures like fishing gear based on the finite element method. (Dr.Ing. Thesis)
MTA-2000-140	Kroneberg, André, MP	Innovation in shipping by using scenarios. (Dr.Ing. Thesis)
MTA-2000-141	Haslum, Herbjørn Alf, MH	Simplified methods applied to nonlinear motion of spar platforms. (Dr.Ing. Thesis)
MTA-2001-142	Samdal, Ole Johan, MM	Modelling of Degradation Mechanisms and Stressor Interaction on Static Mechanical Equipment Residual Lifetime. (Dr.Ing. Thesis)
MTA-2001-143	Baarholm, Rolf Jarle, MH	Theoretical and experimental studies of wave impact underneath decks of offshore platforms. (Dr.Ing. Thesis)
MTA-2001-144	Wang, Lihua, MK	Probabilistic Analysis of Nonlinear Wave-induced Loads on Ships. (Dr.Ing. Thesis)
MTA-2001-145	Kristensen, Odd H. Holt, MK	Ultimate Capacity of Aluminium Plates under Multiple Loads, Considering HAZ Properties. (Dr.Ing. Thesis)
MTA-2001-146	Greco, Marilena, MH	A Two-Dimensional Study of Green-Water

		Loading. (Dr.Ing. Thesis)
MTA-2001-147	Heggelund, Svein E., MK	Calculation of Global Design Loads and Load Effects in Large High Speed Catamarans. (Dr.Ing. Thesis)
MTA-2001-148	Babalola, Olusegun T., MK	Fatigue Strength of Titanium Risers – Defect Sensitivity. (Dr.Ing. Thesis)
MTA-2001-149	Mohammed, Abuu K., MK	Nonlinear Shell Finite Elements for Ultimate Strength and Collapse Analysis of Ship Structures. (Dr.Ing. Thesis)
MTA-2002-150	Holmedal, Lars E., MH	Wave-current interactions in the vicinity of the sea bed. (Dr.Ing. Thesis)
MTA-2002-151	Rognebakke, Olav F., MH	Sloshing in rectangular tanks and interaction with ship motions. (Dr.Ing. Thesis)
MTA-2002-152	Lader, Pål Furset, MH	Geometry and Kinematics of Breaking Waves. (Dr.Ing. Thesis)
MTA-2002-153	Yang, Qinzheng, MH	Wash and wave resistance of ships in finite water depth. (Dr.Ing. Thesis)
MTA-2002-154	Melhus, Øyvin, MM	Utilization of VOC in Diesel Engines. Ignition and combustion of VOC released by crude oil tankers. (Dr.Ing. Thesis)
MTA-2002-155	Ronæss, Marit, MH	Wave Induced Motions of Two Ships Advancing on Parallel Course. (Dr.Ing. Thesis)
MTA-2002-156	Økland, Ole D., MK	Numerical and experimental investigation of whipping in twin hull vessels exposed to severe wet deck slamming. (Dr.Ing. Thesis)
MTA-2002-157	Ge, Chunhua, MK	Global Hydroelastic Response of Catamarans due to Wet Deck Slamming. (Dr.Ing. Thesis)
MTA-2002-158	Byklum, Eirik, MK	Nonlinear Shell Finite Elements for Ultimate Strength and Collapse Analysis of Ship Structures. (Dr.Ing. Thesis)
IMT-2003-1	Chen, Haibo, MK	Probabilistic Evaluation of FPSO-Tanker Collision in Tandem Offloading Operation. (Dr.Ing. Thesis)
IMT-2003-2	Skaugset, Kjetil Bjørn, MK	On the Suppression of Vortex Induced Vibrations of Circular Cylinders by Radial Water Jets. (Dr.Ing. Thesis)
IMT-2003-3	Chezhian, Muthu	Three-Dimensional Analysis of Slamming. (Dr.Ing. Thesis)
IMT-2003-4	Buhaug, Øyvind	Deposit Formation on Cylinder Liner Surfaces in Medium Speed Engines. (Dr.Ing. Thesis)
IMT-2003-5	Tregde, Vidar	Aspects of Ship Design: Optimization of Aft Hull with Inverse Geometry Design. (Dr.Ing. Thesis)
IMT-	Wist, Hanne Therese	Statistical Properties of Successive Ocean Wave

2003-6		Parameters. (Dr.Ing. Thesis)
IMT-2004-7	Ransau, Samuel	Numerical Methods for Flows with Evolving Interfaces. (Dr.Ing. Thesis)
IMT-2004-8	Soma, Torkel	Blue-Chip or Sub-Standard. A data interrogation approach of identity safety characteristics of shipping organization. (Dr.Ing. Thesis)
IMT-2004-9	Ersdal, Svein	An experimental study of hydrodynamic forces on cylinders and cables in near axial flow. (Dr.Ing. Thesis)
IMT-2005-10	Brodtkorb, Per Andreas	The Probability of Occurrence of Dangerous Wave Situations at Sea. (Dr.Ing. Thesis)
IMT-2005-11	Yttervik, Rune	Ocean current variability in relation to offshore engineering. (Dr.Ing. Thesis)
IMT-2005-12	Fredheim, Arne	Current Forces on Net-Structures. (Dr.Ing. Thesis)
IMT-2005-13	Heggernes, Kjetil	Flow around marine structures. (Dr.Ing. Thesis
IMT-2005-14	Fouques, Sebastien	Lagrangian Modelling of Ocean Surface Waves and Synthetic Aperture Radar Wave Measurements. (Dr.Ing. Thesis)
IMT-2006-15	Holm, Håvard	Numerical calculation of viscous free surface flow around marine structures. (Dr.Ing. Thesis)
IMT-2006-16	Bjørheim, Lars G.	Failure Assessment of Long Through Thickness Fatigue Cracks in Ship Hulls. (Dr.Ing. Thesis)
IMT-2006-17	Hansson, Lisbeth	Safety Management for Prevention of Occupational Accidents. (Dr.Ing. Thesis)
IMT-2006-18	Zhu, Xinying	Application of the CIP Method to Strongly Nonlinear Wave-Body Interaction Problems. (Dr.Ing. Thesis)
IMT-2006-19	Reite, Karl Johan	Modelling and Control of Trawl Systems. (Dr.Ing. Thesis)
IMT-2006-20	Smogeli, Øyvind Notland	Control of Marine Propellers. From Normal to Extreme Conditions. (Dr.Ing. Thesis)
IMT-2007-21	Storhaug, Gaute	Experimental Investigation of Wave Induced Vibrations and Their Effect on the Fatigue Loading of Ships. (Dr.Ing. Thesis)
IMT-2007-22	Sun, Hui	A Boundary Element Method Applied to Strongly Nonlinear Wave-Body Interaction Problems. (PhD Thesis, CeSOS)
IMT-2007-23	Rustad, Anne Marthine	Modelling and Control of Top Tensioned Risers. (PhD Thesis, CeSOS)
IMT-2007-24	Johansen, Vegar	Modelling flexible slender system for real-time simulations and control applications
IMT-2007-25	Wroldsen, Anders Sunde	Modelling and control of tensegrity structures.

		(PhD Thesis, CeSOS)
IMT-2007-26	Aronsen, Kristoffer Høye	An experimental investigation of in-line and combined inline and cross flow vortex induced vibrations. (Dr. avhandling, IMT)
IMT-2007-27	Gao, Zhen	Stochastic Response Analysis of Mooring Systems with Emphasis on Frequency-domain Analysis of Fatigue due to Wide-band Response Processes (PhD Thesis, CeSOS)
IMT-2007-28	Thorstensen, Tom Anders	Lifetime Profit Modelling of Ageing Systems Utilizing Information about Technical Condition. (Dr.ing. thesis, IMT)
IMT-2008-29	Refsnes, Jon Erling Gorset	Nonlinear Model-Based Control of Slender Body AUVs (PhD Thesis, IMT)
IMT-2008-30	Berntsen, Per Ivar B.	Structural Reliability Based Position Mooring. (PhD-Thesis, IMT)
IMT-2008-31	Ye, Naiquan	Fatigue Assessment of Aluminium Welded Box-stiffener Joints in Ships (Dr.ing. thesis, IMT)
IMT-2008-32	Radan, Damir	Integrated Control of Marine Electrical Power Systems. (PhD-Thesis, IMT)
IMT-2008-33	Thomassen, Paul	Methods for Dynamic Response Analysis and Fatigue Life Estimation of Floating Fish Cages. (Dr.ing. thesis, IMT)
IMT-2008-34	Pákozdi, Csaba	A Smoothed Particle Hydrodynamics Study of Two-dimensional Nonlinear Sloshing in Rectangular Tanks. (Dr.ing.thesis, IMT/ CeSOS)
IMT-2007-35	Grytøyr, Guttorm	A Higher-Order Boundary Element Method and Applications to Marine Hydrodynamics. (Dr.ing.thesis, IMT)
IMT-2008-36	Drummen, Ingo	Experimental and Numerical Investigation of Nonlinear Wave-Induced Load Effects in Containerships considering Hydroelasticity. (PhD thesis, CeSOS)
IMT-2008-37	Skejic, Renato	Maneuvering and Seakeeping of a Singel Ship and of Two Ships in Interaction. (PhD-Thesis, CeSOS)
IMT-2008-38	Harlem, Alf	An Age-Based Replacement Model for Repairable Systems with Attention to High-Speed Marine Diesel Engines. (PhD-Thesis, IMT)
IMT-2008-39	Alsos, Hagbart S.	Ship Grounding. Analysis of Ductile Fracture, Bottom Damage and Hull Girder Response. (PhD-thesis, IMT)
IMT-2008-40	Graczyk, Mateusz	Experimental Investigation of Sloshing Loading and Load Effects in Membrane LNG Tanks Subjected to Random Excitation. (PhD-thesis, CeSOS)
IMT-2008-41	Taghipour, Reza	Efficient Prediction of Dynamic Response for Flexible amd Multi-body Marine Structures. (PhD-

		thesis, CeSOS)
IMT-2008-42	Ruth, Eivind	Propulsion control and thrust allocation on marine vessels. (PhD thesis, CeSOS)
IMT-2008-43	Nystad, Bent Helge	Technical Condition Indexes and Remaining Useful Life of Aggregated Systems. PhD thesis, IMT
IMT-2008-44	Soni, Prashant Kumar	Hydrodynamic Coefficients for Vortex Induced Vibrations of Flexible Beams, PhD thesis, CeSOS
IMT-2009-45	Amlashi, Hadi K.K.	Ultimate Strength and Reliability-based Design of Ship Hulls with Emphasis on Combined Global and Local Loads. PhD Thesis, IMT
IMT-2009-46	Pedersen, Tom Arne	Bond Graph Modelling of Marine Power Systems. PhD Thesis, IMT
IMT-2009-47	Kristiansen, Trygve	Two-Dimensional Numerical and Experimental Studies of Piston-Mode Resonance. PhD-Thesis, CeSOS
IMT-2009-48	Ong, Muk Chen	Applications of a Standard High Reynolds Number Model and a Stochastic Scour Prediction Model for Marine Structures. PhD-thesis, IMT
IMT-2009-49	Hong, Lin	Simplified Analysis and Design of Ships subjected to Collision and Grounding. PhD-thesis, IMT
IMT-2009-50	Koushan, Kamran	Vortex Induced Vibrations of Free Span Pipelines, PhD thesis, IMT
IMT-2009-51	Korsvik, Jarl Eirik	Heuristic Methods for Ship Routing and Scheduling. PhD-thesis, IMT
IMT-2009-52	Lee, Jihoon	Experimental Investigation and Numerical in Analyzing the Ocean Current Displacement of Longlines. Ph.d.-Thesis, IMT.
IMT-2009-53	Vestbøstad, Tone Gran	A Numerical Study of Wave-in-Deck Impact usin a Two-Dimensional Constrained Interpolation Profile Method, Ph.d.thesis, CeSOS.
IMT-2009-54	Bruun, Kristine	Bond Graph Modelling of Fuel Cells for Marine Power Plants. Ph.d.-thesis, IMT
IMT 2009-55	Holstad, Anders	Numerical Investigation of Turbulence in a Sekwed Three-Dimensional Channel Flow, Ph.d.-thesis, IMT.
IMT 2009-56	Ayala-Uraga, Efren	Reliability-Based Assessment of Deteriorating Ship-shaped Offshore Structures, Ph.d.-thesis, IMT
IMT 2009-57	Kong, Xiangjun	A Numerical Study of a Damaged Ship in Beam Sea Waves. Ph.d.-thesis, IMT/CeSOS.
IMT 2010-58	Kristiansen, David	Wave Induced Effects on Floaters of Aquaculture Plants, Ph.d.-thesis, CeSOS.

IMT 2010-59	Ludvigsen, Martin	An ROV-Toolbox for Optical and Acoustic Scientific Seabed Investigation. Ph.d.-thesis IMT.
IMT 2010-60	Hals, Jørgen	Modelling and Phase Control of Wave-Energy Converters. Ph.d.thesis, CeSOS.
IMT 2010- 61	Shu, Zhi	Uncertainty Assessment of Wave Loads and Ultimate Strength of Tankers and Bulk Carriers in a Reliability Framework. Ph.d. Thesis, IMT/ CeSOS
IMT 2010-62	Shao, Yanlin	Numerical Potential-Flow Studies on Weakly-Nonlinear Wave-Body Interactions with/without Small Forward Speed, Ph.d.thesis,CeSOS.
IMT 2010-63	Califano, Andrea	Dynamic Loads on Marine Propellers due to Intermittent Ventilation. Ph.d.thesis, IMT.
IMT 2010-64	El Khoury, George	Numerical Simulations of Massively Separated Turbulent Flows, Ph.d.-thesis, IMT
IMT 2010-65	Seim, Knut Sponheim	Mixing Process in Dense Overflows with Emphasis on the Faroe Bank Channel Overflow. Ph.d.thesis, IMT
IMT 2010-66	Jia, Huirong	Structural Analysis of Intect and Damaged Ships in a Collission Risk Analysis Perspective. Ph.d.thesis CeSoS.
IMT 2010-67	Jiao, Linlin	Wave-Induced Effects on a Pontoon-type Very Large Floating Structures (VLFS). Ph.D.-thesis, CeSOS.
IMT 2010-68	Abrahamsen, Bjørn Christian	Sloshing Induced Tank Roof with Entrapped Air Pocket. Ph.d.thesis, CeSOS.
IMT 2011-69	Karimirad, Madjid	Stochastic Dynamic Response Analysis of Spar-Type Wind Turbines with Catenary or Taut Mooring Systems. Ph.d.-thesis, CeSOS.
IMT - 2011-70	Erlend Meland	Condition Monitoring of Safety Critical Valves. Ph.d.-thesis, IMT.
IMT – 2011-71	Yang, Limin	Stochastic Dynamic System Analysis of Wave Energy Converter with Hydraulic Power Take-Off, with Particular Reference to Wear Damage Analysis, Ph.d. Thesis, CeSOS.
IMT – 2011-72	Visscher, Jan	Application of Particla Image Velocimetry on Turbulent Marine Flows, Ph.d.Thesis, IMT.
IMT – 2011-73	Su, Biao	Numerical Predictions of Global and Local Ice Loads on Ships. Ph.d.Thesis, CeSOS.
IMT – 2011-74	Liu, Zhenhui	Analytical and Numerical Analysis of Iceberg Collision with Ship Structures. Ph.d.Thesis, IMT.
IMT – 2011-75	Aarsæther, Karl Gunnar	Modeling and Analysis of Ship Traffic by Observation and Numerical Simulation. Ph.d.Thesis, IMT.

Imt – 2011-76	Wu, Jie	Hydrodynamic Force Identification from Stochastic Vortex Induced Vibration Experiments with Slender Beams. Ph.d.Thesis, IMT.
Imt – 2011-77	Amini, Hamid	Azimuth Propulsors in Off-design Conditions. Ph.d.Thesis, IMT.
IMT – 2011-78	Nguyen, Tan-Hoi	Toward a System of Real-Time Prediction and Monitoring of Bottom Damage Conditions During Ship Grounding. Ph.d.thesis, IMT.
IMT- 2011-79	Tavakoli, Mohammad T.	Assessment of Oil Spill in Ship Collision and Grounding, Ph.d.thesis, IMT.
IMT- 2011-80	Guo, Bingjie	Numerical and Experimental Investigation of Added Resistance in Waves. Ph.d.Thesis, IMT.
IMT- 2011-81	Chen, Qiaofeng	Ultimate Strength of Aluminium Panels, considering HAZ Effects, IMT
IMT- 2012-82	Kota, Ravikiran S.	Wave Loads on Decks of Offshore Structures in Random Seas, CeSOS.
IMT- 2012-83	Sten, Ronny	Dynamic Simulation of Deep Water Drilling Risers with Heave Compensating System, IMT.
IMT- 2012-84	Berle, Øyvind	Risk and resilience in global maritime supply chains, IMT.
IMT- 2012-85	Fang, Shaoji	Fault Tolerant Position Mooring Control Based on Structural Reliability, CeSOS.
IMT- 2012-86	You, Jikun	Numerical studies on wave forces and moored ship motions in intermediate and shallow water, CeSOS.
IMT- 2012-87	Xiang ,Xu	Maneuvering of two interacting ships in waves, CeSOS
IMT- 2012-88	Dong, Wenbin	Time-domain fatigue response and reliability analysis of offshore wind turbines with emphasis on welded tubular joints and gear components, CeSOS
IMT- 2012-89	Zhu, Suji	Investigation of Wave-Induced Nonlinear Load Effects in Open Ships considering Hull Girder Vibrations in Bending and Torsion, CeSOS
IMT- 2012-90	Zhou, Li	Numerical and Experimental Investigation of Station-keeping in Level Ice, CeSOS
IMT- 2012-91	Ushakov, Sergey	Particulate matter emission characteristics from diesel enignes operating on conventional and alternative marine fuels, IMT
IMT- 2013-1	Yin, Decao	Experimental and Numerical Analysis of Combined In-line and Cross-flow Vortex Induced Vibrations, CeSOS

IMT-2013-2	Kurniawan, Adi	Modelling and geometry optimisation of wave energy converters, CeSOS
IMT-2013-3	Al Ryati, Nabil	Technical condition indexes doe auxiliary marine diesel engines, IMT
IMT-2013-4	Firoozkoohi, Reza	Experimental, numerical and analytical investigation of the effect of screens on sloshing, CeSOS
IMT-2013-5	Ommani, Babak	Potential-Flow Predictions of a Semi-Displacement Vessel Including Applications to Calm Water Broaching, CeSOS
IMT-2013-6	Xing, Yihan	Modelling and analysis of the gearbox in a floating spar-type wind turbine, CeSOS
IMT-7-2013	Balland, Océane	Optimization models for reducing air emissions from ships, IMT
IMT-8-2013	Yang, Dan	Transitional wake flow behind an inclined flat plate-----Computation and analysis, IMT
IMT-9-2013	Abdillah, Suyuthi	Prediction of Extreme Loads and Fatigue Damage for a Ship Hull due to Ice Action, IMT
IMT-10-2013	Ramìrez, Pedro Agustìn Pèrez	Ageing management and life extension of technical systems- Concepts and methods applied to oil and gas facilities, IMT
IMT-11-2013	Chuang, Zhenju	Experimental and Numerical Investigation of Speed Loss due to Seakeeping and Maneuvering. IMT
IMT-12-2013	Etemaddar, Mahmoud	Load and Response Analysis of Wind Turbines under Atmospheric Icing and Controller System Faults with Emphasis on Spar Type Floating Wind Turbines, IMT
IMT-13-2013	Lindstad, Haakon	Strategies and measures for reducing maritime CO2 emissons, IMT
IMT-14-2013	Haris, Sabril	Damage interaction analysis of ship collisions, IMT
IMT-15-2013	Shainee, Mohamed	Conceptual Design, Numerical and Experimental Investigation of a SPM Cage Concept for Offshore Mariculture, IMT
IMT-16-2013	Gansel, Lars	Flow past porous cylinders and effects of biofouling and fish behavior on the flow in and around Atlantic salmon net cages, IMT
IMT-17-2013	Gaspar, Henrique	Handling Aspects of Complexity in Conceptual Ship Design, IMT
IMT-18-2013	Thys, Maxime	Theoretical and Experimental Investigation of a Free Running Fishing Vessel at Small Frequency of Encounter, CeSOS
IMT-19-2013	Aglen, Ida	VIV in Free Spanning Pipelines, CeSOS

IMT-1-2014	Song, An	Theoretical and experimental studies of wave diffraction and radiation loads on a horizontally submerged perforated plate, CeSOS
IMT-2-2014	Rogne, Øyvind Ygre	Numerical and Experimental Investigation of a Hinged 5-body Wave Energy Converter, CeSOS
IMT-3-2014	Dai, Lijuan	Safe and efficient operation and maintenance of offshore wind farms ,IMT
IMT-4-2014	Bachynski, Erin Elizabeth	Design and Dynamic Analysis of Tension Leg Platform Wind Turbines, CeSOS
IMT-5-2014	Wang, Jingbo	Water Entry of Freefall Wedged – Wedge motions and Cavity Dynamics, CeSOS
IMT-6-2014	Kim, Ekaterina	Experimental and numerical studies related to the coupled behavior of ice mass and steel structures during accidental collisions, IMT
IMT-7-2014	Tan, Xiang	Numerical investigation of ship's continuous- mode icebreaking in leverl ice, CeSOS
IMT-8-2014	Muliawan, Made Jaya	Design and Analysis of Combined Floating Wave and Wind Power Facilities, with Emphasis on Extreme Load Effects of the Mooring System, CeSOS
IMT-9-2014	Jiang, Zhiyu	Long-term response analysis of wind turbines with an emphasis on fault and shutdown conditions, IMT
IMT-10-2014	Dukan, Fredrik	ROV Motion Control Systems, IMT
IMT-11-2014	Grimsmo, Nils I.	Dynamic simulations of hydraulic cylinder for heave compensation of deep water drilling risers, IMT
IMT-12-2014	Kvittem, Marit I.	Modelling and response analysis for fatigue design of a semisubmersible wind turbine, CeSOS
IMT-13-2014	Akhtar, Juned	The Effects of Human Fatigue on Risk at Sea, IMT
IMT-14-2014	Syahroni, Nur	Fatigue Assessment of Welded Joints Taking into Account Effects of Residual Stress, IMT
IMT-1-2015	Bøckmann, Eirik	Wave Propulsion of ships, IMT
IMT-2-2015	Wang, Kai	Modelling and dynamic analysis of a semi-submersible floating vertical axis wind turbine, CeSOS
IMT-3-2015	Fredriksen, Arnt Gunvald	A numerical and experimental study of a two-dimensional body with moonpool in waves and current, CeSOS
IMT-4-2015	Jose Patricio Gallardo Canabes	Numerical studies of viscous flow around bluff bodies, IMT

IMT-5-2015	Vegard Longva	Formulation and application of finite element techniques for slender marine structures subjected to contact interactions, IMT
IMT-6-2015	Jacobus De Vaal	Aerodynamic modelling of floating wind turbines, CeSOS
IMT-7-2015	Fachri Nasution	Fatigue Performance of Copper Power Conductors, IMT
IMT-8-2015	Oleh I Karpa	Development of bivariate extreme value distributions for applications in marine technology,CeSOS
IMT-9-2015	Daniel de Almeida Fernandes	An output feedback motion control system for ROVs, AMOS
IMT-10-2015	Bo Zhao	Particle Filter for Fault Diagnosis: Application to Dynamic Positioning Vessel and Underwater Robotics, CeSOS
IMT-11-2015	Wenting Zhu	Impact of emission allocation in maritime transportation, IMT
IMT-12-2015	Amir Rasekhi Nejad	Dynamic Analysis and Design of Gearboxes in Offshore Wind Turbines in a Structural Reliability Perspective, CeSOS
IMT-13-2015	Arturo Jesùs Ortega Malca	Dynamic Response of Flexibles Risers due to Unsteady Slug Flow, CeSOS
IMT-14-2015	Dagfinn Husjord	Guidance and decision-support system for safe navigation of ships operating in close proximity, IMT
IMT-15-2015	Anirban Bhattacharyya	Ducted Propellers: Behaviour in Waves and Scale Effects, IMT
IMT-16-2015	Qin Zhang	Image Processing for Ice Parameter Identification in Ice Management, IMT
IMT-1-2016	Vincentius Rumawas	Human Factors in Ship Design and Operation: An Experiential Learning, IMT
IMT-2-2016	Martin Storheim	Structural response in ship-platform and ship-ice collisions, IMT
IMT-3-2016	Mia Abrahamsen Prsic	Numerical Simulations of the Flow around single and Tandem Circular Cylinders Close to a Plane Wall, IMT
IMT-4-2016	Tufan Arslan	Large-eddy simulations of cross-flow around ship sections, IMT

IMT-5-2016	Pierre Yves-Henry	Parametrisation of aquatic vegetation in hydraulic and coastal research,IMT
IMT-6-2016	Lin Li	Dynamic Analysis of the Instalation of Monopiles for Offshore Wind Turbines, CeSOS
IMT-7-2016	Øivind Kåre Kjerstad	Dynamic Positioning of Marine Vessels in Ice, IMT
IMT-8-2016	Xiaopeng Wu	Numerical Analysis of Anchor Handling and Fish Trawling Operations in a Safety Perspective, CeSOS
IMT-9-2016	Zhengshun Cheng	Integrated Dynamic Analysis of Floating Vertical Axis Wind Turbines, CeSOS
IMT-10-2016	Ling Wan	Experimental and Numerical Study of a Combined Offshore Wind and Wave Energy Converter Concept
IMT-11-2016	Wei Chai	Stochastic dynamic analysis and reliability evaluation of the roll motion for ships in random seas, CeSOS
IMT-12-2016	Øyvind Selnes Patricksson	Decision support for conceptual ship design with focus on a changing life cycle and future uncertainty, IMT
IMT-13-2016	Mats Jørgen Thorsen	Time domain analysis of vortex-induced vibrations, IMT
IMT-14-2016	Edgar McGuinness	Safety in the Norwegian Fishing Fleet – Analysis and measures for improvement, IMT
IMT-15-2016	Sepideh Jafarzadeh	Energy effiency and emission abatement in the fishing fleet, IMT
IMT-16-2016	Wilson Ivan Guachamin Acero	Assessment of marine operations for offshore wind turbine installation with emphasis on response-based operational limits, IMT
IMT-17-2016	Mauro Candeloro	Tools and Methods for Autonomous Operations on Seabed and Water Coumn using Underwater Vehicles, IMT
IMT-18-2016	Valentin Chabaud	Real-Time Hybrid Model Testing of Floating Wind Tubines, IMT
IMT-1-2017	Mohammad Saud Afzal	Three-dimensional streaming in a sea bed boundary layer
IMT-2-2017	Peng Li	A Theoretical and Experimental Study of Wave-induced Hydroelastic Response of a Circular Floating Collar
IMT-3-2017	Martin Bergström	A simulation-based design method for arctic maritime transport systems

IMT-4-2017	Bhushan Taskar	The effect of waves on marine propellers and propulsion
IMT-5-2017	Mohsen Bardestani	A two-dimensional numerical and experimental study of a floater with net and sinker tube in waves and current
IMT-6-2017	Fatemeh Hoseini Dadmarzi	Direct Numerical Simualtion of turbulent wakes behind different plate configurations
IMT-7-2017	Michel R. Miyazaki	Modeling and control of hybrid marine power plants
IMT-8-2017	Giri Rajasekhar Gunnu	Safety and effiency enhancement of anchor handling operations with particular emphasis on the stability of anchor handling vessels
IMT-9-2017	Kevin Koosup Yum	Transient Performance and Emissions of a Turbocharged Diesel Engine for Marine Power Plants
IMT-10-2017	Zhaolong Yu	Hydrodynamic and structural aspects of ship collisions
IMT-11-2017	Martin Hassel	Risk Analysis and Modelling of Allisions between Passing Vessels and Offshore Installations
IMT-12-2017	Astrid H. Brodtkorb	Hybrid Control of Marine Vessels – Dynamic Positioning in Varying Conditions
IMT-13-2017	Kjersti Bruserud	Simultaneous stochastic model of waves and current for prediction of structural design loads
IMT-14-2017	Finn-Idar Grøtta Giske	Long-Term Extreme Response Analysis of Marine Structures Using Inverse Reliability Methods
IMT-15-2017	Stian Skjong	Modeling and Simulation of Maritime Systems and Operations for Virtual Prototyping using co-Simulations
IMT-1-2018	Yingguang Chu	Virtual Prototyping for Marine Crane Design and Operations
IMT-2-2018	Sergey Gavrilin	Validation of ship manoeuvring simulation models
IMT-3-2018	Jeevith Hegde	Tools and methods to manage risk in autonomous subsea inspection,maintenance and repair operations
IMT-4-2018	Ida M. Strand	Sea Loads on Closed Flexible Fish Cages
IMT-5-2018	Erlend Kvinge Jørgensen	Navigation and Control of Underwater Robotic Vehicles

IMT-6-2018	Bård Stovner	Aided Intertial Navigation of Underwater Vehicles
IMT-7-2018	Erlend Liavåg Grotle	Thermodynamic Response Enhanced by Sloshing in Marine LNG Fuel Tanks
IMT-8-2018	Børge Rokseth	Safety and Verification of Advanced Maritime Vessels
IMT-9-2018	Jan Vidar Ulveseter	Advances in Semi-Empirical Time Domain Modelling of Vortex-Induced Vibrations
IMT-10-2018	Chenyu Luan	Design and analysis for a steel braceless semi-submersible hull for supporting a 5-MW horizontal axis wind turbine
IMT-11-2018	Carl Fredrik Rehn	Ship Design under Uncertainty
IMT-12-2018	Øyvind Ødegård	Towards Autonomous Operations and Systems in Marine Archaeology
IMT-13-2018	Stein Melvær Nornes	Guidance and Control of Marine Robotics for Ocean Mapping and Monitoring
IMT-14-2018	Petter Norgren	Autonomous Underwater Vehicles in Arctic Marine Operations: Arctic marine research and ice monitoring
IMT-15-2018	Minjoo Choi	Modular Adaptable Ship Design for Handling Uncertainty in the Future Operating Context
MT-16-2018	Ole Alexander Eidsvik	Dynamics of Remotely Operated Underwater Vehicle Systems
IMT-17-2018	Mahdi Ghane	Fault Diagnosis of Floating Wind Turbine Drivetrain- Methodologies and Applications
IMT-18-2018	Christoph Alexander Thieme	Risk Analysis and Modelling of Autonomous Marine Systems
IMT-19-2018	Yugao Shen	Operational limits for floating-collar fish farms in waves and current, without and with well-boat presence